

**COLLOIDAL PROCESSING OF METAL OXIDE-  
CARBON NANOTUBE NANOCOMPOSITE  
ELECTRODES FOR SUPERCAPACITORS**

COLLOIDAL PROCESSING OF METAL OXIDE-CARBON NANOTUBE  
NANOCOMPOSITE ELECTRODES FOR SUPERCAPACITORS

BY WENJUAN YANG, M.Sc.

A Thesis Submitted to the School of Graduate Studies in Partial Fulfillment of the  
Requirements for the Degree Doctor of Philosophy

McMaster University © Copyright by Wenjuan Yang, July 2024

McMaster University DOCTOR OF PHILOSOPHY (2024) Hamilton, Ontario (Materials Science and Engineering)

TITLE: Colloidal Processing of Metal oxide-Carbon Nanotube  
Nanocomposite Electrodes for Supercapacitors

AUTHOR: BY Wenjuan Yang, M.Sc. (McMaster University)

SUPERVISOR: Prof. Igor Zhitomirsky

NUMBER OF PAGES: XLI , 283

## Lay Abstract

Due to advancements in technology and the pursuit of a better quality of life, there has been a striking increase in energy consumption. Consequently, many scientists have focused on clean and renewable energy sources to reduce the depletion of non-renewable fossil fuels and carbon emissions. Among these innovations, novel energy storage devices such as capacitors, supercapacitors (SCs) and batteries have garnered much attention.

Electrochemical supercapacitors (ES), in particular, effectively balance the limitations of conventional capacitors' low energy density and batteries' low power density. Because of their relatively attractive power and energy densities, long-time stability, and fast charge-discharge speed, SCs have attracted many researchers.

Our research has achieved significant progress in developing advanced nanocomposite electrode materials and fabricating high-performance SCs through innovative colloidal technologies. By introducing appropriate capping agents during the preparation of  $\text{Mn}_3\text{O}_4$  particles, we have fabricated a cathode with a capacitance of  $9.13 \text{ F cm}^{-2}$  at  $40 \text{ mg cm}^{-2}$  mass loading. Additionally, we used HEBM to prevent particle agglomeration and enhance electrode performance, resulting in a capacitance increase from  $0.69$  to  $3.75 \text{ F cm}^{-2}$  for the LSM electrode at the same mass loading. The use of suitable dispersants has positively impacted the capacitive behavior of active materials, enabling us to successfully prepare symmetric SCs with a high capacitance of  $0.92 \text{ F cm}^{-2}$  within an operating voltage range of

0-1.6 V at an active mass loading of 80 mg cm<sup>-2</sup>.

## Abstract

There is considerable interest in ESs as they have huge potential in energy storage devices, play a key role in advanced power systems, and have the potential to revolutionize hybrid vehicles and electronics. SCs are known for their hybrid power and energy density, fast charge and discharge rates, and long-term cycling stability. The performance of SCs depend largely on the specific capacitance of their electrodes.

Among various cathode materials, unitary transition metal oxides (TMOs), especially manganese oxide, are favored due to their multiple oxidation states, excellent redox properties, abundant availability, simple synthesis, and cost-effectiveness. The low intrinsic conductivity of manganese oxide can be significantly enhanced by adding conductive additives such as multi-walled carbon nanotubes (CNTs). We are developing a novel colloid processing technique to synthesize  $\text{MnO}_x$ -CNT nanocomposites with enhanced electronic conductivity. Our research involves the use of advanced capping agents and co-dispersants to fabricate  $\text{MnO}_x$ -CNTs nanocomposite electrodes that exhibit superior performance and bypass the lengthy activation process commonly cited in our previous results. Testing results indicate that functional catechol-based molecules, including quercetin (QC), rhamnolipid (RL), tetrahydroxy-1,4-quinone (TQ), catechin (CT) and gallicyanine (GA), have excellent dispersion properties for  $\text{MnO}_x$  and CNTs. These compounds form uniform and stable suspensions that improve the nanostructure and electrochemical performance of the electrodes. They also serve as capping agents for

Mn<sub>3</sub>O<sub>4</sub> synthesis, reducing agglomeration and improving morphology. Additionally, murexide was tested as a co-dispersant and capping agent due to its chelating properties, forming a tridentate bond with Mn atoms and adsorbing onto the carbon rings of CNTs. As a capping agent, murexide can promote electrostatic dispersion by forming strong tridentate bonds with Mn<sub>3</sub>O<sub>4</sub> particle surfaces, thereby reducing agglomeration and improving composite morphology.

In addition, binary (MnFe<sub>2</sub>O<sub>4</sub>) or ternary (La<sub>0.65</sub>Sr<sub>0.35</sub>MnO<sub>3</sub>(LSM)) metal oxides can overcome the limitations of single metal oxides through the synergistic effect between metal ions, improve capacitive performance and expand the potential window. These compounds are promising candidates as ES electrode materials. High-energy ball milling (HEBM) helps reduce particle size, enhance electrolyte contact with active material surfaces, achieve high capacitance at high active mass loading, and produce high-performance supercapacitors (SCs).

# Acknowledgements

I am profoundly grateful to my supervisor, Dr. Igor Zhitomirsky, for his unwavering support, invaluable guidance, and immense patience throughout the course of this research.

His extensive expertise in the field of High Active Mass Loading Supercapacitors and insightful foresight have been pivotal in shaping the foundation of this thesis. Dr.

Zhitomirsky is not only among the most humble, kind, and intelligent scientists I have ever had the pleasure of knowing but also a central figure without whom my Ph.D. journey would not have been as enriching.

I extend my sincere appreciation to my committee members, Dr. Xu Gu and Dr. Kish, for their invaluable suggestions and feedback during our committee meetings each year.

Heartfelt thanks go out to the numerous staff members and technicians who provided assistance whenever needed. Special appreciation to Dr. Zeynel Bayindir, Chris Butcher, Jhoynner Martinez, Victoria Jarvis, Xiaogang Li, and Alisha Digba for their unwavering support.

I also wish to acknowledge the members of Igor's lab for making each day more enjoyable in JHEA203B/B. Thank you for their assistance and encouragement in my research, studies, and daily life. To my colleagues Wenyu Liang, Sadman Sakib, Chengwei Zhang, Zhengzheng Wang, Coulton Boucher, Michael Macdonald, Dalue Tang, Silin Chen, and Mahmoud Awad, I am immensely grateful for the camaraderie and stimulating

conversations we shared.

To my family, I owe an immeasurable debt of gratitude for their unwavering love and support. Mom and Dad, thank you for standing by my decisions and for imparting your invaluable life experiences. It is a profound honor to be your child. To my sister and brother, Wenying and Wenchang, your steadfast support and companionship have been invaluable in navigating through challenges.

Finally, I extend my gratitude to all individuals who have contributed to my academic and personal growth, directly or indirectly. Your support has been indispensable on this journey.

# Declaration of Academic Achievements

This dissertation was used to fulfill the requirements of the degree Doctor of Philosophy. The major research project was conducted from September 2020 to July 2024. The results of this dissertation were published in 6 papers in peer-reviewed journals, which were listed below:

- 1) Yang, W.&; Eraky, H.&; Zhang, C.; Hitchcock, A. P.; Zhitomirsky, I. Electrochemical and scanning transmission X-ray microscopy studies of MnO<sub>2</sub> and Mn<sub>3</sub>O<sub>4</sub> for supercapacitor cathodes: Influence of fabrication method and electrochemical activation on charge storage. *Chemical Engineering Journal* 2024, 149391. (&:Authors contribute equally to this publication)
- 2) Yang, L. W.; Zhitomirsky, I. Influence of capping agents on the synthesis of Mn<sub>3</sub>O<sub>4</sub> nanostructures for supercapacitors. *ACS Applied Nano Materials* 2023, 6 (6), 4428-4436.
- 3) Yang, W.; Nawwar, M.; Zhitomirsky, I. Facile route for fabrication of ferrimagnetic Mn<sub>3</sub>O<sub>4</sub> spinel material for supercapacitors with enhanced capacitance. *Energies* 2022, 15 (5), 1812.
- 4) Yang, W.; Zhitomirsky, I. Colloidal processing of Mn<sub>3</sub>O<sub>4</sub>-carbon nanotube nanocomposite electrodes for supercapacitors. *Nanomaterials* 2022, 12 (5), 803.
- 5) Yang, W.&; Eraky, H.&; Zhang, C.; Hitchcock, A. P.; Zhitomirsky, I. Scanning transmission X-ray microscopy studies of electrochemical activation and capacitive behavior of Mn<sub>3</sub>O<sub>4</sub> supercapacitor electrodes. *Journal of Materials Chemistry A*

2022, 10 (35), 18267-18277. (&: Authors contribute equally to this publication)

- 6) Yang, Wenjuan, et al. " High pseudocapacitance of ferromagnetic  $\text{La}_{0.65}\text{Sr}_{0.35}\text{MnO}_3$ ." *Journal of Materials Science*, under review.
- 7) Yang, Wenjuan, and Igor Zhitomirsky. "Ferrimagnetic pseudocapacitive  $\text{MnFe}_2\text{O}_4$  electrodes and supercapacitor devices." *Ceramics International* (2024).

In addition to the work presented above, I have also contributed to 4 papers that are published and submitted in peer-reviewed journals and are not covered in this dissertation.

- 8) Liang, W.; Yang, W.; Sakib, S.; Zhitomirsky, I. Magnetic  $\text{CuFe}_2\text{O}_4$  nanoparticles with pseudocapacitive properties for electrical energy storage. *Molecules* 2022, 27 (16), 5313.
- 9) Yang, W.; Liang, W.; Zhitomirsky, I. Application of Rhamnolipids as Dispersing Agents for the Fabrication of Composite  $\text{MnO}_2$ -Carbon Nanotube Electrodes for Supercapacitors. *Molecules* 2022, 27 (5), 1659

---

## Table of Contents

Lay Abstract .....	III
Abstract.....	V
Acknowledgements .....	VII
Declaration of Academic Achievements .....	IX
Table of Contents .....	XI
Table of Figures.....	XVI
List of Tables.....	XXXVI
List of Abbreviations and Symbols .....	XXXVIII
Chapter 1 Introduction.....	1
Chapter 2 Literature review .....	6
2.1 The development of supercapacitors .....	6
2.2 Application of supercapacitors .....	10
2.3 Classifications of electrochemical supercapacitors .....	12
2.3.1 Electrochemical double layer Supercapacitors.....	13
2.3.2 Pseudo-Supercapacitors.....	17
2.3.3 Hybrid Supercapacitors .....	19
2.4 Electrode materials .....	21
2.4.1 Carbon-based materials for electrode of EDLCs.....	22
2.4.2 Redox-based materials.....	23
2.5 Electrolytes .....	26
2.5.1 Aqueous electrolytes.....	27
2.5.2 Organic electrolytes .....	28
2.5.3 Ionic liquids electrolyte .....	29
Chapter 3 Objectives .....	30
Chapter 4 Proposed approaches.....	33

---

4.1. Wet chemical synthesis of MnO <sub>2</sub> and Mn <sub>3</sub> O <sub>4</sub> .....	33
4.2 Application of new capping agents for Mn <sub>3</sub> O <sub>4</sub> .....	34
4.3 Development and application of new co-dispersants for MnO <sub>2</sub> , Mn <sub>3</sub> O <sub>4</sub> and La <sub>0.65</sub> Sr <sub>0.35</sub> MnO <sub>3</sub> as well as CNTs .....	34
4.4 Development of High energy ball milling (HEBM) using new dispersants.....	35
4.5 Investigation of activation mechanism of Mn <sub>3</sub> O <sub>4</sub> electrodes and development of strategies for acceleration/elimination of activation procedure.....	37
Chapter 5 References.....	38
Chapter 6 Scanning transmission X-ray microscopy studies of electrochemical activation and capacitive behavior of Mn <sub>3</sub> O <sub>4</sub> supercapacitor electrodes .....	46
6.1 Abstract .....	47
6.2 Introduction .....	48
6.3 Experimental procedures .....	51
6.3.1 Materials, synthesis of Mn <sub>3</sub> O <sub>4</sub> particles and electrode fabrication.....	51
6.3.2 Microstructure and electrochemical characterization.....	52
6.3.3 Methods: Scanning Transmission X-ray Microscopy .....	54
6.4 Results and discussion .....	56
6.4.1 Electrochemical and microstructure characterization.....	56
6.4.2 X-ray spectromicroscopy.....	62
6.5 Conclusions .....	71
6.6 Acknowledgements .....	72
6.7 Reference .....	73
6.8 Supporting Information .....	78
Chapter 7 Colloidal Processing of Mn <sub>3</sub> O <sub>4</sub> -Carbon Nanotube Nanocomposite Electrodes for Supercapacitors.....	87

---

---

7.1 Abstract	88
7.2 Introduction	88
7.3 Materials and Methods	92
7.4 Results and Discussion	94
7.5 Conclusions	110
7.6 Acknowledgments	111
7.7 References	111
7.8 Supplementary Materials:	116
Chapter 8 Facile Route for Fabrication of Ferrimagnetic Mn <sub>3</sub> O <sub>4</sub> Spinel Material for Supercapacitors with Enhanced Capacitance	118
8.1 Abstract	119
8.2 Introduction	119
8.3 Materials and Methods	123
8.3.1 Raw Materials	123
8.3.2 Synthesis of Mn <sub>3</sub> O <sub>4</sub> and Electrode Fabrication	123
8.3.3 Characterization Techniques	124
8.4 Results and Discussion	125
8.5 Conclusions	138
8.6 Acknowledgments	139
8.7 References	139
Chapter 9 Influence of Capping Agents on Synthesis of Mn <sub>3</sub> O <sub>4</sub> Nanostructures for Supercapacitors	144
9.1 Abstract	145
9.2 Introduction	146
9.3 Experimental procedures	150

---

9.4 Results and Discussion	153
9.5 Conclusions	166
9.6 Acknowledgments.	167
9.7 Supplementary Information	168
9.8 References	171
Chapter 10 Electrochemical and scanning transmission X-ray microscopy studies of MnO <sub>2</sub> and Mn <sub>3</sub> O <sub>4</sub> for supercapacitor cathodes: influence of fabrication method and electrochemical activation on charge storage	
10.1 Abstract	180
10.2 Introduction	181
10.3 Experimental procedures	185
10.3.1 Materials	185
10.3.2 Fabrication of MnO <sub>2</sub> and Mn <sub>3</sub> O <sub>4</sub> for electrodes	186
10.3.3 Fabrication of electrodes for supercapacitors	187
10.3.4 X-ray diffraction and electrochemical studies.	187
10.3.5 Scanning Transmission X-ray Microscopy	188
10.4 Results and discussion	189
10.4.1 Electrochemical and microstructure characterization	189
10.4.2 X-ray spectromicroscopy	196
10.5 Summary	208
10.6 Acknowledgements	209
10.7 References	210
10.8 Supporting Information	213
Chapter 11 Preparation of ferromagnetic perovskite La <sub>0.65</sub> Sr <sub>0.35</sub> MnO <sub>3</sub> electrodes for supercapacitor applications	
	221

11.1 Abstract	222
11.2 Introduction	222
11.3 Experimental procedures	226
11.3.1. Materials and fabrication methods	226
11.3.2 Characterization techniques	227
11.4 Results and Discussion	228
11.4.1 XRD studies and magnetic measurements	228
11.4.2 TEM and FTIR studies	229
11.4.3 SEM and electrochemical studies of the electrodes	232
11.5 Conclusions	238
11.6 Acknowledgments	239
11.7 References	239
11.8 Supplementary Information	244
Chapter 12 Ferrimagnetic pseudocapacitive MnFe <sub>2</sub> O <sub>4</sub> electrodes and supercapacitor devices	250
12.1 Abstract	251
12.2 Introduction	252
12.3 Experimental	256
12.4 Results and discussion	257
12.5 Conclusions	268
12.6 Acknowledgments	270
12.7 References	270
12.8 Supplementary Information	273
Chapter 13 Conclusions and Future work	278

---

# Table of Figures

Figure 1- 1 Ragone plot for different energy storage devices. <sup>7</sup> .....	2
Figure 1- 2 The count of scholarly publications, including articles, books, and other credible open-access sources from 2000 to 2018 (projected), derived from a search using 'supercapacitor' as a keyword on Google scholar. <sup>9</sup> .....	3
Figure 2- 1 Diagram of a parallel plate capacitor. <sup>33</sup> Reprinted with permission from MDPI. ....	6
Figure 2- 2 Development of supercapacitors in different countries. <sup>35</sup> .....	9
Figure 2- 3 Tramways in Barcelona, Spain <sup>44</sup> .....	11
Figure 2- 4 Overview of supercapacitor types and classification. <sup>47</sup> .....	12
Figure 2- 5 Schematic demonstration of the 3 types of supercapacitors: (A) EDLC, (B) Pseudocapacitor, and (C) Hybrid SC. <sup>52</sup> .....	13
Figure 2- 6 Schematic diagram of 4 types of electric double layers. <sup>53</sup> .....	14
Figure 2- 7 Charge/discharge mechanism of EDCLs. <sup>57</sup> .....	16
Figure 2- 8 Pseudo capacitance charge mechanism in supercapacitors <sup>61</sup> .....	18
Figure 2- 9 Schematic structure of a hybrid supercapacitor. <sup>64</sup> .....	20
Figure 2- 10 Schematic illustration of a supercapacitor. <sup>67</sup> .....	22
Figure 2- 11 Structural illustration of different conducting polymers. <sup>86</sup> .....	25

---

Figure 2- 12 Classification of electrolytes for ES <sup>88</sup> .....	26
Figure 2- 13 The comparison of different supercapacitor electrolytes. <sup>89</sup> .....	27
Figure 2- 14 Pourbaix diagram for water, including equilibrium regions for water <sup>91</sup> . 28	
Figure 4- 1 Chemical synthesis of Mn <sub>3</sub> O <sub>4</sub> .....	33
Figure 4- 2 (a) HEBM system and (b) schematic representation of the NPs synthesis using HEBM method with and without surfactant. <sup>98</sup> .....	36
Figure 6- 1 X-ray diffraction pattern of as-prepared Mn <sub>3</sub> O <sub>4</sub> (●-peaks corresponding to JCPDS file 001-1127).....	56
Figure 6- 2 (A) Chemical structure of QC, (B) adsorption QC on Mn <sub>3</sub> O <sub>4</sub> by chelation of surface Mn atoms. ....	58
Figure 6- 3 SEM images for as-prepared Mn <sub>3</sub> O <sub>4</sub> -MWCNT electrodes (A) without QC and (B) with QC. The scale bars in the figures represent 250 nm, and arrows show MWCNT.....	59
Figure 6- 4 (A) CVs for Mn <sub>3</sub> O <sub>4</sub> -MWCNT electrode at scan rates of (a) 5, (b) 20, (c) 50 and 100 mV s <sup>-1</sup> for VSRP 1, (B) CVs at 10 mV s <sup>-1</sup> for (a-e) VSRPs 1-5, (C) Capacitance derived from CV data for (a-c) VSRPs 1-5, (D) Nyquist plot of complex impedance for (a-c) VSRPs 1-5, (E) real and (F) imaginary components of complex capacitances derived from the complex impedance data versus	

frequency for (a-e) VSRPs 1-5. ....	59
Figure 6- 5 GCD data for current densities of (a) 3, (b) 5, (c) 7 and (d) 10 mA cm <sup>-2</sup> and (B) capacitance versus current density obtained from the GCD data.....	60
Figure 6- 6 Capacitance normalized by capacitance value for FSR cycle 1000 versus cycle number for continuous CV cycling at a scan rate of 50 mV s <sup>-1</sup> . ....	62
Figure 6- 7 (A) Quantitative Mn 2p spectra of Mn(II/III) (dark green) and Mn(IV) (red) on OD1 intensity scales. (B) Quantitative O 1s spectra of Mn(II/III) (dark green) and Mn(IV) (red) on OD1 intensity scales. ....	63
Figure 6- 8 (A) Mn 2p, (B) O 1s absorption spectra extracted from stacks measured for (a) VSRP1, (b) VSRP3 and (c) VSRP5, (C) Mn 2p, (D) O 1s absorption spectra extracted from stacks measured for (f) FSR cycle 100 and (g) FSR cycle 1000 samples. ....	64
Figure 6- 9 Mn L <sub>3</sub> and O 1s → 3d features showing conversion of Mn (II/III) to Mn(IV). (A) and (B) present (a) VSRP1, (b) VSRP2 and (c) VSRP3, (C) and (D) present (f) FSR100 and (g) FSR1000 cycle samples in comparison with as- prepared Mn <sub>3</sub> O <sub>4</sub> catalyst and MnO <sub>2</sub> reference spectra. ....	66
Figure 6- 10 Color coded composites of Mn(II/III) and Mn(IV) component maps derived by SVD fitting Mn 2p stacks measured on (A) VSRPs1, 3, 5 (a-c respectively), (B) FSR100 and FSR1000 cycle samples (f, g respectively), scale bar: 0.5 μm. Color scales are nm thickness. Color wheel indicates color	

expected for specific combinations of the red and green signals. .... 68

Figure 6- 11 Evolution of Mn(II/III) and Mn(IV) signals of (A) VSRP1, VSRP3 and VSRP5, (B) FSR100 and FSR1000 cycle sample represented in volume fractions. .... 69

Figure 6-S 1 Suspensions of (A)  $Mn_3O_4$  and (B) MWCNT, (a) without QC and (b) with QC as dispersants 7 days after preparation; mass ratio of QC: $Mn_3O_4$  and QC: MWCNT is 0.2..... 78

Figure 6-S 2. (A) Schematic diagram of scanning transmission x-ray microscopy (STXM), (B) samples on TEM grids mounted on STXM plate, (C) STXM image of the TEM grid square containing the measured region of the FSR1000 sample at 640 eV. .... 78

Figure 6-S 3 (A)  $F 1s \rightarrow a_{1g}$  absorption peak of sulfur hexafluoride ( $SF_6$ ) gas measured I (a) the  $I_o$  signal of a measurement of  $MnO_2$  in the presence of  $SF_6$  and, (b) at the hole (The inset shows the full  $F 1s$  spectrum of  $SF_6$  gas <sup>[s1]</sup>. (B) Mn(II) signal present in the  $I_o$  of Mn 2p spectra measured in STXM and used to confirm the energy scale. (a) as-prepared  $Mn_3O_4$ , (b) FSR 100 and (c) FSR1000 cycle samples, compared to the digitized spectrum of  $MnO$  <sup>[s2]</sup>..... 79

Figure 6-S 4 Nyquist plot of complex impedance for (a-c) VSRPs 1-5: experimental data 1<sup>st</sup> exp-5<sup>th</sup> exp and simulation data 1<sup>st</sup> cal-5<sup>th</sup> cal, (B) equivalent circuit used

---

for simulation.....	81
Figure 6-S 5 Comparison of the Mn 2p spectrum of MnO <sub>2</sub> from this work (STXM), with that reported in the literature by Gilbert et al., <sup>s2</sup> Toner et al. <sup>s3</sup> and Stuckey et al. <sup>s4</sup> .....	83
Figure 6-S 6 A. Mn <sub>3</sub> O <sub>4</sub> (Mn 2p) absorption spectra of (a) as-prepared catalyst, (b) digitized reference spectra from Gilbert et al. <sup>s2</sup> , (c) previously measured Mn <sub>3</sub> O <sub>4</sub> catalyst and (d) the SGM-TEY spectrum of commercial Mn <sub>3</sub> O <sub>4</sub> (Sigma). B Expansion of the Mn L <sub>3</sub> region, comparing the spectrum of the as-prepared Mn(II,III) catalyst, with the spectra of Mn <sub>3</sub> O <sub>4</sub> reported by Gilbert et al., <sup>s2</sup> and Stuckey et al. <sup>s4</sup> .....	84
Figure 6-S 7 (A) Mn 2p, (B) O 1s SGM-TEY absorption spectra of (a) VSRP1, (b) VSRP3, (c) VSRP5 and (d) FSR1000 cycles, (C) shows comparison of STXM spectra (a), (c), (e), (g), (i) and SGM-TEY spectra, (b), (d), (f), (h), (j) of as- prepared Mn <sub>3</sub> O <sub>4</sub> , VSRP1, VSRP3, VSRP5 and FSR1000 cycles respectively. ..	85
Figure 7- 1 (A) X-ray diffraction patterns for Mn <sub>3</sub> O <sub>4</sub> -MWCNT materials prepared by (a) method 1 and (b) method 2, Miller indexes are presented for Mn <sub>3</sub> O <sub>4</sub> phase, JCPDS file 001-1127, ●—(002) peak of MWCNT, JCPDS file 058-1638 , ▼— (111) peak of MnO <sub>2</sub> , JCPDS file 083-6090, (B–D) XPS data for Mn <sub>3</sub> O <sub>4</sub> - MWCNT materials prepared by (B(a) and C) method 1 and (B(b) and D) method	

2.....	95
Figure 7- 2 Chemical structure of RL. Dashed line shows rhamnose moieties. ....	97
Figure 7- 3 TEM images at different magnifications of Mn <sub>3</sub> O <sub>4</sub> prepared by method 1 (A,B) and method 2 (C,D).....	98
Figure 7- 4 FTIR spectra of (a) as received RL, (b) Mn <sub>3</sub> O <sub>4</sub> prepared without RL by method 1, (c) Mn <sub>3</sub> O <sub>4</sub> prepared without RL by method 1 and dispersed using RL, (d) Mn <sub>3</sub> O <sub>4</sub> prepared using RL as a capping agent by method 2. ....	99
Figure 7- 5 SEM images of electrodes prepared using Mn <sub>3</sub> O <sub>4</sub> -MWCNT composites prepared by (A) method 1 and (B) method 2. Arrows show areas with enlarged MWCNT content. ....	101
Figure 7- 6 (A) CVs at scan rates of (a) 2, (b) 10, (c) 20 and (d) 50 mV s <sup>-1</sup> for TP1 and (B) CVs at a scan rate of 10 mV s <sup>-1</sup> for (a) TP1, (b) TP2, (c) TP3, (d) TP4 and (e) TP5 for electrode prepared by method 1, (C) CVs at scan rates of (a) 2, (b) 10, (c) 20 and (d) 50 mV s <sup>-1</sup> for TP1 and (D) CVs at a scan rate of 10 mV s <sup>-1</sup> for (a) TP1, (b) TP2, and (c) TP3 for electrode prepared by method 2. Each TP involved testing at scan rates of 2, 5, 10, 20, 50 and 100 mV s <sup>-1</sup> . The CVs for scan rate of 10 mV s <sup>-1</sup> for each TP were selected and presented in (B, D). ....	102
Figure 7- 7 (A) Capacitance versus scan rate and (B) impedance data presented in a Nyquist plot for (a) TP 1, (b) TP 2, (c) TP 3, (d) TP 4 and (e) TP 5 for electrode prepared by method 1, (C) capacitance versus scan rate and (D) impedance data	

presented in a Nyquist plot for (a) TP 1, (b) TP 2, and (c) TP 3 for electrode prepared by method 2. .... 104

Figure 7- 8 (A) real and (B) imaginary components of complex capacitance for (a) TP 1, (b) TP 2, (c) TP 3, (d) TP 4 and (e) TP 5 for electrode prepared by method 1, (C) real and (D) imaginary components of complex capacitance for (a) TP 1, (b) TP 2, (c) TP 3 for electrode prepared by method 2. .... 106

Figure 7- 9 GCD data for electrodes prepared by (A,B) method 1 and (C,D) method 2, (A,C) charge-discharge at current densities of (a) 3, (b) 5, (c) 7 and (d) 10 mA cm<sup>-2</sup>, (B,D) capacitance versus current density dependences..... 108

Figure 7- 10 Capacitance ( $C_N$ ) normalized by capacitance value for 2000th cycle for electrodes prepared by (A) method 1 and (B) method 2, obtained from CV data at a scan rate of 50 mV s<sup>-1</sup>. .... 108

Figure 7-S 1 (A) CVs at scan rates of (a) 2, (b) 10, (c) 20 and (d) 50 mV s<sup>-1</sup> for TP 1 and (B) CVs at a scan rate of 10 mV s<sup>-1</sup> for (a) TP 1, (b) TP 2, and (c) TP 3 for electrode prepared by method 2..... 116

Figure 7-S 2 (A) capacitance versus scan rate and (B) impedance data presented in a Nyquist plot for (a) TP 1, (b) TP 2, and (c) TP 3 for electrode prepared by method 2. .... 116

Figure 7-S 3 (A) real and (B) imaginary components of complex capacitance for (a)

TP 1, (b) TP 2, (c) TP 3 for electrode prepared by method 2. ....	117
Figure 7-S 4 GCD data for electrodes prepared by method 2, (A) charge-discharge at current densities of (a) 3, (b) 5, (c) 7 and (d) 10 mA cm <sup>-2</sup> , (B) capacitance versus current density dependence. ....	117
Figure 8- 1 X-ray diffraction patterns of Mn <sub>3</sub> O <sub>4</sub> and MWCNT mixtures prepared by (a) method 1 and (b) method 2, (◆-Mn <sub>3</sub> O <sub>4</sub> , ●-MWCNT).....	125
Figure 8- 2 (A) Chemical structure of murexide, (B) adsorption of murexide on particle, involving tridentate chelation of surface Mn atoms. ....	126
Figure 8- 3 SEM images at different magnifications for electrodes prepared by (A, C) method 1 and (B,D) method 2. ....	128
Figure 8- 4 CVs for electrodes, prepared by method 1 for (A) TP 1, (B) TP 2, (C) TP 3 and (D) TP 5 at scan rates of (a) 2, (b) 10, (c) 20 and (d) 50 mV s <sup>-1</sup> .....	130
Figure 8- 5 Integral capacitances calculated from the CV data, (B) real and (C) imaginary components of differential complex capacitances versus frequency, calculated from the EIS data for (a) TP 1, (b) TP 2, (c) TP 3, and (d) TP 5; (D) integral capacitance obtained from the GCD data after TP 5 versus current density; inset shows corresponding charge discharge curves for current densities of (a) 3, (b) 5, (c) 7, and (d) 10 mA cm <sup>-2</sup> .....	131
Figure 8- 6 CVs for electrode prepared by Method 2 (A) for TP 1 and (B) TP 3 for	

scan rates of (a) 2, (b) 10, (c) 20, and (d) 50 mV s<sup>-1</sup>. ..... 133

Figure 8- 7 (A) Integral capacitances calculated from the CV data, (B) real and (C) imaginary components of differential complex capacitances versus frequency, calculated from the EIS data for (a) TP 1, (b) TP 3; (D) integral capacitance obtained from the GCD data after TP 5 versus current density; inset shows corresponding charge discharge curves for current densities of (a) 3, (b) 5, (c) 7, and (d) 10 mA cm<sup>-2</sup>. ..... 133

Figure 8- 8 Normalized capacitances (C<sub>N</sub>) versus cycle number at a scan rate of 50 mV s<sup>-1</sup> for electrodes prepared by (A) Method 1 and (B) Method 2, normalized by the capacitance for the 2000th cycle. .... 135

Figure 9- 1 Chemical structures of (A) TQ, (B) CT, and (C) GC molecules and (D) catecholate-type bonding, involving Mn atoms on the Mn<sub>3</sub>O<sub>4</sub> particle surface. 149

Figure 9- 2 X-ray diffraction patterns for Mn<sub>3</sub>O<sub>4</sub> powders, (a-c) prepared by adding capping agents: (a) TQ, (b) CT, (c) GC and (d) without capping agent (o- peaks corresponding to JCPDS file 04-007-1841 of Mn<sub>3</sub>O<sub>4</sub>). ..... 154

Figure 9- 3 TEM images at different magnifications of Mn<sub>3</sub>O<sub>4</sub> prepared using capping agents (A,B) TQ and (C,D) CT and (E,F) GC. .... 157

Figure 9- 4 FTIR spectra of Mn<sub>3</sub>O<sub>4</sub> prepared using capping agents (a) TQ (b) CT, (c)

GC and (d)  $Mn_3O_4$  prepared without capping agent. .... 158

Figure 9- 5 SEM images of  $Mn_3O_4$ -MWCNT composite electrodes prepared using (A) TQ, (B)CT and (C)GC as capping and dispersing agents. .... 158

Figure 9- 6 (A-C) CVs at scan rates of (a) 2, (b) 5, (c) 10 and (d) 20  $mV s^{-1}$  for electrodes prepared using (A) TQ, (B) CT and (C) GC as capping agents; (D) capacitance versus scan rate for electrode prepared by (a) TQ (b) CT, (c) GC as capping agents. .... 159

Figure 9- 7 (A) complex impedance data presented in a Nyquist plot, (● experimental data (exp) and —simulation data (sim) for materials prepared using different capping agents, (B) equivalent circuit used for simulation, (C,D) frequency dependences of components of complex capacitance (C)  $Cs'$  and (D)  $Cs''$ , calculated from the EIS data for electrodes prepared using (a) TQ (b) CT, (c) GC as capping agents. .... 161

Figure 9- 8 Galvanostatic charge-discharge curves (GCD) at current densities of (a) 3, (b) 5, (c) 7, and (d) 10  $mA cm^{-2}$  and (D) capacitances, calculated from GCD data versus current density for electrodes prepared by (A and D(a)) TQ, (B and D (b)) CT and (C and D(c)) GC as capping agents. .... 163

Figure 9-S 1 Sedimentation test for  $Mn_3O_4$  suspensions containing 0, 5, 10 and 20 % of GC additive of the mass of  $Mn_3O_4$  (100%). The picture shows suspensions 48

h after preparation. A similar behavior was observed for Mn<sub>3</sub>O<sub>4</sub> suspensions, containing TQ and CT. Suspensions, containing 0 and 5 % GC showed sedimentation. The minimum amount of the capping agent for the formation of stable suspensions was 10%. ..... 168

Figure 9-S 2 TEM images at different magnifications (A, B) of Mn<sub>3</sub>O<sub>4</sub>-MWCNT composite, prepared using GC. Arrows show MWCNT. Talos 200X microscope (Thermo Scientific) was used for analysis. .... 168

Figure 9-S 3 XPS spectra of Mn<sub>3</sub>O<sub>4</sub>-MWCNT: (A)Mn 2p region, (B)O 1s region and (C)C 1s region respectively, was performed using Quentera II Scanning XPS instrument. .... 169

Figure 9-S 4 Capacitance retention of electrodes prepared by (A) TQ, (B)CT and (C)GC as capping and dispersing agents and (D) without capping agent, obtained from CV data at a sweep rate of 50 mV s<sup>-1</sup>. .... 170

Figure 9-S 5 Electrochemical testing results for asymmetric Mn<sub>3</sub>O<sub>4</sub>-MWCNT/FeOOH-MWCNT device. Electrochemical studies were performed in aqueous 0.5 M Na<sub>2</sub>SO<sub>4</sub>electrolyte using PARSTAT 2273 potentiostat (AMETEK): (A) CV curves at (a–c) 2, 5, and 10 mV s<sup>-1</sup>, (B) capacitances versus CV scan rate, (C) Nyquist plots, and (D) complex capacitance Cs'(blue line) and Cs''(red line) versus frequency, (E) GCD curves at (a) 10, (b) 7, (c) 5, and (d) 3 mA cm<sup>-2</sup>, (D)

---

capacitances versus current density. ....	170
Figure 10- 1 XRD patterns of (A) <b>MnO<sub>2</sub>-a</b> and (B) (a) <b>Mn<sub>3</sub>O<sub>4</sub>-a</b> and (b) <b>Mn<sub>3</sub>O<sub>4</sub>-c</b> . .....	190
Figure 10- 2 (A) Chemical structure of QC. (B) Bonding sites of QC for metal ions. .....	191
Figure 10- 3 (A,B) CV data for (A) <b>MnO<sub>2</sub>-a</b> and (B) <b>MnO<sub>2</sub>-b</b> at (a) 2, (b) 5, (c) 10 and (d) 20 mV s <sup>-1</sup> , (C) C <sub>S</sub> and C <sub>m</sub> versus scan rate, calculated from the CVs for (a) <b>MnO<sub>2</sub>-a</b> and (b) <b>MnO<sub>2</sub>-b</b> , (D,E,F) EIS data for complex impedance and capacitance: (D) Nyquist plot, (E) C <sub>s</sub> ' versus frequency, (F) C <sub>s</sub> '' versus frequency for (a) <b>MnO<sub>2</sub>-a</b> (b) <b>MnO<sub>2</sub>-b</b> , (G,H) CP data at (a) 3, (b) 5, (c) 7 and (d) 10 mA cm <sup>-2</sup> for (G) <b>MnO<sub>2</sub>-a</b> , and (H) <b>MnO<sub>2</sub>-b</b> , (I) C <sub>S</sub> and C <sub>m</sub> as functions of current density for (a) <b>MnO<sub>2</sub>-a</b> and (b) <b>MnO<sub>2</sub>-b</b> , calculated from CP data.....	193
Figure 10- 4 (A,B) CV data for (A) <b>Mn<sub>3</sub>O<sub>4</sub>-b</b> and (B) <b>Mn<sub>3</sub>O<sub>4</sub>-c</b> at (a) 2, (b) 5, (c) 10 and (d) 20 mV s <sup>-1</sup> , (C) C <sub>S</sub> and C <sub>m</sub> versus scan rate, calculated from the CVs for (a) <b>Mn<sub>3</sub>O<sub>4</sub>-b</b> and (b) <b>Mn<sub>3</sub>O<sub>4</sub>-c</b> , (D,E,F) EIS data for complex impedance and capacitance: (D) Nyquist plot, (E) C <sub>s</sub> ' versus frequency, (F) C <sub>s</sub> '' versus frequency for (a) <b>Mn<sub>3</sub>O<sub>4</sub>-b</b> (b) <b>Mn<sub>3</sub>O<sub>4</sub>-c</b> , (G,H) CP data at (a) 3, (b) 5, (c) 7 and (d) 10 mA cm <sup>-2</sup> for (G) <b>Mn<sub>3</sub>O<sub>4</sub>-b</b> , and (H) <b>Mn<sub>3</sub>O<sub>4</sub>-c</b> , (I) C <sub>S</sub> and C <sub>m</sub> as functions of current density for (a) <b>Mn<sub>3</sub>O<sub>4</sub>-b</b> and (b) <b>Mn<sub>3</sub>O<sub>4</sub>-c</b> , calculated from	

---

CP data.....	194
Figure 10- 5 Capacitance retention of (A) <b>Mn<sub>3</sub>O<sub>4</sub>-b</b> and (B) <b>Mn<sub>3</sub>O<sub>4</sub>-c</b> electrodes at a scan rate of 50 mV s <sup>-1</sup> . .....	196
Figure 10- 6 O 1s and Mn 2p X-ray absorption spectra of MnO (red), Mn <sub>3</sub> O <sub>4</sub> (green) and MnO <sub>2</sub> (blue) plotted on an absolute intensity scale (OD1, optical density per nm thickness at standard densities).....	197
Figure 10- 7 (A) Mn 2p <sub>3/2</sub> absorption spectra of (h) <b>Mn<sub>3</sub>O<sub>4</sub>-c</b> after VSRP, (i) <b>Mn<sub>3</sub>O<sub>4</sub>-c</b> after FSRP, (j) <b>Mn<sub>3</sub>O<sub>4</sub>-b</b> after VSRP (k) <b>Mn<sub>3</sub>O<sub>4</sub>-b</b> after FSRP. B. O 1s spectra for <b>Mn<sub>3</sub>O<sub>4</sub>-c</b> after VSRP (h1-h3) and after FSRP (i1-i2) C. O 1s spectra for <b>Mn<sub>3</sub>O<sub>4</sub>-b</b> after VSRP (j1-j2) and after FSRP (k1-k2) . The sub-coding (1,2 and 3) indicate different regions of the same sample. ....	198
Figure 10- 8 Mn 2p <sub>3/2</sub> spectra of <b>Mn<sub>3</sub>O<sub>4</sub>-c</b> after (a) VSRP and (b) FSRP. B. Mn 2p <sub>3/2</sub> spectra of <b>Mn<sub>3</sub>O<sub>4</sub>-b</b> after (c) VSRP and (d) FSRP. In each panel a direct comparison is made to the reference spectra. ....	199
Figure 10- 9 A. average of 64 images of O 1s stack of the Mn <sub>3</sub> O <sub>4</sub> -c after VSRP. B. color coded composite of the MnO (red), Mn <sub>3</sub> O <sub>4</sub> (green) and MnO <sub>2</sub> (blue) chemical maps derived from a stack fit to the O 1s stack. B-1, B-2 and B-3 are the component maps derived by fitting the O 1s stack to the O 1s spectra of MnO, Mn <sub>3</sub> O <sub>4</sub> , and MnO <sub>2</sub> . C. O 1s spectra extracted from the B-1, B-2 and B-3 regions. The color of each spectrum corresponds to the color-coding of the	

spatial regions from which the spectra were extracted..... 200

Figure 10- 10 Color coded composites of MnO (red), Mn<sub>3</sub>O<sub>4</sub> (green) and MnO<sub>2</sub> (blue) chemical maps derived by fitting Mn L<sub>3</sub> stacks. **A. Mn<sub>3</sub>O<sub>4</sub>-c** after VSRP. **B. Mn<sub>3</sub>O<sub>4</sub>-c** after FSRP **C. Mn<sub>3</sub>O<sub>4</sub>-b** after VSRP. **D. Mn<sub>3</sub>O<sub>4</sub>-b** after FSRP. The intensity scale of each species is indicated. **E.** Is a color wheel indicating how the color at any pixel indicates a specific combination of the three species. .... 204

Figure 10- 11 Volume fraction determination of the composition of **Mn<sub>3</sub>O<sub>4</sub>-c** after FSRP. **(A)** average STXM image of the measured sample. **(B)** color-coded map in absolute scale. **(C)** average spectrum (dots) compared to the calculated curve fit (grey) using the area of each component and the average thickness of each component. .... 205

Figure 10- 12 Volume fractions of MnO (red), Mn<sub>3</sub>O<sub>4</sub> (green) and MnO<sub>2</sub> (blue) evaluated from the area and thickness of each component map (see the Supplemental Information for a description of the method). **A.** VSRP and FSRP for **Mn<sub>3</sub>O<sub>4</sub>-b**. **B.** VSRP and FSRP for **Mn<sub>3</sub>O<sub>4</sub>-c**. .... 206

Figure 10-S 1 **O 1s chemical mapping.** **A.** average of 64 images of O 1s stack of the **Mn<sub>3</sub>O<sub>4</sub>-c** after FSRP. **B.** color coded composite of two different Mn oxides regions derived from a stack fit to the O 1s stack. **B-1** and **B-2** are the component maps of the two Mn oxides regions. **C.** O 1s spectra extracted from different

region of the sample. The color of each spectrum corresponds to the color-coding in **B**. ..... 214

Figure 10-S 2 **O 1s chemical mapping. A.** average of 64 images of O 1s stack of the **Mn<sub>3</sub>O<sub>4</sub>-b** after VSRP. **B.** color coded composite of two different Mn oxides regions derived from a stack fit to the O 1s stack. **B-1** and **B-2** are the component maps of the two Mn oxides regions. **C.** O 1s spectra extracted from different region of the sample. The color of each spectrum corresponds to the color-coding in **B**. ..... 215

Figure 10-S 3 **O 1s chemical mapping. A.** average of 64 images of O 1s stack of the **Mn<sub>3</sub>O<sub>4</sub>-b** after FSRP. **B.** color coded composite of two different Mn oxides regions derived from a stack fit to the O 1s stack. **B-1** and **B-2** are the component maps of the two Mn oxides regions. **C.** O 1s spectra extracted from different region of the sample. The color of each spectrum corresponds to the color-coding in **B**. ..... 216

Figure 10-S 4 Color coded composites of MnO (red), Mn<sub>3</sub>O<sub>4</sub> (green) and MnO<sub>2</sub> (blue) chemical maps derived by fitting Mn L<sub>3</sub> stacks. **A. MnO<sub>2</sub>-a. B. MnO<sub>2</sub>-b** C. Mn 2p<sub>3/2</sub> absorption spectra of the as-prepared **MnO<sub>2</sub>-a** in comparison to that of **MnO<sub>2</sub>-b** ..... 217

Figure 10-S 5 **O 1s chemical mapping of MnO<sub>2</sub>-a. A.** color coded composite of two different Mn oxides regions derived from a stack fit to the O 1s stack. **A-1** and

**A-2** are the component maps of the two Mn oxides regions. **B.** O 1s spectra extracted from different region of the sample. The color of each spectrum corresponds to the color-coded in **A.** **O 1s chemical mapping of MnO<sub>2</sub>-b.** **C.** color coded composite of two different Mn oxides regions derived from a stack fit to the O 1s stack. **C-1** and **C-2** are the component maps of the two Mn oxides regions. **B.** O 1s spectra extracted from different region of the sample. The color of each spectrum corresponds to the color-coding in **C.** ..... 218

Figure 10-S 6 FTIR spectra obtained using a Bruker Vertex 70 spectrometer for (A) (a) as-received QC, (b) **MnO<sub>2</sub>-a**, (c) **MnO<sub>2</sub>-b**, (B) (a) as-received QC, (b) **Mn<sub>3</sub>O<sub>4</sub>-a**, (c) **Mn<sub>3</sub>O<sub>4</sub>-b**, (d) **Mn<sub>3</sub>O<sub>4</sub>-c**..... 219

Figure 11- 1 X-ray diffraction pattern of LSM ( $\nabla$  - peaks corresponding to JCPDS file 89-0648). ..... 229

Figure 11- 2 (A,B) Magnetization versus magnetic field for LSM, (B) shows the magnetization curve in a low field range..... 229

Figure 11- 3 TEM images at different magnifications for LSM: (A,B) as-received and (C,D) after HEBM. .... 230

Figure 11- 4 Adsorption mechanisms of GLC on La<sub>0.35</sub>Sr<sub>0.65</sub>MnO<sub>3</sub> by chelation (M =

La, Sr or Mn).....	230
Figure 11- 5 FTIR spectra of (a) GLC, (b) LSM and (c) LSM with adsorbed GLC.	231
Figure 11- 6 SEM images at different magnifications for LSM-MWCNT electrodes prepared using (A,B) as-received LSM and (C,D) LSM after HEBM.....	232
Figure 11- 7 (A,B) CVs at (a) 2, (b) 5 and (c) 10 $\text{mV s}^{-1}$ , (C) capacitance versus scan rate, (D,E) CP data at (a)3, (b)5, (c)7 and (d)10 $\text{mA cm}^{-2}$ , (F) capacitance versus current density for electrodes prepared using (A), (C(a)), (D), (F(a)) as received and (B), (C(b)), (E), (F(b)) HEBM LSM.....	234
Figure 11- 8 (A) Nyquist graph and (B, C) components of complex capacitance versus frequency for electrodes prepared using (a) as-received and (b) HEBM LSM.	235
Figure 11- 9 Capacitance retention for electrodes, prepared using (A) as-received and (B) HEBM LSM at 50 $\text{mV s}^{-1}$ . The capacitances were calculated for different CV cycles and normalized by capacitance value for the cycle 10,000. ....	237
Figure 11-S 1. FTIR spectrum of as-received LSM in the low wavenumber range, which shows absorption peak of LSM related to Mn-O vibrations.....	246
Figure 11-S 2. Equivalent circuit used for the analysis of EIS data using ZSimpWin software. It contains a solution resistance $R_s$ , a transmission line $R_1C_1(R_2Q)$ describing a porous electrode, Warburg impedance $W$ , charge transfer resistance	

---

R <sub>3</sub> and double layer capacitance C <sub>2</sub> .....	246
Figure 11-S 3. XPS data for LSM electrodes (A) before and (B) after 2000 CV cycles. .....	247
Figure 11-S 4. SEM images at different magnifications of LSM electrodes prepared without HEBM (A, B) and with HEBM (C, D) after 10,000 cycle retention test. .....	247
Figure 11-S 5. Testing results for a device, containing LSM cathodes and CoFe <sub>2</sub> O <sub>4</sub> - polypyrrole (PPy) anodes in 0.5M Na <sub>2</sub> SO <sub>4</sub> electrolyte: (A) CVs at scan rates of (a)2, (b) 5 and (c) 10 mV s <sup>-1</sup> , (B) capacitance calculated from CV data versus scan rate, (C) galvanostatic charge-discharge data at current densities of (a) 3, (b) 5, (c) 7 and (d) 10 mA cm <sup>-2</sup> , (D) capacitance calculated from the galvanostatic charge-discharge data versus current density. The gravimetric capacitance was normalized by the total mass of both electrodes (80 mg cm <sup>-2</sup> ).....	248
Figure 12- 1 (A)X-ray diffraction pattern (♦- peaks, corresponding to JCPDS 74-2403 file); (B) magnetization (M) versus magnetic field (H), (C) enlarged view of M– H curve at low magnetic field for MFO. ....	258
Figure 12- 2 (A) Chemical structures of (a) MRX and (b) GLC, (B) tridentate chelating bonding of MRX and (C) bidentate chelating bonding of GLC to metal	

---

ions ( $M=Cu^{2+}$ , $Fe^{3+}$ ) on the MFO particle surface.....	259
Figure 12- 3 (A-C) CVs at (a) 2, (b) 5 and (c) 10 $mV s^{-1}$ and (D) capacitances versus scan rate for (A) and (D(a)) MFO, (B) and (D(b)) MFO-MRX, (C) and (D (c)) MFO-GLC. ....	259
Figure 12- 4 (A-C) GCD data at (a) 3, (b) 5, (c) 7, and (d) 10 $mA cm^{-2}$ and (D) capacitance versus current density for (A) and (D(a)) MFO, (B) and (D(b)) MFO-MRX, (C) and (D (c)) MFO-GLC. ....	261
Figure 12- 5 (A-C) CVs at (a) 2, (b) 5 and (c) 10 $mV s^{-1}$ and (D) capacitances versus scan rate for (A) and (D(a)) MFO, (B) and (D(b)) MFO-MRX, (C) and (D (c)) MFO-GLC. ....	262
Figure 12- 6 Redox reaction of GLC.....	262
Figure 12- 7(A-C) GCD data at (a) 3, (b) 5, (c) 7, and (d) 10 $mA cm^{-2}$ and (D) capacitance versus current density for (A) and (D(a)) MFO, (B) and (D(b)) MFO-MRX, (C) and (D (c)) MFO-GLC. ....	263
Figure 12- 8 EIS data: (A) Nyquist plot and (B,C) complex capacitance components versus frequency for (a) MFO, (b) MFO-MRX and (c) MFO-GLC. ....	264
Figure 12- 9 SEM image of MFO-MRX electrode. ....	265
Figure 12- 10 Capacitance versus cycle number for MFO-MRX electrode in (A) positive (0 – +0.9 V) and (B) negative (-0.8 – 0 V) potential ranges at 50 $mV s^{-1}$ .	

---

.....	266
Figure 12- 11 (A) CVs at (a) 2, (b) 5 and (c) 10 mV s <sup>-1</sup> , (B) capacitances versus scan rate, (C) Nyquist plot, (D,E) frequency dependences of components of complex capacitance (D) C <sub>s</sub> ' and (E) C <sub>s</sub> '', (F) GCD curves at (a) 10, (b) 7, (c) 5, and (d) 3 mA cm <sup>-2</sup> , (G) capacitances versus current density, (H) capacitance retention for symmetric MFO-MRX device.....	268

## List of Tables

Table 2- 1 Carbon-based materials used in EDLC <sup>75</sup> .....	23
Table 6-S 1 Mn 2p and F 1s energy features of measured samples compared to reference spectra. ....	80
Table 7- 1 Literature data on capacitances of Mn <sub>3</sub> O <sub>4</sub> based electrodes, containing conductive additives, and tested in Na <sub>2</sub> SO <sub>4</sub> electrolyte.....	109
Table 8- 1 Literature data on capacitances of Mn <sub>3</sub> O <sub>4</sub> - and MnO <sub>2</sub> -based electrodes containing conductive additives and tested in Na <sub>2</sub> SO <sub>4</sub> electrolyte.....	137
Table 9- 1 Size of Mn <sub>3</sub> O <sub>4</sub> particles prepared by different methods. ....	156
Table 9- 2 Capacitances of Mn <sub>3</sub> O <sub>4</sub> and composite electrodes .....	164
Table 11-S 1 A comparison of the LSM-based cathode materials performances for supercapacitors. ....	244
Table 12-S 1 Capacitive properties of MnFe <sub>2</sub> O <sub>4</sub> and composite electrodes .....	273
Table 12-S 2 A comparison of the recent MnFe <sub>2</sub> O <sub>4</sub> -based supercapacitor devices	

capacitance..... 275

# List of Abbreviations and Symbols

A/mA(unit)	Ampere/Milliampere
AC	Activated Carbon
AML	Active mass loading
C/ $\mu$ C (unit)	Coulomb/Microcoulomb
C	Capacitance
C <sup>+</sup>	Cationic species in electrolyte
C*	Complex differential capacitance
C <sub>m</sub>	Gravimetric capacitance
C <sub>s</sub>	Areal capacitance
C <sub>s</sub> '	Real component of complex capacitance
C <sub>s</sub> ''	Imaginary component of complex capacitance
CV	Cyclic voltammetry/cyclic voltammogram
°C (unit)	Temperature in Celsius
CT	Catechin hydrate
DI	Deionized
ES	Electrochemical supercapacitors
e <sup>-</sup>	Electron
$\epsilon_0$	Permittivity of vacuum

$E^0$	Standard electrode potential
E	Electrode potential
EDLC	Electrochemical double layer capacitor
EIS	Electrochemical impedance spectroscopy
F	Faraday constant
$f$	Frequency
F/mF/ $\mu$ F (unit)	Farad, millifarad, microfarad
FTIR	Fourier-transform infrared spectroscopy
g/mg/ $\mu$ g (unit)	Gram, milligram, microgram
GA/GC/ GLC	gallocyanine
h (unit)	Hour
Hz/MHz/kHz (unit)	Hertz/millihertz/Kilohertz
I	Current
K (unit)	Temperature in Kelvin
k	Boltzmann constant
L/mL (unit)	Liter/milliliter
LSM	$\text{La}_{0.65}\text{Sr}_{0.35}\text{MnO}_3$
m/cm/ $\mu$ m/nm (unit)	Meter/ centimeter/micrometer/nanometer

M	Molar concentration
MWCNTs	Multiwalled Carbon nanotubes
MRX	murexide
PVB/PVBAA	Poly (vinyl butyral-co-vinyl alcohol-covinylacetate)
PA	polyacetylene
PANI	polyaniline
PPy	polypyrrole
PF	polyfuran
PPV	poly (phenylenevinylene)
PPP	poly(para-phenylene)
PTH	polythiophene
QC	quercetin
Q	Charge stored
RL	rhamnolipid
R	Resistance
$R_m$	Ratio of active material mass to collector mass
s (unit)	Second
SC	Supercapacitor
SCE	Saturated Calomel Electrode

SEM	Scanning Electron Microscopy
STXM	Scanning Transmission X-ray Microscopy
T	Temperature
TEM	Transmission Electron Microscopy
TQ	Tetrahydroxy-1,4-quinone hydrate
TMOs	transition metal oxides
V	Voltage
$V_{\max}$	Maximum voltage
$V_{\min}$	Minimum voltage
W (unit)	Watt
wt%	Weight percentage
XRD	X-ray diffraction
XPS	X-ray photoelectron spectroscopy
$Z^*$	Total impedance
$Z'$	Real component of impedance
$Z''$	Imaginary component of impedance

# Chapter 1 Introduction

With people's pursuit of a higher quality of life and the speedy improvement of science and technology, global energy consumption has increased sharply.<sup>1</sup> This will inevitably cause serious environmental pollution and economic problems, and it is a challenge that human development must face and deal with.<sup>1,2</sup> Today's energy consumption mainly comes from non-renewable fossil fuels.<sup>2</sup> Its excessive consumption speed will lead to an energy crisis<sup>3</sup>. The energy conversion process will be accompanied by the emission of greenhouse gas and toxic gases such as SO<sub>2</sub> and NO<sub>x</sub>, which will cause harm to the environment and human beings.<sup>4</sup> In order to alleviate the global Climate and environmental crises such as warming and slowing the consumption of fossil fuels many researchers focus on the development of renewable clean energy sources such as solar, tidal and wind power.<sup>5</sup> Electric energy, as a very important form of energy consumption in human life, requires continuous and stable output of renewable energy<sup>5</sup>. To achieve this goal, there is an urgent need to develop sustainable energy conversion and storage technologies<sup>6</sup>.

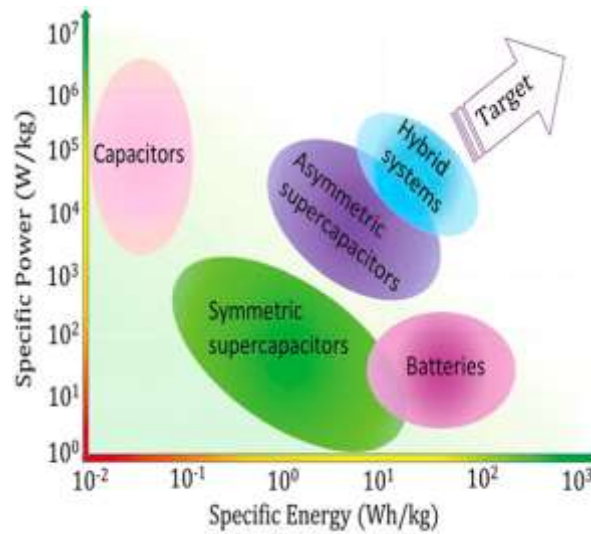


Figure 1- 1 Ragone plot for different energy storage devices.<sup>7</sup>

Among various energy storage technologies, batteries and supercapacitors (SCs) have been the two main electrochemical energy storage devices.<sup>8</sup> From Figure 1-1, we can see that compared with batteries and capacitors, supercapacitors can well balance the limitations imposed by the low energy density of capacitors and the low power density of batteries.<sup>7</sup> In addition to offering comparable energy and power density, SCs also boast long cycle lives, rapid charge and discharge rates, and low cost<sup>6,7</sup>. Due to these unique properties, they are suited for applications that conventional capacitors and batteries cannot fulfill, thus attracting increasing interest from researchers, as depicted in Figure 1-2.<sup>9</sup>

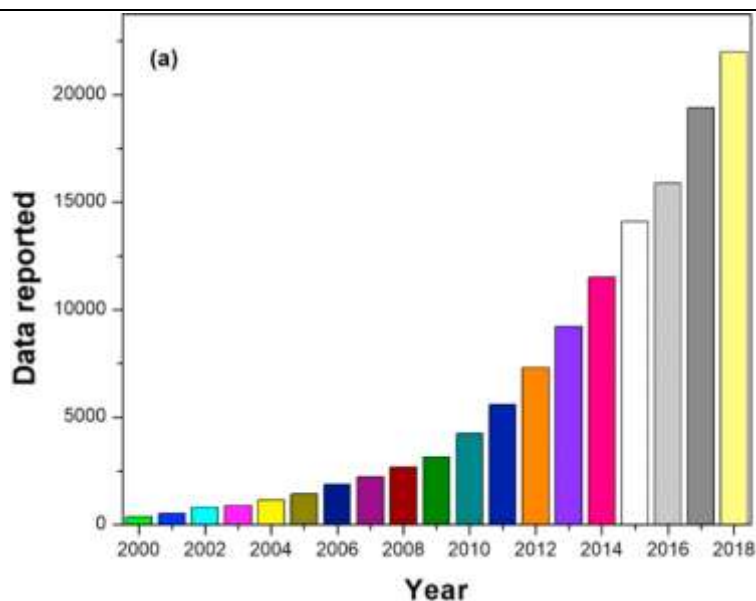


Figure 1- 2 The count of scholarly publications, including articles, books, and other credible open-access sources from 2000 to 2018 (projected), derived from a search using 'supercapacitor' as a keyword on Google scholar.<sup>9</sup>

According to the charge storage mechanism, SCs can be divided into 2 categories, including electrochemical double layer capacitor (EDLC) and pseudo-supercapacitors. EDLC has been a widely commercialized supercapacitor.<sup>10</sup> During the charge-discharge process, only the adsorption-desorption of ions occurs at the electrode interface without any electrochemical reaction.<sup>11</sup> It is also known as a non-faraday capacitor. Electrode materials for EDLCs are usually selected as carbon materials with high surface area and high conductivity, such as carbon aerogels, commercial activated carbon (AC), carbon nanotubes (CNTs), carbon nanofibers and graphene, which enable the electrolyte ions adsorption-desorption process can be performed more and faster.<sup>9,10,12,13</sup> Unlike EDLCs,

---

the capacitance of pseudo-capacitors arises from the fast faradaic reaction at the electrode interface, which transfers charge through fast and reversible redox reactions on and near the surface of the electrode active material for charge storage.<sup>14</sup> Also known as a faraday capacitor, its charge transfer is voltage dependent. The most widely used active electrode materials are conducting polymers (such as ppy) and Metal oxides.<sup>15-19</sup> RuO<sub>2</sub> is recognized for its excellent capacitance when used as the cathode material in supercapacitors, and it was the first metal oxide to capture researchers' attention. However, ongoing research has revealed limitations that hinder its broader practical application, including its high cost, bioincompatibility, and the requirement for strong acid electrolytes.<sup>20-23</sup> In order to reduce costs and enhance the safety of supercapacitors, researchers have shown increased interest in transition metal oxides (TMOs) that can operate in neutral electrolytes while providing high capacitance, such as MnO<sub>2</sub>, Fe<sub>3</sub>O<sub>4</sub>, V<sub>2</sub>O<sub>5</sub> and TiO<sub>2</sub>.<sup>24</sup> Among these electrode materials, manganese oxides have the characteristics of high theoretical capacitance, low cost, abundant resources, and environmental friendliness, and has received extensive attention as an active electrode material for ESs.<sup>15-19</sup> However, the low electrical and ionic conductivity of manganese oxide severely limits the development of manganese oxide pseudocapacitive supercapacitors.<sup>25</sup> To expand the supercapacitor market, hybrid SCs—a third type of supercapacitor characterized by higher energy and power densities—have gained popularity. These hybrid SCs enhance performance by incorporating EDLC material, known for its high conductivity, into the pseudocapacitive material. This combination

---

leverages the synergistic effects of both materials.<sup>3,6,14,26</sup> In this configuration, the charge storage mechanism involves both physical adsorption-desorption and charge transfer through electrochemical redox reactions near the electrolyte interface, achieving higher energy and power densities without compromising cycle stability or cost efficiency.<sup>2</sup>

Mn<sub>3</sub>O<sub>4</sub> and CNTs nanocomposites are formidable contenders as cathode active materials for hybrid supercapacitors. Mn<sub>3</sub>O<sub>4</sub> offers processing advantages that positively impact the synthesis of high-performance electrodes with intricate nanostructures.<sup>27</sup> To maximize the synergistic effects between Mn<sub>3</sub>O<sub>4</sub> and CNTs, achieving uniform dispersion and preventing agglomeration are critical.<sup>28 29</sup> . Consequently, the development of multifunctional dispersants is essential for preparing high-performance composite electrodes.

Our research focuses on developing a novel colloidal processing technique to synthesize non-agglomerated particles, thereby enhancing the capacitive performance of hybrid supercapacitors for practical applications. We are exploring advanced capping and dispersing agents that have successfully reduced the particle size of Mn<sub>3</sub>O<sub>4</sub>, minimized agglomeration, and improved the integration of nanostructures with conductive additives, providing the composite electrodes with increased specific capacitance and decreased impedance. Furthermore, these strategies enhance the synergistic effect of mixed materials, and the resulting electrodes exhibit significant capacitive performance under high active mass loading, which is highly advantageous for the commercial application of Mn<sub>3</sub>O<sub>4</sub>

electrodes. Advanced co-dispersants are also employed to fabricate alternative hybrid SCs electrode with binary and ternary metal oxides like  $\text{MnFe}_2\text{O}_4$  and  $\text{La}_{0.65}\text{Sr}_{0.35}\text{MnO}_3$  (LSM). Additionally, we utilize high-energy ball milling (HEBM), an innovative processing technology, to alter particle shape and size, thereby increasing active sites. Electrochemical tests indicate that this technology yields promising results, facilitating the fabrication of high-performance SC devices with higher capacitance in a broader voltage window.

# Chapter 2 Literature review

## 2.1 The development of supercapacitors

With the rapid development of society, energy has had a huge impact on human life. The current reliance on fossil fuels will cause unpredictable damage to the environment and the economy.<sup>3,30</sup> Therefore, research on environment-friendly, high-performance renewable energy is imminent. Supercapacitors play an important role as electrochemical energy storage devices in sustainable energy conversion and storage applications of renewable energy<sup>31</sup>. SCs are known to combine the properties of conventional capacitors and batteries, providing higher energy density than capacitors, as well as greater power density and a longer cycle life than batteries.<sup>32</sup> Before studying SC, a brief overview of conventional capacitors should be given as they are similar in terms of parameters and mechanisms.<sup>33</sup>

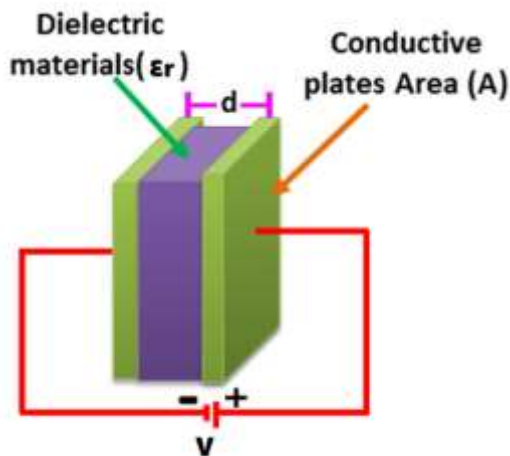


Figure 2- 1 Diagram of a parallel plate capacitor.<sup>33</sup> Reprinted with permission from MDPI.

Unlike SCs, which appeared in the late 20th century, capacitors were manufactured as early as the mid-18th century, and the earliest capacitors, also known as Leiden jars, stored a high-charge between electrical conductors inside and outside a glass jar.<sup>34</sup> Figure 2-1 shows a typical parallel plate capacitor consisting of two conductive plates separated by a dielectric material.<sup>33</sup> When a specific voltage is applied between the two plates, a uniform electric field will appear between the two plates, and the positive and negative charges will be pushed to the two plates of the capacitor respectively under the action of the electric field. The charging process does not stop until the potential difference between the capacitor plates is equal to the applied voltage. The two plates are now positively and negatively charged, also known as electrodes. For parallel plate capacitors, the amount of charge  $Q$  carried by a capacitor electrode is always proportional to its voltage  $V$ . This ratio is called the capacitance of the capacitor. The capacitance of a capacitor is represented by  $C$  as shown in Equation 2.1.

$$C = \frac{Q}{V} \tag{Eq 2.1}$$

In the case of the same voltage, the larger the capacitance  $C$ , the more electricity is stored.

The capacitance of a parallel plate capacitor can be derived from the equation 2.2.

$$C = \epsilon_0 \epsilon_r \frac{A}{d} \tag{Eq 2.2}$$

Where  $A$  represents the relative area of two electrodes,  $d$  represents the distance between

them, electric constant  $\epsilon_0$ , and the relative permittivity of the two electrodes is  $\epsilon_r$ . The stored energy ( $E$ ) of the capacitor is calculated from the work ( $W$ ) done by the electric field force on the charge during the discharge of the capacitor.

$$E = W = \int dw = - \int_Q^0 \frac{q}{C} dq = \frac{1}{2} \frac{Q^2}{C} = \frac{1}{2} CV^2$$

(Eq 2.3)

And the power density can be calculated by:

$$P = \frac{V^2}{4R_{ESR}}$$

(Eq 2.4)

where  $R_{ESR}$  is the equivalent series resistance (ESR). From Equations 2.3 and 2.4 it can be inferred that both  $E$  and  $P$  can be increased by increasing  $V$ . Also,  $E$  can be increased by increasing  $C$ . Regarding the output power provided by the capacitor,  $P$  can also be increased by reducing the ESR. In summary, energy and power density can be increased by increasing capacitance and operating voltage and decreasing resistance.

The structure of SCs is similar to that of a conventional capacitor, yet it can store substantially more energy at the interface between the electrolyte and the solid electrode. It is a device that is somewhere between a traditional capacitor and a battery. Since Beck invented the electric double layer capacitor with activated carbon as the electrode material in 1957, supercapacitors have attracted attention. With the increase in the number of hybrid vehicles in the late 20th century, the SC began to receive more attention, which is verified

in the graph2-2.<sup>35</sup>



Figure 2- 2 Development of supercapacitors in different countries.<sup>35</sup>

The researchers used a variety of different electrode materials, which can be roughly divided into three categories: (1) carbon electrodes; (2) metal oxide electrodes; (3) conductive polymer electrodes.<sup>32,35-37</sup> Due to its excellent electrical conductivity, carbon is the earliest electrode material used to fabricate ES, and it is also the most widely commercialized electrode material.<sup>13</sup> With the development of nanotechnology, porous carbon materials, activated carbon materials, activated carbon fibers, carbon nanofibers and carbon nanotubes have been developed for the manufacture of electrodes.<sup>9</sup> In addition, because the Faradaic capacitance generated by the reversible redox reaction of metal oxides at the electrode solution interface is much larger than the electric double layer capacitance on the surface of carbon materials, an increasing number of researchers began to study various metal oxides.<sup>38</sup> Conductive polymers are a new type of electrode active material. The energy storage mechanism is: through the fast reversible n-type and p-type element doping and de-doping redox reactions in the polymer on the electrode, the polymer

reaches a high charge density for energy storage.<sup>39</sup> When charging, the charge is stored in the entire polymer material and has a large specific capacitance. Conductive polymers are malleable and can be easily fabricated into thin-layer electrodes with low internal resistance, which are widely used in wearable electronic components.<sup>40</sup>

## 2.2 Application of supercapacitors

SC is favored by the market due to its excellent properties and the use of environmentally friendly materials as electrodes, and is widely used in transportation, industry, military, consumer electronics and other fields.<sup>26,41</sup>

Supercapacitors have the advantages of fast charging and discharging rate, high power density and long cycle life, and are widely used in the field of transportation. For conventional combustion engine vehicles, supercapacitors connected to the combustion engine can provide an instant burst of energy that enables the car to start quickly.<sup>42</sup>

Compared with secondary batteries, supercapacitors have the characteristics of wide operating temperature range, good low temperature performance, and high output power.<sup>42</sup>

The application of supercapacitor as an emergency starting power supply device can solve the problem that the battery is difficult to start the car in a low temperature environment.<sup>43</sup>

Cars equipped with a supercapacitor start-stop system can have lower fuel and maintenance costs and a better driving experience than cars with traditional battery start-stop systems.<sup>35</sup> When the supercapacitor is used as one of the power sources of the hybrid

vehicle, the vehicle can obtain higher instantaneous power, thereby improving the acceleration performance of the vehicle; when the vehicle decelerates and brakes, the braking energy can be recovered, and the overall vehicle economy of the vehicle can be improved<sup>44</sup>. In addition, due to this feature, it is very suitable for the characteristics of frequent starting and stopping and frequent braking of urban buses. Supercapacitor can be used as a power source to recover braking energy and improve vehicle economy.



Figure 2- 3 Tramways in Barcelona, Spain<sup>44</sup>

With the acceleration of industrial modernization, industrial production has been increasing, resulting in a large amount of energy waste.<sup>45</sup> In order to improve economic efficiency and save energy, these energy needs to be recycled and reused, such as cranes and pumping units.<sup>45</sup>

Supercapacitors can be used as emergency power supply for military products, such as data backup emergency power supply for military robots, emergency power supply for tanks and armored vehicle fire protection systems that lose their main power supply, etc.<sup>31</sup> Most modern military-derived weapons require electricity from a power source, and

supercapacitors are ideal for providing short-term and instantaneous peak power to these weapons.

Supercapacitors can be used as backup energy storage devices for short-term power outages in portable electronic devices, and can meet functions such as hot swapping, data storage and transmission.<sup>46</sup> Tecate Group's ultracapacitors power portable audio players, setup boxes, remote controls, rechargeable flashlights, and also provide short-term power for GPS devices, allowing devices to be hot-swapped.

## 2.3 Classifications of electrochemical supercapacitors

As shown in Figure 2.4, according to the charge storage mechanism, SCs can be classified into three main types: electrochemical double-layer capacitors (EDLCs), pseudocapacitors, and hybrid supercapacitors.<sup>47</sup>

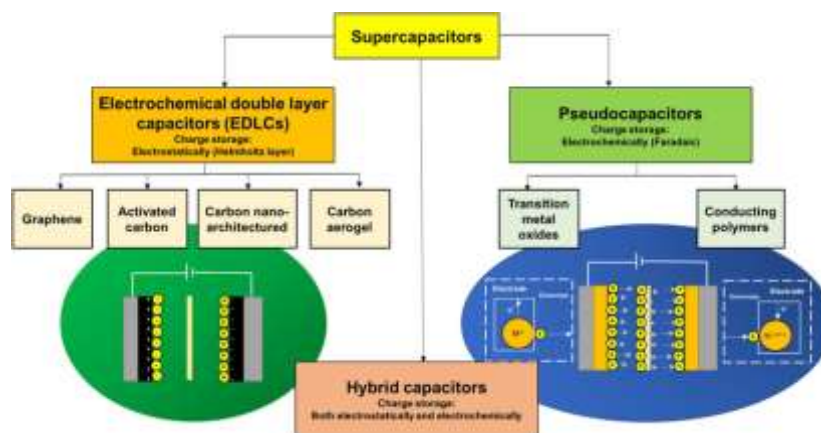


Figure 2- 4 Overview of supercapacitor types and classification.<sup>47</sup>

Figure 2-5 presents a schematic diagram illustrating the components and working mechanisms of three different types of supercapacitors. EDLC generates energy storage through the adsorption of pure electrostatic charge on the electrode surface<sup>48</sup>. Pseudocapacitance mainly generates faraday capacitance through reversible redox reactions on and near the surface of active electrode materials (such as TMOs and polymers), thereby realizing energy storage and conversion.<sup>40,49</sup> Hybrid supercapacitors simultaneously store charge both electrostatically and electrochemically, combining the mechanisms of EDLCs and pseudocapacitance.<sup>50</sup> Figure 2-5 presents a schematic diagram illustrating the components and working mechanisms of three different types of SCs.<sup>51</sup>

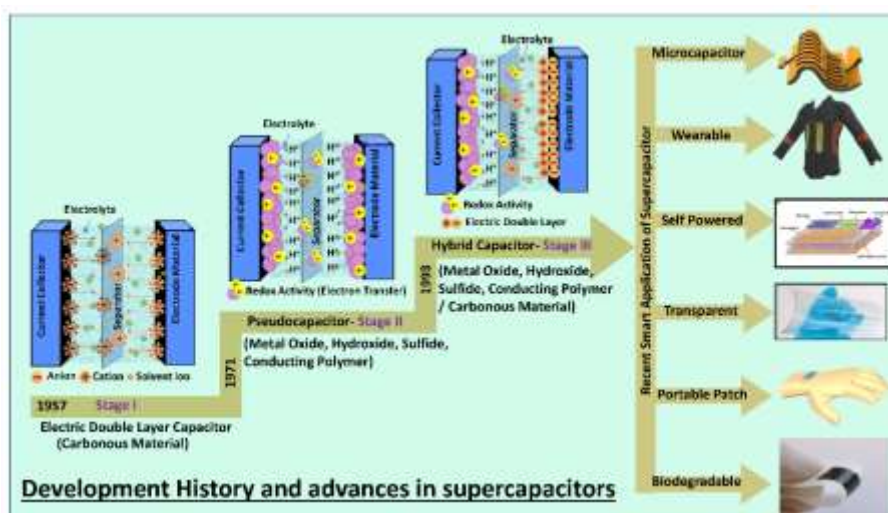


Figure 2- 5 Schematic demonstration of the 3 types of supercapacitors: (A) EDLC, (B) Pseudocapacitor, and (C) Hybrid SC.<sup>52</sup>

### 2.3.1 Electrochemical double layer Supercapacitors

The capacitance of EDLC is generated by the accumulation of the charge at the

electrode/solution interface by the arrangement of electrons or ions. The electric double layer theory plays a crucial role throughout the charging and discharging processes of supercapacitors. It describes the distribution of charged substances at the electrode-electrolyte interface and is essential for understanding the charging and discharging mechanisms of EDLCs. Based on electric double layer theory, there are approximately four models: a) Helmholtz model, b) Gouy-Chapman model, c) Stern model. and d) Bockris, Devanathan, Muller model, depicted in Figure 2-6. This schematic illustrates how the theoretical models of the electric double layer have been refined over time.<sup>50</sup>

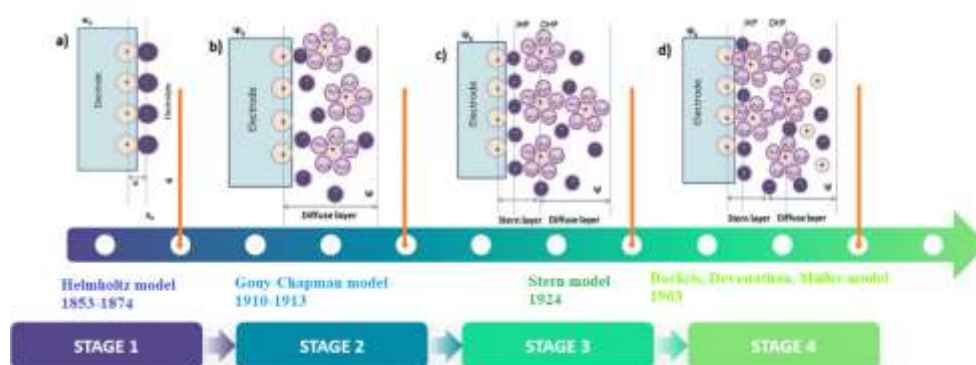


Figure 2- 6 Schematic diagram of 4 types of electric double layers.<sup>53</sup>

In 1853, Helmholtz first discovered the capacitance characteristics at the solid-liquid conductor interface and established the first-generation electric double layer model-the Helmholtz model, in 1874.<sup>54</sup> This model proposes that the charge is evenly distributed at both ends of the electrode-electrolyte interface, as illustrated in Figure 2-6 a). Later, to account for the effects of ion diffusion and the potential difference at the electrode on

capacitance, a revised electric double layer model—the Gouy-Chapman model—was developed in 1913. This model incorporated the Maxwell-Boltzmann distribution and recognized the influence of thermal motion of electrolyte ions near the electrode, leading to the formation of a diffusion layer where ions are not uniformly distributed at the interface, contrary to what the Helmholtz model had described. Additionally, when the potential difference across the interface is larger, more ions are compressed closer to the electrode. with higher electrolyte concentrations, ions can also achieve charge balance with the electrode in a smaller volume, effectively reducing the thickness of the diffusion layer. Subsequently, Stern integrated the first two generations of electric double layer models to propose a third-generation model—the compact layer and diffuse layer series model, as shown in Figure 2-6(c).<sup>55</sup> Based on this model, the electric double layer capacitance ( $C_{DL}$ ) is jointly contributed by the Helmholtz capacitance ( $C_H$ ) and the diffusion layer capacitance ( $C_{DIF}$ ) and can be calculated by Equation 2.5:

$$\frac{1}{C_{DL}} = \frac{1}{C_H} + \frac{1}{C_{DIF}} \quad (\text{Eq 2.5})$$

Stern considered the finite size of the ions, some of which adhere to the electrodes as Helmholtz suggested, forming what are known as Stern layers.<sup>55</sup> This includes the inner Helmholtz plane (IHP) and the outer Helmholtz plane (OHP), which together constitute a two-layer ion adsorption. Beyond these layers, some ions form a diffuse layer, as described in the Gouy-Chapman model.

Subsequently, the impact of solvent molecules on the electric double layer was acknowledged, and the Bockris, Devanathan, Muller model was proposed in the 1960s.<sup>56</sup> Ions with strong solvation, such as most solvated cations and strongly solvated anions, form the OHP. Meanwhile, some anions with weak solvation—specifically those whose contact side with the solid surface are free from solvent molecules—tend to move past the solvation layer and adhere to the electrode surface. This forms the IHP. Compared to the former, the interaction of the latter with the electrode surface results in a greater accumulation of charges on the surface, and cations also migrate into the double layer for charge compensation. This model aligns more closely with experimental observations.

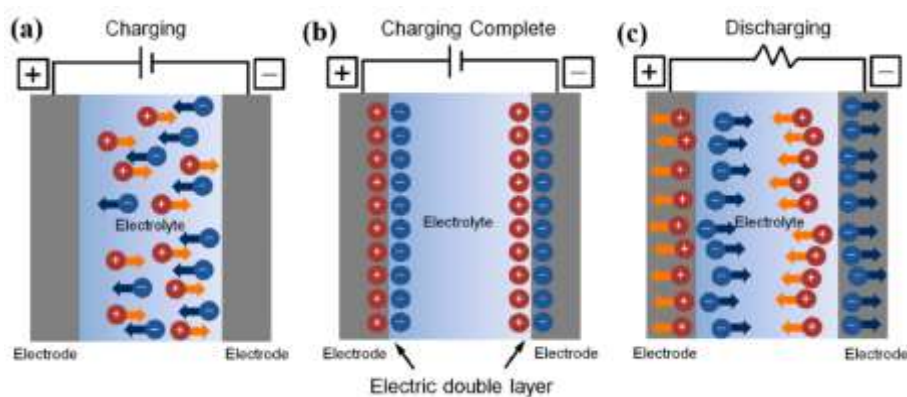


Figure 2- 7 Charge/discharge mechanism of EDCLs.<sup>57</sup>

As shown in Figure 2-7, for electrode/solution systems of EDLC, an electrical double layer is formed at the interface of the conducting electrode and the ionically conducting electrolyte solution.<sup>57</sup> When an electric field is applied to the two electrodes, the anions and cations in the solution migrate to the positive and negative electrodes, respectively, forming an electric double layer on the surface of the electrodes; after the completion of

charge process, the positive and negative charges on the electrodes attract oppositely charged ions in the solution, stabilizing the electric double layer, resulting in a relatively stable potential difference between the positive and negative electrodes. At this time, for a certain electrode, an opposite ion charge equivalent to the charge on the electrode will be generated within a certain distance (diffusion layer), so that it remains electrically neutral.<sup>58</sup> Furthermore, when the two electrodes are connected to an external circuit, charge migration on electrodes generates current in external circuit, and the ions in the solution migrate in the solution, which is the charge and discharge mechanism details of the double layer capacitor.

### **2.3.2 Pseudo-Supercapacitors**

Unlike EDLCs, which store energy through the accumulation of charges on the electrode surface, pseudocapacitors store charge based on rapid and reversible redox reactions occurring within the electrode active material. These reactions are not confined to the electrode surface; the near-surface area also contributes to charge storage through ion diffusion, enhancing the pseudocapacitance. This allows pseudocapacitors to achieve higher capacitance than EDLCs<sup>59</sup>. However, their power density and long-term durability are generally inferior to those of EDLCs. As shown in Figure 2.8, for pseudocapacitors, the theoretical model was first proposed by Conway, that is, the electroactive material stores

charges on the electrode surface and near the surface in the following three ways:<sup>60</sup>

- 1) Underpotential deposition system
- 2) Redox pseudocapacitance
- 3) Intercalation pseudocapacitance

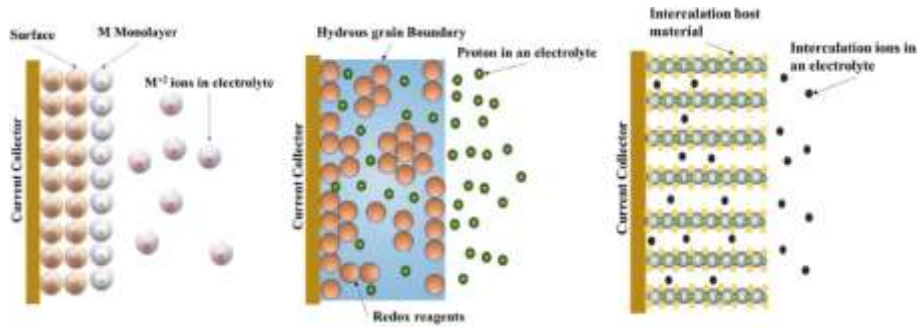
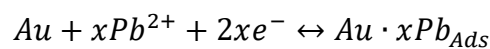


Figure 2- 8 Pseudo capacitance charge mechanism in supercapacitors<sup>61</sup>

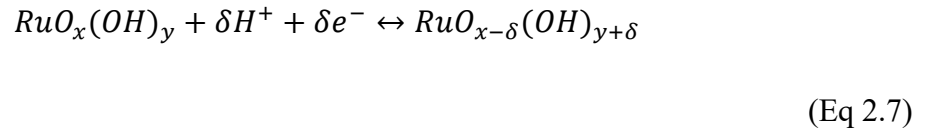
In underpotential deposition, when an external potential is applied, the cations in the electrolyte form an adsorbed monolayer on the surface of a metal electrode with a higher redox potential, typically a noble metal. <sup>62</sup> For instance, using a gold electrode, the electrochemical reaction can be represented as follows:



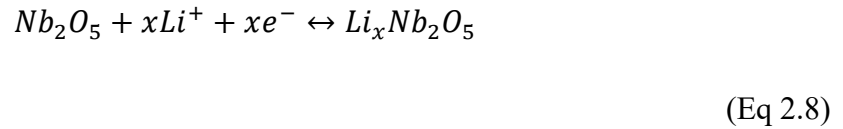
(Eq 2.6)

Redox pseudocapacitance results from the Faradaic reactions that occur on and near the surface of the electrode. The electrode's active materials are primarily composed of TMOs, which undergo rapid transitions between different oxidation states as the potential varies.

<sup>63</sup>For instance, consider RuO<sub>2</sub>, the electrochemical reaction can be represented as follows:



Intercalation pseudocapacitance arises from the insertion of ions from the electrolyte into a material with a layered or tunnel structure. <sup>61</sup>Unlike batteries, during this process, the pseudocapacitive electrode's active material maintains electrical neutrality while storing charge, and its crystal structure remains unchanged. For instance, consider Nb<sub>2</sub>O<sub>5</sub>, the electrochemical reaction can be represented as follows:



### 2.3.3 Hybrid Supercapacitors

As discussed in Sections 2.3.1 and 2.3.2, EDLCs exhibit superb cycle stability and power performance, while pseudosupercapacitors provides higher capacitance. To develop supercapacitors with enhanced performance, many researchers are now focusing on hybrid SCs, aiming to optimize performance and expand the development potential of supercapacitors application.

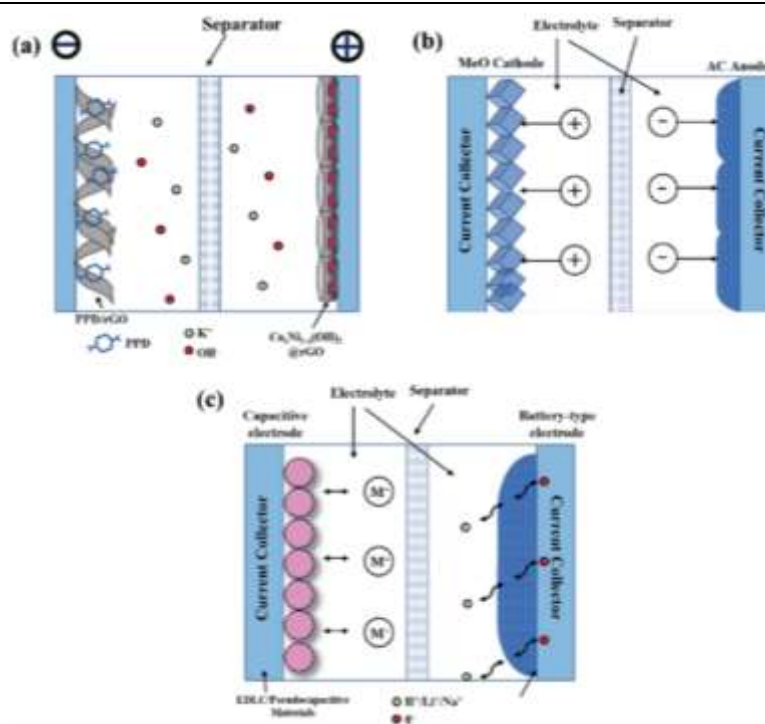


Figure 2- 9 Schematic structure of a hybrid supercapacitor.<sup>64</sup>

As shown in Figure 2.9, three distinct types of hybrids SCs have been developed, based on different electrode configurations: (a) composite type, (b) asymmetric type, and (c) battery-type.<sup>64</sup>

(a) Composite type:

Composite electrodes are created by combining two different types of capacitive materials to form active electrode materials, typically mixing carbon-based materials (EDLC) with metal oxides or conductive polymers (pseudocapacitive).<sup>65</sup> Each single electrode incorporates both non-Faradaic and Faradaic charge storage processes, which are central of

our lab's research.

(b) Asymmetric type:

Two electrodes are coated with active materials that have completely different capacitive properties.<sup>50</sup> For example, one electrode might be coated with an EDLC material, such as activated carbon, which typically serves as the anode, while the other electrode is coated with a pseudocapacitive material like a metal oxide or conductive polymer, usually acting as the cathode.

(c) Battery-type:

The battery-type hybrid combines supercapacitor electrodes with battery electrodes, leveraging the strengths of both technologies.<sup>66</sup>

## 2.4 Electrode materials

As shown in Figure 2.10, SC also call ultracapacitor, consists of two electrodes separated by an ion-permeable membrane (separator) and an electrolyte that ionically connects the two electrodes.<sup>67</sup>

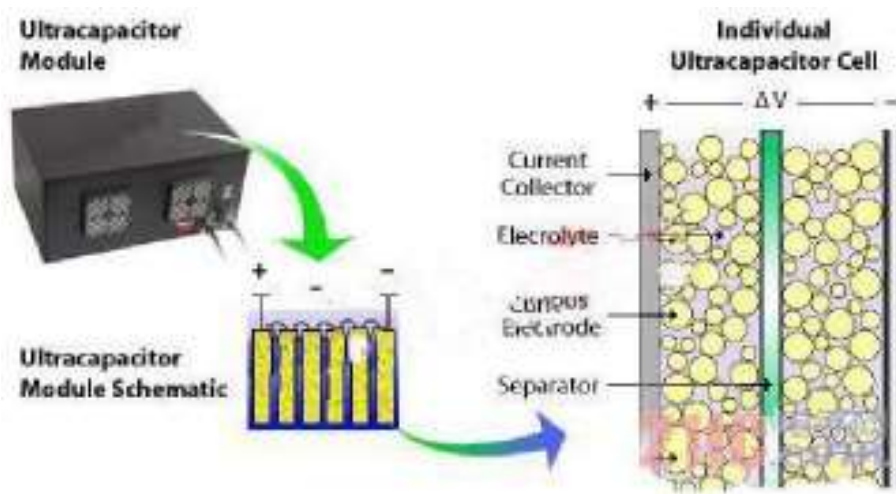


Figure 2- 10 Schematic illustration of a supercapacitor.<sup>67</sup>

In addition, the structure and morphology of the materials have a considerable impact on the electrochemical performance of supercapacitor electrodes. Depending on the electrode material and surface shape, some ions may penetrate into the bilayer to become specifically adsorbed ions and produce pseudocapacitance for the overall capacitance of the supercapacitor, such as TMOs and conducting polymers supercapacitor.<sup>68</sup> For EDLC, electrodes with high specific surface area and good conductivity and adsorption properties are required, and carbon-based electrode materials have the above advantages.

### 2.4.1 Carbon-based materials for electrode of EDLCs

According to the characteristics of EDLC, the electrode material itself is required to have high specific surface area, good conductivity and adsorption performance, and in order to better promote the application of SC, electrode materials with abundant and cheap raw

materials should be selected as much as possible to reduce the preparation cost, and carbon-based electrode materials, such as like carbon nanotubes(CNTs),<sup>28,29,69-71</sup> graphene,<sup>1</sup> carbon aerogels<sup>72,73</sup> and <sup>12</sup> (AC), have exactly the above advantages, and the simple preparation process, easy adjustment of pore size, stable chemical properties, and excellent cycle performance, are widely used as electrode materials for EDLC, and also can be used as conductive additives to form composites with TMOs and conductive polymers.

Therefore, carbon materials are the most widely used and commercially successful class of electrode materials.<sup>74</sup>

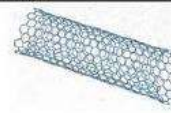
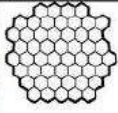
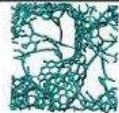
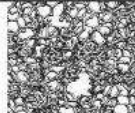
Material	Carbon onions	Carbon nanotubes	Graphene	Activated carbon	Carbide derived carbon	Templated carbon
Dimensionality	0-D	1-D	2-D	3-D	3-D	3-D
Conductivity	High	High	High	Low	Moderate	Low
Volumetric Capacitance	Low	Low	Moderate	High	High	Low
Cost	High	High	Moderate	Low	Moderate	High
Structure						

Table 2- 1 Carbon-based materials used in EDLC<sup>75</sup>

## 2.4.2 Redox-based materials

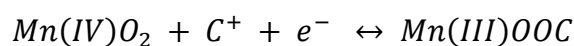
Metal oxides have high specific capacitances, making them suitable for electrode fabrication focused on high-energy and high-power supercapacitors. There are several different metal oxide materials used for electrode fabrication, such as RuO<sub>2</sub>, IrO<sub>2</sub>, MnO<sub>2</sub>, Mn<sub>3</sub>O<sub>4</sub>, NiO, Co<sub>2</sub>O<sub>3</sub>, V<sub>2</sub>O<sub>5</sub>, or MoO<sub>x</sub>. Among them, the most studied are oxides of

ruthenium and manganese.<sup>38,76,77</sup>

Ruthenium oxide ( $\text{RuO}_2$ ) is one of the most popular pseudocapacitive electrode materials due to its high theoretical specific capacitance (about  $1000 \text{ F g}^{-1}$ ). In addition, it possesses a wide potential window, highly reversible redox reaction, high electrical conductivity, good thermal stability, long cycle life and fast charge and discharge rate.<sup>78</sup> There are three different oxidation states in the voltage range of 1.2V, and the more oxidation states, the higher the energy density. In addition to the Faraday capacitance, around 1/10 of the stored charge in the  $\text{RuO}_2$  electrode comes from the electric double-layer capacitance, working in parallel with the pseudocapacitance.<sup>79</sup> As shown in equation 2.7 in Chapter 2.3.2, in electrolyte solutions ( $\text{pH} < 7$ ), a fast reversible electron movement and an electro-adsorption of  $\text{H}^+$  to the surface occurs where Ru oxidation states change between (II) and (IV).<sup>66</sup> But  $\text{RuO}_2$  electrodes are very expensive, which reduces their aerospace and military applications, and their 1 V operating voltage window limits their use in small electronic devices.

In addition, manganese oxides appear to be alternatives to  $\text{RuO}_2$  because of their reasonably low cost, low toxicity and environmental safety, and theoretically high capacitances up to  $1370 \text{ F g}^{-1}$ .<sup>4</sup> In addition, manganese oxides perform equally well in neutral electrolytes due to their unique charge storage mechanism, as shown in equation 2.9.<sup>29,49</sup> The use of acidic electrolytes is often hazardous to the environment due to subsequent disposal issues of equipment and leakage of electrolytes. All these problems

can be avoided by using manganese oxide as the electrode material. The fast charge-discharge rate and long cycling behavior make manganese oxide one of the best electrode materials for ES applications.



C represents the cation of electrolyte. (Eq 2.9)

Besides TMOs, conducting polymers have also been extensively studied as pseudocapacitive electrode materials.<sup>40</sup> Conductive polymers have the advantages of less pollution, easy preparation, and high electrical conductivity. Typical conducting polymers include polyacetylene (PA),<sup>80</sup> polyaniline (PANI),<sup>81</sup> polypyrrole (PPy), polythiophene (PTH),<sup>82</sup> poly(para-phenylene) (PPP),<sup>83</sup> poly(phenylenevinylene) (PPV),<sup>84</sup> and polyfuran (PF).<sup>85</sup> Figure 2.11 shows their different molecular structures.<sup>86</sup>

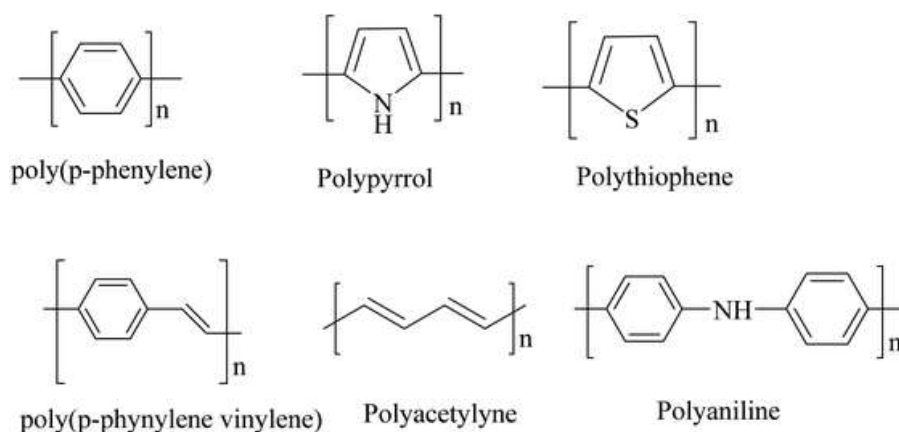


Figure 2- 11 Structural illustration of different conducting polymers.<sup>86</sup>

During charge/discharge, charges are accumulated through redox reactions that occur in the film volume, not just on the surface.<sup>82</sup> Therefore, the specific capacitance of flexible conductive polymers is fairly high. However, the constraint of this kind of material is that

they can only be used during a limited potential window.

## 2.5 Electrolytes

The applied voltage, efficiency, and power handling also depend on the choice of electrolyte, which is also an important part of the SC composition.<sup>87</sup> Electrolytes act as a media that supports the generation of charges at the interface with electrodes, enabling their mobility or providing adsorbed ions as charge carriers.<sup>74</sup> Therefore, an electrolyte matched to the electrode system is critical to achieve maximum energy and power density and to decide its cell voltage.

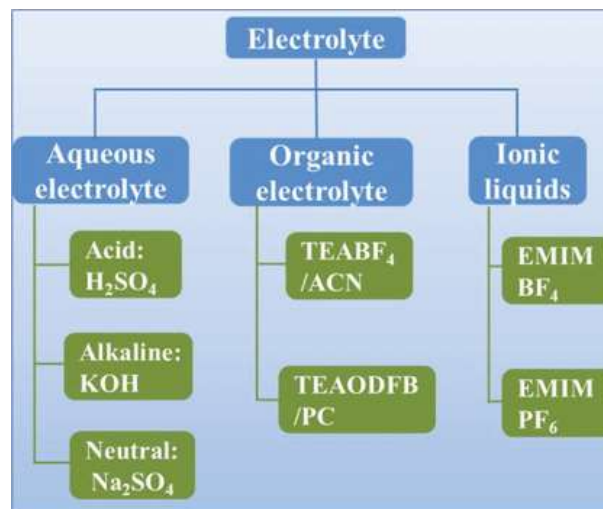


Figure 2- 12 Classification of electrolytes for ES<sup>88</sup>

As shown in Figure 0-12, there are three types of electrolytes: I) aqueous electrolyte, II)

organic electrolyte, and III) ionic electrolyte.<sup>88</sup>

The properties of different electrolytes can be seen from Figure 2-13.<sup>89</sup>

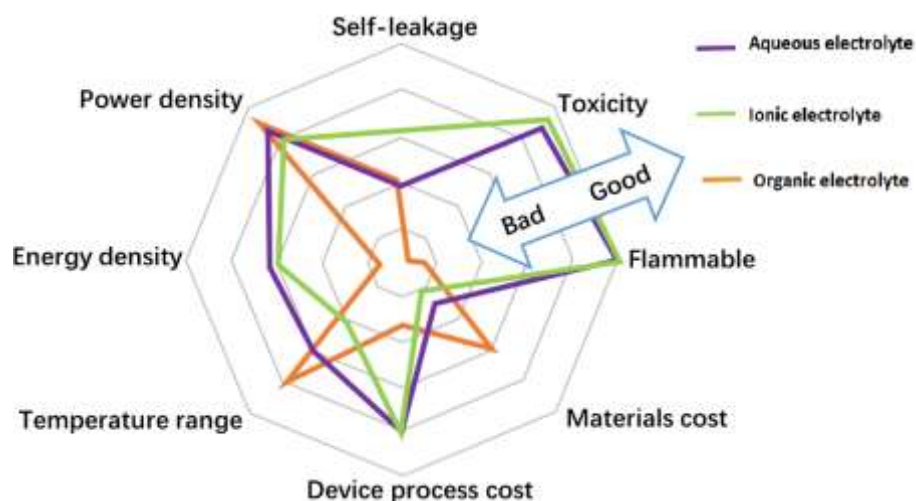


Figure 2- 13 The comparison of different supercapacitor electrolytes.<sup>89</sup>

## 2.5.1 Aqueous electrolytes

Aqueous electrolytes have been used extensively in research and development due to their easy operating in the laboratory as compared to organic electrolytes and ionic liquids electrolyte which require purification procedures. Moreover, aqueous electrolytes provide good conductivity, non-flammable and non-toxicity.<sup>90</sup> However, their maximum voltage range is 1.229 V, which is due to the theoretical voltage of 1.229 V for electrolyzed water, as can be seen from Figure 2-14.<sup>91</sup> Depending on the salt used, the pH of the aqueous electrolyte also varies and can be classified as acidic, basic or neutral. These electrolytes have high ionic conductivity and low equivalent resistance, and common aqueous

electrolytes include  $\text{H}_2\text{SO}_4$ ,  $\text{KOH}$ ,  $\text{KCl}$ , and  $\text{Na}_2\text{SO}_4$ .<sup>92</sup>

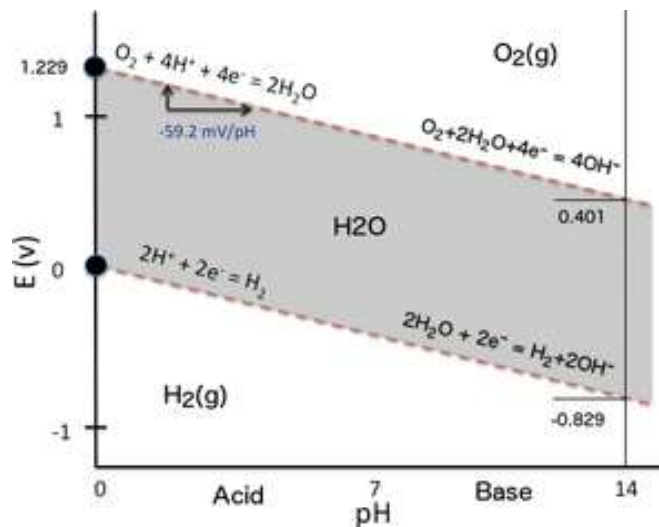


Figure 2- 14 Pourbaix diagram for water, including equilibrium regions for water<sup>91</sup>

## 2.5.2 Organic electrolytes

Organic electrolytes are made of conductive salts dissolved in organic solvents. Compared with aqueous electrolytes, organic electrolytes have an extremely high market share in the commercial market.<sup>93</sup> This is due to its wider operating voltage window allowing higher energy and power density, as can be seen from eq2.3 and eq2.4. However, organic electrolytes have the disadvantages of high cost, low electrical conductivity, flammability, and low capacitance.<sup>94</sup> Another main disadvantage of organic electrolytes is the need for complex purification procedures and controlled environments, especially moisture.<sup>95</sup>

### **2.5.3 Ionic liquids electrolyte**

Ionic liquids (ILs) are made of organic cations and organic or inorganic anions and are liquid at low temperatures. Ionic liquids are the latest advancement in electrolyte development and have recently attracted great interest due to their high stability, low volatility, and non-flammability.<sup>96</sup> In addition, compared with organic electrolytes, this electrolyte is non-toxic, and can further improve the working voltage and ionic conductivity, and improve the energy density.<sup>97</sup> But its further development is restricted by economic cost.

## Chapter 3 Objectives

As mentioned previously, our primary objective is to achieve good performance of hybrid supercapacitor, composition type, cathodes under high mass loading ( $40\text{mg cm}^{-1}$ ) through reasonable morphology and structural design of electrodes and promote the development of hybrid supercapacitors and expand their application market. We are particularly focused on developing active cathode materials based on EDLC and pseudocapacitive composites, such as MnOx-based composites (discussed in Chapters 6-10) and  $\text{La}_{0.65}\text{Sr}_{0.35}\text{MnO}_3$  (outlined in Chapter 11) with CNTs.

Achieving this involves:

- a) Developing new co-dispersants to enhance the dispersion of electrode composites.
- b) Utilizing advanced colloidal processing techniques to produce non-agglomerated particles with innovative capping agents.
- c) Implementing scalable processing technologies, including high-energy ball milling (HEBM), to manufacture advanced nanocomposites, thereby creating supercapacitor devices with superior performance."

## Chapter 4 Proposed approaches

To develop  $\text{MnO}_2$ ,  $\text{Mn}_3\text{O}_4$  and  $\text{La}_{0.65}\text{Sr}_{0.35}\text{MnO}_3$  cathode for advanced asymmetric supercapacitors, we will propose several advanced techniques for synthesis nanostructured electrode.

### 4.1. Wet chemical synthesis of $\text{MnO}_2$ and $\text{Mn}_3\text{O}_4$

This is the method we use to synthesize  $\text{Mn}_3\text{O}_4$ , shown as the box in Figure 4-1. In this approach, the pH of the solution was brought to 10 by adding a base dropwise to the manganese nitrate solution to obtain  $\text{Mn}_3\text{O}_4$ .<sup>29</sup> In addition, 1.6 g  $\text{KMnO}_4$  was dissolved in 50 mL of water, and 25 mL of ethanol was added dropwise. Stirring was performed during 2 h. The reduction in  $\text{KMnO}_4$  with ethanol resulted in the formation of  $\text{MnO}_2$ .<sup>98</sup>



Figure 4- 1 Chemical synthesis of  $\text{Mn}_3\text{O}_4$ .

---

## 4.2 Application of new capping agents for $\text{Mn}_3\text{O}_4$

Besides the method for synthesizing  $\text{Mn}_3\text{O}_4$  mentioned in the previous subsection 4.1., the new method is based on the application of capping agents, such as quercetin (QC), rhamnolipid (RL), murexide, tetrahydroxy-1,4-quinone (TQ), catechin (CT) gallocyanine (GA), to synthesize  $\text{Mn}_3\text{O}_4$  nanoparticles. The size and shape of the  $\text{Mn}_3\text{O}_4$  particles are affected by the capping agents and then the electrode performance was also improved. Most importantly, the application of capping agents during the synthesis also reduced agglomeration due to surface energy reduction and condensation of  $\text{OH}^-$  on the particles. In the new method, a solution of  $\text{Mn}(\text{NO}_3)_2 \cdot 4\text{H}_2\text{O}$  in DI water with addition of capping agent was used to synthesize  $\text{Mn}_3\text{O}_4$  nanoparticles, and the pH of the solution was increased to pH= 10 to synthesize  $\text{Mn}_3\text{O}_4$ .

## 4.3 Development and application of new co-dispersants for $\text{MnO}_2$ , $\text{Mn}_3\text{O}_4$ and $\text{La}_{0.65}\text{Sr}_{0.35}\text{MnO}_3$ as well as CNTs

It is well known that the capacitance of metal oxide-based electrodes prepared without conductive additives is low due to their low conductivity. Higher capacitances can be achieved by using conductive additives that increase electronic conductivity.

However, as shown in Figure 4-1, the MWCNTs we used would agglomerate, which would seriously affect the electrochemical performance of the electrode. To better develop electrodes and achieve high capacitance, advanced co-dispersants are essential. An effective co-dispersant is essential to enhance the synergistic effect between metal oxides and MWCNTs, which is key to developing efficient supercapacitors and capturing a larger market share.

## **4.4 Development of High energy ball milling (HEBM) using new dispersants**

HEBM is a very promising mechanochemical synthesis technique, known for its waste-free and environmentally friendly processing. Mechanochemical alloying stands out as one of the most promising applications of HEBM. Its mechanism is shown in Figure 4-2.<sup>99</sup>

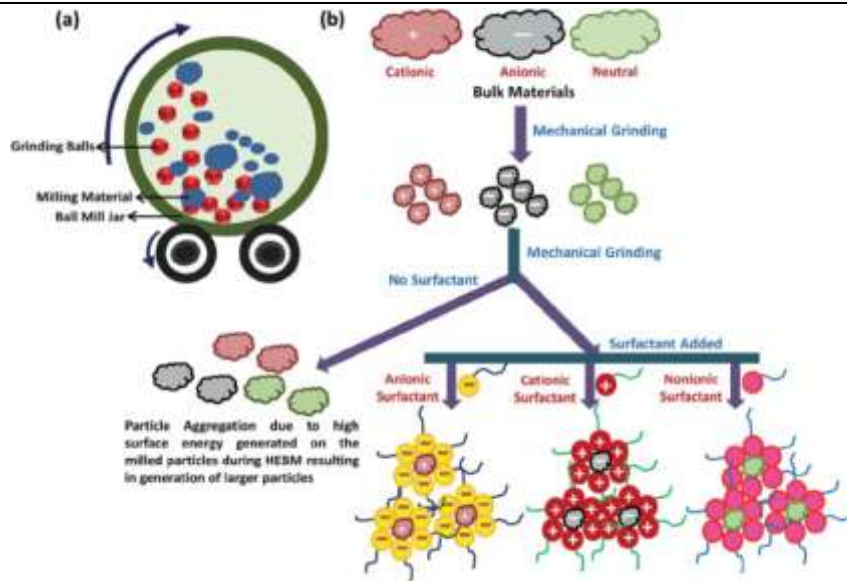


Figure 4- 2 (a) HEBM system and (b) schematic representation of the NPs synthesis using HEBM method with and without surfactant.<sup>99</sup>

The use of HEBM allows the fabrication of improved composites in which ceramic particles are homogeneously dispersed in a metal alloy matrix, allowing them to exhibit excellent mechanical properties. For example, magnesium alloys exhibit remarkable hydrogen storage properties after HEBM.<sup>100</sup> This is because HEBM plays a huge role in reducing the grain size and optimizing the morphology of the catalyst material. In addition, HEBM can also alter the microstructure and properties of magnetic materials, accelerating the development of advanced alloys with hard magnetic properties.<sup>101</sup> HEBM also has obvious benefits for improving the electrochemical performance of energy storage materials.<sup>71</sup> The application of HEBM reduces the particle size of the electrode material, giving it a larger specific surface area, increasing its ability to store charges, and increasing the surface roughness of the

nanoparticles.

## **4.5 Investigation of activation mechanism of Mn<sub>3</sub>O<sub>4</sub> electrodes and development of strategies for acceleration/elimination of activation procedure**

It is mentioned in the literature that although the theoretical capacitance of Mn<sub>3</sub>O<sub>4</sub> is high, it is practically difficult to achieve high capacitance values in the case of large mass loads, and the specific capacitance decreases with the increase of active material mass. Furthermore, applying Mn<sub>3</sub>O<sub>4</sub> to electrodes with high active mass requires a long-time activation process, which must be avoided in practical applications. The first charge-discharge cycles of Mn<sub>3</sub>O<sub>4</sub> electrodes were found to show low capacitance, and to activate the material and achieve large capacitance, an activation cycling procedure was required. This activation process results in a significant increase in capacitance. To investigate the activation mechanism and the changes that occur in the electrodes during activation and correlate this to the increase in capacitance, we performed X-ray photoelectron spectroscopy (XPS) and scanning transmission X-ray microscopy (STXM) tests.

---

## Chapter 5 References

- 1 Cai, X., Sun, K., Qiu, Y. & Jiao, X. Recent Advances in Graphene and Conductive Polymer Composites for Supercapacitor Electrodes: A Review. *Crystals* **11** (2021). <https://doi.org:10.3390/cryst11080947>
- 2 Chatterjee, D. P. & Nandi, A. K. A review on the recent advances in hybrid supercapacitors. *Journal of Materials Chemistry A* **9**, 15880-15918 (2021). <https://doi.org:10.1039/d1ta02505h>
- 3 Zuo, W. *et al.* Battery-Supercapacitor Hybrid Devices: Recent Progress and Future Prospects. *Advanced Science* **4** (2017). <https://doi.org:10.1002/advs.201600539>
- 4 Zhao, W., Rubio, S. J. B., Dang, Y. & Suib, S. L. Green Electrochemical Energy Storage Devices Based on Sustainable Manganese Dioxides. *Acs Es&T Engineering* **2**, 20-42 (2022). <https://doi.org:10.1021/acsestengg.1c00317>
- 5 Sk, M. M., Yue, C. Y., Ghosh, K. & Jena, R. K. Review on advances in porous nanostructured nickel oxides and their composite electrodes for high-performance supercapacitors. *Journal of Power Sources* **308**, 121-140 (2016). <https://doi.org:10.1016/j.jpowsour.2016.01.056>
- 6 Reddy, A. L. M., Gowda, S. R., Shaijumon, M. M. & Ajayan, P. M. Hybrid Nanostructures for Energy Storage Applications. *Advanced Materials* **24**, 5045-5064 (2012). <https://doi.org:10.1002/adma.201104502>
- 7 Attia, S. Y., Mohamed, S. G., Barakat, Y. F., Hassan, H. H. & Zoubi, W. A. Supercapacitor electrode materials: addressing challenges in mechanism and charge storage. *Reviews in Inorganic Chemistry* **42**, 53-88 (2022). <https://doi.org:doi:10.1515/revic-2020-0022>
- 8 Kado, Y., Soneda, Y., Hatori, H. & Kodama, M. Advanced carbon electrode for electrochemical capacitors. *Journal of Solid State Electrochemistry* **23**, 1061-1081 (2019). <https://doi.org:10.1007/s10008-019-04211-x>
- 9 Sridhar, D. *Carbon-nanofiber electrodes directly grown on a nickel foam current collector for electrochemical energy storage devices*, (2020).
- 10 Chen, S., Qiu, L. & Cheng, H.-M. Carbon-Based Fibers for Advanced Electrochemical Energy Storage Devices. *Chemical Reviews* **120**, 2811-2878 (2020). <https://doi.org:10.1021/acs.chemrev.9b00466>
- 11 Lin, Z., Taberna, P.-L. & Simon, P. Electrochemical double layer capacitors: What is next beyond the corner? *Current Opinion in Electrochemistry* **6**, 115-119 (2017). <https://doi.org:10.1016/j.coelec.2017.10.013>
- 12 Shi, K., Ren, M. & Zhitomirsky, I. Activated Carbon-Coated Carbon Nanotubes for Energy Storage in Supercapacitors and Capacitive Water Purification. *ACS Sustainable Chemistry & Engineering* **2**, 1289-1298 (2014).

- 
- <https://doi.org:10.1021/sc500118r>
- 13 Borenstein, A. *et al.* Carbon-based composite materials for supercapacitor electrodes: a review. *Journal of Materials Chemistry A* **5**, 12653-12672 (2017). <https://doi.org:10.1039/c7ta00863e>
- 14 Dubal, D. P., Ayyad, O., Ruiz, V. & Gomez-Romero, P. Hybrid energy storage: the merging of battery and supercapacitor chemistries. *Chemical Society Reviews* **44**, 1777-1790 (2015). <https://doi.org:10.1039/c4cs00266k>
- 15 Cherusseri, J., Choudhary, N., Kumar, K. S., Jung, Y. & Thomas, J. Recent trends in transition metal dichalcogenide based supercapacitor electrodes. *Nanoscale Horizons* **4**, 840-858 (2019). <https://doi.org:10.1039/c9nh00152b>
- 16 Cui, M. & Meng, X. Overview of transition metal-based composite materials for supercapacitor electrodes. *Nanoscale Advances* **2**, 5516-5528 (2020). <https://doi.org:10.1039/d0na00573h>
- 17 Theerthagiri, J. *et al.* Recent progress and emerging challenges of transition metal sulfides based composite electrodes for electrochemical supercapacitive energy storage. *Ceramics International* **46**, 14317-14345 (2020). <https://doi.org:10.1016/j.ceramint.2020.02.270>
- 18 Liu, R. *et al.* Fundamentals, advances and challenges of transition metal compounds-based supercapacitors. *Chemical Engineering Journal* **412** (2021). <https://doi.org:10.1016/j.cej.2021.128611>
- 19 Singhal, R. *et al.* Recent developments in transition metal-based nanomaterials for supercapacitor applications. *Journal of Materials Research* (2022). <https://doi.org:10.1557/s43578-022-00598-y>
- 20 Zheng, J. P. Ruthenium oxide-carbon composite electrodes for electrochemical capacitors. *Electrochemical and Solid-State Letters* **2**, 359 (1999).
- 21 Soudan, P. *et al.* Synthesis, chemical polymerization and electrochemical properties of low band gap conducting polymers for use in supercapacitors Properties of the polymers are available as supplementary data. For direct electronic access see <http://www.rsc.org/suppdata/jm/b0/b006577n>. *Journal of Materials Chemistry* **11**, 773-782 (2001).
- 22 Yoon, Y., Cho, W., Lim, J. & Choi, D. Solid-state thin-film supercapacitor with ruthenium oxide and solid electrolyte thin films. *Journal of power sources* **101**, 126-129 (2001).
- 23 Bi, R.-R. *et al.* Highly dispersed RuO<sub>2</sub> nanoparticles on carbon nanotubes: facile synthesis and enhanced supercapacitance performance. *The Journal of Physical Chemistry C* **114**, 2448-2451 (2010).
- 24 Chen, R., Yu, M., Sahu, R. P., Puri, I. K. & Zhitomirsky, I. The development of pseudocapacitor electrodes and devices with high active mass loading. *Advanced Energy Materials* **10**, 1903848 (2020).
- 25 Poon, R. & Zhitomirsky, I. Supercapacitor electrodes with high active mass loading. *MRS Communications* **8**, 1135-1138 (2018).

- 
- <https://doi.org:10.1557/mrc.2018.165>
- 26 Muzaffar, A., Ahamed, M. B., Deshmukh, K. & Thirumalai, J. A review on recent advances in hybrid supercapacitors: Design, fabrication and applications. *Renewable & Sustainable Energy Reviews* **101**, 123-145 (2019). <https://doi.org:10.1016/j.rser.2018.10.026>
- 27 Guo, W. *et al.* Strategies and insights towards the intrinsic capacitive properties of MnO<sub>2</sub> for supercapacitors: Challenges and perspectives. *Nano Energy* **57**, 459-472 (2019). <https://doi.org:10.1016/j.nanoen.2018.12.015>
- 28 Nawwar, M., Sahu, R. P., Puri, I. K. & Zhitomirsky, I. Functionally Decorated Carbon Nanotube Networks for Energy Storage in Supercapacitors. *Frontiers in Energy Research* **8** (2020). <https://doi.org:10.3389/fenrg.2020.00046>
- 29 Rorabeck, K. & Zhitomirsky, I. Salting-out aided dispersive extraction of Mn<sub>3</sub>O<sub>4</sub> nanoparticles and carbon nanotubes for application in supercapacitors. *Colloids and Surfaces A: Physicochemical and Engineering Aspects* **618**, 126451 (2021). <https://doi.org:https://doi.org/10.1016/j.colsurfa.2021.126451>
- 30 Wang, J. *et al.* Pseudocapacitive materials for electrochemical capacitors: from rational synthesis to capacitance optimization. *National Science Review* **4**, 71-90 (2017). <https://doi.org:10.1093/nsr/nww072>
- 31 Li, Z., Jiao, X., Li, C. & Chen, D. Synthesis and application of nanocages in supercapacitors. *Chemical Engineering Journal* **351**, 135-156 (2018). <https://doi.org:10.1016/j.cej.2018.06.108>
- 32 Simon, P. & Gogotsi, Y. Materials for electrochemical capacitors. *Nature Materials* **7**, 845-854 (2008). <https://doi.org:10.1038/nmat2297>
- 33 Tripathy, A., Pramanik, S., Cho, J., Santhosh, J. & Osman, N. A. A. Role of morphological structure, doping, and coating of different materials in the sensing characteristics of humidity sensors. *Sensors* **14**, 16343-16422 (2014).
- 34 Scholz, F. From the Leiden jar to the discovery of the glass electrode by Max Cremer. *Journal of Solid State Electrochemistry* **15**, 5-14 (2011).
- 35 Yaseen, M. *et al.* A review of supercapacitors: materials design, modification, and applications. *Energies* **14**, 7779 (2021).
- 36 Lin, L., Ning, H., Song, S., Xu, C. & Hu, N. Flexible electrochemical energy storage: The role of composite materials. *Composites Science and Technology* **192** (2020). <https://doi.org:10.1016/j.compscitech.2020.108102>
- 37 Gui, Q. *et al.* Recent advances in materials and device technologies for aqueous hybrid supercapacitors. *Science China-Materials* **65**, 10-31 (2022). <https://doi.org:10.1007/s40843-021-1733-1>
- 38 Wang, D.-G., Liang, Z., Gao, S., Qu, C. & Zou, R. Metal-organic framework-based materials for hybrid supercapacitor application. *Coordination Chemistry Reviews* **404** (2020). <https://doi.org:10.1016/j.ccr.2019.213093>
- 39 Kausar, A. Overview on conducting polymer in energy storage and energy conversion system. *Journal of Macromolecular Science Part a-Pure and Applied Chemistry* **54**, 640-653 (2017).

- 
- <https://doi.org/10.1080/10601325.2017.1317210>
- 40 Shown, I., Ganguly, A., Chen, L.-C. & Chen, K.-H. Conducting polymer-based flexible supercapacitor. *Energy Science & Engineering* **3**, 2-26 (2015). <https://doi.org/10.1002/ese3.50>
- 41 Kandasamy, M., Sahoo, S., Nayak, S. K., Chakraborty, B. & Rout, C. S. Recent advances in engineered metal oxide nanostructures for supercapacitor applications: experimental and theoretical aspects. *Journal of Materials Chemistry A* **9**, 17643-17700 (2021). <https://doi.org/10.1039/d1ta03857e>
- 42 Dutta, A., Mitra, S., Basak, M. & Banerjee, T. A comprehensive review on batteries and supercapacitors: development and challenges since their inception. *Energy Storage*, e339 (2022).
- 43 Chen, T.-W. *et al.* High-Performance-Based Perovskite-Supported Nanocomposite for the Development of Green Energy Device Applications: An Overview. *Nanomaterials* **11** (2021). <https://doi.org/10.3390/nano11041006>
- 44 Guerrieri, M. Tramways in Urban Areas: An Overview on Safety at Road Intersections. *Urban Rail Transit* **4**, 223-233 (2018). <https://doi.org/10.1007/s40864-018-0093-5>
- 45 Azim, M. K. M., Arifutzzaman, A., Saidur, R., Khandaker, M. U. & Bradley, D. A. Recent progress in emerging hybrid nanomaterials towards the energy storage and heat transfer applications: A review. *Journal of Molecular Liquids* **360** (2022). <https://doi.org/10.1016/j.molliq.2022.119443>
- 46 Song, Y.-s. & Kim, Z.-w. (Google Patents, 2011).
- 47 Mohd Abdah, M. A. A., Azman, N. H. N., Kulandaivalu, S. & Sulaiman, Y. Review of the use of transition-metal-oxide and conducting polymer-based fibres for high-performance supercapacitors. *Materials & Design* **186**, 108199 (2020). [https://doi.org:https://doi.org/10.1016/j.matdes.2019.108199](https://doi.org/https://doi.org/10.1016/j.matdes.2019.108199)
- 48 Jiang, H., Lee, P. S. & Li, C. 3D carbon based nanostructures for advanced supercapacitors. *Energy & Environmental Science* **6**, 41-53 (2013). <https://doi.org/10.1039/c2ee23284g>
- 49 Poon, R., Liang, W. & Zhitomirsky, I. Mn<sub>3</sub>O<sub>4</sub> and (ZnFe)OOH Composites for Supercapacitors with High Active Mass. *Metallurgical and Materials Transactions A* **51**, 855-862 (2020). <https://doi.org/10.1007/s11661-019-05561-x>
- 50 Chaudhary, S., Raja, M. & Sinha, O. A review on the different types of electrode materials for aqueous supercapacitor applications. *Advances in Natural Sciences: Nanoscience and Nanotechnology* **12**, 015011 (2021).
- 51 Dutta, A., Mitra, S., Basak, M. & Banerjee, T. A comprehensive review on batteries and supercapacitors: Development and challenges since their inception. *Energy Storage* **5**, e339 (2023).
- 52 Kumar, N., Kim, S.-B., Lee, S.-Y. & Park, S.-J. Recent advanced supercapacitor: a review of storage mechanisms, electrode materials,

- modification, and perspectives. *Nanomaterials* **12**, 3708 (2022).
- 53 Vargheese, S., Rajendra Kumar, R. T. & Haldorai, Y. in *Nanostructured Materials for Supercapacitors* (eds Sabu Thomas, Amadou Belal Gueye, & Ram K. Gupta) 27-52 (Springer International Publishing, 2022).
- 54 González-Tovar, E., Jiménez-Ángeles, F., Messina, R. & Lozada-Cassou, M. A new correlation effect in the Helmholtz and surface potentials of the electrical double layer. *The Journal of chemical physics* **120**, 9782-9792 (2004).
- 55 Carnie, S. L. & Chan, D. Y. The modelling of solvent structure in the electrical double layer. *Advances in Colloid and Interface Science* **16**, 81-100 (1982).
- 56 Gileadi, E. & Stoner, G. The effect of competition with water on the kinetic parameters in electrode reactions. *Journal of The Electrochemical Society* **118**, 1316 (1971).
- 57 Zhang, M., He, L., Shi, T. & Zha, R. Nanocasting and Direct Synthesis Strategies for Mesoporous Carbons as Supercapacitor Electrodes. *Chemistry of Materials* **30** (2018). <https://doi.org:10.1021/acs.chemmater.8b03345>
- 58 Ike, I., Iyuke, S. & Sigalas, I. Understanding Performance Limitation and Suppression of Leakage Current or Self-Discharge in Electrochemical Capacitors: A Review. *Phys. Chem. Chem. Phys.* **18** (2015). <https://doi.org:10.1039/C5CP05459A>
- 59 Meena, D. *et al.* Energy storage in the 21st century: A comprehensive review on factors enhancing the next-generation supercapacitor mechanisms. *Journal of Energy Storage* **72**, 109323 (2023).
- 60 Ranganatha, S. (2019).
- 61 Waqas Hakim, M., Fatima, S., Rizwan, S. & Mahmood, A. in *Nanostructured Materials for Supercapacitors* (eds Sabu Thomas, Amadou Belal Gueye, & Ram K. Gupta) 53-70 (Springer International Publishing, 2022).
- 62 Patra, A. *et al.* Understanding the charge storage mechanism of supercapacitors: in situ/operando spectroscopic approaches and theoretical investigations. *Journal of Materials Chemistry A* **9**, 25852-25891 (2021).
- 63 Liu, Y., Jiang, S. P. & Shao, Z. Intercalation pseudocapacitance in electrochemical energy storage: recent advances in fundamental understanding and materials development. *Materials Today Advances* **7**, 100072 (2020). <https://doi.org:https://doi.org/10.1016/j.mtadv.2020.100072>
- 64 Liew, S. Q. & Jun, H. K. in *Nanostructured Materials for Supercapacitors* (eds Sabu Thomas, Amadou Belal Gueye, & Ram K. Gupta) 71-100 (Springer International Publishing, 2022).
- 65 Yang, L. W. & Zhitomirsky, I. Influence of Capping Agents on the Synthesis of Mn<sub>3</sub>O<sub>4</sub> Nanostructures for Supercapacitors. *ACS Applied Nano Materials* (2023). <https://doi.org:10.1021/acsanm.2c05519>
- 66 Yadav, M. S. Metal oxides nanostructure-based electrode materials for supercapacitor application. *Journal of Nanoparticle Research* **22**, 367 (2020). <https://doi.org:10.1007/s11051-020-05103-2>
- 67 Liu, T. & Liu, G. Block copolymers for supercapacitors, dielectric capacitors

- 
- and batteries. *Journal of Physics: Condensed Matter* **31**, 233001 (2019).  
<https://doi.org/10.1088/1361-648x/ab0d77>
- 68 Ji, C., Mi, H. & Yang, S. Latest advances in supercapacitors: From new  
electrode materials to novel device designs. *Chinese Science Bulletin-Chinese*  
**64**, 9-34 (2019). <https://doi.org/10.1360/n972018-00815>
- 69 Afzal, A. *et al.* Polypyrrole/carbon nanotube supercapacitors: Technological  
advances and challenges. *Journal of Power Sources* **352**, 174-186 (2017).  
<https://doi.org/10.1016/j.jpowsour.2017.03.128>
- 70 Liang, W. & Zhitomirsky, I. Composite Fe<sub>3</sub>O<sub>4</sub>-MXene-Carbon Nanotube  
Electrodes for Supercapacitors Prepared Using the New Colloidal Method.  
*Materials* **14**, 2930 (2021).
- 71 Zhang, C. & Zhitomirsky, I. Influence of High Energy Ball Milling and  
Dispersant on Capacitive Properties of Fe<sub>2</sub>O<sub>3</sub>–Carbon Nanotube  
Composites. *Journal of Composites Science* **6**, 177 (2022).
- 72 Li, J., Wang, X., Huang, Q., Gamboa, S. & Sebastian, P. Studies on  
preparation and performances of carbon aerogel electrodes for the application  
of supercapacitor. *Journal of Power Sources* **158**, 784-788 (2006).
- 73 Kim, S.-J., Hwang, S. & Hyun, S. Preparation of carbon aerogel electrodes for  
supercapacitor and their electrochemical characteristics. *Journal of materials  
science* **40**, 725-731 (2005).
- 74 Hao, L., Li, X. & Zhi, L. (Wiley Online Library, 2013).
- 75 Yao, F., Pham, D. T. & Lee, Y. H. Carbon-based materials for lithium-ion  
batteries, electrochemical capacitors, and their hybrid devices. *ChemSusChem*  
**8**, 2284-2311 (2015).
- 76 Liu, R. *et al.* Carbon coating on metal oxide materials for electrochemical  
energy storage. *Nanotechnology* **32** (2021). <https://doi.org/10.1088/1361-6528/ac21eb>
- 77 Xia, L., Tang, B., Wei, J. & Zhou, Z. Recent Advances in Alkali Metal-Ion  
Hybrid Supercapacitors. *Batteries & Supercaps* **4**, 1108-1121 (2021).  
<https://doi.org/10.1002/batt.202000332>
- 78 Yan, Y., Wang, T., Li, X., Pang, H. & Xue, H. Noble metal-based materials in  
high-performance supercapacitors. *Inorganic Chemistry Frontiers* **4**, 33-51  
(2017). <https://doi.org/10.1039/c6qi00199h>
- 79 Majumdar, D., Maiyalagan, T. & Jiang, Z. A Review on Recent Progress in  
Ruthenium Oxide-based Composites for Supercapacitor Applications.  
*ChemElectroChem* **6** (2019). <https://doi.org/10.1002/celec.201900668>
- 80 Le, T.-H., Kim, Y. & Yoon, H. Electrical and electrochemical properties of  
conducting polymers. *Polymers* **9**, 150 (2017).
- 81 Li, Z. & Gong, L. Research Progress on Applications of Polyaniline (PANI)  
for Electrochemical Energy Storage and Conversion. *Materials* **13** (2020).  
<https://doi.org/10.3390/ma13030548>
- 82 Snook, G. A., Kao, P. & Best, A. S. Conducting-polymer-based supercapacitor

- 
- devices and electrodes. *Journal of power sources* **196**, 1-12 (2011).
- 83 Yang, C. *et al.* Polymer nanocomposites for energy storage, energy saving, and anticorrosion. *Journal of Materials Chemistry A* **3**, 14929-14941 (2015).
- 84 Yin, Z. & Zheng, Q. Controlled synthesis and energy applications of one-dimensional conducting polymer nanostructures: an overview. *Advanced Energy Materials* **2**, 179-218 (2012).
- 85 Mo, D., Zhou, W., Ma, X. & Xu, J. Facile electrochemical polymerization of 2-(thiophen-2-yl) furan and the enhanced capacitance properties of its polymer in acetonitrile electrolyte containing boron trifluoride diethyl etherate. *Electrochimica Acta* **155**, 29-37 (2015).
- 86 Ravichandran, R., Sundarrajan, S., Venugopal, J., Mukherjee, S. & Ramakrishna, S. Applications of conducting polymers and their issues in biomedical engineering. *Journal of the Royal Society, Interface / the Royal Society* **7 Suppl 5**, S559-579 (2010).  
<https://doi.org:10.1098/rsif.2010.0120.focus>
- 87 Meng, F. *et al.* Electrolyte Technologies for High Performance Sodium-Ion Capacitors. *Frontiers in Chemistry* **8** (2020).  
<https://doi.org:10.3389/fchem.2020.00652>
- 88 Pan, Z. *et al.* "Porous and Yet Dense" Electrodes for High-Volumetric-Performance Electrochemical Capacitors: Principles, Advances, and Challenges. *Advanced Science* **9**, 2103953 (2022).  
<https://doi.org:10.1002/advs.202103953>
- 89 Pal, B., Yang, S., Ramesh, S., Thangadurai, V. & Jose, R. Electrolyte selection for supercapacitive devices: A critical review. *Nanoscale Advances* **1**, 3807-3835 (2019).
- 90 Zhong, C. *et al.* A review of electrolyte materials and compositions for electrochemical supercapacitors. *Chemical Society Reviews* **44**, 7484-7539 (2015).
- 91 Wiersma, B. Hydrogen generation during the corrosion of carbon steel in oxalic acid. *The US Department of Energy, USA* (2004).
- 92 Ramachandran, R. & Wang, F. Electrochemical capacitor performance: influence of aqueous electrolytes. *Supercapacitors-Theor Pract Solut InTech*, 51-68 (2018).
- 93 Ue, M., Sasaki, Y., Tanaka, Y. & Morita, M. in *Electrolytes for Lithium and Lithium-Ion Batteries* 93-165 (Springer, 2014).
- 94 Moreno Fernández, M. Á. Types of electrolytes for carbon-based supercapacitors. (2016).
- 95 Liu, S., Wei, L. & Wang, H. Review on reliability of supercapacitors in energy storage applications. *Applied Energy* **278**, 115436 (2020).
- 96 Ortiz-Martínez, V. M., Gómez-Coma, L., Pérez, G., Ortiz, A. & Ortiz, I. The roles of ionic liquids as new electrolytes in redox flow batteries. *Separation and Purification Technology* **252**, 117436 (2020).
- 97 Verma, C., Ebenso, E. E. & Quraishi, M. Ionic liquids as green and sustainable

- 
- corrosion inhibitors for metals and alloys: an overview. *Journal of Molecular Liquids* **233**, 403-414 (2017).
- 98 Dhand, C. *et al.* Methods and strategies for the synthesis of diverse nanoparticles and their applications: a comprehensive overview. *Rsc Advances* **5**, 105003-105037 (2015).
- 99 Krystian, M., Zehetbauer, M., Kropik, H., Mingler, B. & Krexner, G. Hydrogen storage properties of bulk nanostructured ZK60 Mg alloy processed by equal channel angular pressing. *Journal of Alloys and Compounds* **509**, S449-S455 (2011).
- 100 Fecht, H., Hellstern, E., Fu, Z. & Johnson, W. Nanocrystalline metals prepared by high-energy ball milling. *Metallurgical Transactions A* **21**, 2333-2337 (1990).

---

# Chapter 6 Scanning transmission X-ray microscopy studies of electrochemical activation and capacitive behavior of $\text{Mn}_3\text{O}_4$ supercapacitor electrodes

Wenjuan Yang,<sup>1&</sup> Haytham Eraky,<sup>2&</sup> Chunyang Zhang,<sup>2,3</sup> Adam P. Hitchcock<sup>2</sup> and

Igor Zhitomirsky<sup>1\*</sup>

<sup>1</sup>Dept. of Materials Science and Engineering, McMaster University, Hamilton, ON

Canada L8S4M1

<sup>2</sup>Dept of Chemistry & Chemical Biology, McMaster University, Hamilton, ON

Canada L8S4M1

<sup>3</sup>Dept. of Chemical Engineering, McMaster University, Hamilton, ON Canada

L8S4M1

\* zhitom@mcmaster.ca

& the authors contributed equally

Electrode materials fabrication and electrochemical test of SC was performed by

Wenjuan Yang, and STXM synchrotron measurements were performed at the CLS,

which is operated and analyzed by Haytham Eraky.

Copyright 2022, reproduced with permission from The Royal Society of Chemistry.

---

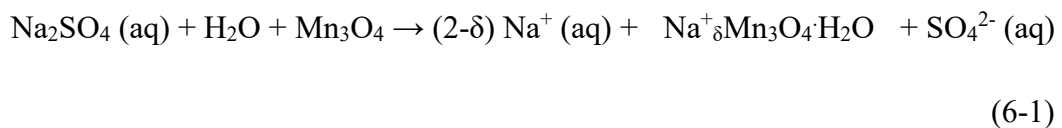
## 6.1 Abstract

This investigation, which is motivated by promising pseudocapacitive properties of  $\text{Mn}_3\text{O}_4$  for energy storage in cathodes of supercapacitors, addresses the need to understand both the activation and the charge storage mechanisms of  $\text{Mn}_3\text{O}_4$  electrodes. Specific activation protocols are shown to result in significant capacitance increase during cycling. For the first time scanning transmission X-ray microscopy (STXM) is used for analysis of  $\text{Mn}_3\text{O}_4$  activation. STXM analyses at the Mn 2p and O 1s edges provide chemical mapping of different oxidation states with high spatial resolution.  $\text{Mn}_3\text{O}_4$ -carbon nanotube composite electrodes with commercially important high active mass loading of  $40 \text{ mg cm}^{-2}$  are prepared using quercetin dispersant. The catecholate type polyaromatic quercetin facilitates co-dispersion of  $\text{Mn}_3\text{O}_4$  with carbon nanotubes and allows enhanced electrode performance at high active mass loadings. Cyclic voltammetry, electrochemical impedance spectroscopy and galvanostatic charge-discharge are used for the capacitance monitoring during electrode activation. Two strategies are used for electrode activation in  $\text{Na}_2\text{SO}_4$  electrolyte: electrochemical cycling at different scan rates and continuous cycling at a fixed scan rate. The capacitance variations are linked to STXM observations, which show gradual oxidation of  $\text{Mn}_3\text{O}_4$  to form  $\text{MnO}_2$  on the particle surface and in the bulk. The pseudocapacitive charge storage mechanism involves in-situ oxidation of  $\text{Mn}_3\text{O}_4$  and redox reactions of  $\text{Mn}^{4+}/\text{Mn}^{3+}$  species on the particle surface and in the

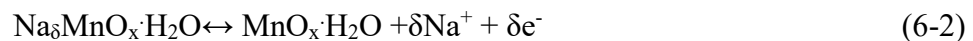
bulk.

## 6.2 Introduction

Mn<sub>3</sub>O<sub>4</sub> is a promising charge storage material for applications in cathodes of asymmetric supercapacitor devices operating in a neutral Na<sub>2</sub>SO<sub>4</sub> electrolyte<sup>1,2</sup>. Such devices offer advantages of enlarged voltage windows and enhanced power-energy characteristics. Investigations are focused on the development of advanced techniques for the deposition of nanostructured Mn<sub>3</sub>O<sub>4</sub> films<sup>1</sup> and synthesis of Mn<sub>3</sub>O<sub>4</sub> nanoparticles<sup>1,3,4</sup> for the fabrication of bulk electrodes with high active mass. Understanding the capacitive behavior and charging mechanism is crucial for the development of efficient electrodes and devices for practical applications<sup>5-7</sup>. Particular attention is focused on the charge storage behavior of nanostructured Mn<sub>3</sub>O<sub>4</sub> and composites<sup>8</sup>. Mn<sub>3</sub>O<sub>4</sub> is usually combined with conductive additives for the fabrication of composites with enhanced conductivity and capacitance<sup>9-11</sup>. The charge storage mechanism of Mn<sub>3</sub>O<sub>4</sub> electrodes in Na<sub>2</sub>SO<sub>4</sub> electrolyte was analyzed in several investigations<sup>2,12</sup>. The first step involves solvation<sup>12</sup>:



The subsequent charge-discharge steps are based on the reaction<sup>12</sup>:



---

Previously, Mn K-edge X-ray absorption spectroscopy (XAS)<sup>12</sup> showed that  $\text{Na}_8\text{MnO}_x$  is formed in the first charge-discharge cycle of  $\text{Mn}_3\text{O}_4$  cathodes, which resulted in the reduction of the average oxidation state of Mn. Another investigation, using *in situ* XAS at the Mn K-edge, showed reduction of  $\text{Mn}^{3+}$  to  $\text{Mn}^{2+}$  at low potentials and oxidation of  $\text{Mn}^{3+}$  to  $\text{Mn}^{4+}$  or  $\text{Mn}^{6+}$  at higher potentials<sup>13</sup>. Significant changes in lattice constants (a and c) of the tetragonal  $\text{Mn}_3\text{O}_4$  unit cell were observed during cycling in the positive potential range in the  $\text{Na}_2\text{SO}_4$  electrolyte<sup>13</sup>.

Despite the recent progress in the investigation of the deposition mechanism, the charge-discharge behavior of  $\text{Mn}_3\text{O}_4$  electrodes is not well understood. The understanding of the charging mechanism is complicated due to the electrode activation phenomena. Several investigations analyzed activation of  $\text{Mn}_3\text{O}_4$  electrodes, which resulted in capacitance increase during initial cycling<sup>2,14,15</sup>. A significant increase in capacitance was observed for electrodes with high active mass loading<sup>16-20</sup>. The activation process was linked to *in-situ* modification of the electrode microstructure<sup>17,19,21,22</sup>. Previous investigations showed that capacitance variations during activation process can be diminished using mixed rhamnolipids as a capping agent for the synthesis of  $\text{Mn}_3\text{O}_4$  particles and modification of particle morphology<sup>20</sup>. However, the origin of the capacitance variation during the activation process and charging mechanism are not well understood. Further analysis of activation behavior is critically important for better understanding of charging mechanism and applications of  $\text{Mn}_3\text{O}_4$  electrodes in asymmetric supercapacitors.

---

Chemical contrast is provided by near-edge X-ray absorption fine structure (NEXAFS) spectral signal<sup>23</sup>. STXM analytical studies provide spectroscopic identification and quantitative mapping of chemical components with 30-nm spatial resolution in both 2D and 3D projections<sup>24-27</sup>. Most of the electrochemical applications, particularly energy conversion and storage-related applications are associated with chemical reactions between the electrolyte and electrode interface<sup>27,28</sup>. STXM determination of the products of electrochemical reactions, along with quantitative spatial mapping, can provide a mechanistic understanding of electrochemical processes such as supercapacitor charging and discharging. The objective of this investigation is the application of STXM for the analysis of activation behavior and charging mechanism of Mn<sub>3</sub>O<sub>4</sub> based electrodes which contain multiwalled carbon nanotubes (MWCNT) as conductive additives. Investigations were performed using electrodes with high active mass loadings of 40 mg cm<sup>-2</sup>, which is necessary for practical applications. High capacitance was achieved by the use of quercetin as a new catecholate-type dispersant, which facilitated co-dispersion of Mn<sub>3</sub>O<sub>4</sub> and MWCNT. Testing results presented below revealed significant increase in capacitance during cycling. We describe the results of Mn 2p and O 1s STXM measurements of Mn<sub>3</sub>O<sub>4</sub> – MWCNT samples subjected to different activation procedures. Our findings demonstrate that, as the number of charge-discharge cycles is increased, Mn<sub>3</sub>O<sub>4</sub> is partially converted to MnO<sub>2</sub>. This was correlated to the steady increase in the obtained capacitance. Testing results provide

---

insight into the mechanism of activation and charge-discharge of  $\text{Mn}_3\text{O}_4$  electrodes. In this case, the capacitance increase was linked to *in-situ* oxidation of  $\text{Mn}_3\text{O}_4$  during cycling.

## 6.3 Experimental procedures

### 6.3.1 Materials, synthesis of $\text{Mn}_3\text{O}_4$ particles and electrode fabrication

Quercetin (QC),  $\text{Mn}(\text{NO}_3)_2 \cdot 4\text{H}_2\text{O}$ , isopropanol, NaOH,  $\text{Na}_2\text{SO}_4$ , poly(vinyl butyral) binder (PVB, MilliporeSigma, Canada), multiwalled carbon nanotubes (MWCNT, ID 4 nm, OD 13 nm, length 1–2  $\mu\text{m}$ , Bayer, Germany) and industrial Ni foam current collectors (95% porosity, 1.6 mm thickness, Vale, Canada) were used. A chemical precipitation method<sup>16,20</sup> was used for the synthesis of  $\text{Mn}_3\text{O}_4$  nanoparticles from 0.07 M  $\text{Mn}(\text{NO}_3)_2$  solution in DI water. The pH of the solution was adjusted to pH=10 by aqueous 0.01M NaOH for the synthesis of  $\text{Mn}_3\text{O}_4$  nanoparticles. The obtained precipitate was washed with water and ethanol. Quercetin was used as a co-dispersant for the fabrication of stable suspensions of  $\text{Mn}_3\text{O}_4$  and MWCNT in isopropanol (see Supplemental Information, Figure S1). The mass ratio of  $\text{Mn}_3\text{O}_4$ :MWCNT:PVB binder in the suspensions was 80:20:3. The Ni foam current collectors were impregnated with the suspensions. The mass of the impregnated material after drying was 40 mg  $\text{cm}^{-2}$ . The impregnated foams were pressed to 30%

of original thickness in order to improve electrical contact of the active material and current collector. Manganese dioxide ( $\text{MnO}_2$ ), and trimanganese tetraoxide ( $\text{Mn}_3\text{O}_4$ ) were purchased from Sigma-Aldrich and used as reference materials for STXM analysis. All reagents were used without further purification.

### 6.3.2 Microstructure and electrochemical characterization

Scanning electron microscopy (SEM) investigations were performed using a JEOL microscope, (JSM-7000F, Japan). X-ray diffraction (XRD) analysis was performed using a diffractometer (Bruker D8, Cu-K $\alpha$  radiation, UK) at the scan rate of 1 deg per min. Electrochemical testing of capacitive behavior of the electrodes by cyclic voltammetry (CV) and electrochemical impedance spectroscopy (EIS) was performed using a PARSTAT 2273 (Ametek) potentiostat. Galvanostatic charge-discharge (GCD) studies were performed using a BioLogic VMP 300 potentiostat. Testing was carried out using aqueous 0.5 M  $\text{Na}_2\text{SO}_4$  electrolyte in a 3-electrode electrochemical cell containing impregnated Ni foam as a working electrode, Pt mesh as a counter-electrode, and a saturated calomel electrode (SCE) as a reference.

Electrode capacitance was obtained from the CV, EIS and GCD data by methodology described in the literature<sup>29,30</sup> and presented as a areal ( $C_s, \text{F cm}^{-2}$ ) and gravimetric ( $C_m, \text{F g}^{-1}$ ) capacitance. Integral capacitances were derived from the CV and GCD data in a potential window of 0-0.9 V. CV was performed at scan rates of 2-100  $\text{mV s}^{-1}$ .

GCD testing was performed at current densities of 3-10  $\text{mA cm}^{-2}$ . Differential

capacitances were derived from the EIS data obtained at a voltage amplitude of 5 mV in the frequency range of 10 mHz-100 Hz at an open circuit potential. Analysis of the impedance data was performed using the commercial ZSimpWin software (Ametek) and an equivalent circuit developed for supercapacitor electrodes with high active mass loadings<sup>31</sup>.

$C_s$  and  $C_m$  were derived from the CV data using the following equation:

$$C = \frac{\Delta Q}{\Delta U} = \frac{|\int_0^{t(U_{max})} I dt| + |\int_{t(U_{max})}^0 I dt|}{2U_{max}} \quad (6-3)$$

where  $\Delta Q$  is charge,  $I$ -current and  $\Delta U$ - the potential range. Capacitance was calculated from the chronopotentiometry data using the equation:

$$C = I\Delta t / \Delta U \quad (6-4)$$

The complex capacitance  $C^*(\omega) = C'(\omega) - iC''(\omega)$  was derived at different frequencies ( $\omega$ ) from the complex impedance  $Z^*(\omega) = Z'(\omega) + i Z''(\omega)$ :

$$C'(\omega) = \frac{-Z''(\omega)}{\omega|Z(\omega)|^2} \quad (6-5)$$

$$C''(\omega) = \frac{Z'(\omega)}{\omega|Z(\omega)|^2} \quad (6-6)$$

The electrode activation was performed using CV at various scan rates (VSR) or at fixed scan rates (FSR). A VSR procedure (VSRP) involved CV at scan rates of 2, 5, 10, 20, 50 and 100 mV s<sup>-1</sup>. EIS studies were performed after each VSRP. GCD testing was performed after five VSRPs. FSR testing involved 1000 CV cycles at a scan rate of 50 mV s<sup>-1</sup>.

---

### 6.3.3 Methods: Scanning Transmission X-ray Microscopy

Imaging, spectroscopy and spectromicroscopy measurements were performed using the ambient STXM at the spectromicroscopy (SM) beamline 10ID1 at the Canadian Light Source (CLS, Saskatoon, Canada)<sup>32</sup>, a brief description of which is presented in Supplemental Information, section S2. The as-prepared active electrode materials (AEM) and AEM after VSRPs 1-5, or after 100 and 1000 FSR cycles were scratched to separate them from the Ni foam substrate. The AEM particles were drop-cast on a formvar coated TEM grids (TED Pella Inc.). The grids were taped to standard trapezoidal STXM sample plates<sup>33</sup>. Spectra, images and image sequences were measured at the Mn 2p and O 1s edges. STXM measurements were performed with the chamber evacuated to  $<10^{-2}$  mbar and then backfilled with Helium (He) to a pressure of  $\sim 100$  mbar. During the measurements, the X-ray beam is monochromated to a specific photon energy, then focused by a Fresnel zone plate (ZP) to a 20-50 nm spot, where the sample is placed (Figure S2). Images were measured by (x,y) raster scanning the sample while recording the intensity of the transmitted X-rays detected by a phosphor/photomultiplier tube (PMT) detector located behind the sample<sup>34,35</sup>. Spectromicroscopic data in the form of multi-energy image sequences (stacks<sup>36</sup>) were obtained at X-ray energies from  $\sim 10$  eV below to  $\sim 40$  eV above the onset of O 1s and Mn 2p absorption. STXM data was analyzed using aXis2000 software<sup>37</sup>. The transmitted X-ray flux through the sample ( $I$ ) was converted to optical density ( $OD$ ) using the Beer Lambert Law:  $OD = \ln(I_0/I) =$

---

$\mu(E) \cdot \rho \cdot t$ , where  $I_0$  is the incident X-ray flux, measured through an area devoid of the sample but with all other components (windows, zone plate, OSA, formvar);  $\mu(E)$  is the energy dependent mass absorption coefficient;  $E$  is X-ray energy;  $\rho$  is sample density and  $t$  is the sample thickness<sup>24</sup>.

After Fourier cross-correlation alignment, the stacks were converted to OD using  $I_0$  to the spectrum from areas of the stack devoid of sample. The OD stacks were then fit to suitable reference spectra, in this case,  $Mn_3O_4$  and  $MnO_2$ , which were measured using both STXM and the CLS spherical grating monochromator (SGM) spectroscopy beamline, 11ID1. The results of the reference spectral study are described in supplemental information (Figure S2, S3, Table S1). The Mn 2p spectrum of the commercial  $Mn_3O_4$  sample, measured by both STXM and SGM, was significantly different from the literature<sup>38-40</sup>. The spectrum of the as-prepared electrode layer was in good agreement with the Mn 2p and O 1s spectra of  $Mn_3O_4$  reported in the literature<sup>38,39</sup>. Thus, we used the Mn 2p and O 1s spectra of the as-prepared material as the reference for  $Mn_3O_4$ . The measured O 1s and Mn 2p spectra of  $Mn_3O_4$  and  $MnO_2$  were energy calibrated (see Supplemental Information, section S3) and placed on quantitative intensity scales, corresponding to the OD for 1 nm thickness of each material at its standard density using a method outlined in detail elsewhere<sup>23</sup>. These spectra were used in a singular value decomposition (SVD) analysis of the Mn 2p and O 1s stacks from each sample (SVD is a single pass matrix manipulation approximating linear least squares fitting<sup>41</sup>). Since quantitative

reference spectra are used, the intensity scales of the resulting component maps give the component thickness in nm<sup>24</sup>.

## 6.4 Results and discussion

### 6.4.1 Electrochemical and microstructure characterization

Figure 6-1 shows X-ray diffraction pattern of obtained Mn<sub>3</sub>O<sub>4</sub> particles. The observed diffraction peaks correspond to data in the JCPDS file 001-1127. It is suggested that the addition of alkali to the Mn(NO<sub>3</sub>)<sub>2</sub> solutions resulted in the formation of unstable<sup>42,43</sup> Mn(OH)<sub>2</sub>, which was oxidized in air to form Mn<sub>3</sub>O<sub>4</sub>.

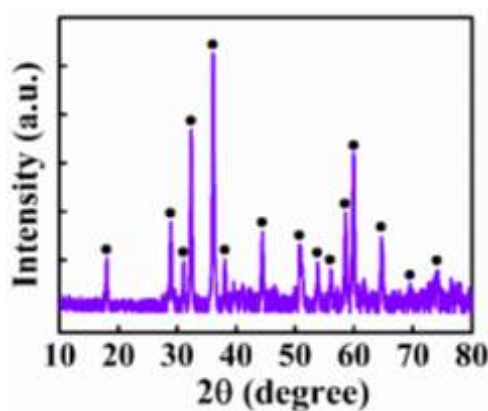


Figure 6- 1 X-ray diffraction pattern of as-prepared Mn<sub>3</sub>O<sub>4</sub> (●-peaks corresponding to JCPDS file 001-1127).

The fabrication of Mn<sub>3</sub>O<sub>4</sub> electrodes with high active mass requires the use of conductive additives because Mn<sub>3</sub>O<sub>4</sub> exhibits low electronic conductivity. Therefore, MWCNT were used as conductive additives. As-received MWCNT formed large agglomerates with a typical diameter of 0.5 mm. The SEM images of such

---

agglomerates were presented in a previous investigation<sup>44</sup>. Nanoparticles of  $\text{Mn}_3\text{O}_4$  are also prone to agglomeration. Therefore, QC was used as a co-dispersant for  $\text{Mn}_3\text{O}_4$  and MWCNT. QC was chosen due to its polyaromatic catecholate structure and redox properties. Figure 6-2A shows the chemical structure of QC, which includes hydroxylated benzene rings. QC is a polyaromatic molecule, containing a catechol group. It has been widely reported that catechol and related molecules exhibit strong adsorption on surfaces of inorganic particles<sup>45-47</sup>. The interest in catechol anchoring groups resulted from the investigation of mussel adsorption on different surfaces, which involved dopamine-type catecholate monomers of proteins<sup>47-51</sup>. Figure 6-2B shows adsorption of QC on the  $\text{Mn}_3\text{O}_4$  surface, involving catecholate-type chelating bonding<sup>45</sup>. The polyaromatic structure of QC is beneficial<sup>52</sup> for its adsorption on MWCNT. This mechanism is based on  $\pi$ - $\pi$  interactions<sup>52</sup>. Owing to its polyphenolic nature, QC exhibits redox-active properties<sup>53-55</sup>. It has previously been shown that catecholate-type redox-active molecules can act as charge transfer mediators, which facilitate charge-discharge reactions of supercapacitor materials<sup>56</sup>. Moreover, adsorbed catecholate molecules facilitate charge transfer in other processes, such as electropolymerization and photovoltaic current generation<sup>45</sup>.

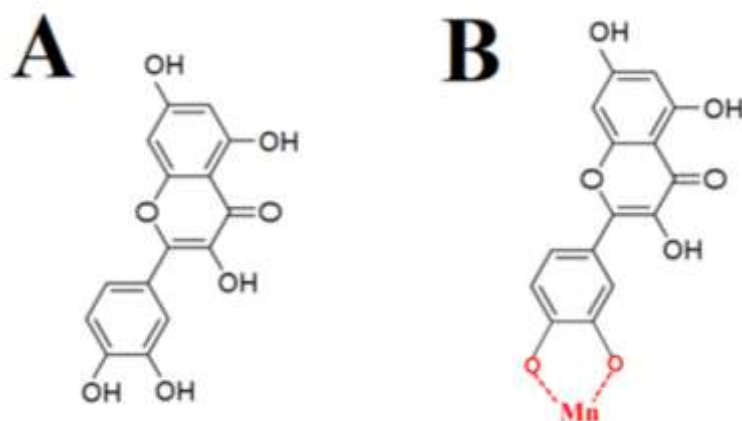


Figure 6- 2 (A) Chemical structure of QC, (B) adsorption QC on  $Mn_3O_4$  by chelation of surface Mn atoms.

Sedimentation tests showed enhanced suspension stability of  $Mn_3O_4$  and MWCNT in the presence of QC as a dispersant (see Figure S1). Therefore, QC can be used as a co-dispersant for  $Mn_3O_4$  and MWCNT. Figure 6-3 shows microstructures of the electrodes prepared with and without QC. The electrodes prepared without QC showed poor mixing of  $Mn_3O_4$  and MWCNT. The SEM image (Figure 6-3A) shows large areas containing only MWCNT or  $Mn_3O_4$ . In contrast, the electrodes prepared using QC as a co-dispersant (Figure 6-3B) showed reduced agglomeration and improved mixing of  $Mn_3O_4$  and MWCNT. The improved mixing is beneficial for the fabrication of electrodes with enhanced capacitance. The electrodes prepared using QC were used for electrochemical characterization. Figure 6-4A shows CVs at different scan rates for VSRP 1 and indicate capacitive behavior in a potential window of 0-0.9V. Figure 6-4B compares CVs at a scan rate of  $10 \text{ mV s}^{-1}$  for VSRPs 1-5. It is seen that CV area increased from VSRP1 to VSRP5, indicating capacitance increase

due to in-situ activation of the electrodes. Moreover, the CV for VSRP 5 is nearly of rectangular shape, which indicates good pseudocapacitive response.

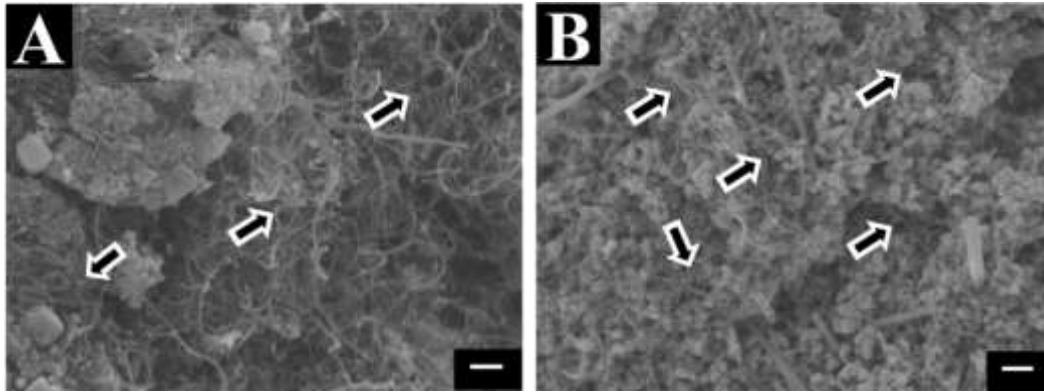


Figure 6- 3SEM images for as-prepared  $\text{Mn}_3\text{O}_4$ -MWCNT electrodes (A) without QC and (B) with QC. The scale bars in the figures represent 250 nm, and arrows show MWCNT.

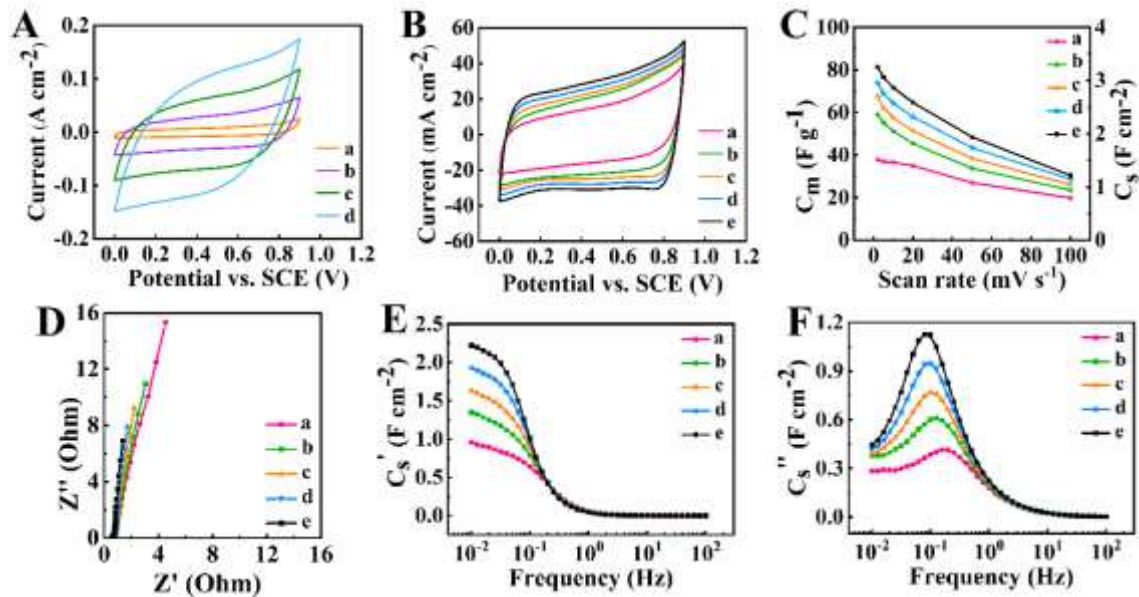


Figure 6- 4 (A) CVs for  $\text{Mn}_3\text{O}_4$ -MWCNT electrode at scan rates of (a) 5, (b) 20, (c) 50 and 100  $\text{mV s}^{-1}$  for VSRP 1, (B) CVs at 10  $\text{mV s}^{-1}$  for (a-e) VSRPs 1-5, (C) Capacitance derived from CV data for (a-c) VSRPs 1-5, (D) Nyquist plot of complex impedance for (a-c) VSRPs 1-5, (E) real and (F) imaginary components of complex capacitances derived from the complex impedance data versus frequency for (a-e) VSRPs 1-5.

Figure 6-4 (C, D) shows capacitances and impedances for VSRPs 1-5. First cycle at  $2 \text{ mV s}^{-1}$  for VSR1 showed a capacitance of  $1.5 \text{ F cm}^{-2}$ . The capacitance decreased with increasing scan rate. The activation procedure resulted in capacitance increase from VSRP1 to VSRP5 (Figure 6-4C). The capacitance at  $2 \text{ mV s}^{-1}$  for VSRP5 was found to be  $3.3 \text{ F cm}^{-2}$ . The decrease of real part of complex impedance with increasing TP number indicated beneficial decrease of resistance during the activation process (Figure 6-4D). The decrease of the imaginary part indicated the increase of capacitance. The analysis of the impedance data using an equivalent circuit for high active mass electrodes<sup>31</sup> (see Supplemental Information, Section S4, Figure S4) for VSRPs 1-5 showed that changes in the real and imaginary parts of complex impedance resulted from the increase in capacitance and reduction of the charge transfer resistance. The components of complex capacitance were calculated from the impedance data and presented in Figure 6-4 E, F.

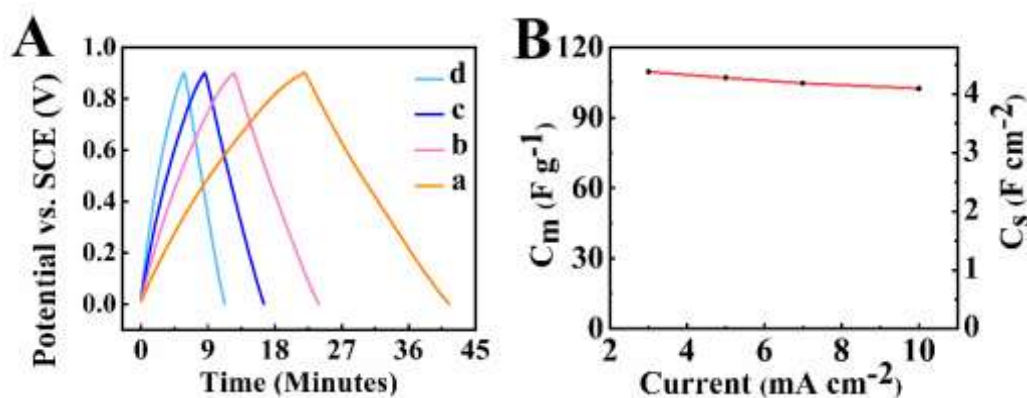


Figure 6- 5 GCD data for current densities of (a) 3, (b) 5, (c) 7 and (d)  $10 \text{ mA cm}^{-2}$  and (B) capacitance versus current density obtained from the GCD data.

---

The AC capacitance derived from the impedance data increased with increasing VSRP number. The GCD data acquired after VSRP5 showed (Figure 6-5) nearly ideal triangular charge-discharge curves. The capacitance decreased from 4.4 to 4.1 F cm<sup>-2</sup> with increasing current density from 3 to 10 mA cm<sup>-2</sup>. The obtained capacitances after VSRP5 were comparable with those reported in previous investigations<sup>17,19,22</sup>. Higher capacitances can be achieved using special techniques, such as electrostatic heterocoagulation<sup>21</sup>, liquid-liquid extraction<sup>16</sup> and synthesis in the presence of a capping agent<sup>20</sup>. However, to avoid the influence of different factors on Mn<sub>3</sub>O<sub>4</sub> particles and with the goal of the developing STXM methodology, a traditional approach was used for the synthesis of Mn<sub>3</sub>O<sub>4</sub> and electrode fabrication. This was important for monitoring the chemical modifications of Mn<sub>3</sub>O<sub>4</sub> during activation and obtaining better understanding of the charging mechanism.

Another activation strategy was based on the continuous cycling at a fast scan rate of 50 mV s<sup>-1</sup>. Figure 6-6 shows a continuous increase in normalized capacitance with increasing cycle number during 1000 FSR cycles. The capacitance for cycle 1 was only 32.7% of the capacitance for FSR cycle 1000. The capacitance for FSR cycle 100 was 55.7%. Significant increase in capacitance was observed during the first 500 FSR cycles.

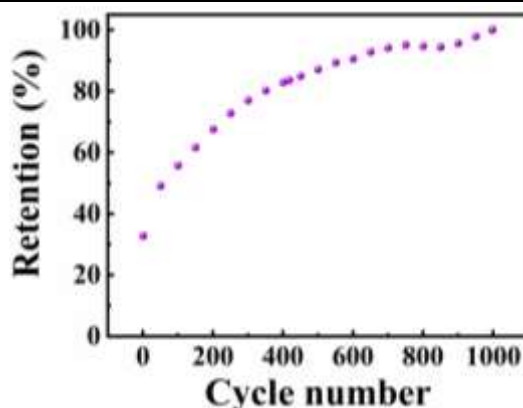


Figure 6- 6 Capacitance normalized by capacitance value for FSR cycle 1000 versus cycle number for continuous CV cycling at a scan rate of  $50 \text{ mV s}^{-1}$ .

## 6.4.2 X-ray spectromicroscopy

### 6.4.2.1 $\text{Mn}_3\text{O}_4$ and $\text{MnO}_2$ reference spectroscopy

Figures 6-7A and 6-7B present Mn 2p and O 1s spectra of the as-prepared  $\text{Mn}_3\text{O}_4$  and  $\text{MnO}_2$  reference spectra on OD1 intensity scales. The positions and relative intensities of the features in the measured Mn  $L_{2,3}$  STXM reference spectra are in agreement in shape with the literature absorption spectra of  $\text{Mn}_3\text{O}_4$  (hausmannite)<sup>38</sup>,  $\text{MnO}_2$  (pyrolusite)<sup>38</sup> and  $-\text{MnO}_2$ <sup>39</sup>. However, there are discrepancies in the energy scales, with deviations from literature reports greater than 1 eV in some cases. These issues are documented and discussed in Supplemental Information, section S5. The first sharp peaks in the  $L_3$  spectra of  $\text{MnO}_2$  and  $\text{Mn}_3\text{O}_4$  occur at 641.3 eV and 640.1 eV respectively, and thus can be used to track sample oxidation. The O 1s  $\rightarrow$  Mn3d electronic transitions in the O 1s spectra of  $\text{MnO}_2$  and the as-prepared catalyst (Figure 6-7B) occur at 529.7 eV and 530.6 eV respectively, again providing a useful tool to

track oxidation. The shapes and energy positions of main features in the measured O 1s spectra are similar to those in the O 1s absorption spectra of  $\text{MnO}_2$  and  $\text{Mn}_3\text{O}_4$  reported previously<sup>38</sup>.

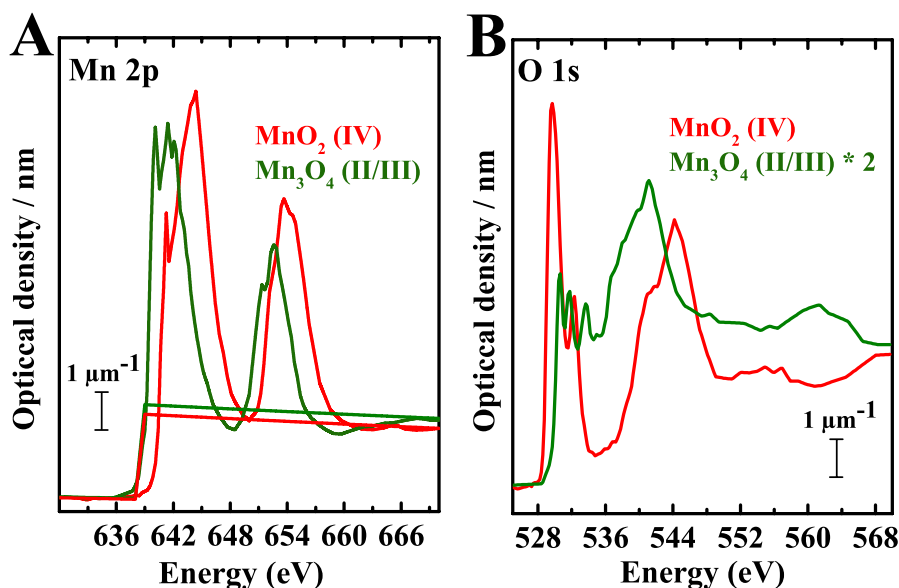


Figure 6- 7 (A) Quantitative Mn 2p spectra of Mn(II/III) (dark green) and Mn(IV) (red) on OD1 intensity scales. (B) Quantitative O 1s spectra of Mn(II/III) (dark green) and Mn(IV) (red) on OD1 intensity scales.

#### 6.4.2.2 Mn 2p and O 1s results for the $\text{MnO}_x$ samples

Figures 6-8A and 6-8B present Mn  $L_{2,3}$  and O 1s spectra of as-prepared  $\text{Mn}_3\text{O}_4$  and  $\text{MnO}_2$  in comparison with spectra extracted from STXM stack measurements of the VSRP1, VSRP3 and VSRP5 processed samples. Mn  $L_{2,3}$  and O 1s results for samples after FSR100 and FSR1000 cycles are presented in Figures 6-8C and 6-8D. The Mn  $L_{2,3}$  spectra were calibrated as discussed in Supplemental Information (Figure 6-S3, Table 6-S1).

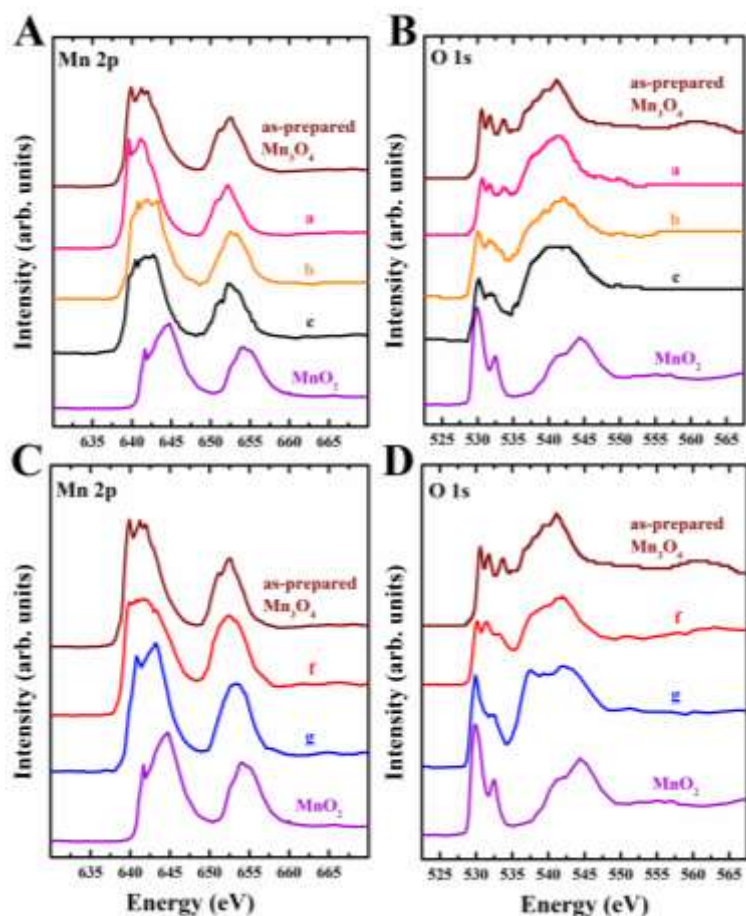


Figure 6- 8 (A) Mn 2p, (B) O 1s absorption spectra extracted from stacks measured for (a) VSRP1, (b) VSRP3 and (c) VSRP5, (C) Mn 2p, (D) O 1s absorption spectra extracted from stacks measured for (f) FSR cycle 100 and (g) FSR cycle 1000 samples.

The Mn  $L_{2,3}$  spectra (Figure 6-8A) show that the Mn oxide in the as-prepared material is predominantly  $Mn_3O_4$  showing three sharp Mn  $L_3$  peaks at 639.91 eV, 641.23 eV and 641.89 eV which is consistent with the XAS spectrum of an ensemble of the as-prepared material measured in TEY mode (SI section S6, Figure 6-S7), and also with previous reports (Figure 6-S6B)<sup>38,39</sup>. At the early stages of the charge/discharge testing procedures (VSR1-VSR5), the Mn 2p spectra showed a noticeable change in the Mn  $L_{2,3}$  peak positions, indicating partial conversion of Mn(II/III) to Mn(IV). On

---

the contrary, the extracted spectra of the electrode material after FSR1000 cycles exhibited the Mn L<sub>2,3</sub> features characteristic of MnO<sub>2</sub>, with sharp Mn 2p → 3d peaks at 641.1 (L<sub>3</sub>) and 653.7 eV (L<sub>2</sub>) and broad peak at (643.5 eV), respectively, indicating a remarkable change in both shape and peak positions compared to the spectra of as-prepared Mn<sub>3</sub>O<sub>4</sub> which has a sharp L<sub>3</sub> peak at 640.1 and two broad peaks at (641.4 eV and 642.1 eV), respectively. In addition, the O 1s spectra after VSRP1, VSRP3 and VSRP5 (Figure 6-8B) were consistent with the Mn 2p measurements, indicating a significant change in the O 1s → 3d features in the 528-534 eV region consistent with partial conversion of the original Mn (II/III) (Mn<sub>3</sub>O<sub>4</sub>) material to Mn (IV) (MnO<sub>2</sub>). The O 1s → Mn3d transition in the as-prepared material occurs at 530.6 eV, while after 1000 FSR cycles the O 1s → Mn3d transition occurs at 529.9 eV (Figure 6-8D). Figure 9 is an expansion of the low energy O 1s → Mn 3d region of the O 1s spectra and the Mn 2p<sub>3/2</sub> region, showing more clearly the systematic shift in the spectral peak positions with VSRPs 1,3,5 and FSR100, 1000 cycle samples.

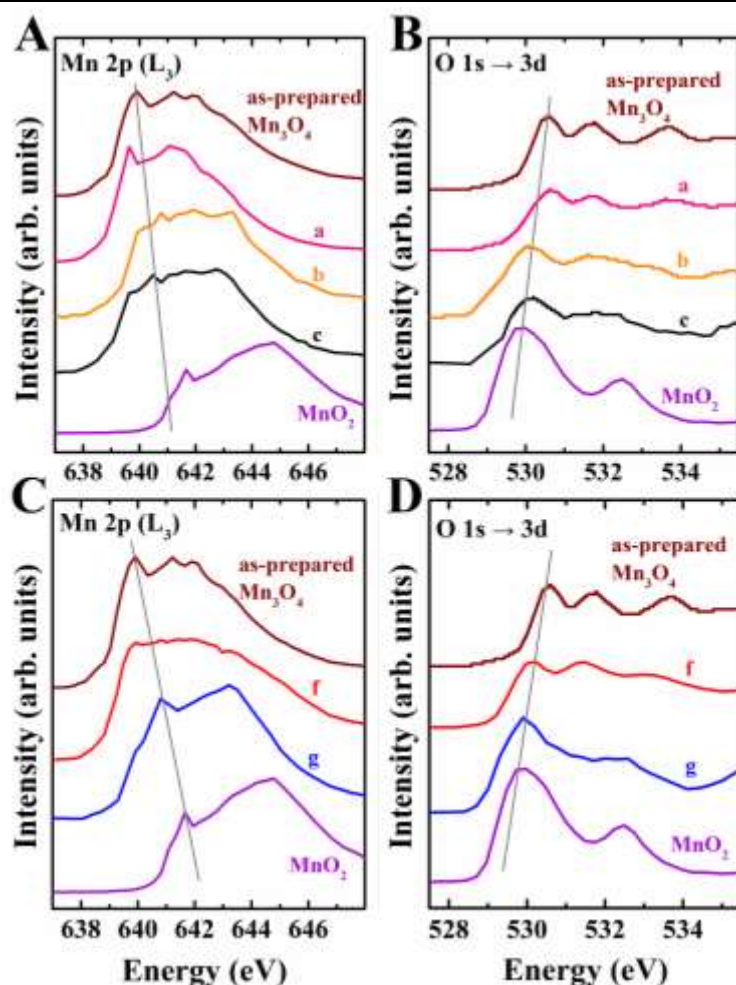


Figure 6- 9 Mn  $L_3$  and O  $1s \rightarrow 3d$  features showing conversion of Mn (II/III) to Mn(IV). (A) and (B) present (a) VSRP1, (b) VSRP2 and (c) VSRP3, (C) and (D) present (f) FSR100 and (g) FSR1000 cycle samples in comparison with as-prepared  $Mn_3O_4$  catalyst and  $MnO_2$  reference spectra.

The SGM-TEY measurements of Mn 2p spectra presented in Figure S7 showed a remarkable change in the Mn  $L_{2,3}$  peak positions of VSRs1,3,5 and FSR1000 cycles samples compared to the as-prepared  $Mn_3O_4$ , which are consistent with the STXM measurements of the same samples. However, the measured spectra of the VSR and FSR samples are similar, indicating that each consists of a mixture of  $Mn_3O_4$  and

MnO<sub>2</sub> species. On the other hand, the O 1s spectra of VSR1, VSR3, VSR5 and FSR1000 cycle samples showed the same O 1s → 3d features at 528-534 eV and are similar to the O 1s spectra of MnO<sub>2</sub>, while the 536 - 548 eV region is different with no obvious trend. In contrast, the O 1s spectrum to the as-prepared Mn<sub>3</sub>O<sub>4</sub> is very different from the measured spectra of the VSR and FSR samples (3 peaks instead of 2 in the 529-534 eV region).

### **6.4.2.3 Mapping of Mn species from the Mn 2p spectromicroscopy of the MnO<sub>x</sub> samples**

The quantitative chemical mapping of the Mn (II/III) and Mn (IV) species on the VSRs1,3,5 and FSR100 and 1000 cycle samples that derived from fitting of Mn 2p stacks in a photon energy range of 630 – 670 eV to absolute intensity scale of MnO<sub>2</sub> and Mn<sub>3</sub>O<sub>4</sub> reference spectrum showed a steady conversion of Mn(II/III) to Mn(IV) by increasing number of cycles.

Figure 6-10A presents quantitative chemical mapping of the Mn (II/III) and Mn (IV) species in each of VSRs 1, 3 and 5, while data for FSR100 and FSR1000 cycle samples presented in Figure 6-10B. Each image is a color-coded composite of quantitative component maps derived by fitting the measured stacks with quantitative OD1 reference spectra of MnO<sub>2</sub> and Mn<sub>3</sub>O<sub>4</sub> which are presented in Figure 6-7A.

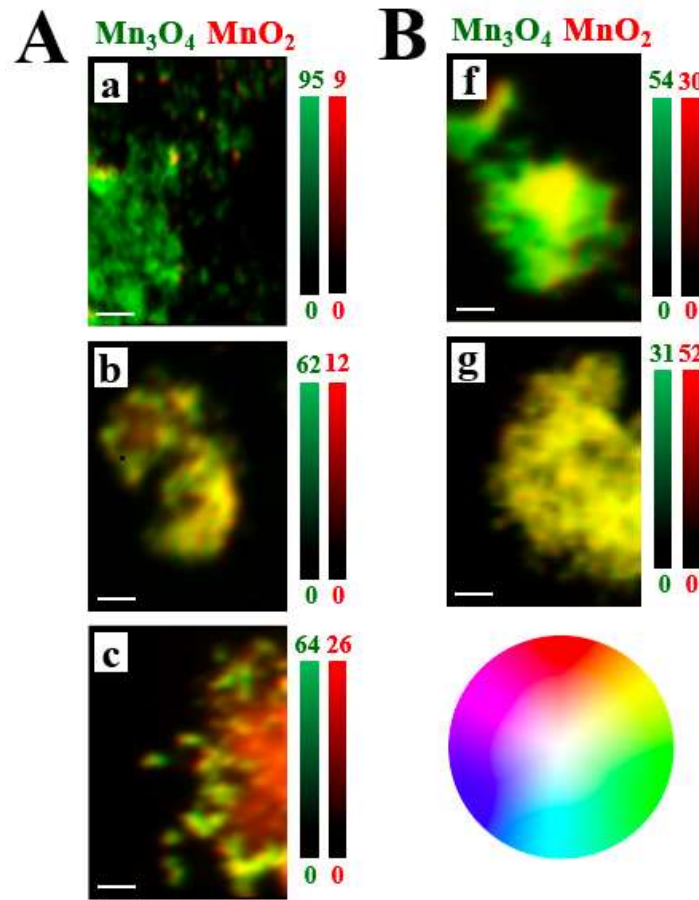


Figure 6- 10 Color coded composites of Mn(II/III) and Mn(IV) component maps derived by SVD fitting Mn 2p stacks measured on (A) VSRPs1, 3, 5 (a-c respectively), (B) FSR100 and FSR1000 cycle samples (f, g respectively), scale bar: 0.5  $\mu\text{m}$ . Color scales are nm thickness. Color wheel indicates color expected for specific combinations of the red and green signals.

Figure 6-11A and 6-11B plot the average volume of Mn (II/III) and Mn(IV) present for VSRPs1,3,5 samples and FSR100 and FSR1000 cycle samples. The chemical mapping and spatial distribution of Mn<sub>3</sub>O<sub>4</sub> and MnO<sub>2</sub> illustrates small volume fraction of MnO<sub>2</sub> after VSRP1. Conversely, a considerable increase in MnO<sub>2</sub> contribution was observed after VSRPs 3 and 5. After FSR1000 cycles a 0.6 volume fraction of MnO<sub>2</sub> was obtained.

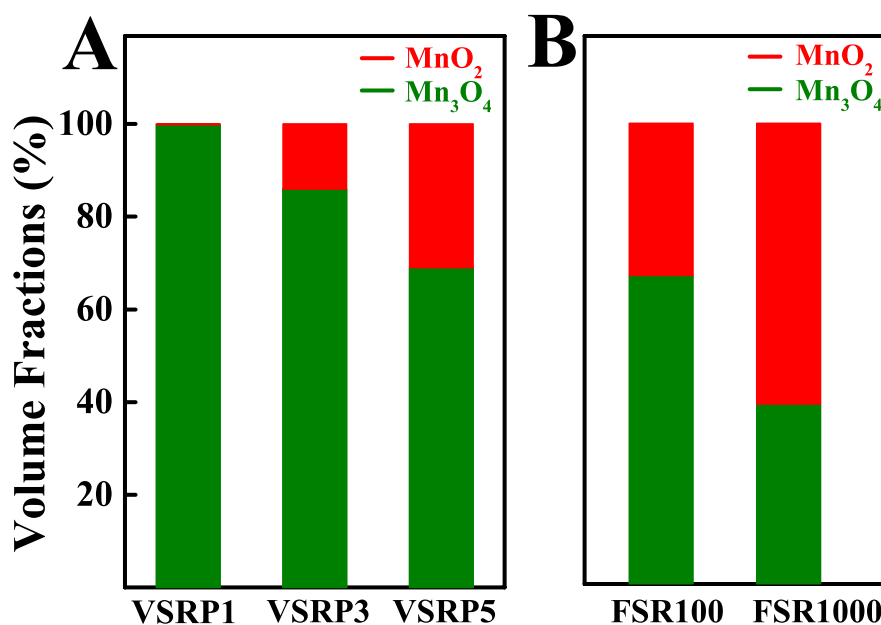


Figure 6- 11 Evolution of Mn(II/III) and Mn(IV) signals of (A) VSRP1, VSRP3 and VSRP5, (B) FSR100 and FSR1000 cycle sample represented in volume fractions.

#### 6.4.2.4 STXM spectromicroscopy

When compared to published Mn K-edge XAS results<sup>12,13</sup>, Mn L-edge spectromicroscopy has the advantages of (i) higher energy resolution, thus achieving better chemical sensitivity – there are remarkable changes in both the Mn 2p and O 1s spectra when the oxidation state changes (Figure 6-7), and (ii) nanoscale chemical imaging (Figure 6-10). In particular, for the regions studied, it appears that the conversion of Mn (II/III) to Mn(IV) occurs to a greater extent in the core of the particles rather than at the edges. This is especially evident for the FSR 1000 cycles sample. The high spectral sensitivity has enabled observation of subtle changes in the Mn<sub>3</sub>O<sub>4</sub> supercapacitor electrode material during the activation process. In

---

particular, the improved capacitance can be seen to be the consequence of the increasing fraction of  $\text{MnO}_2$ . In contrast to the mechanism suggested in previous investigations<sup>12,13</sup> we did not observe capacitance decrease during initial cycling (Figure 6-6). Very small  $\text{Mn}^{4+}$  content (Figure 6-11A) in the particles after VSRP1 indicated that oxidation of  $\text{Mn}^{3+}$  ions on the particle surface contributed to pseudocapacitive behavior. Continuous cycling resulted in oxidation of  $\text{Mn}^{2+}$  species in the bulk and enhanced contributions of bulk material to the total capacitance according to the reaction (6-2). It should be noted that previous investigations did not show a correlation between capacitance and BET surface area of  $\text{MnO}_2$ <sup>57,58</sup>. It was suggested that some pores accessible by nitrogen gas are not accessible by the solvated ions in the electrolyte. The STXM studies of this work showed that the bulk of the particles contributes significantly to the total capacitance.

Since this work is one of the first applications of STXM to supercapacitor materials, it is appropriate to compare its capabilities to complementary analytical imaging methods being applied to such problems. In terms of spectroscopies, X-ray photoelectron spectroscopy (XPS) is often used to determine oxidation states of metal oxides. In the case of Mn oxides the range of oxidation state shifts from Mn(II) to Mn(IV) is less than 1 eV and the peak positions reported various authors vary by up to 1 eV (see Table 2 in ref.<sup>59</sup>). XPS is a very surface sensitive technique which is an advantage for studying surface dependent phenomena such as the mechanisms of charge transfer in supercapacitors. It is possible to perform XPS imaging, but the

---

typical spatial resolution is 1-2 orders of magnitude lower than that provided by STXM. In terms of imaging, it is clear that electron microscopies such as SEM and TEM provide 1-2 orders of magnitude higher spatial resolution than STXM. However, the analytical information provided is generally less sensitive than X-ray absorption. X-ray fluorescence (TEM-EDX) only provides elemental, not oxidation state, sensitivity. Core level electron energy loss (TEM-EELS) is the direct analog to STXM spectromicroscopy and thus has the same potential for oxidation state determination, but with the advantage of much higher spatial resolution. The most modern implementations of TEM-EELS are as good as STXM, but such measurements can be challenging due to the much greater extent of radiation damage in TEM than STXM<sup>60</sup>. In addition, since STXM is a photon-in, photon-out method, it is possible to adapt the system to *in situ* and *operando* studies of aqueous electrochemical phenomena such as charge/discharge mechanisms at supercapacitor electrodes. Such studies are currently underway.

## 6.5 Conclusions

For the first time scanning transmission X-ray microscopy (STXM) was used for the analysis of Mn<sub>3</sub>O<sub>4</sub> activation. The use of QC as a dispersant facilitated fabrication of composite electrodes with high active mass and high areal capacitance. The beneficial effect of catecholate-type polyaromatic QC is related to co-dispersion and efficient mixing of different materials: pseudocapacitive Mn<sub>3</sub>O<sub>4</sub> and conductive MWCNT

---

additives. Monitoring the capacitance change by CV, EIS and GCD using VSRP and FSR activation methods and analysis of active material by STXM linked capacitance increase during activation and corresponding  $\text{Mn}_3\text{O}_4$  oxidation on the surface and in the bulk of the particles. The capacitance increases during activation resulted from the gradual oxidation of  $\text{Mn}_3\text{O}_4$  and increased contribution of the particle bulk to the total capacitance. The charge storage mechanism involved redox  $\text{Mn}^{3+}/\text{Mn}^{4+}$  reactions on the particle surface and in the bulk. It is expected that the approach developed in this investigation can be used for the analysis of activation behavior and charge storage mechanisms of other pseudocapacitive materials, such as  $\text{V}_2\text{O}_3$ <sup>44</sup>. In addition, we are actively developing in situ flow electrochemical devices for STXM<sup>61,62</sup>, which will enable in situ and operando types of studies of supercapacitor electrode materials.

## 6.6 Acknowledgements

Research supported by the Natural Sciences and Engineering Research Council of Canada. Electron microscopy studies were performed at the Canadian Centre for Electron Microscopy. STXM synchrotron measurements were performed at the CLS, which is supported by CFI, NSERC, CIHR, NRC and the University of Saskatchewan. We thank CLS staff scientists Dr. Jian Wang and Dr. James Dynes for their support in carrying out these experiments. Furthermore, Wenjuan Yang received a scholarship from the China Scholarship Council.

---

## 6.7 References

- 1 Patil, T. S., Gangawane, S. A. & Takale, M. V. A Review on Mn<sub>3</sub>O<sub>4</sub> and Its Composite Nanomaterials of Diverse Morphologies as an Electrode Material in Supercapacitors. *International Journal of Scientific Research in Science and Technology* **8**, 520-526 (2021).
- 2 Sayyed, S. G., Shaikh, A. V., Dubal, D. P. & Pathan, H. M. Paving the Way towards Mn<sub>3</sub>O<sub>4</sub> Based Energy Storage Systems. *ES Energy & Environment* **14**, 3-21 (2021).
- 3 Liu, C. *et al.* Coherent Mn<sub>3</sub>O<sub>4</sub>-carbon nanocomposites with enhanced energy-storage capacitance. *Nano Research* **8**, 3372-3383 (2015).
- 4 Wang, Z., Fang, J., Hao, Y., Chen, C. & Zhang, D. High-performance Mn<sub>3</sub>O<sub>4</sub> nanomaterials synthesized via a new two-step hydrothermal method in asymmetric supercapacitors. *Materials Science in Semiconductor Processing* **130**, 105823 (2021).
- 5 Lee, H.-M., Jeong, G. H., Kang, D. W., Kim, S.-W. & Kim, C.-K. Direct and environmentally benign synthesis of manganese oxide/graphene composites from graphite for electrochemical capacitors. *Journal of Power Sources* **281**, 44-48 (2015).
- 6 Kerangueven, G., Faye, J., Royer, S. & Pronkin, S. N. Electrochemical properties and capacitance of Hausmannite Mn<sub>3</sub>O<sub>4</sub>-carbon composite synthesized by in situ autocombustion method. *Electrochimica Acta* **222**, 755-764 (2016).
- 7 Aswathy, R., Ulaganathan, M. & Ragupathy, P. Mn<sub>3</sub>O<sub>4</sub> nanoparticles grown on surface activated graphite paper for aqueous asymmetric supercapacitors. *Journal of Alloys and Compounds* **767**, 141-150 (2018).
- 8 Vatamanu, J., Borodin, O., Olguin, M., Yushin, G. & Bedrov, D. Charge storage at the nanoscale: understanding the trends from the molecular scale perspective. *Journal of Materials Chemistry A* **5**, 21049-21076 (2017).
- 9 Wu, Y. *et al.* A novel solvothermal synthesis of Mn<sub>3</sub>O<sub>4</sub>/graphene composites for supercapacitors. *Electrochimica Acta* **90**, 210-218 (2013).
- 10 Nabti, Z. *et al.* Free-standing and binder-free electrochemical capacitor electrode based on hierarchical microfibrillar carbon-graphene-Mn<sub>3</sub>O<sub>4</sub> nanocomposites materials. *Journal of Materials Science: Materials in Electronics* **29**, 14813-14826 (2018).
- 11 Long, Y., Xie, J., Li, H., Liu, Z. & Xie, Y. Solvothermal synthesis, electromagnetic and electrochemical properties of jellylike cylinder graphene-Mn<sub>3</sub>O<sub>4</sub> composite with highly coupled effect. *Journal of Solid State Chemistry* **256**, 256-265 (2017).
- 12 Suktha, P., Phattharasupakun, N., Dittanet, P. & Sawangphruk, M. Charge storage mechanisms of electrospun Mn<sub>3</sub>O<sub>4</sub> nanofibres for high-performance

- 
- supercapacitors. *RSC advances* **7**, 9958-9963 (2017).
- 13 Yeager, M. P. *et al.* Pseudocapacitive Hausmannite Nanoparticles with (101) Facets: Synthesis, Characterization, and Charge-Transfer Mechanism. *ChemSusChem* **6**, 1983-1992 (2013).
- 14 Liu, C. *et al.* The effect of electrolyte cation on electrochemically induced activation and capacitive performance of Mn<sub>3</sub>O<sub>4</sub> electrodes. *Electrochimica Acta* **324**, 134894 (2019).
- 15 Wu, T.-H. *et al.* Charge storage mechanism of activated manganese oxide composites for pseudocapacitors. *Journal of Materials Chemistry A* **3**, 12786-12795 (2015).
- 16 Rorabeck, K. & Zhitomirsky, I. Salting-out aided dispersive extraction of Mn<sub>3</sub>O<sub>4</sub> nanoparticles and carbon nanotubes for application in supercapacitors. *Colloids and Surfaces A: Physicochemical and Engineering Aspects* **618**, 126451 (2021).
- 17 Poon, R. & Zhitomirsky, I. High areal capacitance of Mn<sub>3</sub>O<sub>4</sub>-carbon nanotube electrodes. *Materials Letters* **215**, 4-7 (2018).
- 18 Nagarajan, N., Cheong, M. & Zhitomirsky, I. Electrochemical capacitance of MnO<sub>x</sub> films. *Materials Chemistry and Physics* **103**, 47-53 (2007).  
[https://doi.org:https://doi.org/10.1016/j.matchemphys.2007.01.005](https://doi.org/https://doi.org/10.1016/j.matchemphys.2007.01.005)
- 19 Milne, J. & Zhitomirsky, I. Application of octanohydroxamic acid for liquid-liquid extraction of manganese oxides and fabrication of supercapacitor electrodes. *Journal of Colloid and Interface Science* **515**, 50-57 (2018).  
<https://doi.org:https://doi.org/10.1016/j.jcis.2018.01.021>
- 20 Yang, W. & Zhitomirsky, I. Colloidal Processing of Mn<sub>3</sub>O<sub>4</sub>-Carbon Nanotube Nanocomposite Electrodes for Supercapacitors. *Nanomaterials* **12**, 803 (2022).
- 21 Poon, R., Liang, W. & Zhitomirsky, I. Mn<sub>3</sub>O<sub>4</sub> and (ZnFe) OOH Composites for Supercapacitors with High Active Mass. *Metallurgical and Materials Transactions A* **51**, 855-862 (2020).
- 22 Ata, M. S., Milne, J. & Zhitomirsky, I. Fabrication of Mn<sub>3</sub>O<sub>4</sub>-carbon nanotube composites with high areal capacitance using cationic and anionic dispersants. *Journal of Colloid and Interface Science* **512**, 758-766 (2018).  
<https://doi.org:https://doi.org/10.1016/j.jcis.2017.10.110>
- 23 Stöhr, J. *NEXAFS spectroscopy*. (Springer Series in Surface Sciences Vol. 25, (Springer, Germany, 1992)).
- 24 Hitchcock, A. P. *Soft X-ray imaging and spectromicroscopy, Chapter 22 in Volume II of the Handbook on Nanoscopy, eds. Gustaaf Van Tendeloo, Dirk Van Dyck and Stephen J. Pennycook (Wiley), p 745-791. (2012).*
- 25 Hitchcock, A. P. Soft X-ray spectromicroscopy and ptychography. *Journal of Electron Spectroscopy and Related Phenomena* **200**, 49-63 (2015).
- 26 Ade, H. & Hitchcock, A. P. NEXAFS microscopy and resonant scattering: Composition and orientation probed in real and reciprocal space. *Polymer* **49**,

- 
- 643-675 (2008).
- 27 Hitchcock, A. P. & Toney, M. F. Spectromicroscopy and coherent diffraction imaging: focus on energy materials applications. *Journal of Synchrotron Radiation* **21**, 1019-1030 (2014).
- 28 Arul, K. T., Chang, H.-W., Shiu, H.-W., Dong, C.-L. & Pong, W.-F. A review of energy materials studied by in situ/operando synchrotron x-ray spectromicroscopy. *Journal of Physics D: Applied Physics* **54**, 343001 (2021).
- 29 Chen, R., Yu, M., Sahu, R. P., Puri, I. K. & Zhitomirsky, I. The Development of Pseudocapacitor Electrodes and Devices with High Active Mass Loading. *Advanced Energy Materials* **10**, 1903848 (2020).  
<https://doi.org:10.1002/aenm.201903848>
- 30 Nawwar, M. *et al.* High areal capacitance of Fe<sub>3</sub>O<sub>4</sub>-decorated carbon nanotubes for supercapacitor electrodes. *Carbon Energy* **1**, 124-133 (2019).  
<https://doi.org:https://doi.org/10.1002/cey2.6>
- 31 Wang, Y., Liu, Y. & Zhitomirsky, I. Surface modification of MnO<sub>2</sub> and carbon nanotubes using organic dyes for nanotechnology of electrochemical supercapacitors. *Journal of Materials Chemistry A* **1**, 12519-12526 (2013).
- 32 Kaznatcheev, K. V. *et al.* Soft X-ray spectromicroscopy beamline at the CLS: commissioning results. *Nuclear Instruments and Methods in Physics Research Section A: Accelerators, Spectrometers, Detectors and Associated Equipment* **582**, 96-99 (2007).
- 33 Kilcoyne, A. *et al.* Interferometer-controlled scanning transmission X-ray microscopes at the Advanced Light Source. *Journal of synchrotron radiation* **10**, 125-136 (2003).
- 34 Takeichi, Y. *et al.* Design and performance of a compact scanning transmission X-ray microscope at the Photon Factory. *Review of Scientific Instruments* **87**, 013704 (2016).
- 35 Warwick, T. *et al.* A scanning transmission x-ray microscope for materials science spectromicroscopy at the advanced light source. *Review of Scientific Instruments* **69**, 2964-2973 (1998).
- 36 Jacobsen, C., Wirick, S., Flynn, G. & Zimba, C. Soft X-ray spectroscopy from image sequences with sub-100 nm spatial resolution. *Journal of Microscopy* **197**, 173-184 (2000).
- 37 Hitchcock, A.-P. *is written in Interactive Data Language (IDL). It is available free for non-commercial use from <http://unicorn.mcmaster.ca/aXis2000.html>.*
- 38 Gilbert, B. *et al.* Multiple scattering calculations of bonding and X-ray absorption spectroscopy of manganese oxides. *The Journal of Physical Chemistry A* **107**, 2839-2847 (2003).
- 39 Toner, B., Fakra, S., Villalobos, M., Warwick, T. & Sposito, G. Spatially resolved characterization of biogenic manganese oxide production within a bacterial biofilm. *Applied and environmental microbiology* **71**, 1300-1310 (2005).
- 40 Kim, J. *et al.* In Situ Spectroscopic and Computational Studies on a MnO<sub>2</sub>-

- 
- CuO Catalyst for Use in Volatile Organic Compound Decomposition. *ACS omega* **2**, 7424-7432 (2017).
- 41 Koprinarov, I., Hitchcock, A., McCrory, C. & Childs, R. Quantitative mapping of structured polymeric systems using singular value decomposition analysis of soft X-ray images. *The Journal of Physical Chemistry B* **106**, 5358-5364 (2002).
- 42 Wang, L. *et al.* Composite structure and properties of Mn<sub>3</sub>O<sub>4</sub>/graphene oxide and Mn<sub>3</sub>O<sub>4</sub>/graphene. *Journal of Materials Chemistry A* **1**, 8385-8397 (2013).
- 43 Sukhdev, A. *et al.* Synthesis, phase transformation, and morphology of hausmannite Mn<sub>3</sub>O<sub>4</sub> nanoparticles: photocatalytic and antibacterial investigations. *Heliyon* **6**, e03245 (2020).
- 44 Wallar, C., Poon, R. & Zhitomirsky, I. High Areal Capacitance of V<sub>2</sub>O<sub>3</sub>-Carbon Nanotube Electrodes. *Journal of The Electrochemical Society* **164**, A3620-A3627 (2017).
- 45 Ata, M., Liu, Y. & Zhitomirsky, I. A review of new methods of surface chemical modification, dispersion and electrophoretic deposition of metal oxide particles. *Rsc Advances* **4**, 22716-22732 (2014).
- 46 Wu, K., Wang, Y. & Zhitomirsky, I. Electrophoretic deposition of TiO<sub>2</sub> and composite TiO<sub>2</sub>-MnO<sub>2</sub> films using benzoic acid and phenolic molecules as charging additives. *Journal of colloid and interface science* **352**, 371-378 (2010). <https://doi.org/10.1016/j.jcis.2010.08.059>
- 47 Dalsin, J. L., Hu, B.-H., Lee, B. P. & Messersmith, P. B. Mussel adhesive protein mimetic polymers for the preparation of nonfouling surfaces. *Journal of the American Chemical Society* **125**, 4253-4258 (2003).
- 48 Lee, B. P., Messersmith, P. B., Israelachvili, J. N. & Waite, J. H. Mussel-inspired adhesives and coatings. *Annual review of materials research* **41**, 99-132 (2011).
- 49 Lee, H., Lee, B. P. & Messersmith, P. B. A reversible wet/dry adhesive inspired by mussels and geckos. *Nature* **448**, 338-341 (2007).
- 50 Petrone, L. Molecular surface chemistry in marine bioadhesion. *Advances in colloid and interface science* **195**, 1-18 (2013).
- 51 Yu, M. & Deming, T. J. Synthetic polypeptide mimics of marine adhesives. *Macromolecules* **31**, 4739-4745 (1998).
- 52 Ata, M. S., Poon, R., Syed, A. M., Milne, J. & Zhitomirsky, I. New developments in non-covalent surface modification, dispersion and electrophoretic deposition of carbon nanotubes. *Carbon* **130**, 584-598 (2018). <https://doi.org/10.1016/j.carbon.2018.01.066>
- 53 Mattarei, A. *et al.* (Wiley Online Library, 2011).
- 54 Heřmánková, E. *et al.* Redox properties of individual quercetin moieties. *Free Radical Biology and Medicine* **143**, 240-251 (2019).
- 55 Brett, A. M. O. & Ghica, M. E. Electrochemical oxidation of quercetin. *Electroanalysis: An International Journal Devoted to Fundamental and*

- 
- Practical Aspects of Electroanalysis* **15**, 1745-1750 (2003).
- 56 Nawwar, M., Poon, R., Sahu, R. P., Puri, I. K. & Zhitomirsky, I. Fe<sub>3</sub>O<sub>4</sub> spinel-Mn<sub>3</sub>O<sub>4</sub> spinel supercapacitor prepared using Celestine blue as a dispersant, capping agent and charge transfer mediator. *Ceramics International* **46**, 18851-18858 (2020).
- 57 Reddy, R. N. & Reddy, R. G. Sol-gel MnO<sub>2</sub> as an electrode material for electrochemical capacitors. *Journal of Power Sources* **124**, 330-337 (2003).
- 58 Jeong, Y. & Manthiram, A. Nanocrystalline manganese oxides for electrochemical capacitors with neutral electrolytes. *Journal of the Electrochemical Society* **149**, A1419 (2002).
- 59 Nesbitt, H. & Banerjee, D. Interpretation of XPS Mn (2p) spectra of Mn oxyhydroxides and constraints on the mechanism of MnO<sub>2</sub> precipitation. *American Mineralogist* **83**, 305-315 (1998).
- 60 Wang, J., Botton, G. A., West, M. M. & Hitchcock, A. P. Quantitative evaluation of radiation damage to polyethylene terephthalate by soft X-rays and high-energy electrons. *The Journal of Physical Chemistry B* **113**, 1869-1876 (2009).
- 61 Prabu, V. *et al.* Instrumentation for in situ flow electrochemical scanning transmission X-ray microscopy (STXM). *Review of Scientific Instruments* **89**, 063702 (2018).
- 62 Hitchcock, A. P. *et al.* In-situ and Operando Studies with Soft X-Ray Transmission Spectromicroscopy. *Microscopy and Microanalysis* **27**, 59-60 (2021).

## 6.8 Supporting Information

### Section 6-S1. Results of sedimentation tests

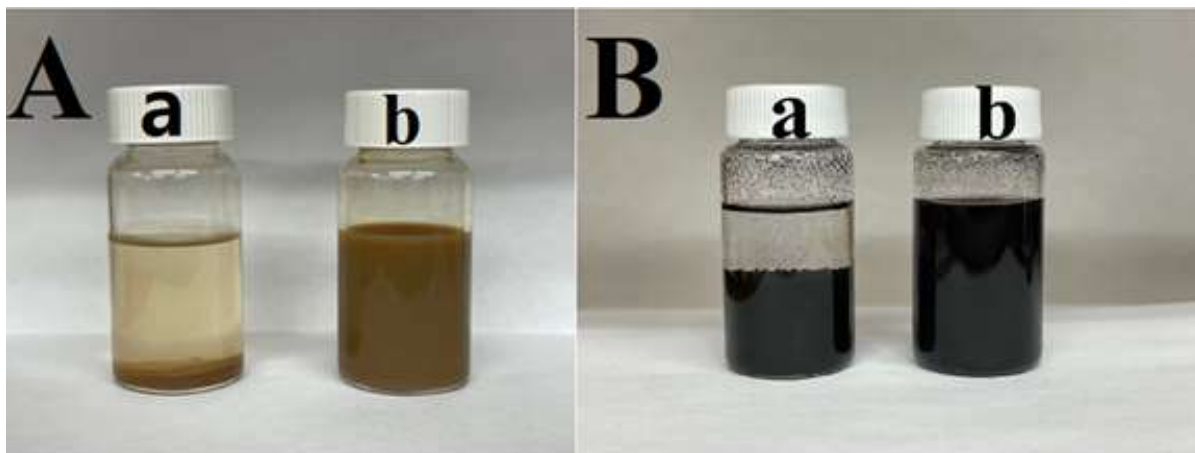


Figure 6-S 1 Suspensions of (A)  $\text{Mn}_3\text{O}_4$  and (B) MWCNT, (a) without QC and (b) with QC as dispersants 7 days after preparation; mass ratio of QC: $\text{Mn}_3\text{O}_4$  and QC: MWCNT is 0.2.

### Section 6-S2. Schematic of STXM

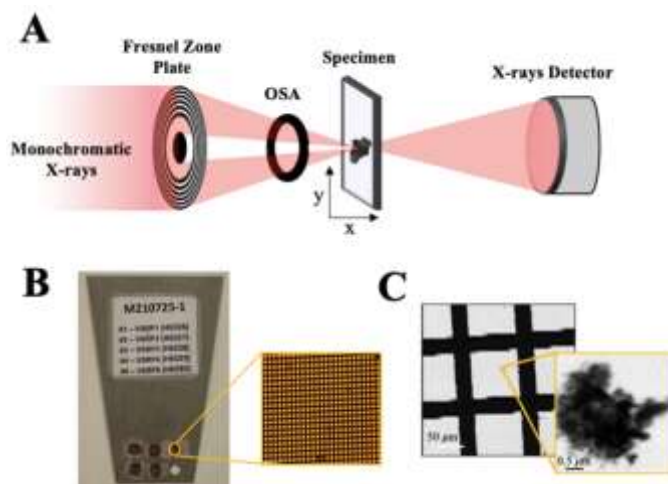


Figure 6-S 2. (A) Schematic diagram of scanning transmission x-ray microscopy (STXM), (B) samples on TEM grids mounted on STXM plate, (C) STXM image of the TEM grid square containing the measured region of the FSR1000 sample at 640 eV.

Figure 6-S2A shows a schematic diagram of scanning transmission x-ray microscopy (STXM). Figure 6-S2B shows VSRPs samples mounted on formvar coated TEM grids. Samples were prepared by attaching the TEM grid with a tape to the STXM plate, then drop-cast  $<1$  mg powder on the support. This procedure was followed by tapping the edge of the STXM plate on a hard surface to detach weakly adhering particles. The TEM grid with remaining particles is then covered with a second TEM grid to avoid particles flying off the TEM grid due to sample charging when the X-ray beam hits the sample. Figure S-2C shows a STXM image of the TEM grid square containing the measured region of the FSR1000 sample.

### Section 6-S3. Spectral energy calibration

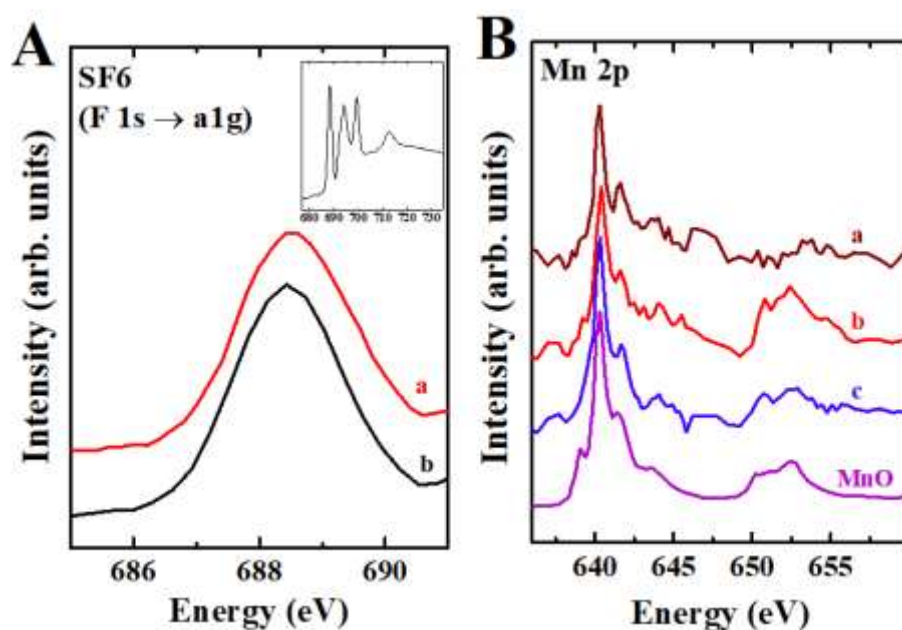


Figure 6-S 3 (A) F 1s → a<sub>1g</sub> absorption peak of sulfur hexafluoride (SF<sub>6</sub>) gas measured (a) the I<sub>o</sub> signal of a measurement of MnO<sub>2</sub> in the presence of SF<sub>6</sub> and, (b) at the hole (The inset shows the full F 1s spectrum of SF<sub>6</sub> gas<sup>[s1]</sup>). (B) Mn(II) signal present in the I<sub>o</sub> of Mn 2p

spectra measured in STXM and used to confirm the energy scale. (a) as-prepared  $\text{Mn}_3\text{O}_4$ , (b) FSR 100 and (c) FSR1000 cycle samples, compared to the digitized spectrum of  $\text{MnO}$  <sup>[s2]</sup>.

Table 6-S 1 Mn 2p and F 1s energy features of measured samples compared to reference spectra.

Sample	edge	peak position (eV)	E (eV)
$\text{MnO}_2$	F 1s (F 1s $\rightarrow$ a <sub>1g</sub> )	688.41	0.14
At the hole	F 1s (F 1s $\rightarrow$ a <sub>1g</sub> )	688.42	0.15
F 1s reference spectra <sup>S1</sup>	F 1s (F 1s $\rightarrow$ a <sub>1g</sub> )	688.27	-
As-prepared $\text{Mn}_3\text{O}_4$	Mn 2p (L <sub>3</sub> )	640.10	-
FSR100 cycle sample	Mn 2p (L <sub>3</sub> )	640.23	-
FSR1000 cycle sample	Mn 2p (L <sub>3</sub> )	641.10	-
$\text{MnO}$ digitized spectra <sup>S2</sup>	Mn 2p (L <sub>3</sub> )	640.28	-

In order to calibrate the spectrum of  $\text{MnO}_2$  and other species, sulfur hexafluoride ( $\text{SF}_6$ ) gas (P = 5 mbar) was introduced into the STXM tank and its F 1s spectrum measured as part of Mn 2p stack measurements. The F 1s  $\rightarrow$  a<sub>1g</sub> peak (688.27 eV)<sup>s1</sup> is observed in the I<sub>o</sub> signal of the measured Mn 2p stacks. Shifts of up to 0.15 eV were observed in the position of the F 1s  $\rightarrow$  a<sub>1g</sub> absorption peak (see table 6-S1) which were tracking some irreproducibility of the beamline energy scale. These shifts were used to set the Mn 2p energy scale accurately. Additionally, during some measurements, Mn(II) signal was observed in the I<sub>o</sub> spectrum (see Figure 6-S3B).

This arises from contamination of the STXM zone plate or exit window. This signal was used to validate the Mn 2p energy scale of the as-prepared Mn<sub>3</sub>O<sub>4</sub> and samples FSR 100 and 1000 cycle samples. The main L<sub>3</sub> peak Mn 2p spectrum of the Mn(II) contamination occurred at 640.4 eV, after calibration with the SF<sub>6</sub> signal measured at the same time.

#### Section 6-S4 Analysis of impedance spectroscopy data using equivalent circuit

Figure 6-S4 (A) shows experimental EIS data presented in a Nyquist plot and simulation data obtained using (B) equivalent circuit.

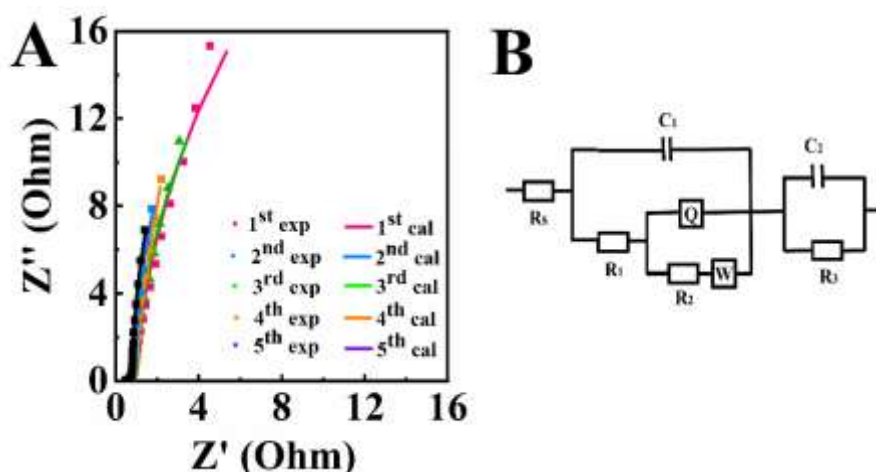


Figure 6-S 4 Nyquist plot of complex impedance for (a-c) VSRPs 1-5: experimental data 1<sup>st</sup> exp-5<sup>th</sup> exp and simulation data 1<sup>st</sup> cal-5<sup>th</sup> cal, (B) equivalent circuit used for simulation.

The equivalent circuit was similar to that developed in a previous investigation (ref.<sup>31</sup> in manuscript) for the analysis of porous electrodes with high active mass. The equivalent circuit contains R-C(Q) transmission line, Warburg impedance (W) and solution resistance  $R_s$ . In this circuit, capacitance (C) and constant phase element (Q)

---

represented double-layer capacitance at the electrode material -electrolyte interface and pseudocapacitance of the active material, respectively.  $C_2$  and  $R_3$  represent capacitance at the current collector-active material interface and charge transfer resistance, respectively. Simulation results showed that reduction of imaginary component of capacitance can be mainly attributed to increase in pseudocapacitance  $Q$ . The decrease of the real component resulted from the reduction of resistance of the transmission line.

Section 6-S5. Comparison of Mn 2p spectra of  $MnO_2$  and  $Mn_3O_4$  with literature

Figure 6-S5 compares the Mn 2p spectrum of  $MnO_2$  we measured by STXM, with the Mn 2p spectra of  $MnO_2$  reported by Gilbert et al.,<sup>s2</sup> Toner et al.<sup>s3</sup> and Stuckey et al.<sup>s4</sup>

The data plotted in figure 6-S4 was digitized from the figures in these papers. Every effort was made to accurately reproduce the spectral shape and peak positions as reported in these papers. Gilbert et al.<sup>s2</sup> report the sharp low lying peak in  $MnO_2$  at 640.5 eV, while Toner et al.<sup>s3</sup> report the corresponding peak at 639.3 eV, and Stuckey et al.<sup>s4</sup> report the peak at 640.5 eV. Due to the presence of calibration signals above the Mn L signal (F 1s spectrum of  $SF_6$ ), and exactly in the Mn L region (from the contaminant), we are confident our energy scale is accurate to within  $\pm 0.1$  eV.

Here we are pointing out the existence of significant discrepancies in the energies of the Mn 2p spectrum of  $MnO_2$  reported in the literature, we are preparing a more detailed evaluation of the soft X-ray NEXAFS spectroscopy of manganese oxides,

which will be presented elsewhere.

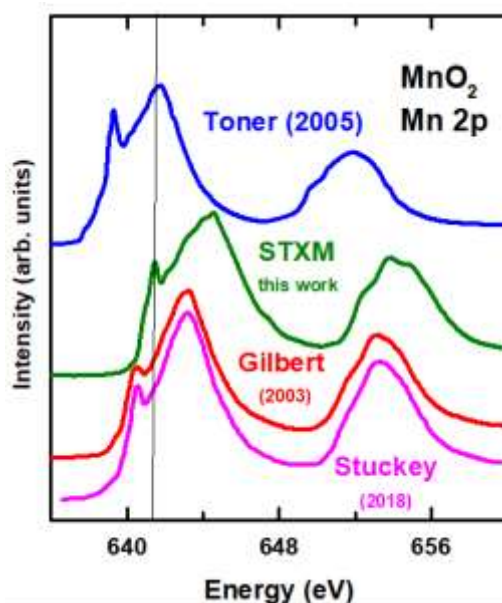


Figure 6-S 5 Comparison of the Mn 2p spectrum of  $\text{MnO}_2$  from this work (STXM), with that reported in the literature by Gilbert et al.,<sup>s2</sup> Toner et al.<sup>s3</sup> and Stuckey et al.<sup>s4</sup>

Figure 6-S6 compares the Mn 2p spectrum of  $\text{Mn}_3\text{O}_4$  reported by Gilbert et al.<sup>s2</sup> and Stuckey et al.<sup>s4</sup> with spectra of a commercial  $\text{Mn}_3\text{O}_4$  sample, and of the as-prepared Mn(II,III) sample, that we measured by STXM. For the comparison shown in Fig. 6-S6, the energy scale of each spectrum was set by assigning the position of the first Mn  $L_3$  peak to 639.9 eV, which is that observed in the as-prepared  $\text{Mn}_3\text{O}_4$  catalyst spectra. The digitized reference spectrum<sup>s2</sup> and that of the  $\text{Mn}_3\text{O}_4$  catalyst previously measured showed the same Mn ( $L_{2,3}$ ) features, indicating first  $L_3$  sharp peak at 639.9 eV. Although the main features of the Mn 2p spectrum of the commercial  $\text{Mn}_3\text{O}_4$  sample measured by TEY are present, the intensity of the first peak is considerably reduced. For this reason we chose to use the spectra of the as-prepared material as the

reference spectrum of  $\text{Mn}_3\text{O}_4$  in the detailed analysis.

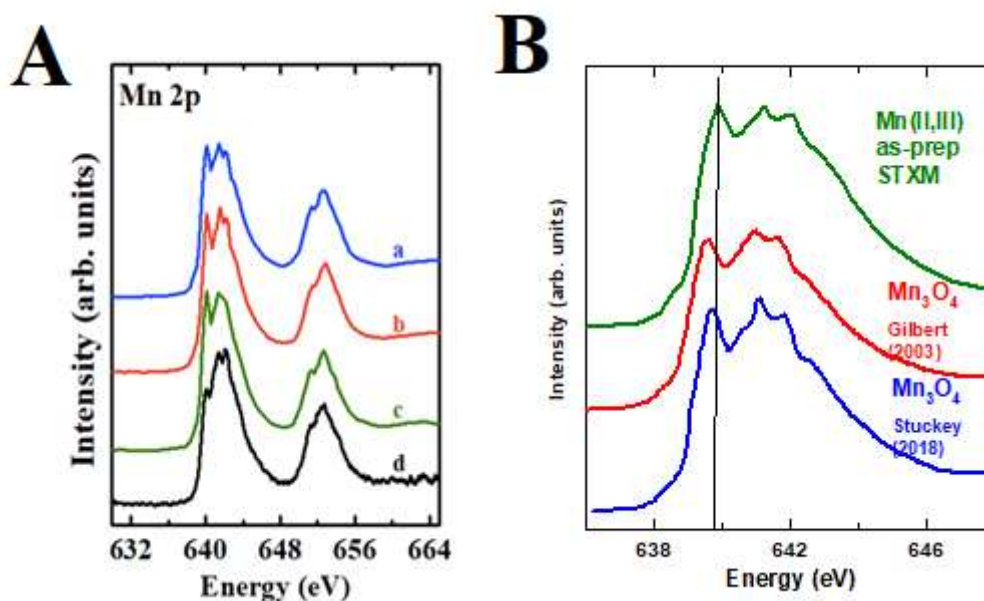


Figure 6-S 6 A.  $\text{Mn}_3\text{O}_4$  (Mn 2p) absorption spectra of (a) as-prepared catalyst, (b) digitized reference spectra from Gilbert et al.<sup>s2</sup>, (c) previously measured  $\text{Mn}_3\text{O}_4$  catalyst and (d) the SGM-TEY spectrum of commercial  $\text{Mn}_3\text{O}_4$  (Sigma). B Expansion of the Mn L<sub>3</sub> region, comparing the spectrum of the as-prepared Mn(II,III) catalyst, with the spectra of  $\text{Mn}_3\text{O}_4$  reported by Gilbert et al.,<sup>s2</sup> and Stuckey et al.<sup>s4</sup>

#### Section 6-S6. Comparison of STXM and SGM spectra

Figure 6-S7A and 6-S6B present Mn L<sub>2,3</sub> and O 1s SGM spectra of the as-prepared  $\text{Mn}_3\text{O}_4$  catalyst and  $\text{MnO}_2$  reference spectra in comparison with measured spectra of VSRP1, VSRP3, VSRP5 and FSR1000 cycle samples. STXM and SGM spectra of the samples are presented in Figure S7C. The differences between SGM-TEY and STXM measurements might be related to the TEY spectra being dominated by the surface (sampling depth of ~5-10 nm) while STXM is representative of the bulk (100-150 nm).

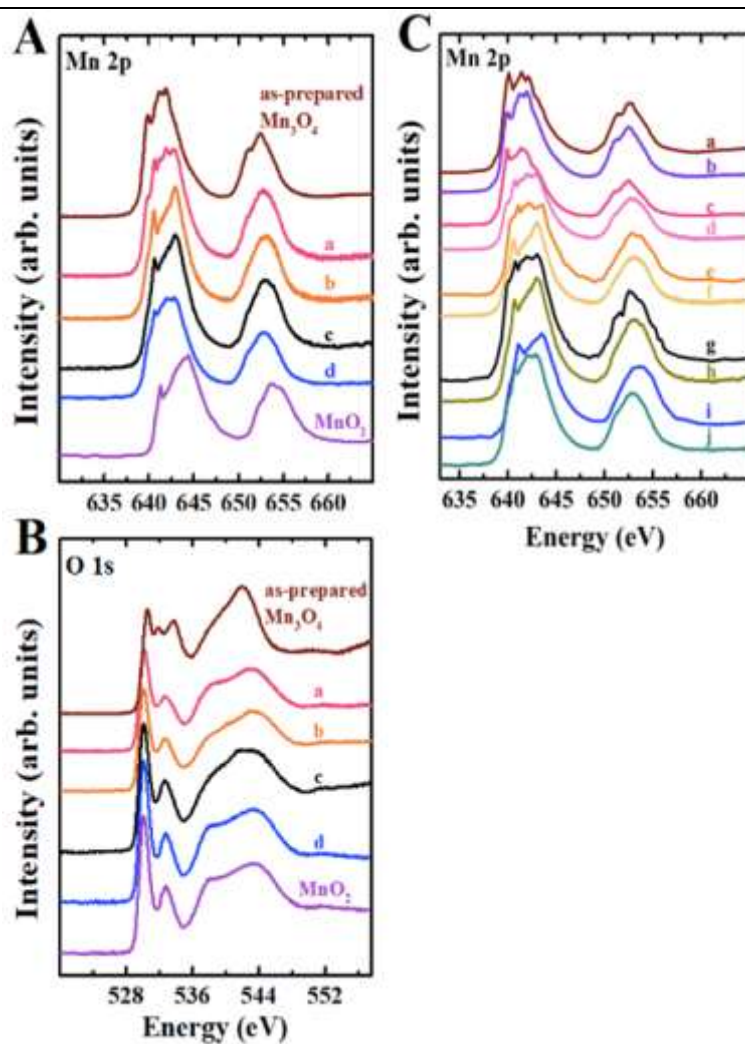


Figure 6-S 7 (A) Mn 2p, (B) O 1s SGM-TEY absorption spectra of (a) VSRP1, (b) VSRP3, (c) VSRP5 and (d) FSR1000 cycles, (C) shows comparison of STXM spectra (a), (c), (e), (g), (i) and SGM-TEY spectra, (b), (d), (f), (h), (j) of as-prepared  $\text{Mn}_3\text{O}_4$ , VSRP1, VSRP3, VSRP5 and FSR1000 cycles respectively.

## References for SI

S1. R.N.S. Sodhi & C.E. Brion, *J. Electron Spectroscopy & Rel. Phenom.* **34** 363 (1984).

S2 B. Gilbert, B. Frazer, A. Belz, P. Conrad, K. Neilson, D. Haskel, J. Lang, G. Srajer

and G. De Stasio, *The Journal of Physical Chemistry A* **107**, 2839 (2003)

S3 B. Toner, S. Fakra, M. Villalobos, T. Warwick and G. Sposito, *Applied and environmental microbiology* **71**, 1300 (2005)

S4 J. W. Stuckey, C. Goodwin, J. Wang, L.A. Kaplan, P. Vidal-Esquivel, T.P. Beebe Jr. and D.L. Sparks, *Geochem Trans* **19**, 6 (2018).

# **Chapter 7 Colloidal Processing of Mn<sub>3</sub>O<sub>4</sub>-Carbon Nanotube Nanocomposite Electrodes for Supercapacitors**

Wenjuan Yang and Igor Zhitomirsky \*

Department of Materials Science and Engineering, McMaster University, Hamilton,

ON L8S 4L7, Canada; yangw48@mcmaster.ca

\* Correspondence: zhitom@mcmaster.ca

Copyright 2022, reproduced with permission from the MDPI.

---

## 7.1 Abstract

This investigation addresses the challenges in the development of efficient nanostructured  $\text{Mn}_3\text{O}_4$  cathodes for supercapacitors. A high areal capacitance and the ability to avoid a time-consuming activation procedure for electrodes with high active mass loading of  $40 \text{ mg cm}^{-2}$  are reported. This facilitates practical applications of  $\text{Mn}_3\text{O}_4$  based electrodes. The highest capacitance of  $6.11 \text{ F cm}^{-2}$  ( $153 \text{ F g}^{-1}$ ) is obtained from cyclic voltammetry at a scan rate of  $2 \text{ mV s}^{-1}$  and  $6.07 \text{ F cm}^{-2}$  ( $151.9 \text{ F g}^{-1}$ ) from the chronopotentiometry at a current density of  $3 \text{ mA cm}^{-2}$  in a potential window of  $0.9 \text{ V}$  in a neutral  $\text{Na}_2\text{SO}_4$  electrolyte. The new approach is based on the application of rhamnolipids (RL) as a capping agent for the synthesis of  $\text{Mn}_3\text{O}_4$  particles and a co-dispersant for  $\text{Mn}_3\text{O}_4$  and carbon nanotubes, which are used as conductive additives. The size and shape of the  $\text{Mn}_3\text{O}_4$  particles are influenced by RL. The enhanced performance of the electrodes is linked to the chemical structure and properties of RL molecules, which exert influence on  $\text{Mn}_3\text{O}_4$  particle size and shape during synthesis, reduce agglomeration, facilitate RL adsorption on  $\text{Mn}_3\text{O}_4$  and carbon nanotubes, their co-dispersion and mixing at the nanometric scale.

## 7.2 Introduction

Colloidal methods are widely used for the fabrication of advanced nanomaterials and nanocomposites<sup>1-3</sup>. The use of surfactants for colloidal nanofabrication allows

---

efficient control of particle size and prevention of their agglomeration <sup>4-7</sup>. Of particular interest is the use of surfactants for the fabrication of nanocomposite electrodes for energy storage in supercapacitors. It was found that surfactants facilitate the fabrication of nanoparticles of inorganic charge storage materials with small particle size and prevent their agglomeration <sup>8</sup>. Significant interest has been generated in co-dispersants for efficient mixing of the charge storage materials with conductive additives <sup>8</sup>. The use of such co-dispersants for colloidal fabrication allowed for significant improvement of electrochemical performance of supercapacitors and batteries for practical applications <sup>8,9</sup>. Electrode porosity is an important factor controlling electrochemical performance <sup>10-12</sup>. High porosity facilitates good electrolyte access to the active material. Significant attention focused on the development of electrodes with hierarchical porosity <sup>13,14</sup>, which allows for superior electrode performance. Advanced techniques were developed for the fabrication of activated carbon, graphene, carbon fiber, MXene, metal oxide and hydroxide electrodes with high porosity <sup>15-19</sup>.

This research was motivated by the need in efficient capping agents and dispersants for the fabrication of advanced electrodes for supercapacitors. It has previously been shown that nanocomposites, based on  $Mn_3O_4$  are promising materials for cathodes of asymmetric supercapacitors <sup>8</sup>. However, challenges in  $Mn_3O_4$  applications are related to the development of efficient electrodes with commercially important high active mass <sup>8</sup>. The specific capacitance decreased with increasing active mass <sup>8</sup>. Moreover,

the application of  $\text{Mn}_3\text{O}_4$  electrodes with high active mass requires time-consuming activation procedures<sup>20-22</sup>, which must be avoided for practical applications. It was found that first charge-discharge cycles of  $\text{Mn}_3\text{O}_4$  electrodes showed low capacitance and activation cycling procedure was necessary in order to activate material and achieve high capacitance. Such activation procedures resulted in significant capacitance increase<sup>20,22-24</sup>. Several XPS studies revealed oxidation of  $\text{Mn}^{2+}$  and  $\text{Mn}^{3+}$  ions on the  $\text{Mn}_3\text{O}_4$  particle surface during cycling and linked this process to the increasing capacitance<sup>20-22,25</sup>. The challenges related to  $\text{Mn}_3\text{O}_4$  applications can be addressed using advanced capping agents for the  $\text{Mn}_3\text{O}_4$  synthesis and co-dispersants for  $\text{Mn}_3\text{O}_4$  and conductive additives.

The search for advanced dispersants for colloidal nanotechnology of energy storage materials has generated our interest in rhamnolipids (RL). RL are natural biosurfactants, which offer many benefits because their critical micelle concentration is 10–100 times lower than that of traditional chemical surfactants<sup>26</sup>. RL can solubilize highly hydrophobic organic molecules in aqueous solutions<sup>27</sup>. RL are biocompatible, chemically stable and low cost biosurfactants<sup>26</sup>, which have many applications in environmental field, food industry, and biotechnology<sup>28-30</sup>. RL are used for prevention of marine oil pollution, removing oil from sand<sup>31</sup> and various applications in agriculture<sup>32,33</sup>, laundry products and medicine<sup>26</sup>. RL exhibit valuable antimicrobial and anticancer properties<sup>33,34</sup>. Significant interest has been generated in applications of RL as dispersants for  $\text{BaTiO}_3$ <sup>35</sup>, alumina<sup>36,37</sup>, zirconia<sup>38</sup>, and hematite

---

<sup>39</sup> particles in aqueous suspensions. RL were used as capping agents for synthesis of ZnS <sup>40</sup>, NiO <sup>41</sup> and Ag <sup>42</sup> nanoparticles.

The goal of this investigation was the fabrication of Mn<sub>3</sub>O<sub>4</sub>-carbon nanotube composites for cathodes of asymmetric supercapacitors. The use of carbon nanotubes as conductive additives was critically important due to the low electronic conductivity of Mn<sub>3</sub>O<sub>4</sub> <sup>8,43</sup>. For the first time we report the application of RL as a capping agent for the synthesis of Mn<sub>3</sub>O<sub>4</sub> nanoparticles. The results presented below indicated that the shape and size of the synthesized Mn<sub>3</sub>O<sub>4</sub> particles is influenced by RL. Moreover, RL prevent agglomeration of Mn<sub>3</sub>O<sub>4</sub> particles during synthesis. Another important finding was good co-dispersion of Mn<sub>3</sub>O<sub>4</sub> and carbon nanotubes by RL, which adsorbed on both materials and facilitated their electrostatic dispersion. It is in this regard that various commercial surfactants are efficient in dispersion of only one type of material, such as inorganic particles or carbon materials <sup>44,45</sup>. The ability of efficient co-dispersion of Mn<sub>3</sub>O<sub>4</sub> and carbon nanotubes by RL allowed for their efficient mixing and facilitated the fabrication of nanocomposite electrodes with high capacitance. Moreover, the time-consuming activation procedure for the fabrication of Mn<sub>3</sub>O<sub>4</sub> electrodes can be avoided. The results of this investigation indicated that Mn<sub>3</sub>O<sub>4</sub>-carbon nanotube composites are promising for practical applications for energy storage in cathodes of asymmetric supercapacitors.

---

## 7.3 Materials and Methods

RL, ethanol,  $\text{Mn}(\text{NO}_3)_2 \cdot 4\text{H}_2\text{O}$ , NaOH,  $\text{Na}_2\text{SO}_4$ , poly(vinyl butyral-co-vinyl alcohol-co-vinyl acetate) (PVB, MilliporeSigma, Canada) and multiwalled carbon nanotubes (MWCNT, ID 4 nm, OD 13 nm, length 1–2  $\mu\text{m}$ , Bayer, Germany) were used as starting materials. The as-received MWCNT formed large agglomerates with a typical diameter of 0.5  $\mu\text{m}$ . PVB is advanced co-polymer binder<sup>46,47</sup> designed for colloidal processing of inorganic particles. Polyvinyl alcohol functional groups facilitate PVB adsorption on inorganic particles by formation of hydrogen bonds with hydroxyl groups on the particle surface<sup>46,47</sup>. Butyral segments are directed toward the organic solvent, providing steric stabilization<sup>46,47</sup>.

$\text{Mn}_3\text{O}_4$  nanoparticles were prepared by a modified chemical precipitation method<sup>29</sup> and mixed with MWCNT. In method 1, a solution of 330 mg of  $\text{Mn}(\text{NO}_3)_2 \cdot 4\text{H}_2\text{O}$  in 20 ml of DI water was prepared and then the pH of the solution was increased to pH = 10 with aqueous NaOH for the  $\text{Mn}_3\text{O}_4$  synthesis. The synthesis was performed without the use of RL. In this method, RL were used as co-dispersants for  $\text{Mn}_3\text{O}_4$  and MWCNT. As-prepared  $\text{Mn}_3\text{O}_4$  was mixed in the aqueous phase with MWCNT and then RL were added. The mass ratio of  $\text{Mn}_3\text{O}_4$ :CNT:RL was 4:1:1.

In method 2, RL were used as a capping agent for  $\text{Mn}_3\text{O}_4$  synthesis and a co-dispersant for  $\text{Mn}_3\text{O}_4$  and MWCNT. A solution of 330 mg of  $\text{Mn}(\text{NO}_3)_2 \cdot 4\text{H}_2\text{O}$  in DI water was prepared and RL were added as a capping agent for the synthesis of  $\text{Mn}_3\text{O}_4$  nanoparticles to achieve  $\text{Mn}_3\text{O}_4$ :RL ratio of 4:2. The pH of the solution was increased

---

to pH = 10 with aqueous NaOH for the Mn<sub>3</sub>O<sub>4</sub> synthesis and then MWCNT were added to Mn<sub>3</sub>O<sub>4</sub> in the aqueous phase. The mass ratio of Mn<sub>3</sub>O<sub>4</sub>:CNT:RL was 4:1:2. Additional experiments were performed for mass ratio of Mn<sub>3</sub>O<sub>4</sub>:CNT:RL = 4:1:1 (Figures 7-S1–4). The mixtures of Mn<sub>3</sub>O<sub>4</sub> with MWCNT, containing RL and prepared by both methods were ultrasonicated for achieving improved dispersion and mixing, and then washed and dried. In both methods the Mn(NO<sub>3</sub>)<sub>2</sub> solutions were stirred for 30 min before adding NaOH. The amount of added NaOH was the same in both methods. Obtained powders were used for the fabrication of electrodes using slurries of Mn<sub>3</sub>O<sub>4</sub> and MWCNT in ethanol, containing PVB as a binder. The PVB binder content was 3% of the total mass of Mn<sub>3</sub>O<sub>4</sub> and MWCNT. The slurries were used for impregnation of commercial Ni foam (Vale, Canada) current collectors. The total mass of impregnated material after drying was 40 mg cm<sup>-2</sup>.

Microstructure investigations were performed using transmission electron microscopy (TEM, Talos 200X microscope, USA) and scanning electron microscopy (SEM, JEOL, JSM-7000F microscope, Japan) methods. X-ray diffraction (XRD) analysis (diffractometer Bruker D8, UK) was performed using Cu-K $\alpha$  radiation at the rate of 0.01 degrees per second. Fourier Transform Infrared Spectroscopy (FTIR) studies were performed using a Bruker Vertex 70 spectrometer. XPS analysis was performed using Quantera II Scanning XPS instrument. Electrochemical studies were performed in aqueous 0.5 M Na<sub>2</sub>SO<sub>4</sub> electrolyte using PARSTAT 2273 (Ametek) potentiostat for cyclic voltammetry (CV) and electrochemical impedance spectroscopy (EIS). A

---

BioLogic VMP 300 potentiostat was used for galvanostatic charge-discharge (GCD) investigations. Testing was performed using a 3-electrode electrochemical cell containing a working electrode (impregnated Ni foam), counter-electrode (Pt mesh), and a reference electrode (SCE, saturated calomel electrode). The capacitive properties of electrode material were presented in gravimetric ( $C_m, \text{Fg}^{-1}$ ) and areal ( $C_s, \text{F cm}^{-2}$ ) capacitance forms. Capacitances  $C_m$  and  $C_s$  were calculated from the CV, EIS and GCD data as it was described in reference <sup>24</sup>. The capacitances calculated from the CV and GCD data represented integral capacitances measured in a potential window of 0–0.9 V versus SCE. The capacitances calculated from the EIS data represented differential capacitances measured at an open circuit potential at voltage amplitude of 5 mV. CV testing procedures (TP) involved obtaining CV at scan rates of 2, 5, 10, 20, 50 and 100  $\text{mV s}^{-1}$ . EIS measurements were performed after each TP. GCD measurements were performed after the last TP.

## 7.4 Results and Discussion

Figure 7-1A shows X-ray diffraction patterns of  $\text{Mn}_3\text{O}_4$ -MWCNT composites prepared by methods 1 and 2. The diffraction patterns show major peaks of  $\text{Mn}_3\text{O}_4$ , corresponding to the JCPDS file 001-1127 and peaks of MWCNT, corresponding to the JCPDS file 058-1638. The X-ray diffraction pattern of the material prepared by method 1 showed a very small peak of  $\text{MnO}_2$ , corresponding to the JCPDS file 083-6090. The relative intensity of this peak was higher for the material prepared by

method 2. In this investigation  $\text{Mn}^{2+}$  salt was used for the synthesis of manganese oxide. However,  $\text{Mn}^{2+}\text{O}$  and  $\text{Mn}^{2+}(\text{OH})_2$  are unstable and converted to oxides with higher oxidation state in air<sup>20-22,48</sup>.

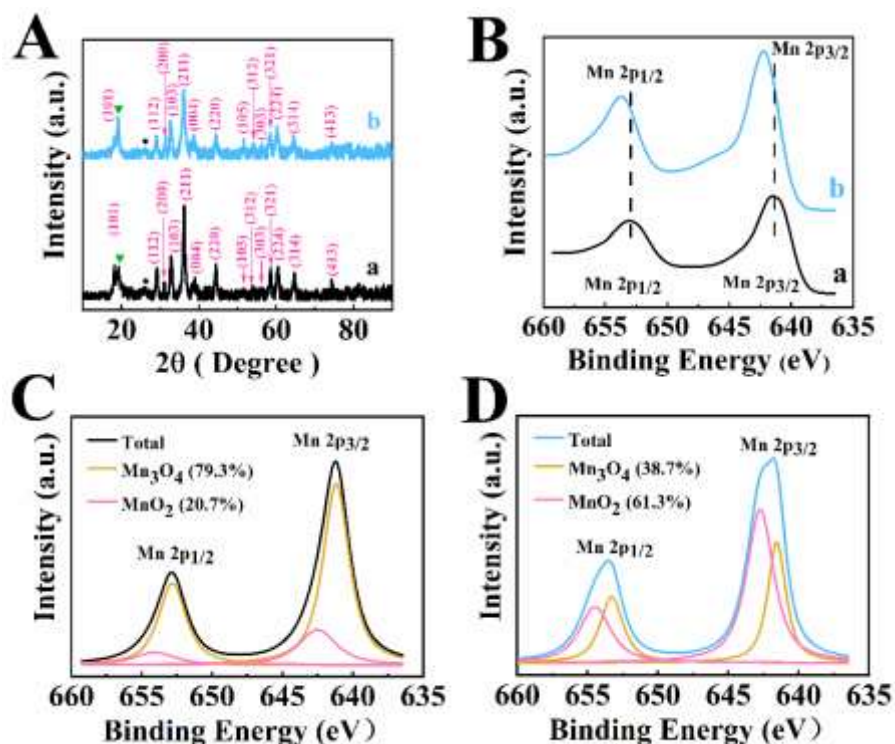


Figure 7- 1 (A) X-ray diffraction patterns for  $\text{Mn}_3\text{O}_4$ -MWCNT materials prepared by (a) method 1 and (b) method 2, Miller indexes are presented for  $\text{Mn}_3\text{O}_4$  phase, JCPDS file 001-1127, ●—(002) peak of MWCNT, JCPDS file 058-1638 , ▼—(111) peak of  $\text{MnO}_2$ , JCPDS file 083-6090, (B–D) XPS data for  $\text{Mn}_3\text{O}_4$ -MWCNT materials prepared by (B(a) and C) method 1 and (B(b) and D) method 2.

The XPS data for the materials prepared by methods 1 and 2 is presented in Figure 1C–D. It should be noted that literature XPS data<sup>49-51</sup> for  $\text{Mn}_3\text{O}_4$  showed co-existence of  $\text{Mn}^{2+}$ ,  $\text{Mn}^{3+}$  and  $\text{Mn}^{4+}$ . The peaks corresponding to the  $2p_{3/2}$ - $2p_{1/2}$  doublet shifted to higher energies for electrodes, prepared by method 2, compared to the electrodes,

---

prepared by method 1 (Figure 7-1B). Such shift indicated larger  $Mn^{4+}$  content<sup>51,52</sup> in the samples prepared by method 2. A similar shift was observed in  $Mn_3O_4$ - $MnO_2$  hetero-nanorods<sup>52</sup>. Deconvoluted XPS spectra confirmed enlarged  $MnO_2$  surface content in the samples, prepared by method 2 (Figure 7-1C,D).

In this investigation RL were used as a capping agent for the synthesis of  $Mn_3O_4$  in method 2 and a co-dispersing agent for  $Mn_3O_4$  and MWCNT in methods 1 and 2. RL biosurfactants are amphiphilic glycolipids, produced by *Pseudomonas aeruginosa*<sup>26</sup>. As received RL was a mixture of mono-RL and di-RL. Figure 2 shows chemical structures of RL. The structures contain rhamnose and fatty acid moieties<sup>26</sup>. The amphiphilic structure of RL and electric charge of their carboxylic groups in solutions are important factors, which make RL promising dispersants for electrostatic dispersion of materials. For the investigation of dispersion properties of RL,  $Mn_3O_4$  particles were prepared by method 1 without MWCNT, washed, dried and redispersed in water in the presence of RL with  $Mn_3O_4$ :RL mass ratio 4:1. MWCNT were dispersed in water in the presence of RL with MWCNT:RL mass ratio of 1:1. Sedimentation tests showed colloidal stability of the obtained suspensions for more than 1 week. It should be noted that metal oxide nanoparticles often form agglomerates due to their high surface energy. The condensation of surface OH groups also promote agglomeration. The as-received MWCNT used in this investigation consisted of large agglomerates with a typical size of 0.5  $\mu m$ <sup>53</sup>. The ability to co-disperse  $Mn_3O_4$  and MWCNT using a RL as a co-dispersant is important

for their efficient mixing. It is suggested that RL adsorbed on  $\text{Mn}_3\text{O}_4$  and MWCNT and allowed for their electrostatic dispersion. The adsorption of RL on MWCNT resulted from hydrophobic interactions of fatty acid moieties of RL with carbon nanotubes<sup>54</sup>. It is known that RL forms complexes with Mn<sup>55,56</sup>. Therefore, the complexation Mn atoms on the  $\text{Mn}_3\text{O}_4$  particle surface with RL can explain the RL adsorption on  $\text{Mn}_3\text{O}_4$ .

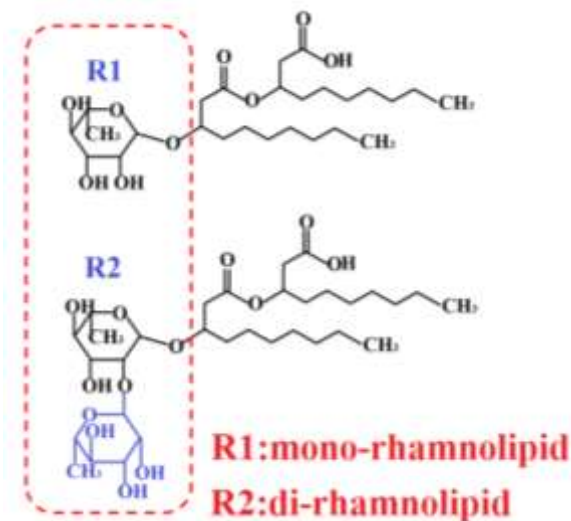


Figure 7- 2 Chemical structure of RL. Dashed line shows rhamnose moieties.

Figure 7-3 shows TEM images of  $\text{Mn}_3\text{O}_4$  prepared by methods 1 and 2 without MWCNT.

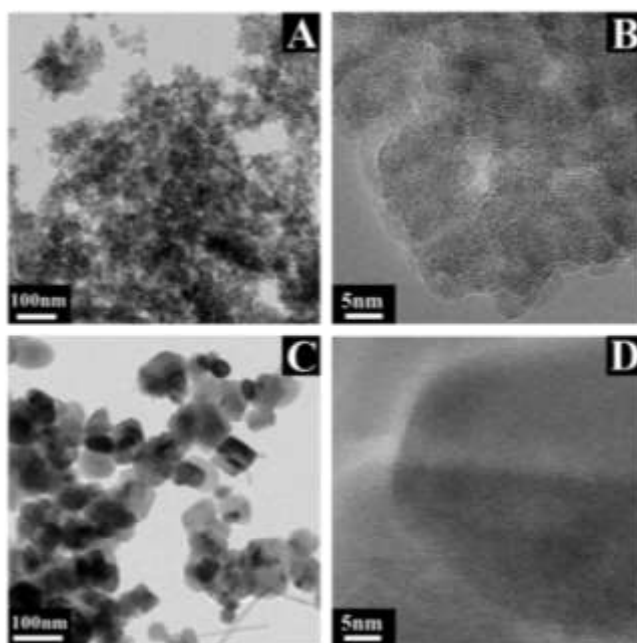


Figure 7- 3 TEM images at different magnifications of  $Mn_3O_4$  prepared by method 1 (A,B) and method 2 (C,D).

The TEM images of  $Mn_3O_4$  prepared by method 1 without a capping agent contained large agglomerates of particles of irregular shape (Figure 7-3A,B). The morphology of  $Mn_3O_4$  particles prepared using RL as a capping agent in method 2 was different (Figure 7-3C,D). The primary particles were larger and showed crystalline faces. The typical size of the particles was about 50 nm. The particles prepared in the presence of RL as a capping agent showed reduced agglomeration (Figure 7-3C,D). Therefore, the results of TEM studies showed that the morphology of the synthesized  $Mn_3O_4$  was influenced by RL.

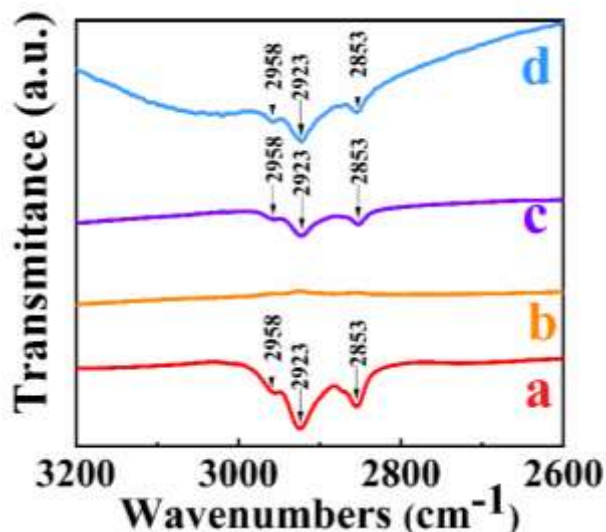


Figure 7- 4 FTIR spectra of (a) as received RL, (b)  $\text{Mn}_3\text{O}_4$  prepared without RL by method 1, (c)  $\text{Mn}_3\text{O}_4$  prepared without RL by method 1 and dispersed using RL, (d)  $\text{Mn}_3\text{O}_4$  prepared using RL as a capping agent by method 2.

FTIR studies were performed to analyze the RL adsorption. The FTIR spectrum of as-received RL (Figure 7-4a) showed absorptions at 2853, 2923 and 2958  $\text{cm}^{-1}$ , which can be attributed to the asymmetric and symmetric stretching vibrations of the  $\text{CH}_2$  and  $\text{CH}_3$  groups<sup>57</sup> of RL. Such absorptions were not observed in the spectrum of  $\text{Mn}_3\text{O}_4$  prepared by method 1 without RL (Figure 7-4b).

For comparison, the  $\text{Mn}_3\text{O}_4$  particles prepared by method 1 were dispersed in the presence of RL. The obtained suspensions were filtered, washed and dried. The FTIR spectrum of obtained powders (Figure 7-4c) showed absorption peaks, similar to those observed in the spectrum of RL (Figure 7-4a). Similar absorptions were observed in the spectrum of  $\text{Mn}_3\text{O}_4$  prepared by method 2 (Figure 7-4d). Therefore, the results of FTIR studies showed that RL adsorbed on the  $\text{Mn}_3\text{O}_4$  particles during or after

---

synthesis.

Figure 7-5 shows SEM images of composite electrodes, which were fabricated using  $\text{Mn}_3\text{O}_4$ -MWCNT composites, prepared by methods 1 and 2. The SEM image of electrodes prepared by method 1 showed that the size of primary  $\text{Mn}_3\text{O}_4$  particles was below 100 nm, however  $\text{Mn}_3\text{O}_4$  particles formed agglomerates. This resulted in the areas with larger contents of  $\text{Mn}_3\text{O}_4$  or MWCNT and indicated poor mixing of the components. In contrast, such areas were not observed in the SEM images of the electrodes prepared by method 2, which facilitated improved mixing of  $\text{Mn}_3\text{O}_4$  or MWCNT. CV studies of the electrodes prepared by method 1 showed nearly rectangular CVs for TP 1 (Figure 7-6A). However, CV areas increased during cycling. Figure 6B presents CVs for TP 1–5 at a scan rate of  $10 \text{ mV s}^{-1}$ . Significant increase in CV areas indicates increase in capacitance during cycling. This agrees with previous investigations<sup>20-22</sup>, which showed that time consuming activation is required for  $\text{Mn}_3\text{O}_4$  electrodes with high active mass. Such a time-consuming activation procedure must be avoided for practical applications. Activation of the electrodes prepared by method 1 required 5 TPs and each TP involved testing a scan rates of 2, 5, 10, 20, 50 and  $100 \text{ mV s}^{-1}$ . The electrodes prepared by method 2 showed significantly higher currents for TP1 (Figure 7-6C), compared to electrodes prepared by method 1 (Figure 7-6A). The higher currents indicated higher capacitance. The electrodes prepared by method 2 showed reduced variations in CV areas during cycling. Figure 7-6D presents CVs at a scan rate of  $10 \text{ mV s}^{-1}$ . Very small variations in CV were observed

for TP 1–3. The CV obtained at TP3 showed slightly improved rectangular shape, compared to the CV for TP1.

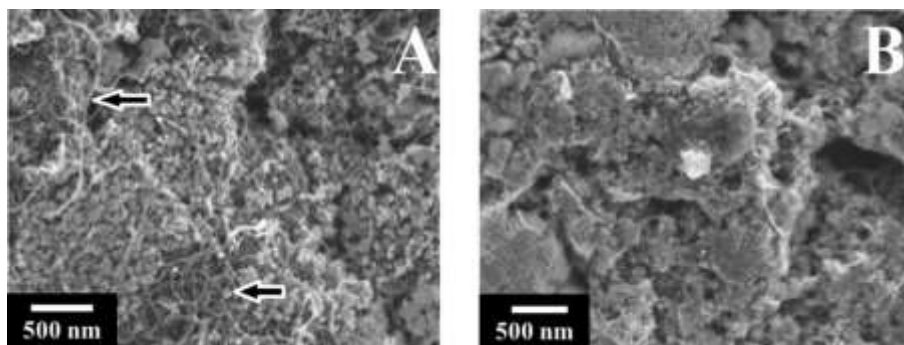


Figure 7- 5 SEM images of electrodes prepared using  $Mn_3O_4$ -MWCNT composites prepared by (A) method 1 and (B) method 2. Arrows show areas with enlarged MWCNT content.

The areas of CV remained practically without change for TP4 and TP5 for electrodes prepared by method 2. CV area for TP1 for electrode prepared by method 2 (Figure 7-6D(a)) was larger than the area of CV for TP 5 for the electrode prepared by method 1 (Figure 7-6B(e)). This indicates higher capacitance of the electrodes prepared by method 2, compared to method 1. Moreover, the need in time consuming activation process can be avoided for electrodes prepared by method 2.

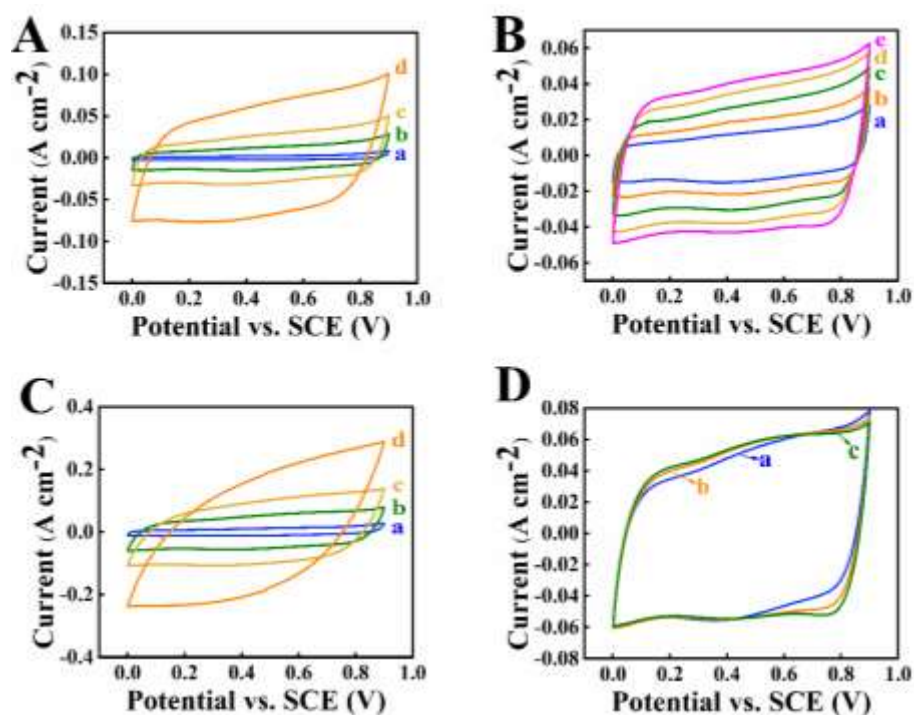


Figure 7- 6 (A) CVs at scan rates of (a) 2, (b) 10, (c) 20 and (d) 50  $\text{mV s}^{-1}$  for TP1 and (B) CVs at a scan rate of 10  $\text{mV s}^{-1}$  for (a) TP1, (b) TP2, (c) TP3, (d) TP4 and (e) TP5 for electrode prepared by method 1, (C) CVs at scan rates of (a) 2, (b) 10, (c) 20 and (d) 50  $\text{mV s}^{-1}$  for TP1 and (D) CVs at a scan rate of 10  $\text{mV s}^{-1}$  for (a) TP1, (b) TP2, and (c) TP3 for electrode prepared by method 2. Each TP involved testing at scan rates of 2, 5, 10, 20, 50 and 100  $\text{mV s}^{-1}$ . The CVs for scan rate of 10  $\text{mV s}^{-1}$  for each TP were selected and presented in (B, D).

Figure 7-7A shows capacitances calculated from the CV data for electrodes prepared by method 1 for TP 1–5. The capacitance of supercapacitor electrodes usually decreases with increasing scan rate<sup>58</sup> due to the diffusion limitations in pores. However, capacitances for TP1 and TP2 showed maxima at a scan rate of 20  $\text{mV s}^{-1}$ . This can be attributed to electrode activation during initial cycling at low scan rates. Numerous XPS studies showed that the activation process results in oxidation of  $\text{Mn}^{2+}$

---

and  $\text{Mn}^{3+}$  ions on the  $\text{Mn}_3\text{O}_4$  particle surface during cycling in the positive potential range and linked this process to the capacitance increase<sup>20-22,25</sup>. The oxidation process was influenced by the duration of the application of a positive potential. Therefore, it is not surprising that the activation process was enhanced at low scan rates.

Capacitance increased and impedance decreased with increasing number of TP (Figure 7-7A,B). The highest capacitance at a scan rate of  $2 \text{ mV s}^{-1}$  was found to be  $4.14 \text{ F cm}^{-2}$  ( $104.4 \text{ F g}^{-1}$ ) for TP 5 in the method 1. Testing results indicated that activation process is necessary for achieving high capacitance and reducing impedance of electrodes prepared by method 1. As pointed out above, such time-consuming activation process must be avoided for practical applications.

Electrodes, prepared by method 2, did not show significant variations of capacitance and impedance during cycling. The capacitance obtained for the first cycle of TP 1 at a scan rate of  $2 \text{ mV s}^{-1}$  was  $5.67 \text{ F cm}^{-2}$  ( $141.6 \text{ F g}^{-1}$ ) for electrodes prepared by method 2. It is higher than the capacitance obtained at the same scan rate for TP5 for electrodes prepared by method 1. A capacitance of  $6.11 \text{ F cm}^{-2}$  ( $153 \text{ F g}^{-1}$ ) was obtained at a scan rate of  $2 \text{ mV s}^{-1}$  for TP 3. The real and imaginary parts of impedance for electrode, prepared by method 2 for TP 1 were lower than the corresponding values for TP 5 for electrode, prepared by method 1. This indicated lower resistance and higher capacitance of the electrodes prepared by method 2. The electrodes, prepared by method 2 showed very small variations in capacitance and impedance for TP 4 and TP 5, compared to TP 3.

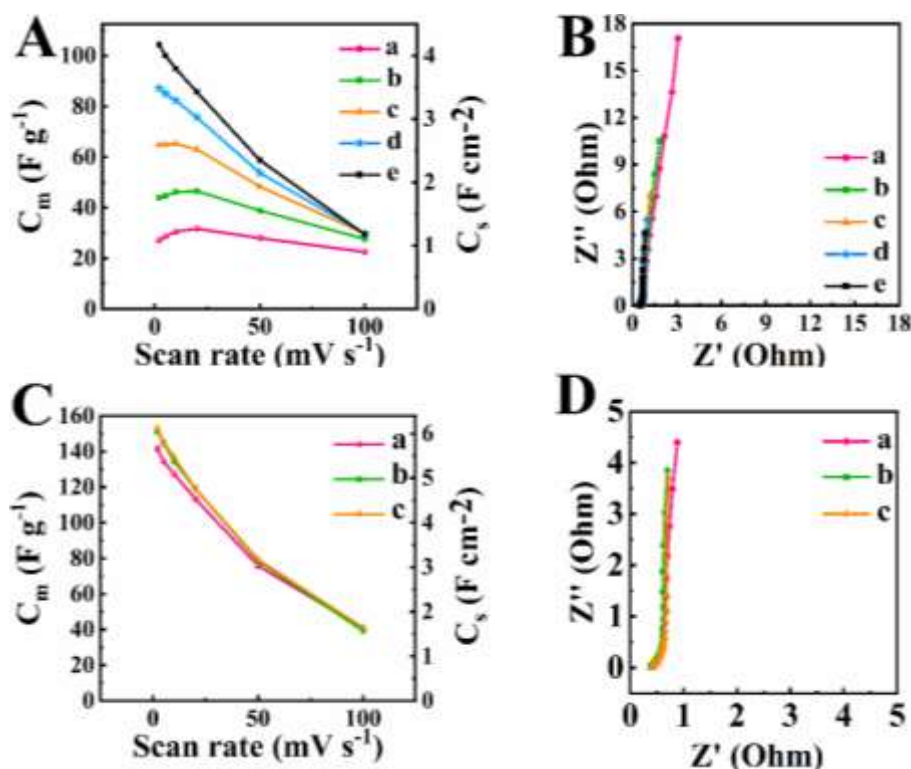


Figure 7-7 (A) Capacitance versus scan rate and (B) impedance data presented in a Nyquist plot for (a) TP 1, (b) TP 2, (c) TP 3, (d) TP 4 and (e) TP 5 for electrode prepared by method 1, (C) capacitance versus scan rate and (D) impedance data presented in a Nyquist plot for (a) TP 1, (b) TP 2, and (c) TP 3 for electrode prepared by method 2.

CV data indicated that significantly higher capacitance was achieved by method 2 and in this method the time-consuming activation procedure can be avoided. This opens an avenue for practical applications of  $\text{Mn}_3\text{O}_4$  based electrodes with high active mass loading. It should be noted that small variations in capacitance were observed in method 2. However, variations in capacitance were also observed for other electrodes, such as  $\text{MnO}_2$  electrodes during initial cycling<sup>59</sup>. Such capacitance increase of the  $\text{MnO}_2$  electrodes was attributed to other factors, such as microstructure changes

during initial cycling<sup>59</sup>.

Figure 7-8 shows frequency dependences of real ( $C_S'$ ) and imaginary ( $C_S''$ ) components of AC capacitance, derived from the impedance data. In contrast to integral capacitance measured by CV method in a potential window of 0.9 V, the components of the differential AC capacitance were measured at voltage amplitude of 5 mV at an open circuit potential.

Figure 7-8A shows significant increase of low frequency capacitance  $C_S'$  with increasing TP number for electrodes prepared by method 1. The highest  $C_S'$  of 3.33 F  $\text{cm}^{-2}$  was obtained at a frequency of 10 mHz for TP 5. The analysis of frequency dependences of  $C_S''$  showed significant reduction of the relaxation frequency, corresponding to the  $C_S''$  maximum with increasing TP number (Figure 7-8B). The electrode prepared by method 2 showed  $C_S'$  of 3.48 F  $\text{cm}^{-2}$  at a frequency of 10 mHz (Figure 7-8C) for TP 1, which is higher than  $C_S'$  for electrode prepared by method 1 for TP 5. The  $C_S'$  increased for T2 and showed very small variation for TP 3–5. The relaxation frequency of the electrodes prepared by method 2 showed very small changes (Figure 7-8D), especially after TP 2. Therefore, the behavior of the differential capacitance during TP 1–5 correlated with behavior of the integral capacitance, derived from the CV data.

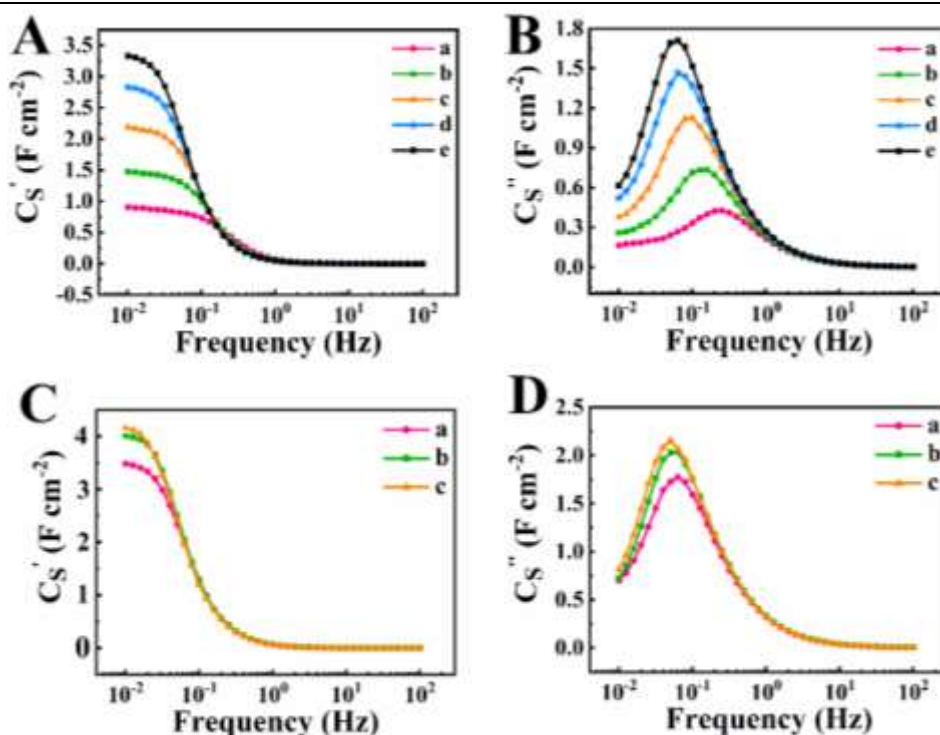


Figure 7- 8 (A) real and (B) imaginary components of complex capacitance for (a) TP 1, (b) TP 2, (c) TP 3, (d) TP 4 and (e) TP 5 for electrode prepared by method 1, (C) real and (D) imaginary components of complex capacitance for (a) TP 1, (b) TP 2, (c) TP 3 for electrode prepared by method 2.

The results of the GCD testing of electrodes, prepared by methods 1 and 2, after TP 5 are presented in Figure 7-9. The GCD curves at different currents showed nearly ideal linear dependences (Figure 7-9 A, C). The electrodes prepared by method 1 and method 2 showed capacitances of  $5.83 \text{ F cm}^{-2}$  ( $145.8 \text{ F g}^{-1}$ ) and  $6.07 \text{ F cm}^{-2}$  ( $151.9 \text{ F g}^{-1}$ ), respectively at a current density of  $3 \text{ mA cm}^{-2}$  (Figure 7-9B, D). The capacitances showed slight decrease with increasing current density in the range of 3– $10 \text{ mA cm}^{-2}$ .

The influence of cycling on capacitive properties of electrodes prepared by methods 1

---

and 2 was also studied by analyzing CVs at a scan rate of  $50 \text{ mV s}^{-1}$ . The capacitances for different cycles were normalized by the capacitance obtained at 2000th cycle and presented in Figure 7-10. The normalized capacitance ( $C_N$ ) for electrodes prepared by method 1 was only 8.3% for the cycle 1.

The electrodes prepared by method 1 showed significant increase of  $C_N$  during first 500 cycles and further continuous capacitance increase at a reduced rate. The electrodes, prepared by method 2 showed  $C_N$  of 71% for the cycle 1 and  $C_N$  of 99% for the cycle 7. The  $C_N$  showed a maximum of 128% for cycle 151 and then decreased. The rate of the  $C_N$  decrease reduced after 1000 cycles. The CV data provided additional evidence of significantly faster electrode activation in method 2. However, as pointed out above the activation process is also influenced by the scan rate.

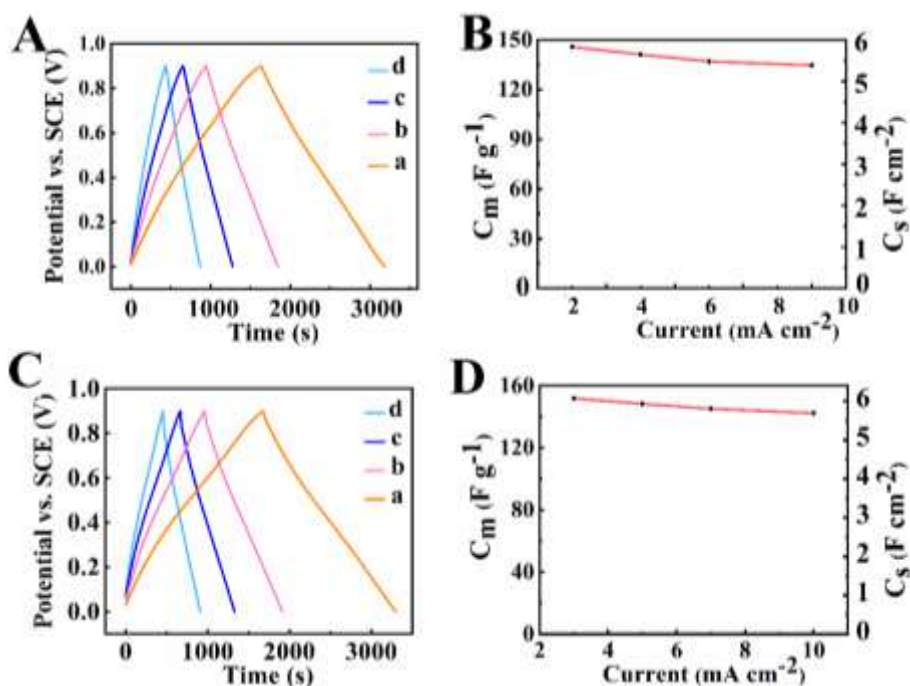


Figure 7- 9 GCD data for electrodes prepared by (A,B) method 1 and (C,D) method 2, (A,C) charge-discharge at current densities of (a) 3, (b) 5, (c) 7 and (d) 10 mA cm<sup>-2</sup>, (B,D) capacitance versus current density dependences.

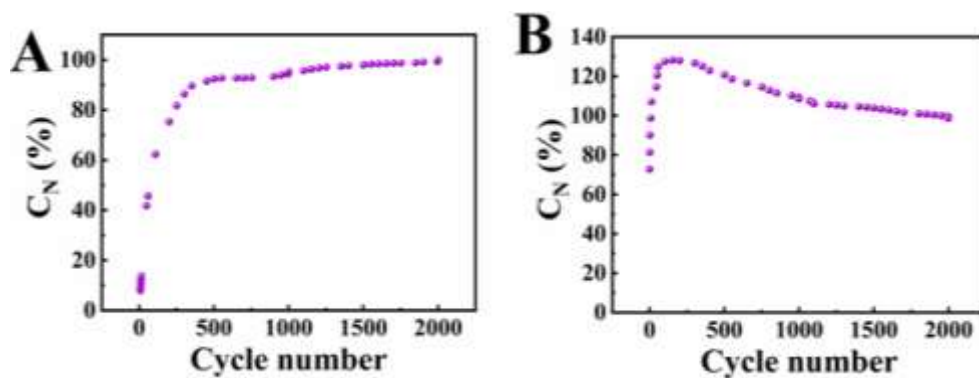


Figure 7- 10 Capacitance (C<sub>N</sub>) normalized by capacitance value for 2000th cycle for electrodes prepared by (A) method 1 and (B) method 2, obtained from CV data at a scan rate of 50 mV s<sup>-1</sup>.

Recent comprehensive review<sup>8</sup> of supercapacitor electrodes with high active mass loadings provided a summary of capacitances for Mn<sub>3</sub>O<sub>4</sub> and MnO<sub>2</sub> based electrodes.

Table 7-1 shows capacitances of Mn<sub>3</sub>O<sub>4</sub> electrodes with high active mass loading

reported in literature.

Table 7- 1 Literature data on capacitances of  $Mn_3O_4$  based electrodes, containing conductive additives, and tested in  $Na_2SO_4$  electrolyte.

Active Mass ( $mg\ cm^{-2}$ )	Areal Capacitance ( $F\ cm^{-2}$ )	Reference
28.4	2.8	21
30.4	2.63	60
33.0	4.2	22
35.0	3.5	20
36.0	3.1	57
36.0	3.79	61
40.1	4.3	62
40.0	6.11	this work

It is seen that the areal capacitance achieved in this investigation by method 2 is higher, than that reported in the literature for  $Mn_3O_4$  based electrodes of high mass. The method used in this investigation is simple and it is based on the use of a natural co-dispersant. Moreover, the capacitance of  $Mn_3O_4$  based electrodes, prepared by method 2 is comparable with capacitance of advanced  $MnO_2$  based electrodes<sup>8</sup>. The time-consuming activation procedure, which limits the applications of  $Mn_3O_4$  based electrodes, can be practically eliminated in method 2. Therefore,  $Mn_3O_4$  electrodes represent a promising alternative to the  $MnO_2$  based electrodes for the development of asymmetric devices for operation in enlarged voltage window in a neutral electrolyte.

It should be noted that the application of capping agents, such as RL for the  $\text{MnO}_2$  synthesis presents difficulties due to the use of permanganate precursors, which react with organic additives. It can be expected that  $\text{Mn}_3\text{O}_4$  electrodes with advanced particle morphologies, prepared using capping agents, can outperform  $\text{MnO}_2$  electrodes. Moreover, in contrast to  $\text{MnO}_2$ , the spinel type  $\text{Mn}_3\text{O}_4$  forms a large variety of spinel solid solutions. Such solutions can enhance capacitance, reduce resistance, and impart other functional properties, such as ferrimagnetic, catalytic and other properties to the  $\text{Mn}_3\text{O}_4$  based electrodes.

## 7.5 Conclusions

For the first time RL were used as a capping agent for the synthesis of  $\text{Mn}_3\text{O}_4$  nanoparticles and as a dispersant for  $\text{Mn}_3\text{O}_4$  and MWCNT. The morphology of the synthesized  $\text{Mn}_3\text{O}_4$  particles and their dispersion were influenced by RL. The chemical structure of RL facilitated their adsorption on materials of different types, such as  $\text{Mn}_3\text{O}_4$  and MWCNT and allowed for their electrostatic dispersion. The ability to co-disperse  $\text{Mn}_3\text{O}_4$  and MWCNT facilitated their efficient mixing at the nanometric scale and allowed for the fabrication of advanced cathode materials for asymmetric supercapacitors. The use of RL as a capping agent resulted in higher capacitance of electrodes prepared by method 2, compared to method 1. The highest capacitance of  $6.11 \text{ F cm}^{-2}$  ( $153 \text{ F g}^{-1}$ ) was obtained from CV data at a scan rate of  $2 \text{ mV s}^{-1}$  and  $6.07 \text{ F cm}^{-2}$  ( $151.9 \text{ F g}^{-1}$ ) at a GCD current density of  $3 \text{ mA cm}^{-2}$  in a potential

window of 0.9 V in a neutral Na<sub>2</sub>SO<sub>4</sub> electrolyte. The problem of time-consuming activation of Mn<sub>3</sub>O<sub>4</sub> based electrodes can be avoided in the method 2. This makes Mn<sub>3</sub>O<sub>4</sub> a promising material for practical applications in supercapacitors. Of particular importance for future research is the ability to form spinel solid solutions, based on Mn<sub>3</sub>O<sub>4</sub>. The development of such solid solutions can result in the development of materials with higher capacitance, reduced resistance and multifunctional materials, combining capacitive, ferrimagnetic, catalytic and other functional properties.

## 7.6 Acknowledgments

SEM investigations were performed at the Canadian Centre for Electron Microscopy.

## 7.7 References

- 1 Jansen, F. *et al.* Low-Temperature Synthesis of Titanium Oxynitride Nanoparticles. *Nanomaterials* **11**, 847 (2021).
- 2 Mourdikoudis, S. *et al.* Heat-Up Colloidal Synthesis of Shape-Controlled Cu-Se-S Nanostructures—Role of Precursor and Surfactant Reactivity and Performance in N<sub>2</sub> Electroreduction. *Nanomaterials* **11**, 3369 (2021).
- 3 Zhitomirsky, I. & Gal-Or, L. Formation of hollow fibers by electrophoretic deposition. *Materials Letters* **38**, 10-17 (1999).  
[https://doi.org:https://doi.org/10.1016/S0167-577X\(98\)00124-4](https://doi.org/https://doi.org/10.1016/S0167-577X(98)00124-4)
- 4 Pranyoto, N. *et al.* Facile Synthesis of Silane-Modified Mixed Metal Oxide as Catalyst in Transesterification Processes. *Nanomaterials* **12**, 245 (2022).
- 5 Wang, Q., Yan, Q., Zhao, Y., Ren, J. & Ai, N. Preparation of Amine-Modified Cu-Mg-Al LDH Composite Photocatalyst. *Nanomaterials* **12**, 127 (2022).
- 6 Parveen, S., Vilela, B., Lagido, O., Rana, S. & Figueiro, R. Development of

- 
- Multi-Scale Carbon Nanofiber and Nanotube-Based Cementitious Composites for Reliable Sensing of Tensile Stresses. *Nanomaterials* **12**, 74 (2022).
- 7 Wu, K., Wang, Y. & Zhitomirsky, I. Electrophoretic deposition of TiO<sub>2</sub> and composite TiO<sub>2</sub>-MnO<sub>2</sub> films using benzoic acid and phenolic molecules as charging additives. *Journal of colloid and interface science* **352**, 371-378 (2010). <https://doi.org/10.1016/j.jcis.2010.08.059>
- 8 Chen, R., Yu, M., Sahu, R. P., Puri, I. K. & Zhitomirsky, I. The Development of Pseudocapacitor Electrodes and Devices with High Active Mass Loading. *Advanced Energy Materials* **10**, 1903848 (2020). <https://doi.org/10.1002/aenm.201903848>
- 9 Hussain, S. *et al.* Robust TiN nanoparticles polysulfide anchor for Li-S storage and diffusion pathways using first principle calculations. *Chemical Engineering Journal* **391**, 123595 (2020).
- 10 Salunkhe, R. R., Kaneti, Y. V. & Yamauchi, Y. Metal-organic framework-derived nanoporous metal oxides toward supercapacitor applications: progress and prospects. *ACS nano* **11**, 5293-5308 (2017).
- 11 He, T., Fu, Y., Meng, X., Yu, X. & Wang, X. A novel strategy for the high performance supercapacitor based on polyacrylonitrile-derived porous nanofibers as electrode and separator in ionic liquid electrolyte. *Electrochimica Acta* **282**, 97-104 (2018).
- 12 Wang, J. *et al.* A flexible Zinc-ion hybrid supercapacitor constructed by porous carbon with controllable structure. *Applied Surface Science* **579**, 152247 (2022).
- 13 Wang, D.-W., Li, F. & Cheng, H.-M. Hierarchical porous nickel oxide and carbon as electrode materials for asymmetric supercapacitor. *Journal of Power Sources* **185**, 1563-1568 (2008).
- 14 You, B., Jiang, J. & Fan, S. Three-dimensional hierarchically porous all-carbon foams for supercapacitor. *ACS applied materials & interfaces* **6**, 15302-15308 (2014).
- 15 Xiong, C. *et al.* The recent progress on three-dimensional porous graphene-based hybrid structure for supercapacitor. *Composites Part B: Engineering* **165**, 10-46 (2019).
- 16 Liu, C., Hou, Y., Li, Y. & Xiao, H. Heteroatom-doped porous carbon microspheres derived from ionic liquid-lignin solution for high performance Supercapacitors. *Journal of Colloid and Interface Science* (2022).
- 17 Zhang, H. *et al.* Oxygen-defect-rich 3D porous cobalt-gallium layered double hydroxide for high-performance supercapacitor application. *Journal of Colloid and Interface Science* **608**, 1837-1845 (2022).
- 18 Yan, Q., Cheng, Y., Wang, R. & Sun, J. Recent advances in 3D porous MXenes: structures, properties and applications. *Journal of Physics D: Applied Physics* (2021).
- 19 Wang, T. *et al.* Three-dimensional, heteroatom-enriched, porous carbon nanofiber flexible paper for free-standing supercapacitor electrode materials

- 
- derived from microalgae oil. *Fuel Processing Technology* **225**, 107055 (2022).
- 20 Poon, R. & Zhitomirsky, I. High areal capacitance of Mn<sub>3</sub>O<sub>4</sub>-carbon nanotube electrodes. *Materials Letters* **215**, 4-7 (2018).
- 21 Ata, M. S., Milne, J. & Zhitomirsky, I. Fabrication of Mn<sub>3</sub>O<sub>4</sub>-carbon nanotube composites with high areal capacitance using cationic and anionic dispersants. *Journal of Colloid and Interface Science* **512**, 758-766 (2018).  
[https://doi.org:https://doi.org/10.1016/j.jcis.2017.10.110](https://doi.org/https://doi.org/10.1016/j.jcis.2017.10.110)
- 22 Milne, J. & Zhitomirsky, I. Application of octanohydroxamic acid for liquid-liquid extraction of manganese oxides and fabrication of supercapacitor electrodes. *Journal of Colloid and Interface Science* **515**, 50-57 (2018).  
<https://doi.org:https://doi.org/10.1016/j.jcis.2018.01.021>
- 23 Rorabeck, K. & Zhitomirsky, I. Salting-out aided dispersive extraction of Mn<sub>3</sub>O<sub>4</sub> nanoparticles and carbon nanotubes for application in supercapacitors. *Colloids and Surfaces A: Physicochemical and Engineering Aspects* **618**, 126451 (2021).
- 24 Nagarajan, N., Cheong, M. & Zhitomirsky, I. Electrochemical capacitance of MnO<sub>x</sub> films. *Materials Chemistry and Physics* **103**, 47-53 (2007).  
<https://doi.org:https://doi.org/10.1016/j.matchemphys.2007.01.005>
- 25 Poon, R., Liang, W. & Zhitomirsky, I. Mn<sub>3</sub>O<sub>4</sub> and (ZnFe) OOH Composites for Supercapacitors with High Active Mass. *Metallurgical and Materials Transactions A* **51**, 855-862 (2020).
- 26 Marchant, R. & Banat, I. M. Microbial biosurfactants: challenges and opportunities for future exploitation. *Trends in biotechnology* **30**, 558-565 (2012).
- 27 Guo, Y.-P. & Hu, Y.-Y. Solubilization of moderately hydrophobic 17 $\alpha$ -ethynylestradiol by mono- and di-rhamnolipid solutions. *Colloids and Surfaces A: Physicochemical and Engineering Aspects* **445**, 12-20 (2014).
- 28 Costa, S. G., Nitschke, M., Lépine, F., Déziel, E. & Contiero, J. Structure, properties and applications of rhamnolipids produced by *Pseudomonas aeruginosa* L2-1 from cassava wastewater. *Process Biochemistry* **45**, 1511-1516 (2010).
- 29 Nitschke, M., Costa, S. G. & Contiero, J. Structure and applications of a rhamnolipid surfactant produced in soybean oil waste. *Applied biochemistry and biotechnology* **160**, 2066-2074 (2010).
- 30 Perfumo, A. *et al.* Rhamnolipids are conserved biosurfactants molecules: implications for their biotechnological potential. *Applied microbiology and biotechnology* **97**, 7297-7306 (2013).
- 31 Lang, S. & Wullbrandt, D. Rhamnose lipids—biosynthesis, microbial production and application potential. *Applied microbiology and biotechnology* **51**, 22-32 (1999).
- 32 Liu, H., Shao, B., Long, X., Yao, Y. & Meng, Q. Foliar penetration enhanced by biosurfactant rhamnolipid. *Colloids and Surfaces B: Biointerfaces* **145**,

- 
- 548-554 (2016).
- 33 Chen, J. *et al.* Potential applications of biosurfactant rhamnolipids in agriculture and biomedicine. *Applied microbiology and biotechnology* **101**, 8309-8319 (2017).
- 34 Vatsa, P., Sanchez, L., Clement, C., Baillieul, F. & Dorey, S. Rhamnolipid biosurfactants as new players in animal and plant defense against microbes. *International journal of molecular sciences* **11**, 5095-5108 (2010).
- 35 Tripathy, S. S. & Raichur, A. M. Dispersibility of barium titanate suspension in the presence of polyelectrolytes: a review. *Journal of Dispersion Science and Technology* **29**, 230-239 (2008).
- 36 Raichur, A. M. Dispersion of colloidal alumina using a rhamnolipid biosurfactant. *Journal of dispersion science and technology* **28**, 1272-1277 (2007).
- 37 Quevedo, I. R., Olsson, A. L. & Tufenkji, N. Deposition kinetics of quantum dots and polystyrene latex nanoparticles onto alumina: Role of water chemistry and particle coating. *Environmental science & technology* **47**, 2212-2220 (2013).
- 38 Biswas, M. & Raichur, A. M. Electrokinetic and rheological properties of nano zirconia in the presence of rhamnolipid biosurfactant. *Journal of the American Ceramic Society* **91**, 3197-3201 (2008).
- 39 Szymanska, A. & Sadowski, Z. Effects of biosurfactants on surface properties of hematite. *Adsorption* **16**, 233-239 (2010).
- 40 Narayanan, J., Ramji, R., Sahu, H. & Gautam, P. Synthesis, stabilisation and characterisation of rhamnolipid-capped ZnS nanoparticles in aqueous medium. *IET nanobiotechnology* **4**, 29-34 (2010).
- 41 Palanisamy, P. & Raichur, A. M. Synthesis of spherical NiO nanoparticles through a novel biosurfactant mediated emulsion technique. *Materials Science and Engineering: C* **29**, 199-204 (2009).
- 42 Salazar-Bryam, A. M. *et al.* Silver nanoparticles stabilized by rhamnolipids: Effect of pH. *Colloids and Surfaces B: Biointerfaces* **205**, 111883 (2021).
- 43 Zhu, J., Wu, Q. & Li, J. Review And Prospect of Mn<sub>3</sub>O<sub>4</sub>-Based Composite Materials For Supercapacitor Electrodes. *ChemistrySelect* **5**, 10407-10423 (2020).
- 44 Van der Biest, O. O. & Vandeperre, L. J. Electrophoretic deposition of materials. *Annual Review of Materials Science* **29**, 327-352 (1999).
- 45 Su, Y. & Zhitomirsky, I. Electrophoretic deposition of graphene, carbon nanotubes and composite films using methyl violet dye as a dispersing agent. *Colloids and Surfaces A: Physicochemical and Engineering Aspects* **436**, 97-103 (2013). [https://doi.org:https://doi.org/10.1016/j.colsurfa.2013.06.024](https://doi.org/10.1016/j.colsurfa.2013.06.024)
- 46 Zhitomirsky, I. & Petric, A. Electrophoretic deposition of electrolyte materials for solid oxide fuel cells. *Journal of materials science* **39**, 825-831 (2004).
- 47 Zhitomirsky, I. & Petric, A. Electrophoretic deposition of ceramic materials for fuel cell applications. *Journal of the European Ceramic Society* **20**, 2055-

- 
- 2061 (2000).
- 48 Moon, J., Awano, M., Takagi, H. & Fujishiro, Y. Synthesis of nanocrystalline manganese oxide powders: Influence of hydrogen peroxide on particle characteristics. *Journal of materials research* **14**, 4594-4601 (1999).
- 49 Sambandam, B. *et al.* A sponge network-shaped Mn<sub>3</sub>O<sub>4</sub>/C anode derived from a simple, one-pot metal organic framework-combustion technique for improved lithium ion storage. *Inorganic Chemistry Frontiers* **3**, 1609-1615 (2016).
- 50 Raj, A. M. E. *et al.* XRD and XPS characterization of mixed valence Mn<sub>3</sub>O<sub>4</sub> hausmannite thin films prepared by chemical spray pyrolysis technique. *Applied Surface Science* **256**, 2920-2926 (2010).
- 51 Tholkappiyan, R., Naveen, A. N., Vishista, K. & Hamed, F. Investigation on the electrochemical performance of hausmannite Mn<sub>3</sub>O<sub>4</sub> nanoparticles by ultrasonic irradiation assisted co-precipitation method for supercapacitor electrodes. *Journal of Taibah University for Science* **12**, 669-677 (2018).
- 52 Zeng, F. *et al.* Facile construction of Mn<sub>3</sub>O<sub>4</sub>-MnO<sub>2</sub> hetero-nanorods/graphene nanocomposite for highly sensitive electrochemical detection of hydrogen peroxide. *Electrochimica Acta* **196**, 587-596 (2016).
- 53 Wallar, C., Poon, R. & Zhitomirsky, I. High Areal Capacitance of V<sub>2</sub>O<sub>3</sub>-Carbon Nanotube Electrodes. *Journal of The Electrochemical Society* **164**, A3620-A3627 (2017).
- 54 Vadi, M. & Ghaseminejhad, E. Comparative study of isotherms adsorption of Oleic acid by activated carbon and multi-wall carbon nanotube. *Oriental Journal of Chemistry* **27**, 973 (2011).
- 55 Stacey, S. P. *et al.* Root uptake of lipophilic zinc-rhamnolipid complexes. *Journal of agricultural and food chemistry* **56**, 2112-2117 (2008).
- 56 Hogan, D. E., Curry, J. E., Pemberton, J. E. & Maier, R. M. Rhamnolipid biosurfactant complexation of rare earth elements. *Journal of hazardous materials* **340**, 171-178 (2017).
- 57 Milne, J., Silva, R. M. & Zhitomirsky, I. Surface modification and dispersion of ceramic particles using liquid-liquid extraction method for application in supercapacitor electrodes. *Journal of the European Ceramic Society* **39**, 3450-3455 (2019).
- 58 Shi, K. & Zhitomirsky, I. Fabrication of Polypyrrole-Coated Carbon Nanotubes Using Oxidant-Surfactant Nanocrystals for Supercapacitor Electrodes with High Mass Loading and Enhanced Performance. *ACS Applied Materials & Interfaces* **5**, 13161-13170 (2013).  
<https://doi.org/10.1021/am404159b>
- 59 Rorabeck, K. & Zhitomirsky, I. Dispersant Molecules with Functional Catechol Groups for Supercapacitor Fabrication. *Molecules* **26**, 1709 (2021).
- 60 Poon, R., Zhao, X., Ata, M. S., Clifford, A. & Zhitomirsky, I. Phase transfer of oxide particles for application in thin films and supercapacitors. *Ceramics International* **43**, 8314-8320 (2017).

<https://doi.org/https://doi.org/10.1016/j.ceramint.2017.03.167>

- 61 Poon, R. & Zhitomirsky, I. Application of Cyrene as a solvent and dispersing agent for fabrication of Mn<sub>3</sub>O<sub>4</sub>-carbon nanotube supercapacitor electrodes. *Colloid and Interface Science Communications* **34**, 100226 (2020).
- 62 Rorabeck, K. & Zhitomirsky, I. Application of Octanohydroxamic Acid for Salting out Liquid–Liquid Extraction of Materials for Energy Storage in Supercapacitors. *Molecules* **26**, 296 (2021).

## 7.8 Supplementary Materials:

Testing results for Mn<sub>3</sub>O<sub>4</sub> electrodes prepared by method 2 with mass ratio

Mn<sub>3</sub>O<sub>4</sub>:MWCNT:RL = 4:1:1

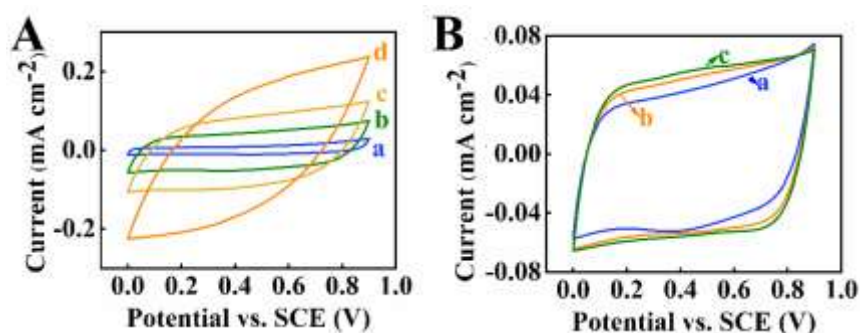


Figure 7-S 1 (A) CVs at scan rates of (a) 2, (b) 10, (c) 20 and (d) 50 mV s<sup>-1</sup> for TP 1 and (B) CVs at a scan rate of 10 mV s<sup>-1</sup> for (a) TP 1, (b) TP 2, and (c) TP 3 for electrode prepared by method 2.

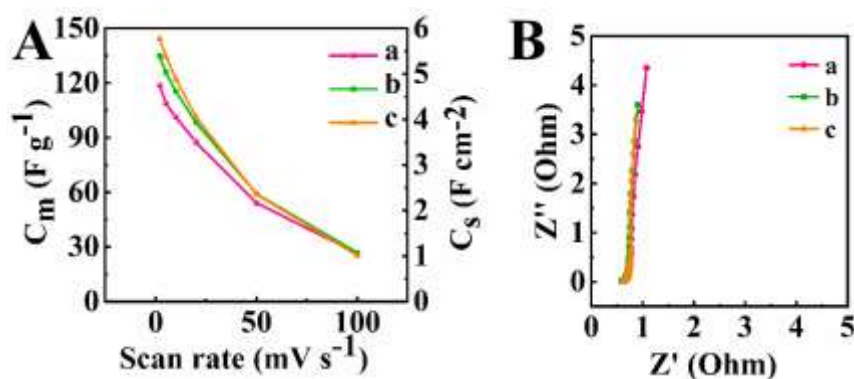


Figure 7-S 2 (A) capacitance versus scan rate and (B) impedance data presented in a Nyquist plot for (a) TP 1, (b) TP 2, and (c) TP 3 for electrode prepared by method 2.

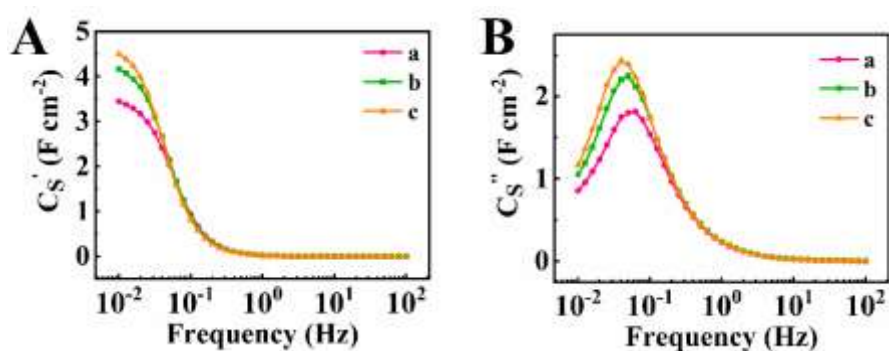


Figure 7-S 3 (A) real and (B) imaginary components of complex capacitance for (a) TP 1, (b) TP 2, (c) TP 3 for electrode prepared by method 2.

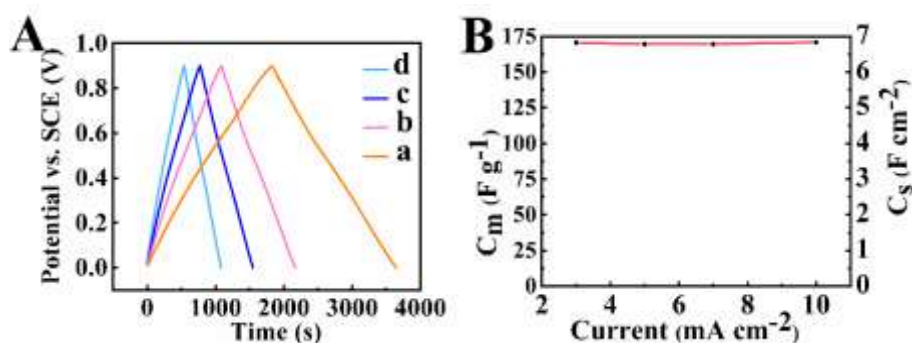


Figure 7-S 4 GCD data for electrodes prepared by method 2, (A) charge-discharge at current densities of (a) 3, (b) 5, (c) 7 and (d) 10 mA cm<sup>-2</sup>, (B) capacitance versus current density dependence.

Capacitances, calculated from CV data at a scan rate of 2 mV s<sup>-1</sup> are 4.75 F cm<sup>-2</sup> (118.8 F g<sup>-1</sup>), 5.39 F cm<sup>-2</sup> (134.8 F g<sup>-1</sup>) and 5.77 F cm<sup>-2</sup> (144.3 F g<sup>-1</sup>) for TP 1, TP 2 and TP 3, respectively.

Capacitances, calculated from EIS data at 10 mHz are 4.05 F cm<sup>-2</sup> (101.3 F g<sup>-1</sup>), 4.62 F cm<sup>-2</sup> (115.5 F g<sup>-1</sup>), 4.90 F cm<sup>-2</sup> (122.3 F g<sup>-1</sup>) for TP 1, TP2 and TP 3, respectively.

Capacitance calculated from the GCD data after TP 5 at a current density of 3 mA cm<sup>-2</sup> is 6.82 F cm<sup>-2</sup> (170.5 F g<sup>-1</sup>).

# **Chapter 8 Facile Route for Fabrication of Ferrimagnetic Mn<sub>3</sub>O<sub>4</sub> Spinel Material for Supercapacitors with Enhanced Capacitance**

Wenjuan Yang, Mohamed Nawwar and Igor Zhitomirsky \*

Department of Materials Science and Engineering, McMaster University,

Hamilton, ON L8S4L7, Canada;

yangw48@mcmaster.ca (W.Y.);

nawwarm@mcmaster.ca (M.N.)

\* Correspondence: zhitom@mcmaster.ca (I.Z.)

Copyright 2022, reproduced with permission from the MDPI.

## 8.1 Abstract

The purpose of this investigation was the development of a new colloidal route for the fabrication of  $\text{Mn}_3\text{O}_4$  electrodes for supercapacitors with enhanced charge storage performance.  $\text{Mn}_3\text{O}_4$ -carbon nanotube electrodes were fabricated with record-high capacitances of  $6.67 \text{ F cm}^{-2}$  obtained from cyclic voltammetry tests at a scan rate of  $2 \text{ mV s}^{-1}$  and  $7.55 \text{ F cm}^{-2}$  obtained from the galvanostatic charge–discharge tests at a current density of  $3 \text{ mA cm}^{-2}$  in  $0.5 \text{ M Na}_2\text{SO}_4$  electrolyte in a potential window of  $0.9 \text{ V}$ . The approach involves the use of murexide as a capping agent for the synthesis of  $\text{Mn}_3\text{O}_4$  and a co-dispersant for  $\text{Mn}_3\text{O}_4$  and carbon nanotubes. Good electrochemical performance of the electrode material was achieved at a high active mass loading of  $40 \text{ mg cm}^{-2}$  and was linked to a reduced agglomeration of  $\text{Mn}_3\text{O}_4$  nanoparticles and efficient co-dispersion of  $\text{Mn}_3\text{O}_4$  with carbon nanotubes. The mechanisms of murexide adsorption on  $\text{Mn}_3\text{O}_4$  and carbon nanotube are discussed. With the proposed method, the time-consuming electrode activation procedure for  $\text{Mn}_3\text{O}_4$  electrodes can be avoided. The approach developed in this investigation paves the way for the fabrication of advanced cathodes for asymmetric supercapacitors and multifunctional devices, combining capacitive, magnetic, and other functional properties.

## 8.2 Introduction

In recent years, advanced materials have emerged for energy storage in

supercapacitors, including metal oxides, conductive polymers, graphene, and other carbon materials, MXenes, complex hydroxides, and composites<sup>1-7</sup>. Oxide materials such as  $\text{MnO}_2$ ,  $\text{Fe}_3\text{O}_4$ ,  $\text{BiMn}_2\text{O}_5$ , and  $\text{V}_2\text{O}_3$  are increasingly being explored due to their large potential windows and high capacitance<sup>6</sup>. Spinel-type oxide materials have generated significant interest due to their promising performance and beneficial materials science aspects<sup>8-11</sup>. Atoms of transition metal elements with different valence states were incorporated into the spinel structure and exhibited redox behavior, imparting advanced pseudocapacitive properties to the spinel oxides<sup>8,12-14</sup>. A large pool of spinel oxides provides a basis for the fabrication of spinel solid solutions with advanced properties<sup>15</sup>. Solid solutions allow a significant improvement in functional properties of materials by a controlled variation in their composition. Solid solutions are widely utilized in energy storage and other fields and often outperform individual spinel oxides for various applications<sup>16-19</sup>. Spinel materials are of particular interest because they exhibit advanced magnetic, catalytic, and other properties and can be used for the fabrication of multifunctional materials<sup>14,20-24</sup>.  $\text{Mn}_3\text{O}_4$  is a spinel-type ferrimagnetic material that is widely used for the fabrication of advanced spinel solid solutions with enhanced magnetization, catalytic, and energy storage properties in batteries<sup>25-27</sup>. However, the potential of  $\text{Mn}_3\text{O}_4$  for supercapacitor technology is only beginning to be recognized<sup>28,29</sup>.  $\text{Mn}_3\text{O}_4$  can potentially outperform  $\text{MnO}_2$ , which is currently one of the best materials for cathodes of asymmetric supercapacitors.

---

The use of  $\text{Mn}_3\text{O}_4$  offers many advantages for supercapacitor technology compared to  $\text{MnO}_2$ . The modification of composition and properties of  $\text{MnO}_2$  presents difficulties because of the limited possibility of this oxide to form solid solutions. The low electrical conductivity of  $\text{MnO}_2$  is detrimental for applications of this material in supercapacitors. In contrast,  $\text{Mn}_3\text{O}_4$  can form solid solutions with enhanced conductivity and other functional properties. The fabrication of  $\text{MnO}_2$  nanoparticles of controlled size and modification of their morphology generates problems attributed to the use of permanganate precursors for the  $\text{MnO}_2$  synthesis. Such precursors react with dispersants, which are critically important for control of particle size, shape, and prevention of agglomeration during synthesis. In contrast,  $\text{Mn}_3\text{O}_4$  can be synthesized from aqueous solutions of  $\text{Mn}^{2+}$  salts in the presence of dispersants.

Previous investigations<sup>6</sup> have showed that the capacitance of  $\text{Mn}_3\text{O}_4$  is significantly lower than that of  $\text{MnO}_2$ . However, a significant increase in the capacitance of  $\text{Mn}_3\text{O}_4$  was observed during cycling<sup>30-33</sup>. Numerous XPS studies revealed oxidation of  $\text{Mn}^{2+}$  and  $\text{Mn}^{3+}$  ions on the  $\text{Mn}_3\text{O}_4$  particle surface during cycling and linked this process to the capacitance increase<sup>31,33-35</sup>. The application of  $\text{Mn}_3\text{O}_4$  for supercapacitors requires the use of time-consuming activation procedures<sup>31,33,35</sup>. The problems related to applications of  $\text{Mn}_3\text{O}_4$  in cathodes of supercapacitors can be addressed using dispersing agents for the synthesis of nanoparticles.

This investigation was motivated by the strong potential of  $\text{Mn}_3\text{O}_4$  spinel material for the fabrication of supercapacitors and multifunctional devices. The goal of this

---

investigation was the fabrication of  $\text{Mn}_3\text{O}_4$  cathodes for supercapacitors with an enhanced capacitance using murexide as a new capping and dispersion agent. An additional goal was the elimination of the time-consuming activation procedure, which limits practical applications of  $\text{Mn}_3\text{O}_4$  for supercapacitors. For the first time, we demonstrated that murexide can be used as a dispersant for inorganic nanoparticles and carbon nanotubes. The approach developed in this investigation involved the use of advanced techniques for a wet chemical synthesis and colloidal processing of  $\text{Mn}_3\text{O}_4$ -carbon nanotube electrodes with high capacitance. We describe the advantages of the murexide dispersant, which allowed for strong tridentate bonding to the particle surface and facilitated electrostatic dispersion. Building on this insight, new chelating dispersants can be used for advanced colloidal nanofabrication technologies. The use of murexide offered benefits for the fabrication of  $\text{Mn}_3\text{O}_4$ -carbon nanotube electrodes because murexide allowed co-dispersion of  $\text{Mn}_3\text{O}_4$  and carbon nanotubes, which served as conductive additives. The approach of this investigation resulted in an enhanced electrode performance at a high active mass loading, which is critical for practical applications. In this approach, a record high capacitance of  $\text{Mn}_3\text{O}_4$  electrodes was achieved, and the problems related to capacitance variation during initial cycling were avoided. This eliminated the need for the preparation of  $\text{Mn}_3\text{O}_4$  based electrodes in time-consuming activation procedures. The results of this investigation open the door for the application of  $\text{Mn}_3\text{O}_4$  and its solid solutions for energy storage in advanced supercapacitors and multifunctional energy storage devices.

---

## 8.3 Materials and Methods

### 8.3.1 Raw Materials

Murexide,  $\text{Mn}(\text{NO}_3)_2 \cdot 4\text{H}_2\text{O}$ ,  $\text{Na}_2\text{SO}_4$ ,  $\text{NaOH}$ , ethanol, poly(vinyl butyral) (PVB, MilliporeSigma, Oakville, ON, Canada) and multiwalled carbon nanotubes (MWCNTs, Bayer, Leverkusen, Germany) were used as starting materials.

### 8.3.2 Synthesis of $\text{Mn}_3\text{O}_4$ and Electrode Fabrication

$\text{Mn}_3\text{O}_4$  nanoparticles were prepared by a modified chemical precipitation method<sup>29</sup> and mixed with MWCNTs. A solution of 0.33 g of  $\text{Mn}(\text{NO}_3)_2 \cdot 4\text{H}_2\text{O}$  in DI water was prepared, and then the pH of the solution was increased to pH = 10 with aqueous  $\text{NaOH}$  for the  $\text{Mn}_3\text{O}_4$  synthesis. In method 1, the synthesized  $\text{Mn}_3\text{O}_4$  was mixed with MWCNTs, and murexide was added as a co-dispersant. In method 2, murexide was added to  $\text{Mn}(\text{NO}_3)_2$  solution in DI water before pH adjustment as a capping agent for synthesis, and MWCNTs were added after the synthesis. In both methods,  $\text{Mn}_3\text{O}_4$  and MWCNTs were co-dispersed using murexide. The mass ratio of  $\text{Mn}_3\text{O}_4$ :CNT:murexide was 4:1:1. The obtained mixtures of  $\text{Mn}_3\text{O}_4$  with MWCNTs, containing murexide, were ultrasonicated to achieve improved dispersion and mixing, washed, and dried. Obtained powders were used for the fabrication of electrodes using slurries of  $\text{Mn}_3\text{O}_4$  and MWCNTs in ethanol with a PVB binder. The binder content was 3% of the total mass of  $\text{Mn}_3\text{O}_4$  and MWCNTs. The slurries were used for

---

impregnation of commercial Ni foam (Vale, Canada) current collectors. The total mass of impregnated material after drying was  $40 \text{ mg cm}^{-2}$ .

### 8.3.3 Characterization Techniques

Electron microscopy studies were performed using a JEOL SEM (scanning electron microscope, JEOL, JSM-7000F). X-ray diffraction (XRD) analysis (diffractometer Bruker D8, UK) was performed using Cu-K $\alpha$  radiation at the rate of 0.01 degrees per second. Electrochemical studies were performed in an aqueous 0.5 M Na<sub>2</sub>SO<sub>4</sub> electrolyte using PARSTAT 2273 (Ametek) potentiostat for cyclic voltammetry (CV) and electrochemical impedance spectroscopy (EIS), and BioLogic VMP 300 potentiostat for the galvanostatic charge-discharge (GCD) investigations. Testing was performed using a 3-electrode electrochemical cell containing a working electrode (impregnated Ni foam), counter-electrode (Pt mesh), and reference electrode (SCE, saturated calomel electrode). The capacitive properties of electrode material were presented in gravimetric ( $C_m, \text{F g}^{-1}$ ) and areal ( $C_s, \text{F cm}^{-2}$ ) capacitance forms. Capacitances  $C_m$  and  $C_s$  were calculated from the CV, EIS, and GCD data as described in reference <sup>6</sup>. The capacitances calculated from the CV and GCD data represented the integral capacitances measured in a voltage window of 0-0.9 V versus SCE. The capacitances calculated from the EIS data represented differential capacitances measured at an open circuit potential at a voltage amplitude of 5 mV. CV

testing procedures (TP) involved obtaining CV at scan rates of 2, 5, 10, 20, 50, and 100  $\text{mV s}^{-1}$ . EIS measurements were performed after each TP. GCD measurements were performed after the last TP.

## 8.4 Results and Discussion

Figure 8-1 shows X-ray diffraction patterns of  $\text{Mn}_3\text{O}_4$  prepared by methods 1 and 2.

The diffraction patterns show peaks of  $\text{Mn}_3\text{O}_4$  and MWCNTs.

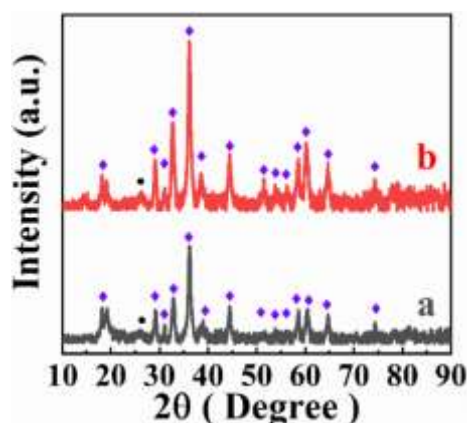


Figure 8- 1 X-ray diffraction patterns of  $\text{Mn}_3\text{O}_4$  and MWCNT mixtures prepared by (a) method 1 and (b) method 2, ( $\blacklozenge$ - $\text{Mn}_3\text{O}_4$ ,  $\bullet$ -MWCNT).

The approach developed in this investigation was based on colloidal processing, which offers benefits for the fabrication of materials with advanced microstructures<sup>36-39</sup>. In colloidal processing methods, advanced capping agents and dispersants are necessary for the synthesis of nanomaterials and the fabrication of advanced composites. Capping agents and dispersants must be adsorbed on the particles. A non-adsorbed ionic species can stimulate particle agglomeration. Previous investigations<sup>40</sup>

highlighted the benefits of chelating dispersants, which are strongly adsorbed on inorganic particles by bidentate bonding to the surface metal atoms. Figure 8-2A shows a chemical structure of murexide used in this investigation as a capping and dispersing agent.

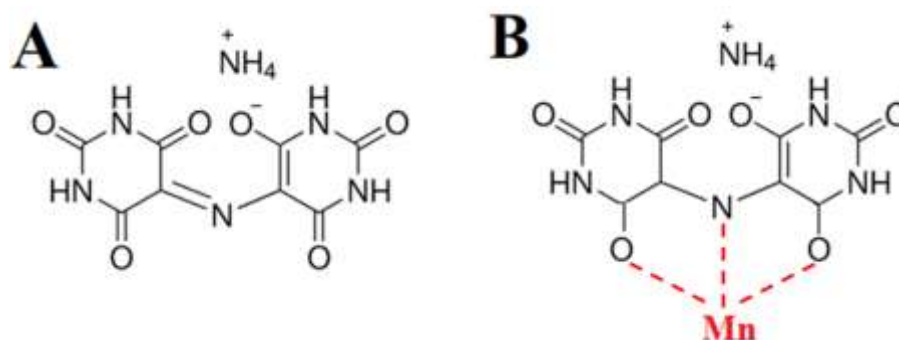


Figure 8- 2 (A) Chemical structure of murexide, (B) adsorption of murexide on particle, involving tridentate chelation of surface Mn atoms.

Murexide exhibits chelating properties<sup>41,42</sup>, which are related to its strong tridentate bonding to different metal atoms. Dissociated murexide acquires a negative charge in solutions (Figure 8-2). It was hypothesized that murexide was adsorbed on the  $Mn_3O_4$  surface by creating a tridentate bonding to Mn atoms on the surface (Figure 8-2B). The adsorption of murexide on MWCNTs involved interactions<sup>43</sup> of two barbiturate rings of murexide with carbon rings of MWCNTs. The adsorbed murexide imparted a negative charge to the  $Mn_3O_4$  particles and MWCNTs for their electrostatic co-dispersion. It should be noted that many commercial dispersants allow for the dispersion of only inorganic particles or carbon materials. In contrast, murexide allows for the dispersion of both  $Mn_3O_4$  and MWCNTs, facilitating their efficient co-

dispersion and mixing.

In this investigation, MWCNTs were used as conductive additives. Previous investigations of as-received MWCNT powders showed that MWCNTs formed large agglomerates with a typical size of 0.5  $\mu\text{m}$ <sup>44</sup>. Therefore, efficient dispersion of MWCNTs was critically important for the fabrication of nanocomposites. Figure 8-3 shows SEM images of the electrodes prepared by Methods 1 and 2. The SEM images at low magnification show the porous structure of electrodes (Figure 8-3A, B). The images at higher magnification (Figure 8-3C, D) show that the size of primary  $\text{Mn}_3\text{O}_4$  particles was below 100 nm. MWCNTs were distributed between the  $\text{Mn}_3\text{O}_4$  particles, which was beneficial for the enhancement of electronic conductivity of the composite. The electrodes prepared by Methods 1 and 2 were tested in 0.5 M  $\text{Na}_2\text{SO}_4$  electrolyte. Figure 8-4 shows CVs for the electrodes prepared by Method 1 for different TPs. The CVs obtained at low sweep rates were nearly rectangular. The comparison of the CVs obtained at the same sweep rates for different TPs showed that the area of CV increased with increasing TP number.

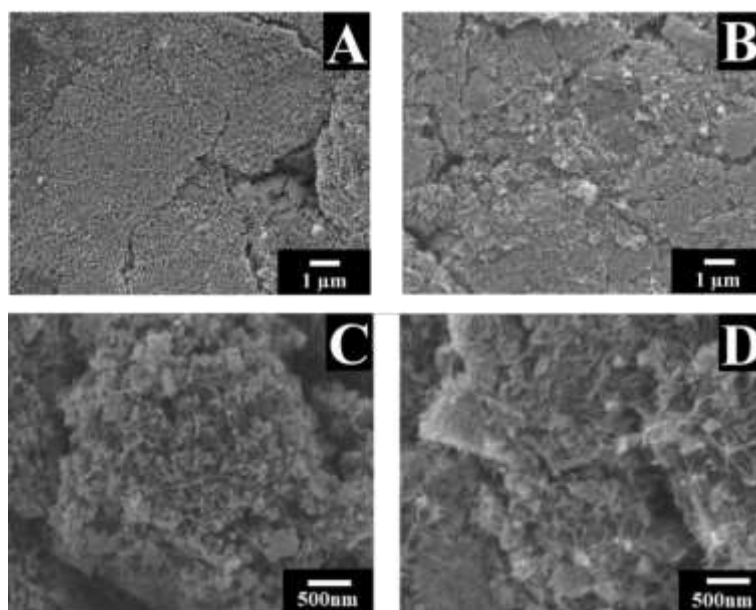


Figure 8- 3 SEM images at different magnifications for electrodes prepared by (A, C) method 1 and (B,D) method 2.

This is in agreement with previous investigations, which showed a capacitance increase during cycling<sup>30-33</sup>. Several previous XPS investigations showed an oxidation of  $Mn^{2+}$  and  $Mn^{3+}$  ions with an increased content of  $Mn^{4+}$  ions on the  $Mn_3O_4$  particle surface during cycling and linked this process to the capacitance increase<sup>31,33-35</sup>. Moreover, previous investigations showed that the application of  $Mn_3O_4$  for supercapacitors requires the use of time-consuming activation procedures<sup>31,33,35</sup>. Such procedures are detrimental for practical applications of  $Mn_3O_4$  in supercapacitors.

It should be noted that we investigated electrodes with high active mass loadings of  $40 \text{ mg cm}^{-2}$ . In this investigation, commercial Ni foam current collectors were used, which were designed for batteries and supercapacitors, based on inorganic active

---

materials with a typical electrode mass of 30–50 mg cm<sup>-2</sup>. High active mass loading is important for practical applications for reducing the contribution of current collectors and other passive components to the total electrode mass. An active mass of about 10 mg cm<sup>-2</sup> is required for commercial activated carbon electrodes<sup>6,45</sup>.

Inorganic materials, such as Mn<sub>3</sub>O<sub>4</sub>, have a significantly higher density than the density of activated carbon. Therefore, larger mass loadings can be achieved at the same electrode volume.

The higher gravimetric capacitance of Mn<sub>3</sub>O<sub>4</sub> and the higher active mass can potentially result in significantly higher capacitances of Mn<sub>3</sub>O<sub>4</sub>-based electrodes, compared to activated carbon electrodes of the same volume. However, it is challenging to achieve good electrode performance at a high active mass. It is known that gravimetric capacitance drops with active mass increase<sup>6</sup>. Moreover, the use of electrodes with high active mass loading aggravated the problem of Mn<sub>3</sub>O<sub>4</sub> electrode activation, compared to the thin-film Mn<sub>3</sub>O<sub>4</sub> electrodes. This is attributed to better electrolyte access to thin film electrodes, compared to the bulk electrodes with high active mass.

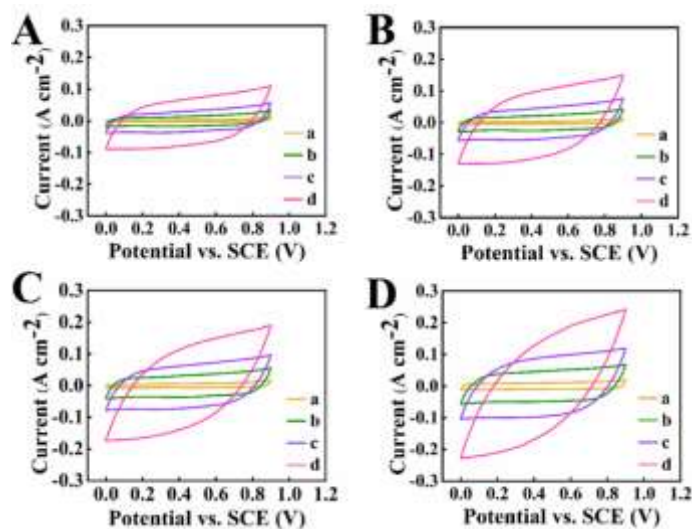


Figure 8- 4 CVs for electrodes, prepared by method 1 for (A) TP 1, (B) TP 2, (C) TP 3 and (D) TP 5 at scan rates of (a) 2, (b) 10, (c) 20 and (d) 50  $\text{mV s}^{-1}$ .

Figure 8-5A shows  $C_m$  and  $C_s$ , derived from the CV data for different TPs. The dependence of capacitance on scan rate for TP 1 (Figure 8-5A(a)) shows a maximum at  $20 \text{ mV s}^{-1}$ . It is suggested that the electrode activation during cycling at lower scan rates resulted in the capacitance increase.

However, the capacitance decreased at scan rates of 50 and  $100 \text{ mV s}^{-1}$ , resulting in a maximum (Figure 8-5A(a)). The capacitance increased with increasing TP number from 1 to 5 (Figure 8-5). The highest integral capacitance of  $4.87 \text{ F cm}^{-2}$  ( $121.8 \text{ F g}^{-1}$ ) was achieved at  $2 \text{ mV s}^{-1}$  for TP 5. The components of the differential complex capacitance, obtained from the EIS data, showed significant variations for TP 1–5 (Figure 8-5B, C). The frequency dependences of the capacitance components showed relaxation-type<sup>46</sup> dispersions. The real part of the differential complex capacitance increased with increasing TP number in agreement with the CV data. The GCD data

obtained after TP 5 showed linear charge–discharge behavior, indicating good capacitive performance (Figure 8-5D). The integral capacitance of  $6.77 \text{ F cm}^{-2}$  ( $169.3 \text{ F g}^{-1}$ ) was obtained at a current density of  $3 \text{ mA cm}^{-2}$ . The capacitance slightly decreased with increasing current density and showed good capacitance retention.

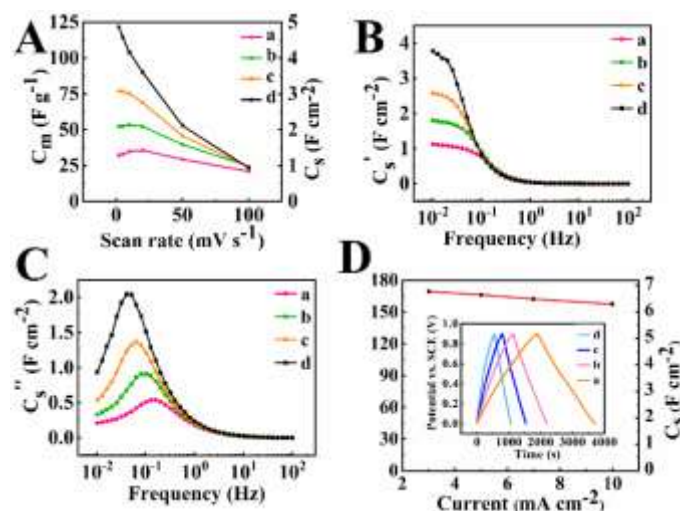


Figure 8- 5 Integral capacitances calculated from the CV data, (B) real and (C) imaginary components of differential complex capacitances versus frequency, calculated from the EIS data for (a) TP 1, (b) TP 2, (c) TP 3, and (d) TP 5; (D) integral capacitance obtained from the GCD data after TP 5 versus current density; inset shows corresponding charge discharge curves for current densities of (a) 3, (b) 5, (c) 7, and (d)  $10 \text{ mA cm}^{-2}$ .

Testing of the electrodes prepared by method 2 showed reduced capacitance variations during cycling, and significantly higher capacitances were obtained compared to method 1. Figure 8-6 compares CV data for TP 1 and TP 3. The areas of CVs increased from TP 1 to TP 3 only at low scan rates. At scan rates of  $20 \text{ mV s}^{-1}$  and higher, the CV areas were nearly similar for TP1 and TP3. The CV areas for TP 4

and TP 5 were practically the same as for TP 3 for all scan rates.

Figure 8-7A shows integral capacitances, calculated from the CV data for the electrode prepared by Method 2. The capacitance for TP 1 (Figure 8-7A(a)) showed a maximum for a scan rate of  $10 \text{ mV s}^{-1}$ . A similar maximum was observed for TP 1 for the electrode prepared by method 1 (Figure 8-5A(a)). As pointed out above, such a maximum resulted from the activation of the electrode by cycling at low scan rates.

Therefore, some activation occurred for the electrodes prepared by Method 2.

However, it should be noted that the capacitance obtained for the first cycle at  $2 \text{ mV s}^{-1}$  for TP 1 for electrode prepared by Method 2 was  $5.46 \text{ F cm}^{-2}$  ( $136.4 \text{ F g}^{-1}$ ), which is higher than the capacitance of  $4.87 \text{ F cm}^{-2}$  ( $121.8 \text{ F g}^{-1}$ ) at  $2 \text{ mV s}^{-1}$  for TP 5 for the electrode prepared by Method 1. The highest capacitance of  $6.67 \text{ F cm}^{-2}$  ( $166.7 \text{ F g}^{-1}$ ) was achieved at  $2 \text{ mV s}^{-1}$  for TP 3 for the electrode prepared by Method 2. Turning again to the data presented in Figure 8-7A, it is seen that very small variations in the capacitance were observed for TP1 and TP3 for scan rates of  $20\text{--}100 \text{ mV s}^{-1}$ . The capacitance measurements at different scan rates for TPs 3-5 did not show significant variations in capacitances.

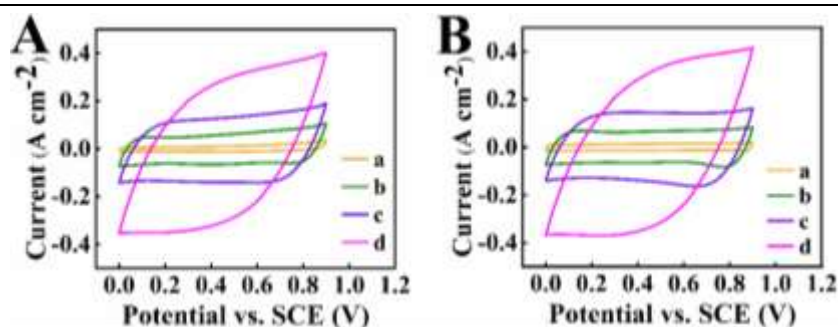


Figure 8- 6 CVs for electrode prepared by Method 2 (A) for TP 1 and (B) TP 3 for scan rates of (a) 2, (b) 10, (c) 20, and (d) 50  $\text{mV s}^{-1}$ .

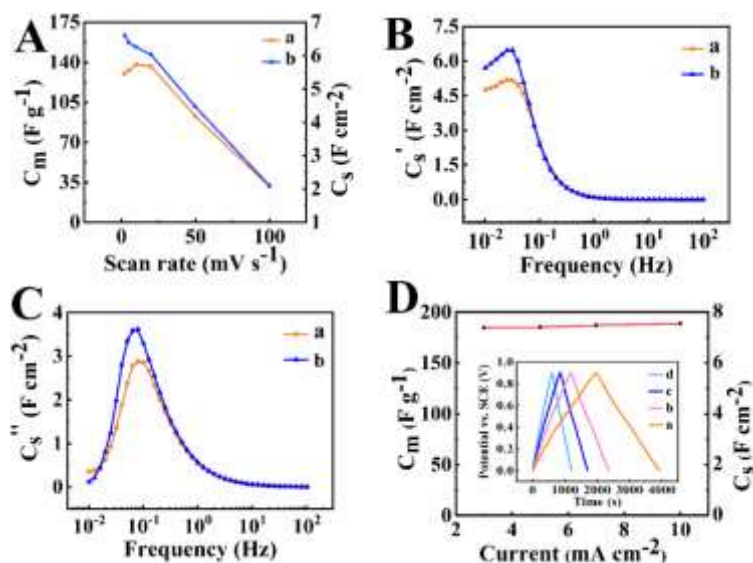


Figure 8- 7 (A) Integral capacitances calculated from the CV data, (B) real and (C) imaginary components of differential complex capacitances versus frequency, calculated from the EIS data for (a) TP 1, (b) TP 3; (D) integral capacitance obtained from the GCD data after TP 5 versus current density; inset shows corresponding charge discharge curves for current densities of (a) 3, (b) 5, (c) 7, and (d) 10  $\text{mA cm}^{-2}$ .

The results of capacitance measurements from the EIS data (Figure 8-7B, C) correlated with the results obtained by CV. The real part of capacitance for TP 1 at 10 mHz for the electrode prepared by Method 2 was  $4.75 \text{ F cm}^{-2}$  ( $118.8 \text{ F g}^{-1}$ ), which is higher than the capacitance of  $3.77 \text{ F cm}^{-2}$  ( $94.25 \text{ F g}^{-1}$ ) for the electrode prepared by

---

Method 1 at the same frequency and TP 5. The analysis of EIS data for TP 1 and TP 3 revealed changes in both real and imaginary capacitance, which indicates that some activation process occurs for the electrodes prepared by Method 2. The highest real part of the capacitance obtained at 10 mHz for TP 3 for the electrode prepared by Method 2 was found to be  $5.70 \text{ F cm}^{-2}$  ( $142.5 \text{ F g}^{-1}$ ). EIS capacitance data did not show significant variation for TP 4 and TP 5 compared to TP 3.

The results of CV and EIS data indicate that Method 2 resulted in a significant acceleration of the activation process. This can potentially eliminate the need in the time-consuming activation process for  $\text{Mn}_3\text{O}_4$ -based electrodes. Indeed, relatively small variations in capacitance were obtained for the electrodes prepared by Method 2. The first cycle of capacitance measurements for the electrodes prepared by this method showed higher capacitance than that for TP 5 for the electrode prepared by Method 1. Turning again to the comparison of  $\text{MnO}_2$  and  $\text{Mn}_3\text{O}_4$  electrodes, it should be noted that some activation process was also reported for the  $\text{MnO}_2$  electrodes, which also exhibited a small increase in the capacitance during initial cycling<sup>47</sup>. Such a capacitance increase in the  $\text{MnO}_2$  electrodes was attributed to the microstructure changes during initial cycling<sup>47</sup>. GCD testing of the electrodes prepared by Method 2 showed linear charge–discharge curves (Figure 8-7D), indicating good capacitive behavior. The capacitance of  $7.55 \text{ F cm}^{-2}$  ( $188.8 \text{ F cm}^{-2}$ ) was achieved at a current density of  $3 \text{ mA cm}^{-2}$ . The electrodes prepared by Method 2 showed energy density of  $18.8 \text{ Wh kg}^{-1}$  at power density of  $0.11 \text{ kW kg}^{-1}$ .

In order to analyze the difference in the activation of electrodes prepared by methods 1 and 2, CV studies were performed for fresh electrodes at a scan rate of  $50 \text{ mV s}^{-1}$  for 2000 cycles, and the obtained capacitances were normalized by the capacitance obtained for the 2000th cycle (Figure 8-8).

The normalized capacitance  $C_N$  for the first cycle for the electrode prepared by method 1 was only 23% and it was slowly increased with cycle numbers. In contrast, the capacitance for the first cycle for the electrode prepared by Method 2 was 70% and rapidly increased with an increasing cycle number. The comparison with the data presented in Figure 8-7 also indicates that a lower scan rate can result in a faster activation process for the electrodes prepared by Method 2.

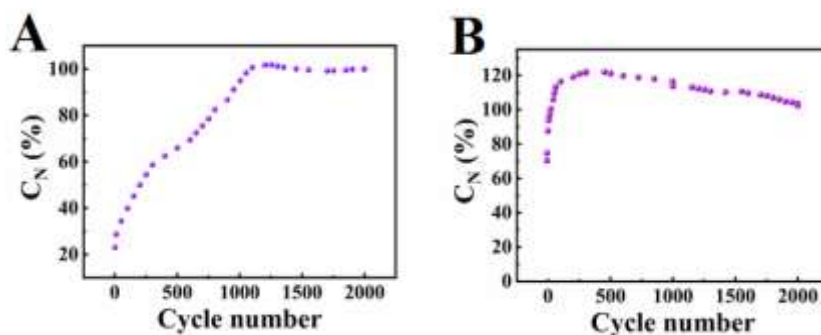


Figure 8- 8 Normalized capacitances ( $C_N$ ) versus cycle number at a scan rate of  $50 \text{ mV s}^{-1}$  for electrodes prepared by (A) Method 1 and (B) Method 2, normalized by the capacitance for the 2000th cycle.

The capacitances obtained from CV, EIS, and GCD data for electrodes prepared by Method 2 are significantly higher than the capacitances obtained by the same testing techniques for electrodes prepared by Method 1. The results of this investigation indicated that the use of murexide as a capping agent allowed for an enhanced

---

performance of the Mn<sub>3</sub>O<sub>4</sub>-MWCNT electrodes. It should be noted that MWCNTs have a low electrical double-layer-type specific capacitance <sup>48</sup> of about 20 F g<sup>-1</sup>. The use of MWCNTs as conductive additives is critically important for the utilization of capacitive properties of Mn<sub>3</sub>O<sub>4</sub>, which has low conductivity. Due to small MWCNT content in the Mn<sub>3</sub>O<sub>4</sub>-MWCNT electrode material, the high capacitance of the composite electrodes resulted from pseudocapacitive properties of Mn<sub>3</sub>O<sub>4</sub>.

A recent comprehensive review <sup>6</sup> summarized capacitances for Mn<sub>3</sub>O<sub>4</sub> and MnO<sub>2</sub> electrodes with high active mass reported in the literature. A comparison with the literature data for Mn<sub>3</sub>O<sub>4</sub> showed that the areal capacitance of Mn<sub>3</sub>O<sub>4</sub>-MWCNT electrodes achieved in this investigation is significantly higher than in the literature data (Table 8-1). Moreover, the capacitance of the Mn<sub>3</sub>O<sub>4</sub>-MWCNT electrodes was higher than the capacitances of MnO<sub>2</sub>-MWCNT electrodes of a similar mass reported in the literature (Table 8-1).

Table 8- 1 Literature data on capacitances of Mn<sub>3</sub>O<sub>4</sub>- and MnO<sub>2</sub>-based electrodes containing conductive additives and tested in Na<sub>2</sub>SO<sub>4</sub> electrolyte.

<b>Material</b>	<b>Active Mass (mg cm<sup>-2</sup>)</b>	<b>Areal Capacitance (F cm<sup>-2</sup>)</b>	<b>Reference</b>
Mn <sub>3</sub> O <sub>4</sub>	28.4	2.8	35
Mn <sub>3</sub> O <sub>4</sub>	30.4	2.63	49
Mn <sub>3</sub> O <sub>4</sub>	33.0	4.2	33
Mn <sub>3</sub> O <sub>4</sub>	35.0	3.5	31
Mn <sub>3</sub> O <sub>4</sub>	36.0	3.1	50
Mn <sub>3</sub> O <sub>4</sub>	36.0	3.79	51
Mn <sub>3</sub> O <sub>4</sub>	40.1	4.3	52
Mn <sub>3</sub> O <sub>4</sub>	40.0	6.67	this work
MnO <sub>2</sub>	40.0	5.26	53
MnO <sub>2</sub>	40.0	5.3	54
MnO <sub>2</sub>	40.0	5.9	55
MnO <sub>2</sub>	40.0	6.2	56

Therefore, the results of this investigation indicate that Mn<sub>3</sub>O<sub>4</sub> is a promising alternative to MnO<sub>2</sub> as a cathode material for asymmetric supercapacitors. The strategy developed in this investigation opens up an avenue for a further improvement of capacitive properties of Mn<sub>3</sub>O<sub>4</sub>-based electrodes. Of particular importance for

---

future investigations is the ability of  $\text{Mn}_3\text{O}_4$  to form solid solutions with other spinel compounds. The fabrication and testing of such solid solutions can result in electrodes with higher capacitive properties, which can be combined with improved magnetic and other functional properties.

## 8.5 Conclusions

For the first time, murexide was used as a capping agent for the synthesis of  $\text{Mn}_3\text{O}_4$  nanoparticles and as a co-dispersant for  $\text{Mn}_3\text{O}_4$  and MWCNTs. The adsorption of murexide on  $\text{Mn}_3\text{O}_4$  and MWCNTs involved two different mechanisms and facilitated electrostatic co-dispersion of  $\text{Mn}_3\text{O}_4$  with MWCNTs and their enhanced mixing. The use of murexide as a capping agent in Method 2 allowed for a reduced agglomeration. As a result, the capacitance of the  $\text{Mn}_3\text{O}_4$ -MWCNT electrodes prepared by Method 2 was significantly higher than the capacitance of the  $\text{Mn}_3\text{O}_4$ -MWCNT electrodes prepared by Method 1. The simple approach developed in this investigation resulted in record-high capacitances of  $6.67 \text{ F cm}^{-2}$  obtained from cyclic voltammetry data at a scan rate of  $2 \text{ mV s}^{-1}$  and  $7.55 \text{ F cm}^{-2}$  obtained from the galvanostatic charge-discharge data at a current density of  $3 \text{ mA cm}^{-2}$ . The good electrochemical performance was achieved at a high active mass loading of  $40 \text{ mg cm}^{-2}$ . It was found that the time-consuming electrode activation procedure for  $\text{Mn}_3\text{O}_4$  electrodes can be avoided. The approach developed in this investigation paved the way for the development of advanced cathodes for asymmetric supercapacitors for operation in a

---

neutral electrolyte. It is expected that future progress in the fabrication of  $\text{Mn}_3\text{O}_4$  electrodes will result in a superior performance compared to  $\text{MnO}_2$  electrodes for practical applications. Further development of chelating dispersants offers a promising strategy for the synthesis and the colloidal processing of advanced energy storage materials. The ability to achieve high capacitance for a spinel material in a neutral electrolyte opens the door for the fabrication of multifunctional devices, combining capacitive, magnetic, and other functional properties.

## 8.6 Acknowledgments

SEM investigations were performed at the Canadian Centre for Electron Microscopy.

## 8.7 References

- 1 Xiong, C. *et al.* The recent progress on three-dimensional porous graphene-based hybrid structure for supercapacitor. *Composites Part B: Engineering* **165**, 10-46 (2019).
- 2 Liu, C., Hou, Y., Li, Y. & Xiao, H. Heteroatom-doped porous carbon microspheres derived from ionic liquid-lignin solution for high performance Supercapacitors. *Journal of Colloid and Interface Science* (2022).
- 3 Zhang, H. *et al.* Oxygen-defect-rich 3D porous cobalt-gallium layered double hydroxide for high-performance supercapacitor application. *Journal of Colloid and Interface Science* **608**, 1837-1845 (2022).
- 4 Yan, Q., Cheng, Y., Wang, R. & Sun, J. Recent advances in 3D porous MXenes: structures, properties and applications. *Journal of Physics D: Applied Physics* (2021).
- 5 Wang, T. *et al.* Three-dimensional, heteroatom-enriched, porous carbon nanofiber flexible paper for free-standing supercapacitor electrode materials

- derived from microalgae oil. *Fuel Processing Technology* **225**, 107055 (2022).
- 6 Chen, R., Yu, M., Sahu, R. P., Puri, I. K. & Zhitomirsky, I. The Development of Pseudocapacitor Electrodes and Devices with High Active Mass Loading. *Advanced Energy Materials* **10**, 1903848 (2020).  
<https://doi.org:10.1002/aenm.201903848>
- 7 Gogotsi, Y. & Anasori, B. The rise of MXenes. *ACS Nano* **13**, 8491-8494 (2019).
- 8 Huang, T., Cui, W., Qiu, Z., Hu, Z. & Zhang, Z. 2D porous layered NiFe<sub>2</sub>O<sub>4</sub> by a facile hydrothermal method for asymmetric supercapacitor. *Ionics* **27**, 1347-1355 (2021). <https://doi.org:10.1007/s11581-021-03904-6>
- 9 Gao, X. *et al.* Morphology-controllable preparation of NiFe<sub>2</sub>O<sub>4</sub> as high performance electrode material for supercapacitor. *Electrochimica Acta* **296**, 181-189 (2019). <https://doi.org:https://doi.org/10.1016/j.electacta.2018.11.054>
- 10 Nawwar, M., Sahu, R. P., Puri, I. K. & Zhitomirsky, I. Pseudocapacitive behavior of ferrimagnetic NiFe<sub>2</sub>O<sub>4</sub>-carbon nanotube electrodes prepared with a multifunctional dispersing agent. *Open Ceramics*, 100127 (2021).
- 11 Wang, C. *et al.* NiCo<sub>2</sub>O<sub>4</sub>-based supercapacitor nanomaterials. *Nanomaterials* **7**, 41 (2017).
- 12 Meena, S. *et al.* Impact of temperature-induced oxygen vacancies in polyhedron MnFe<sub>2</sub>O<sub>4</sub> nanoparticles: As excellent electrochemical sensor, supercapacitor and active photocatalyst. *Ceramics International* **47**, 14723-14740 (2021). <https://doi.org:https://doi.org/10.1016/j.ceramint.2020.12.217>
- 13 Alshehri, S. M., Ahmed, J., Alhabarah, A. N., Ahamad, T. & Ahmad, T. Nitrogen-Doped Cobalt Ferrite/Carbon Nanocomposites for Supercapacitor Applications. *ChemElectroChem* **4**, 2952-2958 (2017).  
<https://doi.org:10.1002/celec.201700602>
- 14 Nawwar, M. *et al.* High areal capacitance of Fe<sub>3</sub>O<sub>4</sub>-decorated carbon nanotubes for supercapacitor electrodes. *Carbon Energy* **1**, 124-133 (2019).  
<https://doi.org:https://doi.org/10.1002/cey2.6>
- 15 Deshmukh, V. V., Nagaswarupa, H. P. & Raghavendra, N. Development of Co-doped MnFe<sub>2</sub>O<sub>4</sub> nanoparticles for electrochemical supercapacitors. *Ceramics International* **47**, 10268-10273 (2021).  
<https://doi.org:https://doi.org/10.1016/j.ceramint.2020.07.191>
- 16 Angelopoulou, P. *et al.* Enhanced Performance of LiAl<sub>0.1</sub>Mn<sub>1.9</sub>O<sub>4</sub> Cathode for Li-Ion Battery via TiN Coating. *Energies* **14**, 825 (2021).
- 17 Abdel-Ghany, A., Hashem, A. M., Mauger, A. & Julien, C. M. Lithium-Rich Cobalt-Free Manganese-Based Layered Cathode Materials for Li-Ion Batteries: Suppressing the Voltage Fading. *Energies* **13**, 3487 (2020).
- 18 Vu, N. H., Dao, V.-D., Tran Huu, H. & Im, W. B. Effect of Synthesis Temperature on Structure and Electrochemical Performance of Spinel-Layered Li<sub>1.33</sub>MnTiO<sub>4+z</sub> in Li-Ion Batteries. *Energies* **13**, 2962 (2020).
- 19 Venevtsev, Y. N., Gagulin, V. V. & Zhitomirsky, I. D. Material science aspects of seignette-magnetism problem. *Ferroelectrics* **73**, 221-248 (1987).

- 
- <https://doi.org/10.1080/00150198708227919>
- 20 Nawwar, M., Poon, R., Sahu, R. P., Puri, I. K. & Zhitomirsky, I. Fe<sub>3</sub>O<sub>4</sub> spinel-Mn<sub>3</sub>O<sub>4</sub> spinel supercapacitor prepared using Celestine blue as a dispersant, capping agent and charge transfer mediator. *Ceramics International* **46**, 18851-18858 (2020).
- 21 Guan, D. *et al.* Hydrothermal synthesis of carbon nanotube/cubic Fe<sub>3</sub>O<sub>4</sub> nanocomposite for enhanced performance supercapacitor electrode material. *Materials Science and Engineering: B* **178**, 736-743 (2013).
- 22 Nipan, G. *et al.* Transformation of Solid Solution with Spinel-Type Structure Within the Range LiMn<sub>2-x</sub>(Ni<sub>0.33</sub>Co<sub>0.33</sub>Fe<sub>0.33</sub>)<sub>x</sub>O<sub>4</sub> (0 ≤ x ≤ 2). *Journal of Phase Equilibria and Diffusion* **41**, 819-826 (2020).
- 23 Joo, H., Lee, J. & Yoon, J. Short Review: Timeline of the Electrochemical Lithium Recovery System Using the Spinel LiMn<sub>2</sub>O<sub>4</sub> as a Positive Electrode. *Energies* **13**, 6235 (2020).
- 24 Abbas, S. M. *et al.* Ag-Modified LiMn<sub>2</sub>O<sub>4</sub> Cathode for Lithium-Ion Batteries: Coating Functionalization. *Energies* **13**, 5194 (2020).
- 25 Cao, K., Jia, Y., Wang, S., Huang, K.-J. & Liu, H. Mn<sub>3</sub>O<sub>4</sub> nanoparticles anchored on carbon nanotubes as anode material with enhanced lithium storage. *Journal of Alloys and Compounds* **854**, 157179 (2021).
- 26 Dai, Y. *et al.* Tailoring the morphology and crystal facet of Mn<sub>3</sub>O<sub>4</sub> for highly efficient catalytic combustion of ethanol. *Colloids and Surfaces A: Physicochemical and Engineering Aspects* **627**, 127216 (2021).
- 27 Rizal, M. Y., Saleh, R., Taufik, A. & Yin, S. Photocatalytic decomposition of methylene blue by persulfate-assisted Ag/Mn<sub>3</sub>O<sub>4</sub> and Ag/Mn<sub>3</sub>O<sub>4</sub>/graphene composites and the inhibition effect of inorganic ions. *Environmental Nanotechnology, Monitoring & Management* **15**, 100408 (2021).
- 28 Patil, T. S., Gangawane, S. A. & Takale, M. V. A Review on Mn<sub>3</sub>O<sub>4</sub> and Its Composite Nanomaterials of Diverse Morphologies as an Electrode Material in Supercapacitors. (2021).
- 29 Sayyed, S. G., Shaikh, A. V., Dubal, D. P. & Pathan, H. M. Paving the Way towards Mn<sub>3</sub>O<sub>4</sub> Based Energy Storage Systems. *ES Energy & Environment* **14**, 3-21 (2021).
- 30 Rorabeck, K. & Zhitomirsky, I. Salting-out aided dispersive extraction of Mn<sub>3</sub>O<sub>4</sub> nanoparticles and carbon nanotubes for application in supercapacitors. *Colloids and Surfaces A: Physicochemical and Engineering Aspects* **618**, 126451 (2021).
- 31 Poon, R. & Zhitomirsky, I. High areal capacitance of Mn<sub>3</sub>O<sub>4</sub>-carbon nanotube electrodes. *Materials Letters* **215**, 4-7 (2018).
- 32 Nagarajan, N., Cheong, M. & Zhitomirsky, I. Electrochemical capacitance of MnO<sub>x</sub> films. *Materials Chemistry and Physics* **103**, 47-53 (2007).  
[https://doi.org:https://doi.org/10.1016/j.matchemphys.2007.01.005](https://doi.org/https://doi.org/10.1016/j.matchemphys.2007.01.005)
- 33 Milne, J. & Zhitomirsky, I. Application of octanohydroxamic acid for liquid-liquid extraction of manganese oxides and fabrication of supercapacitor

- 
- electrodes. *Journal of Colloid and Interface Science* **515**, 50-57 (2018).  
<https://doi.org/10.1016/j.jcis.2018.01.021>
- 34 Poon, R., Liang, W. & Zhitomirsky, I. Mn<sub>3</sub>O<sub>4</sub> and (ZnFe) OOH Composites for Supercapacitors with High Active Mass. *Metallurgical and Materials Transactions A* **51**, 855-862 (2020).
- 35 Ata, M. S., Milne, J. & Zhitomirsky, I. Fabrication of Mn<sub>3</sub>O<sub>4</sub>-carbon nanotube composites with high areal capacitance using cationic and anionic dispersants. *Journal of Colloid and Interface Science* **512**, 758-766 (2018).  
<https://doi.org/10.1016/j.jcis.2017.10.110>
- 36 Stanley, P. M. & Warnan, J. Molecular Dye-Sensitized Photocatalysis with Metal-Organic Framework and Metal Oxide Colloids for Fuel Production. *Energies* **14**, 4260 (2021).
- 37 Zhang, C. *et al.* One-Step Synthesis of Highly Dispersed and Stable Ni Nanoparticles Confined by CeO<sub>2</sub> on SiO<sub>2</sub> for Dry Reforming of Methane. *Energies* **13**, 5956 (2020).
- 38 Zhitomirsky, I. & Gal-Or, L. Formation of hollow fibers by electrophoretic deposition. *Materials Letters* **38**, 10-17 (1999).  
[https://doi.org/10.1016/S0167-577X\(98\)00124-4](https://doi.org/10.1016/S0167-577X(98)00124-4)
- 39 Lee, S. H., Woo, S. P., Kakati, N., Kim, D.-J. & Yoon, Y. S. A Comprehensive Review of Nanomaterials Developed Using Electrophoresis Process for High-Efficiency Energy Conversion and Storage Systems. *Energies* **11**, 3122 (2018).
- 40 Ata, M., Liu, Y. & Zhitomirsky, I. A review of new methods of surface chemical modification, dispersion and electrophoretic deposition of metal oxide particles. *Rsc Advances* **4**, 22716-22732 (2014).
- 41 Martin, R. L., White, A. H. & Willis, A. C. Structural studies in metal-purpurate complexes. Part 1. Crystal structures of potassium purpurate trihydrate and ammonium purpurate monohydrate (murexide). *Journal of the Chemical Society, Dalton Transactions*, 1336-1342 (1977).
- 42 Masoud, M., Kassem, T., Shaker, M. & Ali, A. Studies on transition metal murexide complexes. *Journal of thermal analysis and calorimetry* **84**, 549-555 (2006).
- 43 Zhao, H. *et al.* Multiwalled carbon nanotubes as a solid-phase extraction adsorbent for the determination of three barbiturates in pork by ion trap gas chromatography-tandem mass spectrometry (GC/MS/MS) following microwave assisted derivatization. *Analytica chimica acta* **586**, 399-406 (2007).
- 44 Wallar, C., Poon, R. & Zhitomirsky, I. High Areal Capacitance of V<sub>2</sub>O<sub>3</sub>-Carbon Nanotube Electrodes. *Journal of The Electrochemical Society* **164**, A3620-A3627 (2017).
- 45 Gogotsi, Y. & Simon, P. True performance metrics in electrochemical energy storage. *Science* **334**, 917-918 (2011).
- 46 Shi, K. & Zhitomirsky, I. Fabrication of Polypyrrole-Coated Carbon Nanotubes Using Oxidant-Surfactant Nanocrystals for Supercapacitor

- 
- Electrodes with High Mass Loading and Enhanced Performance. *ACS Applied Materials & Interfaces* **5**, 13161-13170 (2013).  
<https://doi.org/10.1021/am404159b>
- 47 Rorabeck, K. & Zhitomirsky, I. Dispersant Molecules with Functional Catechol Groups for Supercapacitor Fabrication. *Molecules* **26**, 1709 (2021).
- 48 Shi, K., Ren, M. & Zhitomirsky, I. Activated Carbon-Coated Carbon Nanotubes for Energy Storage in Supercapacitors and Capacitive Water Purification. *ACS Sustainable Chemistry & Engineering* **2**, 1289-1298 (2014).
- 49 Poon, R., Zhao, X., Ata, M. S., Clifford, A. & Zhitomirsky, I. Phase transfer of oxide particles for application in thin films and supercapacitors. *Ceramics International* **43**, 8314-8320 (2017).  
[https://doi.org:https://doi.org/10.1016/j.ceramint.2017.03.167](https://doi.org/https://doi.org/10.1016/j.ceramint.2017.03.167)
- 50 Milne, J., Silva, R. M. & Zhitomirsky, I. Surface modification and dispersion of ceramic particles using liquid-liquid extraction method for application in supercapacitor electrodes. *Journal of the European Ceramic Society* **39**, 3450-3455 (2019).
- 51 Poon, R. & Zhitomirsky, I. Application of Cyrene as a solvent and dispersing agent for fabrication of Mn<sub>3</sub>O<sub>4</sub>-carbon nanotube supercapacitor electrodes. *Colloid and Interface Science Communications* **34**, 100226 (2020).
- 52 Rorabeck, K. & Zhitomirsky, I. Application of Octanohydroxamic Acid for Salting out Liquid-Liquid Extraction of Materials for Energy Storage in Supercapacitors. *Molecules* **26**, 296 (2021).
- 53 Liu, Y. & Zhitomirsky, I. Aqueous electrostatic dispersion and heterocoagulation of multiwalled carbon nanotubes and manganese dioxide for the fabrication of supercapacitor electrodes and devices. *RSC Advances* **4**, 45481-45489 (2014).
- 54 Liu, Y., Shi, K. & Zhitomirsky, I. New colloidal route for electrostatic assembly of oxide nanoparticle-carbon nanotube composites. *Colloids and Surfaces A: Physicochemical and Engineering Aspects* **446**, 15-22 (2014).
- 55 Wang, Y., Liu, Y. & Zhitomirsky, I. Surface modification of MnO<sub>2</sub> and carbon nanotubes using organic dyes for nanotechnology of electrochemical supercapacitors. *Journal of Materials Chemistry A* **1**, 12519-12526 (2013).
- 56 Li, J., Yang, Q. M. & Zhitomirsky, I. Nickel foam-based manganese dioxide-carbon nanotube composite electrodes for electrochemical supercapacitors. *Journal of Power Sources* **185**, 1569-1574 (2008).

# Chapter 9 Influence of Capping Agents on Synthesis of $\text{Mn}_3\text{O}_4$ Nanostructures for Supercapacitors

Lory Wenjuan Yang and Igor Zhitomirsky\*

Department of Materials Science and Engineering,  
McMaster University, Hamilton, ON L8S 4L7, Canada

\*Corresponding author: [zhitom@mcmaster.ca](mailto:zhitom@mcmaster.ca)

Phone 905-525-9140

Copyright 2023, reproduced with permission from ACS.

---

## 9.1 Abstract

Nanotechnology offers powerful strategies for the fabrication of advanced materials for energy storage in supercapacitors. It is hypothesized that the size reduction of  $\text{Mn}_3\text{O}_4$  nanoparticles can eliminate time-consuming electrochemical activation and increase electrochemical pseudocapacitance of this material. Moreover, due to redox properties and specific features of its chemical synthesis procedure,  $\text{Mn}_3\text{O}_4$  can potentially outperform other promising cathode materials for energy storage in supercapacitors. A facile room temperature method to fabricate  $\text{Mn}_3\text{O}_4$  nanoparticles is described, which is based on the use of advanced capping agents for synthesis. Building on the strong adsorption power of the catechol ligand, we utilize tetrahydroxy-1,4-quinone, catechin, and galloyanine as capping agents for the synthesis of  $\text{Mn}_3\text{O}_4$ . The use of the catecholate molecules as capping agents for synthesis facilitates the fabrication of  $\text{Mn}_3\text{O}_4$  platelet nanoparticles with a typical size of 5 nm. The reduction of particle size allows the fabrication of advanced  $\text{Mn}_3\text{O}_4$ -multiwalled carbon nanotube cathodes with high active mass loadings of  $40 \text{ mg cm}^{-2}$ , which show significant increase in capacitance in  $0.5 \text{ M Na}_2\text{SO}_4$  electrolyte. The highest capacitance of  $7.03 \text{ F cm}^{-2}$  ( $175.8 \text{ F g}^{-1}$ ) at cyclic voltammetry scan rate of  $2 \text{ mV s}^{-1}$  and  $9.13 \text{ F cm}^{-2}$  ( $228.3 \text{ F g}^{-1}$ ) at galvanostatic charge-discharge current density of  $3 \text{ mA cm}^{-2}$  is obtained using galloyanine as a capping agent. The high capacitance is achieved at a low electrode resistance. Obtained electrodes outperform  $\text{MnO}_2$  based cathodes of a similar mass. Another important finding is the possibility to avoid the

time-consuming activation process for Mn<sub>3</sub>O<sub>4</sub> based electrodes. The analysis of testing results provides an insight into the influence of the chemical structure of the capping agents on electrode performance. The results of this investigation pave the way for application of Mn<sub>3</sub>O<sub>4</sub> in advanced high active mass supercapacitor cathodes.

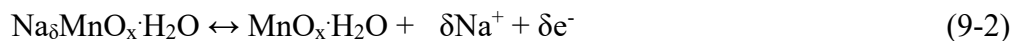
## 9.2 Introduction

Mn<sub>3</sub>O<sub>4</sub> is gaining attention as a pseudocapacitive charge storage material for supercapacitors<sup>1-3</sup>. Investigations focused on the fabrication of thin films and high active mass bulk electrodes<sup>1,4-6</sup> by various techniques and analysis of charging mechanism<sup>7-10</sup>. The investigation of Mn<sub>3</sub>O<sub>4</sub> behavior in Na<sub>2</sub>SO<sub>4</sub> electrolyte<sup>11-13</sup> is of particular importance for the development of asymmetric supercapacitors with large voltage windows in the range of 1.6-2.0 V. The first step of the charging mechanism in Na<sub>2</sub>SO<sub>4</sub> electrolyte involves solvation<sup>14</sup>:



Mn K-edge X-ray absorption spectroscopy (XAS)<sup>14</sup> studies confirmed Na<sub>δ</sub>MnO<sub>x</sub> formation during initial cycling and revealed reduction of the average oxidation state of Mn. Another XAS investigation confirmed reduction of Mn<sup>3+</sup> to Mn<sup>2+</sup> at low potentials and revealed oxidation of Mn<sup>3+</sup> to Mn<sup>4+</sup> or Mn<sup>6+</sup> at higher potentials<sup>15</sup>.

The subsequent charging behavior involved the following reaction<sup>14</sup>:



---

Other investigations demonstrated  $\text{Mn}_3\text{O}_4$  activation at the beginning of cycling, which resulted in significant capacitance increase<sup>2,16,17</sup>. A significant activation effect was reported for high active mass electrodes<sup>18-22</sup> and it was attributed to the changes of the electrode microstructure and oxidation state of Mn<sup>19,21,23,24</sup>. Numerous X-ray photoelectron spectroscopy (XPS) studies<sup>19,21,23,24</sup> demonstrated increase of the oxidation state of Mn after long cycling. Recent scanning transmission X-ray microscopy (STXM) investigations<sup>25</sup> analyzed  $\text{Mn}_3\text{O}_4$  activation by cycling at different scan rates and at a fixed scan rate. The capacitance increase during electrode activation was linked to STXM observations, which demonstrated  $\text{Mn}_3\text{O}_4$  oxidation to form  $\text{MnO}_2$  on the particle surface and in the bulk. The pseudocapacitive charge storage mechanism involves *in-situ* oxidation of  $\text{Mn}_3\text{O}_4$  and redox reactions of  $\text{Mn}^{4+}/\text{Mn}^{3+}$  species on the particle surface and in the bulk<sup>25</sup>.

The high capacitance values obtained in investigation of  $\text{Mn}_3\text{O}_4$  electrodes indicated that this material can potentially outperform other promising cathode materials, such as  $\text{MnO}_2$ . It should be noted that  $\text{KMnO}_4$  or  $\text{NaMnO}_4$  precursors are usually used for the synthesis of  $\text{MnO}_2$  particles<sup>26-29</sup>. Such precursors react with organic capping agents and conductive carbon additives and generate problems in the synthesis of non-agglomerated nanoparticles of controlled size and fabrication of composites. The use on  $\text{Mn}^{2+}$  salts for the synthesis of  $\text{Mn}_3\text{O}_4$  eliminates such difficulties. The success of  $\text{Mn}_3\text{O}_4$  practical applications will depend largely on the ability to avoid the time-consuming activation steps. It is hypothesized that the reduction of particles size can

potentially facilitate their fast oxidation, avoiding long activation procedures.

Moreover, the reduction of particles size can result in enhanced capacitance. These challenges can be addressed by the development of advanced nanotechnologies for synthesis of  $\text{Mn}_3\text{O}_4$  nanoparticles.

The reduction of particle size of  $\text{Mn}_3\text{O}_4$  can be achieved using capping agents during synthesis. Organic molecules, containing OH groups, such as glucose, salicylates and molecules from chromotropic acid family show adsorption on inorganic particles and generate interest for application as capping and dispersing agents<sup>30-33</sup>. Tetrahydroxy-1,4-quinone (TQ), catechin (CT), and galloycyanine (GC) are promising materials for capping agent application. They belong to a catechol family of materials (Figure 9-1 A-C), which allow for a strong bonding to the metal atoms on the particle surface (Figure 9-1D). The interest in catecholate-type dispersants and capping agents<sup>33</sup> resulted from the investigation of strong mussel proteins bonding to different surfaces, involving their catecholate monomers. Therefore TQ, CT and GC can potentially be adsorbed on  $\text{Mn}_3\text{O}_4$  nanoparticles during synthesis and limit their growth.

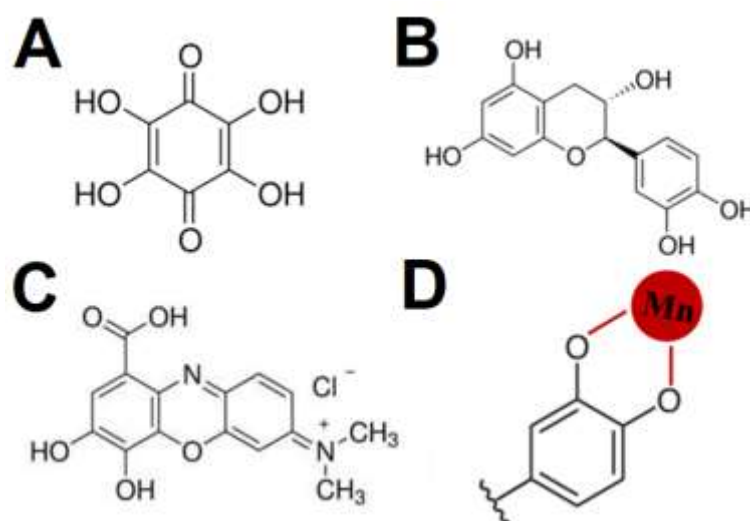


Figure 9- 1 Chemical structures of (A) TQ, (B) CT, and (C) GC molecules and (D) catechol-type bonding, involving Mn atoms on the  $Mn_3O_4$  particle surface.

The chemical structure of TQ contains adjacent OH groups, which allow catechol-type bonding to various metal atoms<sup>34</sup>. Such bonding sites are important for TQ applications as metal atom linkers for the formation of metal organic frameworks for catalysis, electrochemical sensors, lithium ion battery and lithium ion hybrid supercapacitor applications<sup>35-39</sup>. CT showed strong adsorption on stainless steel and it was used as a corrosion inhibitor<sup>40</sup>. The adsorption of CT on hydroxyapatite involved chelation of surface Ca atoms<sup>41</sup>. The CT adsorption on alumina particles resulted in significant changes of their zeta-potential<sup>42</sup>. Catechol-type bonding<sup>43</sup> was involved in GC adsorption on  $Fe_2O_3$  particles and the positive charge of the adsorbed GC facilitated particle dispersion. Moreover TQ, CT and GC exhibit interesting redox-active properties<sup>44-48</sup> which can potentially be used for energy storage applications. The goal of this investigation was the use of TQ, CT, and GC molecules as capping

---

agents for the synthesis of  $\text{Mn}_3\text{O}_4$  nanoparticles and application of the obtained particles for the fabrication of advanced  $\text{Mn}_3\text{O}_4$  cathodes for supercapacitors. The experimental results presented below indicated that TQ, CT, and GC molecules adsorbed on  $\text{Mn}_3\text{O}_4$  particles and acted as capping agents. The use of capping agents for  $\text{Mn}_3\text{O}_4$  synthesis allowed significant particle size reduction. Electrochemical studies revealed multiple benefits of particle size reduction for practical applications of  $\text{Mn}_3\text{O}_4$  in cathodes of supercapacitors. The electrochemical activation process has been significantly accelerated and practically eliminated. Moreover, the reduction of particles size facilitated their dispersion and mixing with conductive carbon nanotube additives and allowed for significant increase of capacitance. The use of nanotechnology strategies for the synthesis of  $\text{Mn}_3\text{O}_4$  nanoparticles was crucial for the development of supercapacitor electrodes with enhanced electrochemical performance. The analysis of the testing results provided an insight into the influence of chemical structures of the capping agents on capacitive properties of  $\text{Mn}_3\text{O}_4$  based electrodes.

### 9.3 Experimental procedures

Tetrahydroxy-1,4-quinone hydrate (TQ), catechin hydrate (CT), galloycyanine (GC),

$\text{Mn}(\text{NO}_3)_2 \cdot 4\text{H}_2\text{O}$ , ethanol, NaOH,  $\text{Na}_2\text{SO}_4$ , poly(vinyl butyral) binder (PVB,

MilliporeSigma, Oakville, ON, Canada), multiwalled carbon nanotubes (MWCNT, ID

4 nm, OD 13 nm, length 1–2  $\mu\text{m}$ , Bayer, Leverkusen, Germany) and industrial Ni

---

foam current collectors (95% porosity, 1.6 mm thickness, Vale, Mississauga, ON, Canada) were used.

Mn<sub>3</sub>O<sub>4</sub> nanoparticles were prepared using a chemical precipitation method, described in a previous investigation<sup>273</sup> by chemical precipitation from aqueous Mn(NO<sub>3</sub>)<sub>2</sub> solution at pH=10. The size of the particles prepared by this method was in the range of 50-120 nm<sup>49</sup>. Mn<sub>3</sub>O<sub>4</sub> particles were also prepared by a modified method, using TQ, CT, and GC as capping agents. In the modified method, solutions of 330 mg Mn(NO<sub>3</sub>)<sub>2</sub>·4H<sub>2</sub>O, containing a capping agent, were prepared in DI water and pH of the solutions was adjusted to pH = 10 with aqueous NaOH. MWCNT were used as conductive additives<sup>50</sup>. For the fabrication of composites, MWCNT were dispersed in the Mn(NO<sub>3</sub>)<sub>2</sub> solutions. The mass ratio Mn<sub>3</sub>O<sub>4</sub>:MWCNT:capping agent was 8:2:1. The concentration of the capping agents were selected on the basis of sedimentation tests, which indicated that minimum amount of capping agent for the fabrication of stable suspensions was 10% (Supplementary information, Figure 9-S 1). Obtained powders were washed, dried, re-dispersed in ethanol, containing dissolved PVB binder, and obtained slurries were used for the fabrication of electrodes by impregnation of Ni foam current collectors. The PVB binder content was 3% of the total mass of Mn<sub>3</sub>O<sub>4</sub> and MWCNT. The impregnated current collectors were pressed to 30% of original thickness to improve electrical contact with active material. The total mass of impregnated material after drying was 40 mg cm<sup>-2</sup>.

Microstructure investigations were performed using transmission electron microscopy

---

(TEM, Talos 200X microscope, Thermo Scientific, Waltham, MA, USA) and scanning electron microscopy (SEM, JEOL, JSM-7000F microscope, Tokyo, Japan) methods. X-ray diffraction (XRD) analysis (diffractometer Bruker D8, Coventry, UK) was performed using Cu-K $\alpha$  radiation at the rate of 0.01 degrees per second. Fourier Transform Infrared Spectroscopy (FTIR) studies were performed using a Bruker Vertex 70 spectrometer (Billerica, MA, USA). Zeta potential measurements were performed using a dynamic light scattering instrument (DelsaMax Pro, Beckman Coulter, Brea, CA, USA). Electrochemical studies were performed in aqueous 0.5 M Na<sub>2</sub>SO<sub>4</sub> electrolyte using PARSTAT 2273 potentiostat (AMETEK, Berwyn, PA, USA) for cyclic voltammetry (CV) and electrochemical impedance spectroscopy (EIS). A BioLogic VMP 300 potentiostat was used for galvanostatic charge-discharge (GCD) investigations (BioLogic, Claix, France). Testing was performed using a 3-electrode electrochemical cell containing a working electrode (impregnated Ni foam), counter-electrode (Pt mesh), and a reference electrode (SCE, saturated calomel electrode). The capacitive properties of electrode material were presented in gravimetric ( $C_m$ , F g<sup>-1</sup>) and areal ( $C_s$ , F cm<sup>-2</sup>) capacitance forms. Capacitances  $C_m$  and  $C_s$  were calculated from the CV, EIS and GCD data as it was described in reference<sup>51</sup>. The capacitances calculated from the CV and GCD data represented integral capacitances measured in a potential window of 0–0.9 V versus SCE. The complex capacitances calculated from the EIS data represented differential capacitances measured at an open circuit potential at a voltage amplitude of 5 mV. A commercial ZSimpWin software (Ametek,

USA) was used for the analysis and modeling of EIS data.

## 9.4 Results and Discussion

In this investigation we targeted the development of  $\text{Mn}_3\text{O}_4$  nanoparticles of reduced size and their efficient mixing with conductive MWCNT additives for the formation of advanced nanocomposites for supercapacitor electrodes with enhanced charge storage properties. Figure 9-2 shows X-ray diffraction patterns of powders, prepared without and with capping agents. The X-ray diffraction patterns showed peaks of hausmannite  $\text{Mn}_3\text{O}_4$  phase, corresponding to JCPDS file 04-007-1841. However, the XRD peaks of the materials prepared using capping agents showed diffraction peak broadening, which can result from a smaller crystal size. Relatively low peak intensity indicated that the samples, prepared using capping agents, also contain an amorphous phase. Previous investigations of  $\text{Mn}_3\text{O}_4$  nanoparticles prepared by chemical precipitation, sol-gel and hydrothermal method showed that crystalline size obtained from the XRD data was significantly smaller than the particle size obtained from the electron microscopy data<sup>52,53</sup>. The difference can be attributed to the surface amorphous layer on the particles<sup>53</sup>. Therefore, TEM investigations were performed for the particles prepared using different capping agents.

As pointed out above, the method<sup>49</sup> used in this investigation, is capable of producing 50-120 nm particles without the use of capping agents. In a previous investigation<sup>24</sup> we explored a possibility of particle size reduction using a chelating polyelectrolyte as

a capping agent. The use of a co-polymer of 4-styrenesulfonic acid and maleic acid as a capping agent facilitated the fabrication of smaller spherical particles with a diameter<sup>54</sup> of 40-50 nm. Despite the particle size reduction, the obtained Mn<sub>3</sub>O<sub>4</sub>-MWCNT electrodes required a time-consuming activation procedure<sup>54</sup>, which resulted in a highest capacitance of 2.8 F cm<sup>-2</sup>. In contrast, the experimental data presented below indicated that significant reduction of nanoparticle size can be achieved using TQ, CT, and GC and the activation procedure can be practically avoided. Moreover, the nanostructured electrodes showed significantly higher capacitance.

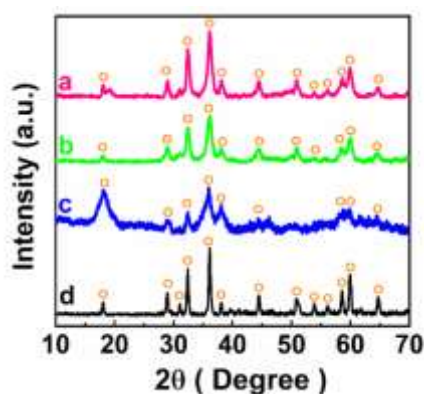


Figure 9- 2 X-ray diffraction patterns for Mn<sub>3</sub>O<sub>4</sub> powders, (a-c) prepared by adding capping agents: (a) TQ, (b) CT, (c) GC and (d) without capping agent (o- peaks corresponding to JCPDS file 04-007-1841 of Mn<sub>3</sub>O<sub>4</sub>).

---

Figure 9-3 shows TEM images at different magnifications for  $\text{Mn}_3\text{O}_4$  particles, prepared using TQ, CT, and GC as capping agents. The TEM images of dried powders at low magnification showed significant reduction of particle size, however drying resulted in the formation of a small number of fibrous agglomerates. The analysis of the powders at higher magnification revealed the formation of platelet-shape primary nanoparticles with a typical size of about 5 nm. The use of capping agents was a key factor for the size reduction of the  $\text{Mn}_3\text{O}_4$  nanoparticles, as compared with experiments performed at similar synthesis conditions without capping agents<sup>273</sup> and using other techniques (Table 9-1). It is suggested that catecholate ligands of the capping agents (Figure 9-1) were beneficial for TQ, CT, and GC adsorption on  $\text{Mn}_3\text{O}_4$  particles and the adsorbed molecules limited the particle growth during synthesis. TEM observations showed nearly similar size of primary particles, prepared using different catecholate capping agents. However, electrokinetic measurements revealed difference in zeta-potentials, which were found to be -18.4, -26.6 and -35.3 mV for the particles prepared using TQ, CT and GC, respectively.

Table 9- 1 Size of  $Mn_3O_4$  particles prepared by different methods.

Synthesis method	Particle morphology	Particle size	Reference
Co-precipitation	Plates like nano-grains	600-800 nm	52
Sol-gel	Coin-like nano-spheres	100-400 nm	52
Hydrothermal	Nano-petals	40-80 nm	52
Hydrothermal	Nanoparticles	40-70 nm	55
Co-precipitation	Nanoparticles	80-100 nm	56
Hydrothermal	Nanorods	Diameter 100 nm, length 15-20 $\mu m$	57
Electrodeposition	Elongated cuboctahedron-shaped particles	500 nm	58
Electrodeposition	Porous nanospheres	50 nm	59
Electrodeposition	Nanorods	Diameter 15 nm, length 200 nm	53

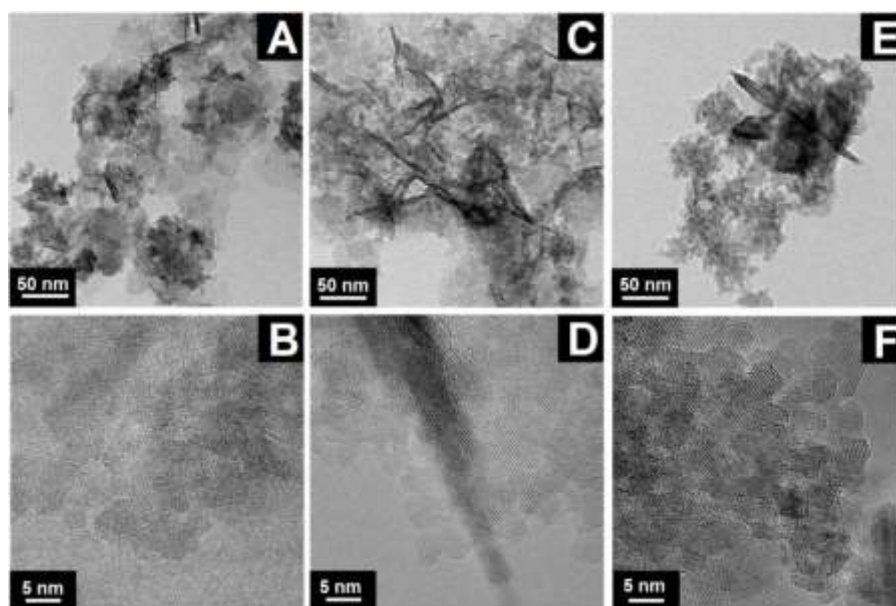


Figure 9- 3 TEM images at different magnifications of  $Mn_3O_4$  prepared using capping agents (A,B) TQ and (C,D) CT and (E,F) GC.

The adsorption of TQ and CT and GC on  $Mn_3O_4$  nanoparticles was confirmed by FTIR spectroscopy (Figure 9-4). The FTIR spectra of particles, prepared in the presence of TQ, CT and GC showed absorptions in the range 1368-1640 attributed to stretching C-C vibrations of aromatic rings of the adsorbed capping agent molecules<sup>60-62</sup>. Moreover, the adsorbed molecules showed absorptions at 1069, 949, and 805  $cm^{-1}$  related to stretching C-C vibrations<sup>60,63</sup>, stretching C-O vibrations<sup>63</sup>, and out of plane C-H vibrations<sup>63</sup>, respectively. The broad absorptions centered around 3080  $cm^{-1}$  resulted from stretching O-H and C-H vibrations<sup>60,63</sup>. Such absorptions were not observed in the spectrum of  $Mn_3O_4$  prepared without capping agents (Figure 9-4). Figure 9-5 shows SEM images of the  $Mn_3O_4$  electrodes, prepared using TQ, CT and GC. The use of capping agents, which also acted as dispersants, facilitated good

mixing of the  $Mn_3O_4$  particles with conductive additives. The formation of composites was also confirmed by TEM and X-ray photoelectron spectroscopy (XPS) analysis (supplementary information, Figures 9-S 2 and 9-S 3).

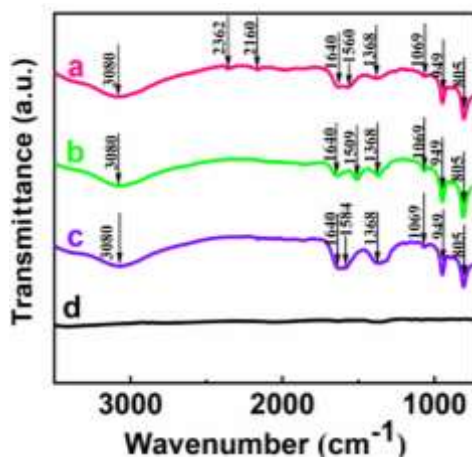


Figure 9- 4 FTIR spectra of  $Mn_3O_4$  prepared using capping agents (a) TQ (b) CT, (c) GC and (d)  $Mn_3O_4$  prepared without capping agent.

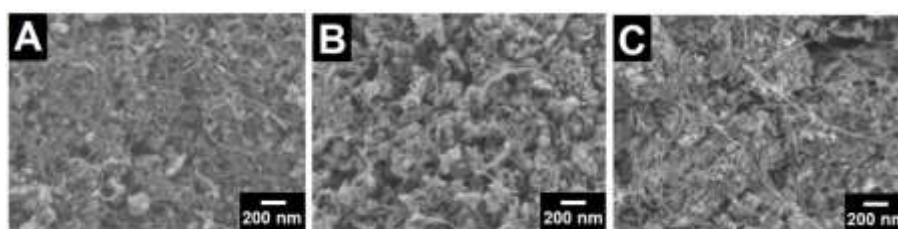


Figure 9- 5 SEM images of  $Mn_3O_4$ -MWCNT composite electrodes prepared using (A) TQ, (B)CT and (C)GC as capping and dispersing agents.

Cyclic voltammetry studies involved testing at scan rates of 2, 5, 10, 20, 50 and 100  $mV s^{-1}$ . This various scan rate testing procedure (VSRP) was similar to the VSRP used in a previous investigation<sup>25</sup> for  $Mn_3O_4$  prepared without capping agents. The obtained CVs were of nearly rectangular shape without redox peaks (Figure 9-6(A-C)). The obtained capacitances were  $4.34 F cm^{-2}$  ( $108.5 F g^{-1}$ ),  $5.93 F cm^{-2}$  ( $148.2 F g^{-1}$ ) and  $7.03 F cm^{-2}$  ( $175.8 F g^{-1}$ ) for electrodes, prepared using TQ, CT and GC,

respectively, at a scan rate of  $2 \text{ mV s}^{-1}$ . It should be noted that in a previous investigation<sup>25</sup> the first VSRP (VSRP1) resulted in a capacitance of only  $1.5 \text{ F cm}^{-2}$  for the  $\text{Mn}_3\text{O}_4$ -MWCNT electrode of the same active mass. The testing was repeated 5 times (VSRPs1-5) and the capacitance of  $3.3 \text{ F cm}^{-2}$  was obtained<sup>25</sup> for VSRP5. Therefore, the use of capping agents for synthesis and particle size reduction resulted in significantly higher capacitance and the activation procedure was practically eliminated. The obtained capacitance was higher than that obtained for  $\text{MnO}_2$ -MWCNT electrodes of the same active mass<sup>64</sup>.

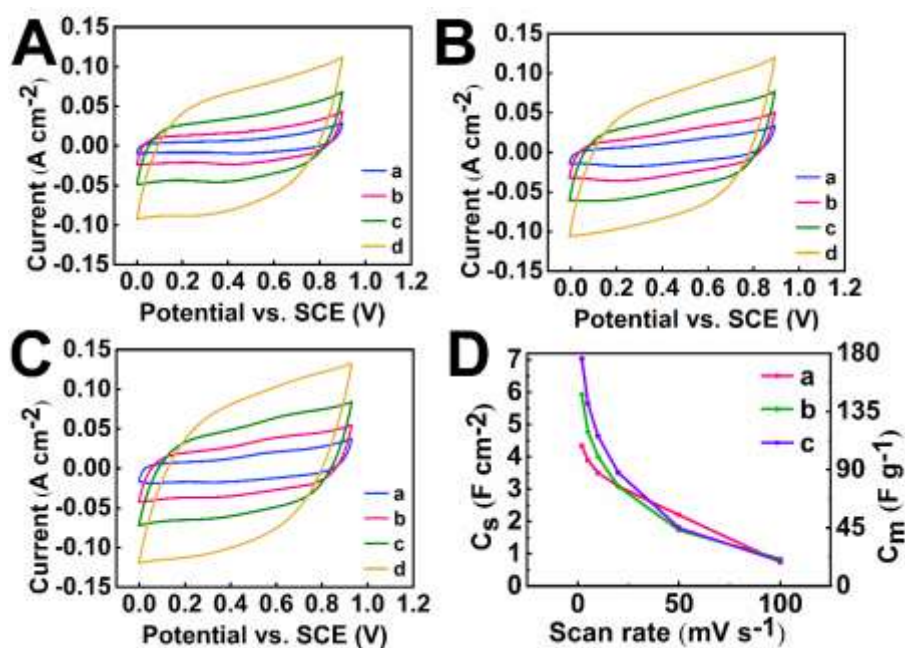


Figure 9- 6 (A-C) CVs at scan rates of (a) 2, (b) 5, (c) 10 and (d)  $20 \text{ mV s}^{-1}$  for electrodes prepared using (A) TQ, (B) CT and (C) GC as capping agents; (D) capacitance versus scan rate for electrode prepared by (a) TQ (b) CT, (c) GC as capping agents.

---

Previous investigation<sup>25</sup> showed relatively high Mn<sub>3</sub>O<sub>4</sub>-MWCNT electrode resistance after VSRP1. The resistance decreased during continuous testing procedures from VSRP1 to VSRP5. The use of capping agents for the synthesis facilitated the fabrication of electrodes with lower resistance than that reported in the previous investigation<sup>25</sup> (Figure 9-7A). The low resistance is beneficial for efficient charge and discharge. The impedance spectroscopy data was analyzed using an equivalent circuit (Figure 9-7B), which was developed for electrodes with high active mass loadings<sup>65</sup>. In this circuit,  $R_1C_1QR_2$  represents a transmission line, describing a porous electrode,  $R_s$  is a solution resistance,  $W$  is Warburg element,  $C_{DL}$  and  $R_t$  are double layer capacitance and a charge transfer resistance, respectively. The  $R_t$  values were found to be 0.062, 0.059 and 0.048 for electrodes prepared using TH, CT and GC, respectively. The lowest  $R_t$  for electrodes prepared using GC is beneficial for supercapacitor applications.

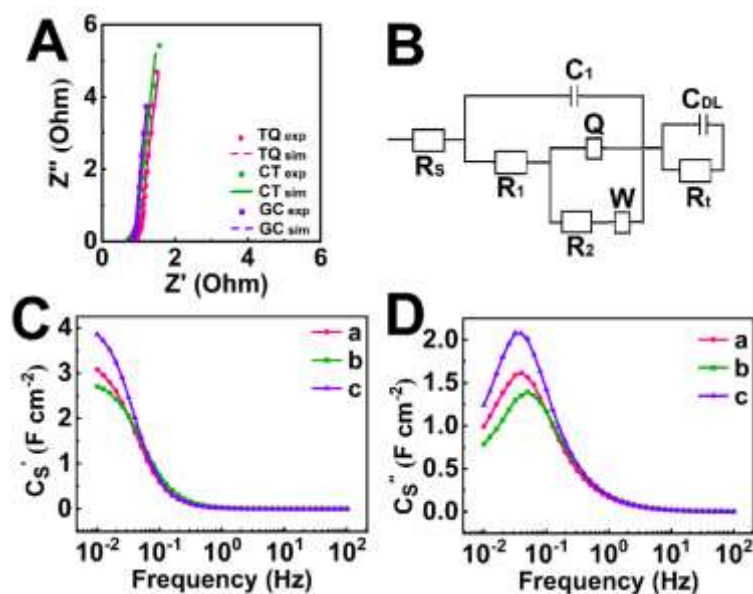


Figure 9- 7 (A) complex impedance data presented in a Nyquist plot, (● experimental data (exp) and —simulation data (sim) for materials prepared using different capping agents, (B) equivalent circuit used for simulation, (C,D) frequency dependences of components of complex capacitance (C)  $C_s'$  and (D)  $C_s''$ , calculated from the EIS data for electrodes prepared using (a) TQ (b) CT, (c) GC as capping agents.

Differential complex capacitances were also calculated from the AC impedance data (Figure 9-7 C, D) at different frequencies. The electrodes prepared using TQ (b) CT, (c) GC showed capacitances  $C'$  of 3.08, 2.71 and 3.86  $F\ cm^{-2}$ , respectively, at a frequency of 10 mHz, which were higher than reported in a previous investigation<sup>25</sup> after long activation procedures, involving VSRPs 1-5. Measuring the real and imaginary components of complex capacitance also provided insight into the capacitive behavior at different frequencies. The reduction of real components with frequency and maxima in the imaginary components indicated a relaxation-type dispersion of capacitance. It is known<sup>66,67</sup> that charging process requires a specific

---

charging time  $t$ . At frequencies higher than  $1/t$ , the charging process cannot contribute to capacitance, resulting in a relaxation-type dispersion. In this case, the real part of capacitance shows fast decrease at frequencies above  $1/t$  and becomes low at higher frequencies<sup>66</sup>. The imaginary part of capacitance shows a corresponding maximum<sup>67,68</sup> at the relaxation frequency  $f=1/t$ .

The results of GCD studies provide further evidence of enhanced capacitive behavior of  $\text{Mn}_3\text{O}_4$ -based electrodes prepared using capping agents. Figure 9-8 shows GCD data for electrodes, prepared using TQ, CT, and GC as capping agents. The GCD curves obtained at different current densities were of nearly triangular shape. The capacitances obtained at a current density of  $3 \text{ mA cm}^{-2}$  were found to be  $7.11 \text{ F cm}^{-2}$  ( $177.7 \text{ F g}^{-1}$ ),  $8.36 \text{ F cm}^{-2}$  ( $208.9 \text{ F g}^{-1}$ ) and  $9.13 \text{ F cm}^{-2}$  ( $228 \text{ F g}^{-1}$ ) for electrodes prepared using TQ, CT, and GC, respectively. The capacitance decreased with increasing current density. The highest capacitance was obtained for electrodes prepared using GC. The obtained areal capacitance was higher than literature data (Table 9-2). Turning again to the structural features of the capping agents it is seen that catechol groups of the capping agents facilitated their adsorption on  $\text{Mn}_3\text{O}_4$  nanoparticles and limited particle growth during synthesis. The larger size of the capping agent molecules resulted in higher zeta-potentials. The increase in zeta-potential of the electrodes prepared using different capping agents correlates with increase of zeta potential of  $\text{Mn}_3\text{O}_4$  particles. The small particle size and high zeta-potential of  $\text{Mn}_3\text{O}_4$  particles is beneficial for their improved dispersion and mixing

with conductive MWCNT on the nanometric scale. Moreover, polyaromatic GC and CT can provide enhanced  $\pi$ - $\pi$  interactions with carbon nanotubes<sup>69</sup> and facilitate the fabrication of nanocomposites.

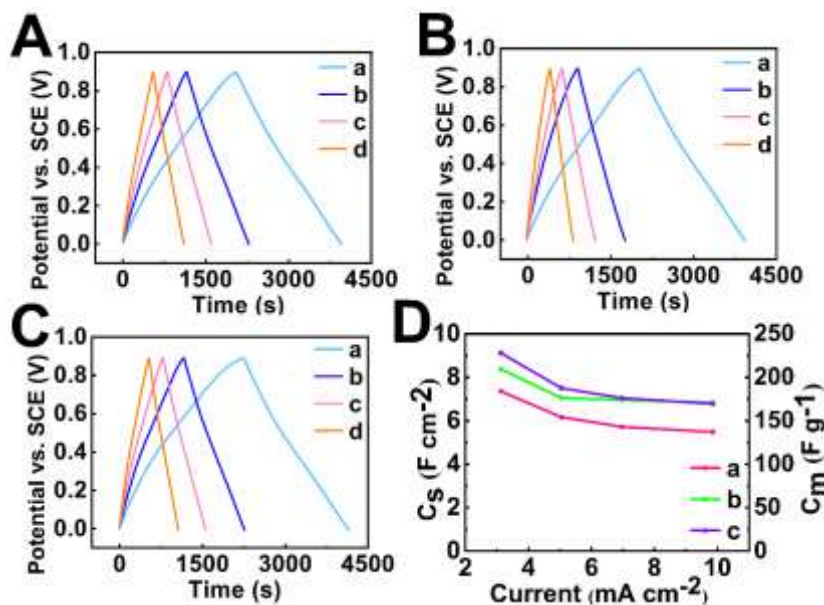


Figure 9- 8 Galvanostatic charge-discharge curves (GCD) at current densities of (a) 3, (b) 5, (c) 7, and (d) 10 mA cm<sup>-2</sup> and (D) capacitances, calculated from GCD data versus current density for electrodes prepared by (A and D(a)) TQ, (B and D (b)) CT and (C and D(c)) GC as capping agents.

Table 9- 2 Capacitances of Mn<sub>3</sub>O<sub>4</sub> and composite electrodes

A <sub>m</sub> mgcm <sup>-2</sup>	Electrolyte	Potential range, V	Reference electrode	v, mVs <sup>-1</sup>	i, Ag <sup>-1</sup>	C <sub>m</sub> , Fg <sup>-1</sup>	C <sub>s</sub> , Fcm <sup>-2</sup>	Ref.
1.21	3M Na <sub>2</sub> SO <sub>4</sub>	-0.2 – +0.8	Ag/AgCl		0.5	210	0.25	70
0.01	2M KCl	0 – +0.7	SCE	5		420	0.0042	71
7.8	0.5M Na <sub>2</sub> SO <sub>4</sub>	0 – +1.0	Ag/AgCl		1	205	1.60	72
3.0	1M Na <sub>2</sub> SO <sub>4</sub>	-0.2 – +0.8	SCE		0.1	171	0.51	73
40	0.5M Na <sub>2</sub> SO <sub>4</sub>	0 – +0.9	SCE	2		153	6.11	22
40	0.5M Na <sub>2</sub> SO <sub>4</sub>	0 – +0.9	SCE	2		82.5	3.3	25
35	0.5M Na <sub>2</sub> SO <sub>4</sub>	0 – +0.9	SCE	2		101	3.52	19
40	0.5M Na <sub>2</sub> SO <sub>4</sub>	0 – +0.9	SCE	2		175.8	7.03	this work*
40	0.5M Na <sub>2</sub> SO <sub>4</sub>	0 – +0.9	SCE		0.075	228	9.13	this work*

A<sub>m</sub>-active mass of electrode, *i*- current density, v scan rate, C<sub>S</sub>=C<sub>m</sub>×A<sub>m</sub>, \*prepared using GC

It was demonstrated previously that activation of Mn<sub>3</sub>O<sub>4</sub> electrodes is less efficient at high scan rates. Therefore, the as-prepared electrodes were also tested at a high scan rate of 50 mV s<sup>-1</sup>. Figure S 9-4 shows variations of capacitances during 1000 cycles

---

for electrodes prepared with different capping agents and without capping agent. The capacitances were normalized by corresponding capacitance value obtained for cycle 1000. The capacitance increased by 21.5, 25.1, and 25.6% for electrodes, prepared using TQ, CT, and GC, respectively. The electrodes, prepared without capping agents showed capacitance variation of 63.7%.

Therefore, the investigations performed at a high scan rate also indicated accelerated activation for electrodes prepared using capping agents. Turning again to the comparison of electrochemical performance of  $\text{Mn}_3\text{O}_4$  and  $\text{MnO}_2$  materials, it should be noted that the capacitance increase of 10-15% was also observed<sup>211</sup> during cycling of  $\text{MnO}_2$  electrodes at a scan rate of  $50 \text{ mV s}^{-1}$  and attributed to changes of electrode morphology. The ability to accelerate and practically avoid activation procedure of  $\text{Mn}_3\text{O}_4$ , coupled with high capacitance achieved in this investigation indicates that  $\text{Mn}_3\text{O}_4$  can outperform  $\text{MnO}_2$  as a cathode material for supercapacitors. From this study it becomes obvious that the reduction of the size of  $\text{Mn}_3\text{O}_4$  nanoparticles to the scale of few nanometers is crucial for enhanced electrochemical performance of this material in supercapacitor electrodes. It should be noted that  $\text{Mn}_3\text{O}_4$  belongs to the spinel family of materials. The rich materials chemistry of spinels allows the fabrication of advanced solid solutions with enhanced properties, such as enhanced capacitance and electrical conductivity<sup>75-77</sup>. Moreover, magnetic properties can be combined with pseudocapacitive properties in solid solutions for the fabrication of magnetically controlled capacitive devices<sup>78,79</sup>. The approach developed in this

---

investigation can be used for accelerating activation of other promising materials<sup>80</sup> for supercapacitor applications.

The Mn<sub>3</sub>O<sub>4</sub>-based positive electrodes prepared in this investigation were combined with FeOOH based negative electrodes<sup>81</sup> for the fabrication of an asymmetric device for operation in Na<sub>2</sub>SO<sub>4</sub> electrolyte in a voltage window of 1.5V (Supplementary Information, Figure 9-S 5).

## 9.5 Conclusions

The use of TQ, CT and GC as capping agents for the synthesis of Mn<sub>3</sub>O<sub>4</sub> facilitated the fabrication of platelet Mn<sub>3</sub>O<sub>4</sub> nanoparticles with a typical size of 5 nm and their efficient mixing with conductive MWCNT additives. The catechol ligands of the capping agents and a positive charge of GC facilitated TQ, CT and GC adsorption on Mn<sub>3</sub>O<sub>4</sub> nanoparticles during synthesis. The reduction of particle size of Mn<sub>3</sub>O<sub>4</sub> during synthesis in the presence of capping agents allowed the fabrication of advanced Mn<sub>3</sub>O<sub>4</sub>-multiwalled carbon nanotube cathodes with high active mass loadings of 40 mg cm<sup>-2</sup>, which showed significant increase in capacitance in 0.5 M Na<sub>2</sub>SO<sub>4</sub> electrolyte. The reduction of the particle size of Mn<sub>3</sub>O<sub>4</sub> to the scale of few nanometers was a key factor for enhanced electrochemical performance of Mn<sub>3</sub>O<sub>4</sub> based supercapacitor electrodes. The highest capacitance of 7.03 F cm<sup>-2</sup> (175.8 F g<sup>-1</sup>) at cyclic voltammetry scan rate of 2 mV s<sup>-1</sup> and 9.13 F cm<sup>-2</sup> (228 F g<sup>-1</sup>) at galvanostatic charge-discharge current density of 3 mA cm<sup>-2</sup> were obtained using GC as a capping

agent. The high capacitance was achieved at a low electrode resistance. Obtained nanostructured  $\text{Mn}_3\text{O}_4$  electrodes outperform  $\text{MnO}_2$  based cathodes of a similar mass. Another important finding is the possibility to avoid the time-consuming activation process for  $\text{Mn}_3\text{O}_4$  based electrodes. The results of this investigation paved the way for application of nanostructured  $\text{Mn}_3\text{O}_4$  in advanced high active mass supercapacitor cathodes. The approach developed in this investigation is promising for the fabrication of other advanced electrode materials for supercapacitors and elimination of their activation procedure.

## **9.6 Acknowledgments.**

This research was funded by the Natural Sciences and Engineering Research Council of Canada, grant number RGPIN-2018-04014. SEM investigations were performed at the Canadian Centre for Electron Microscopy. Lory Wenjuan Yang received a scholarship from the China Scholarship Council.

## 9.7 Supplementary Information

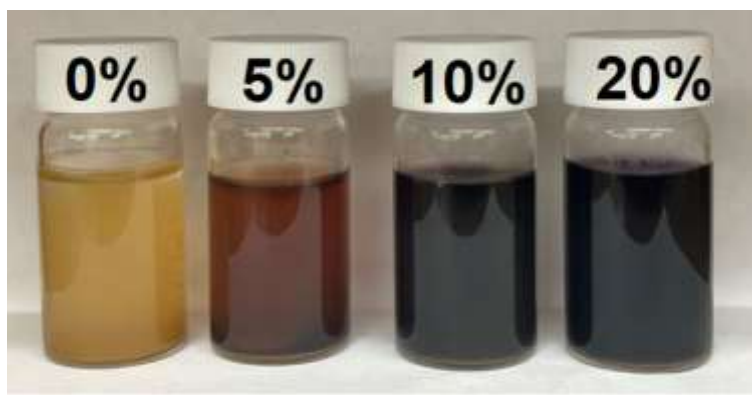


Figure 9-S 1 Sedimentation test for  $\text{Mn}_3\text{O}_4$  suspensions containing 0, 5, 10 and 20 % of GC additive of the mass of  $\text{Mn}_3\text{O}_4$  (100%). The picture shows suspensions 48 h after preparation. A similar behavior was observed for  $\text{Mn}_3\text{O}_4$  suspensions, containing TQ and CT. Suspensions, containing 0 and 5 % GC showed sedimentation. The minimum amount of the capping agent for the formation of stable suspensions was 10%.

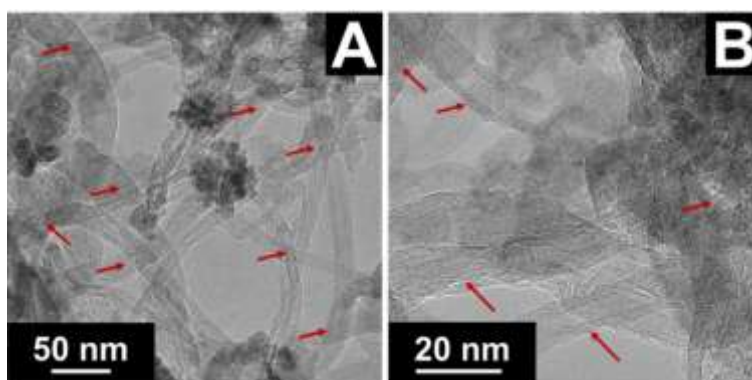


Figure 9-S 2 TEM images at different magnifications (A, B) of  $\text{Mn}_3\text{O}_4$ -MWCNT composite, prepared using GC. Arrows show MWCNT. Talos 200X microscope (Thermo Scientific) was used for analysis.

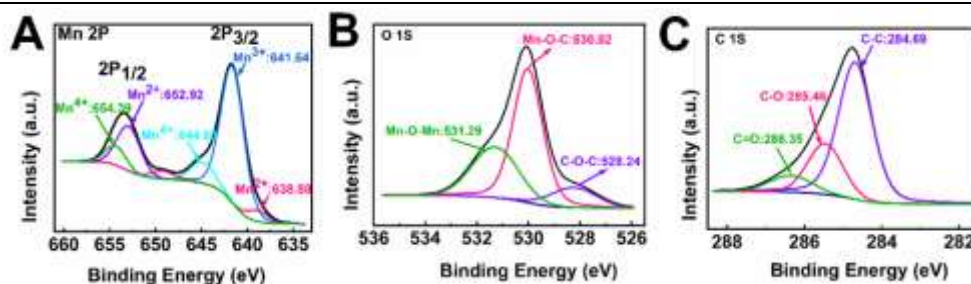


Figure 9-S 3 XPS spectra of Mn<sub>3</sub>O<sub>4</sub>-MWCNT: (A) Mn 2p region, (B) O 1s region and (C) C 1s region respectively, was performed using Quentera II Scanning XPS instrument.

XPS characterization was performed to investigate and verify the chemical composition and bonding state in the Mn<sub>3</sub>O<sub>4</sub>-MWCNT composites. The fitted XPS data are shown in Figure 9-S3. The 2 symmetrical peaks in the Mn 2p<sub>1/2</sub> and Mn 2p<sub>3/2</sub> regions are located at binding energies (BE) of 653.443 and 641.743 eV, respectively<sup>82</sup>. The deconvoluted Mn 2p spectrum shows the coexistence of different valence states of Mn, namely Mn<sup>2+</sup> (638.88 eV), Mn<sup>3+</sup> (641.64 eV) and Mn<sup>4+</sup> (644.88 eV) species. In Figure 9-S3B and C, both O 1s and C 1s spectra were deconvoluted into three peaks, which elucidated the different chemical ambient states of oxygen and carbon, further confirming the coexistence of Mn and C in our samples. In Figure 9-S3B, the three peaks of O 1s are located at 528.24, 530.02 and 531.29 eV, which are attributed to C–O–C, Mn–O–C, and Mn–O–Mn<sup>82,83</sup>. Furthermore, three bonding modes of C–C, C–O, and C=O corresponded to three deconvoluted peaks at 284.69, 285.46, and 286.35 eV in the O1s profile, respectively.<sup>84</sup>

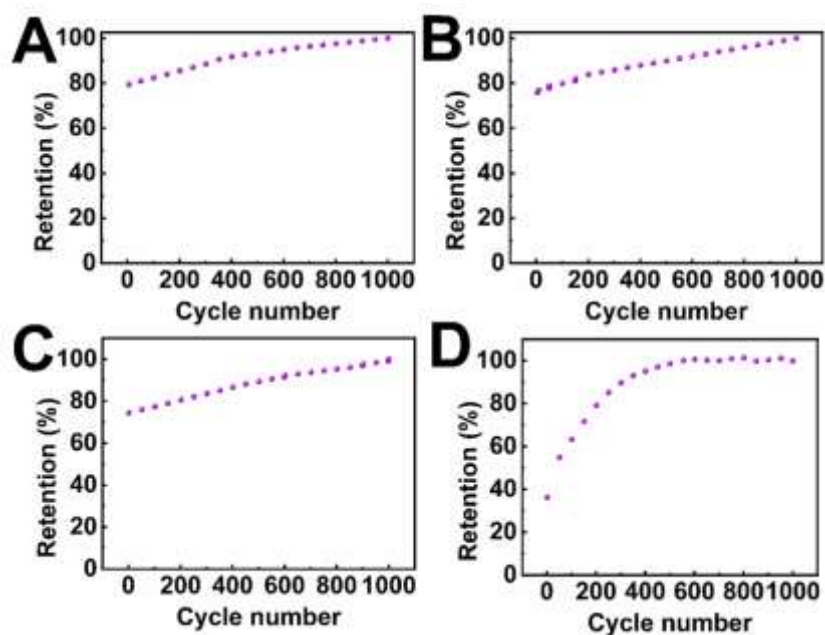


Figure 9-S 4 Capacitance retention of electrodes prepared by (A) TQ, (B) CT and (C) GC as capping and dispersing agents and (D) without capping agent, obtained from CV data at a sweep rate of  $50 \text{ mV s}^{-1}$ .

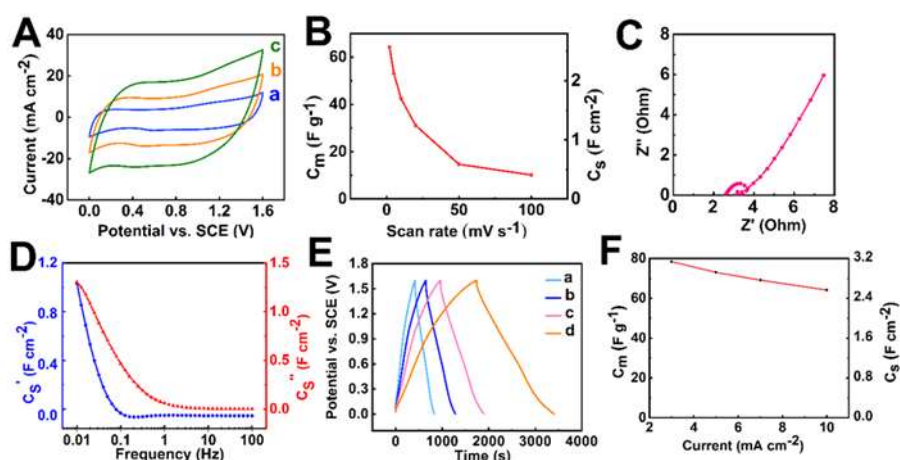


Figure 9-S 5 Electrochemical testing results for asymmetric  $\text{Mn}_3\text{O}_4\text{-MWCNT/ FeOOH-MWCNT}$  device. Electrochemical studies were performed in aqueous  $0.5 \text{ M Na}_2\text{SO}_4$  electrolyte using PARSTAT 2273 potentiostat (AMETEK): (A) CV curves at (a–c) 2, 5, and  $10 \text{ mV s}^{-1}$ , (B) capacitances versus CV scan rate, (C) Nyquist plots, and (D) complex capacitance  $C_s'$  (blue line) and  $C_s''$  (red line) versus frequency, (E) GCD curves at (a) 10, (b) 7, (c) 5, and (d)  $3 \text{ mA cm}^{-2}$ , (D) capacitances versus current density.

---

## 9.8 References

- 1 Patil, T. S., Gangawane, S. A. & Takale, M. V. A Review on Mn<sub>3</sub>O<sub>4</sub> and Its Composite Nanomaterials of Diverse Morphologies as an Electrode Material in Supercapacitors. *International Journal of Scientific Research in Science and Technology* **8**, 520-526 (2021).
- 2 Sayyed, S. G., Shaikh, A. V., Dubal, D. P. & Pathan, H. M. Paving the Way towards Mn<sub>3</sub>O<sub>4</sub> Based Energy Storage Systems. *ES Energy & Environment* **14**, 3-21 (2021).
- 3 Priyadarsini, S. S., Saxena, S., Pradhan, J. R. & Dasgupta, S. Inkjet-printed transparent micro-supercapacitors with morphology tailored co-continuous mesoporous Mn<sub>3</sub>O<sub>4</sub>. *Journal of Materials Chemistry A* **10**, 21551-21564 (2022). <https://doi.org:10.1039/D2TA04901E>
- 4 Liu, C. *et al.* Coherent Mn<sub>3</sub>O<sub>4</sub>-carbon nanocomposites with enhanced energy-storage capacitance. *Nano Research* **8**, 3372-3383 (2015).
- 5 Wang, Z., Fang, J., Hao, Y., Chen, C. & Zhang, D. High-performance Mn<sub>3</sub>O<sub>4</sub> nanomaterials synthesized via a new two-step hydrothermal method in asymmetric supercapacitors. *Materials Science in Semiconductor Processing* **130**, 105823 (2021).
- 6 Sahoo, S., Kumar, R., Joanni, E., Singh, R. K. & Shim, J.-J. Advances in pseudocapacitive and battery-like electrode materials for high performance supercapacitors. *Journal of Materials Chemistry A* **10**, 13190-13240 (2022). <https://doi.org:10.1039/D2TA02357A>
- 7 Lee, H.-M., Jeong, G. H., Kang, D. W., Kim, S.-W. & Kim, C.-K. Direct and environmentally benign synthesis of manganese oxide/graphene composites from graphite for electrochemical capacitors. *Journal of Power Sources* **281**, 44-48 (2015).
- 8 Kerangueven, G., Faye, J., Royer, S. & Pronkin, S. N. Electrochemical properties and capacitance of Hausmannite Mn<sub>3</sub>O<sub>4</sub>-carbon composite synthesized by in situ autocombustion method. *Electrochimica Acta* **222**, 755-764 (2016).
- 9 Aswathy, R., Ulaganathan, M. & Ragupathy, P. Mn<sub>3</sub>O<sub>4</sub> nanoparticles grown on surface activated graphite paper for aqueous asymmetric supercapacitors. *Journal of Alloys and Compounds* **767**, 141-150 (2018).
- 10 Patra, A. *et al.* Understanding the charge storage mechanism of supercapacitors: in situ/operando spectroscopic approaches and theoretical investigations. *Journal of Materials Chemistry A* **9**, 25852-25891 (2021). <https://doi.org:10.1039/D1TA07401F>
- 11 Xiao, Y. *et al.* Electrolyte and composition effects on the performances of asymmetric supercapacitors constructed with Mn<sub>3</sub>O<sub>4</sub> nanoparticles-graphene nanocomposites. *Journal of Power Sources* **246**, 926-933 (2014).

- 
- <https://doi.org/https://doi.org/10.1016/j.jpowsour.2013.07.118>
- 12 Liu, C.-L., Chang, K.-H., Hu, C.-C. & Wen, W.-C. Microwave-assisted hydrothermal synthesis of Mn<sub>3</sub>O<sub>4</sub>/reduced graphene oxide composites for high power supercapacitors. *Journal of Power Sources* **217**, 184-192 (2012).  
<https://doi.org/https://doi.org/10.1016/j.jpowsour.2012.05.109>
- 13 Nawwar, M., Poon, R., Sahu, R. P., Puri, I. K. & Zhitomirsky, I. Fe<sub>3</sub>O<sub>4</sub> spinel-Mn<sub>3</sub>O<sub>4</sub> spinel supercapacitor prepared using Celestine blue as a dispersant, capping agent and charge transfer mediator. *Ceramics International* **46**, 18851-18858 (2020).
- 14 Suktha, P., Phattharasupakun, N., Dittanet, P. & Sawangphruk, M. Charge storage mechanisms of electrospun Mn<sub>3</sub>O<sub>4</sub> nanofibres for high-performance supercapacitors. *RSC advances* **7**, 9958-9963 (2017).
- 15 Yeager, M. P. *et al.* Pseudocapacitive Hausmannite Nanoparticles with (101) Facets: Synthesis, Characterization, and Charge-Transfer Mechanism. *ChemSusChem* **6**, 1983-1992 (2013).
- 16 Liu, C. *et al.* The effect of electrolyte cation on electrochemically induced activation and capacitive performance of Mn<sub>3</sub>O<sub>4</sub> electrodes. *Electrochimica Acta* **324**, 134894 (2019).
- 17 Wu, T.-H. *et al.* Charge storage mechanism of activated manganese oxide composites for pseudocapacitors. *Journal of Materials Chemistry A* **3**, 12786-12795 (2015).
- 18 Rorabeck, K. & Zhitomirsky, I. Salting-out aided dispersive extraction of Mn<sub>3</sub>O<sub>4</sub> nanoparticles and carbon nanotubes for application in supercapacitors. *Colloids and Surfaces A: Physicochemical and Engineering Aspects* **618**, 126451 (2021).
- 19 Poon, R. & Zhitomirsky, I. High areal capacitance of Mn<sub>3</sub>O<sub>4</sub>-carbon nanotube electrodes. *Materials Letters* **215**, 4-7 (2018).
- 20 Nagarajan, N., Cheong, M. & Zhitomirsky, I. Electrochemical capacitance of MnO<sub>x</sub> films. *Materials Chemistry and Physics* **103**, 47-53 (2007).  
<https://doi.org/https://doi.org/10.1016/j.matchemphys.2007.01.005>
- 21 Milne, J. & Zhitomirsky, I. Application of octanohydroxamic acid for liquid-liquid extraction of manganese oxides and fabrication of supercapacitor electrodes. *Journal of Colloid and Interface Science* **515**, 50-57 (2018).  
<https://doi.org/https://doi.org/10.1016/j.jcis.2018.01.021>
- 22 Yang, W. & Zhitomirsky, I. Colloidal Processing of Mn<sub>3</sub>O<sub>4</sub>-Carbon Nanotube Nanocomposite Electrodes for Supercapacitors. *Nanomaterials* **12**, 803 (2022).
- 23 Poon, R., Liang, W. & Zhitomirsky, I. Mn<sub>3</sub>O<sub>4</sub> and (ZnFe) OOH Composites for Supercapacitors with High Active Mass. *Metallurgical and Materials Transactions A* **51**, 855-862 (2020).
- 24 Ata, M. S., Milne, J. & Zhitomirsky, I. Fabrication of Mn<sub>3</sub>O<sub>4</sub>-carbon nanotube composites with high areal capacitance using cationic and anionic dispersants. *Journal of Colloid and Interface Science* **512**, 758-766 (2018).

- 
- <https://doi.org/https://doi.org/10.1016/j.jcis.2017.10.110>
- 25 Yang, W., Eraky, H., Zhang, C., Hitchcock, A. P. & Zhitomirsky, I. Scanning transmission X-ray microscopy studies of electrochemical activation and capacitive behavior of Mn<sub>3</sub>O<sub>4</sub> supercapacitor electrodes. *Journal of Materials Chemistry A* **10**, 18267-18277 (2022).
- 26 Li, J. & Zhitomirsky, I. Cathodic electrophoretic deposition of manganese dioxide films. *Colloids and Surfaces A: Physicochemical and Engineering Aspects* **348**, 248-253 (2009).
- 27 Luo, Y. Preparation of MnO<sub>2</sub> nanoparticles by directly mixing potassium permanganate and polyelectrolyte aqueous solutions. *Materials Letters* **61**, 1893-1895 (2007).
- 28 Lim, Y. G., Kim, H. J. & Park, K. A novel method for synthesizing manganese dioxide nanoparticles using diethylenetriamine pentaacetic acid as a metal ion chelator. *Journal of Industrial and Engineering Chemistry* **93**, 407-414 (2021).
- 29 Kamata, K. *et al.* β-MnO<sub>2</sub> nanoparticles as heterogenous catalysts for aerobic oxidative transformation of alcohols to carbonyl compounds, nitriles, and amides. *Catalysis Science & Technology* **12**, 6219-6230 (2022).
- 30 Jin, M. *et al.* Shape-controlled synthesis of copper nanocrystals in an aqueous solution with glucose as a reducing agent and hexadecylamine as a capping agent. *Angewandte Chemie International Edition* **50**, 10560-10564 (2011).
- 31 Jeyarani, W. J., Tenkyong, T., Bachan, N., Kumar, D. A. & Shyla, J. M. An investigation on the tuning effect of glucose-capping on the size and bandgap of CuO nanoparticles. *Advanced Powder Technology* **27**, 338-346 (2016).
- 32 Pawar, M. & Chaure, S. Synthesis of CdS nanoparticles using glucose as a capping agent. *Chalcogenide Lett* **6**, 689-693 (2009).
- 33 Ata, M., Liu, Y. & Zhitomirsky, I. A review of new methods of surface chemical modification, dispersion and electrophoretic deposition of metal oxide particles. *Rsc Advances* **4**, 22716-22732 (2014).
- 34 Chalmers, R. A. & Telling, G. M. A reassessment of rhodizonic acid as a qualitative reagent. *Microchimica Acta* **55**, 1126-1135 (1967).
- 35 Yao, M.-S. *et al.* A comparative study of honeycomb-like 2D π-conjugated metal-organic framework chemiresistors: conductivity and channels. *Dalton Transactions* **50**, 13236-13245 (2021).
- 36 Zhao, Z.-H. *et al.* A Cu (111)@ metal-organic framework as a tandem catalyst for highly selective CO<sub>2</sub> electroreduction to C<sub>2</sub>H<sub>4</sub>. *Chemical Communications* **57**, 12764-12767 (2021).
- 37 Jiang, Q. *et al.* A redox-active 2D metal-organic framework for efficient lithium storage with extraordinary high capacity. *Angewandte Chemie International Edition* **59**, 5273-5277 (2020).
- 38 Zhao, J. *et al.* Additive Manufacturing of Two-Dimensional Conductive Metal-Organic Framework with Multidimensional Hybrid Architectures for High-Performance Energy Storage. *Nano Letters* **22**, 1198-1206 (2022).

- 
- <https://doi.org/10.1021/acs.nanolett.1c04367>
- 39 Ye, R.-H., Chen, J.-Y., Huang, D.-H., Wang, Y.-J. & Chen, S. Electrochemical Sensor Based on Glassy-Carbon Electrode Modified with Dual-Ligand EC-MOFs Supported on rGO for BPA. *Biosensors* **12**, 367 (2022).
- 40 Lekbach, Y. *et al.* Catechin hydrate as an eco-friendly biocorrosion inhibitor for 304L stainless steel with dual-action antibacterial properties against *Pseudomonas aeruginosa* biofilm. *Corrosion Science* **157**, 98-108 (2019).
- 41 Yusoff, A. H. M., Salimi, M. N., Gopinath, S. C. B., Abdullah, M. M. A. & Samsudin, E. M. Catechin adsorption on magnetic hydroxyapatite nanoparticles: A synergistic interaction with calcium ions. *Materials Chemistry and Physics* **241**, 122337 (2020).  
[https://doi.org:https://doi.org/10.1016/j.matchemphys.2019.122337](https://doi.org/https://doi.org/10.1016/j.matchemphys.2019.122337)
- 42 Ramos-Tejada, M. M. *et al.* Investigation of alumina/(+)-catechin system properties. Part II:  $\zeta$ -potential and surface free energy changes of alumina. *Colloids and Surfaces B: Biointerfaces* **24**, 309-320 (2002).  
[https://doi.org:https://doi.org/10.1016/S0927-7765\(01\)00285-5](https://doi.org/https://doi.org/10.1016/S0927-7765(01)00285-5)
- 43 Zhang, C. & Zhitomirsky, I. Influence of High Energy Ball Milling and Dispersant on Capacitive Properties of Fe<sub>2</sub>O<sub>3</sub>—Carbon Nanotube Composites. *Journal of Composites Science* **6**, 177 (2022).
- 44 Preisler, P. W., Berger, L. & Hill, E. S. Oxidation—Reduction Potentials and Ionization Constants of the Reversible Series: Hexahydroxybenzene—Tetrahydroxyquinone—Rhodizonic Acid. *Journal of the American Chemical Society* **69**, 326-329 (1947).
- 45 Salimi, A., Abdi, K. & Khayatian, G.-R. Amperometric Detection of Dopamine in the Presence of Ascorbic Acid Using a Nafion Coated Glassy Carbon Electrode Modified with Catechin Hydrate as a Natural Antioxidant. *Microchimica Acta* **144**, 161-169 (2004). [https://doi.org:10.1007/s00604-003-0048-7](https://doi.org/10.1007/s00604-003-0048-7)
- 46 Suroviec, A. H., Jones, K. & Sarabia, G. Quantification of catechins in tea using cyclic voltammetry. *Journal of Chemical Education* **96**, 366-371 (2019).
- 47 Xu, B., Jiao, K., Ren, Y. & Sun, W. Electrochemical and Spectroscopic Studies on the Interaction of Gallocyanine with DNA. *Journal of the Chinese Chemical Society* **54**, 917-924 (2007).
- 48 Kim, S.-H., Song, S.-H. & Yoo, Y.-J. Characteristics of mediated enzymatic nitrate reduction by gallocyanine-bound nanoporous electrode. *Journal of microbiology and biotechnology* **16**, 505-510 (2006).
- 49 Giovannelli, F. *et al.* Synthesis of manganese spinel nanoparticles at room temperature by coprecipitation. *Journal of Solid State Chemistry* **192**, 109-112 (2012).
- 50 Pang, X., Imin, P., Zhitomirsky, I. & Adronov, A. Amperometric detection of glucose using a conjugated polyelectrolyte complex with single-walled carbon nanotubes. *Macromolecules* **43**, 10376-10381 (2010).
- 51 Chen, R., Yu, M., Sahu, R. P., Puri, I. K. & Zhitomirsky, I. The Development

- of Pseudocapacitor Electrodes and Devices with High Active Mass Loading. *Advanced Energy Materials* **10**, 1903848 (2020).  
<https://doi.org/10.1002/aenm.201903848>
- 52 Rani, B. J. *et al.* Synthesis and characterization of hausmannite (Mn<sub>3</sub>O<sub>4</sub>) nanostructures. *Surfaces and Interfaces* **11**, 28-36 (2018).
- 53 Yousefi, T., Golikand, A. N., Mashhadizadeh, M. H. & Aghazadeh, M. Hausmannite nanorods prepared by electrodeposition from nitrate medium via electrogeneration of base. *Journal of the Taiwan Institute of Chemical Engineers* **43**, 614-618 (2012).
- 54 Ata, M., Milne, J. & Zhitomirsky, I. Fabrication of Mn<sub>3</sub>O<sub>4</sub>-carbon nanotube composites with high areal capacitance using cationic and anionic dispersants. *Journal of colloid and interface science* **512**, 758-766 (2018).
- 55 Dhaouadi, H., Madani, A. & Touati, F. Synthesis and spectroscopic investigations of Mn<sub>3</sub>O<sub>4</sub> nanoparticles. *Materials Letters* **64**, 2395-2398 (2010).
- 56 Li, Q. *et al.* Performance of chemically synthesized Mn<sub>3</sub>O<sub>4</sub>/rGO nanocomposite for electrochemical supercapacitor: a cost-effective high-performance electrode. *Nanotechnology* **31**, 415403 (2020).
- 57 Du, J. *et al.* Hausmannite Mn<sub>3</sub>O<sub>4</sub> nanorods: synthesis, characterization and magnetic properties. *Nanotechnology* **17**, 4923 (2006).
- 58 Purushothaman, S., Jeyasubramanian, K. & Hikku, G. In-situ fabrication of sulphur decorated elongated cuboctahedron shaped Mn<sub>3</sub>O<sub>4</sub> as high-performance active charge storage material for supercapacitor application. *Surface and Coatings Technology* **426**, 127782 (2021).
- 59 Yousefi, T., Golikand, A. N., Mashhadizadeh, M. H. & Aghazadeh, M. High temperature and low current density synthesis of Mn<sub>3</sub>O<sub>4</sub> porous nano spheres: characterization and electrochemical properties. *Current Applied Physics* **12**, 544-549 (2012).
- 60 Philip, D., John, A., Panicker, C. Y. & Varghese, H. T. FT-Raman, FT-IR and surface enhanced Raman scattering spectra of sodium salicylate. *Spectrochimica Acta Part A: Molecular and Biomolecular Spectroscopy* **57**, 1561-1566 (2001).
- 61 Wu, K., Wang, Y. & Zhitomirsky, I. Electrophoretic deposition of TiO<sub>2</sub> and composite TiO<sub>2</sub>-MnO<sub>2</sub> films using benzoic acid and phenolic molecules as charging additives. *Journal of colloid and interface science* **352**, 371-378 (2010). <https://doi.org/https://doi:10.1016/j.jcis.2010.08.059>
- 62 Su, Y. & Zhitomirsky, I. Electrophoretic deposition of graphene, carbon nanotubes and composite films using methyl violet dye as a dispersing agent. *Colloids and Surfaces A: Physicochemical and Engineering Aspects* **436**, 97-103 (2013).
- 63 Mohammed-Ziegler, I. & Billes, F. Vibrational spectroscopic calculations on pyrogallol and gallic acid. *Journal of Molecular Structure: THEOCHEM* **618**,

- 259-265 (2002).
- 64 Li, J., Yang, Q. M. & Zhitomirsky, I. Nickel foam-based manganese dioxide–carbon nanotube composite electrodes for electrochemical supercapacitors. *Journal of Power Sources* **185**, 1569-1574 (2008).
- 65 Wang, Y., Liu, Y. & Zhitomirsky, I. Surface modification of MnO<sub>2</sub> and carbon nanotubes using organic dyes for nanotechnology of electrochemical supercapacitors. *Journal of Materials Chemistry A* **1**, 12519-12526 (2013).
- 66 Kötz, R. & Carlen, M. Principles and applications of electrochemical capacitors. *Electrochimica acta* **45**, 2483-2498 (2000).
- 67 Shi, K. & Zhitomirsky, I. Fabrication of polypyrrole-coated carbon nanotubes using oxidant–surfactant nanocrystals for supercapacitor electrodes with high mass loading and enhanced performance. *ACS applied materials & interfaces* **5**, 13161-13170 (2013).
- 68 Nawwar, M. *et al.* High areal capacitance of Fe<sub>3</sub>O<sub>4</sub>-decorated carbon nanotubes for supercapacitor electrodes. *Carbon Energy* **1**, 124-133 (2019). <https://doi.org/10.1002/cey2.6>
- 69 Ata, M. S., Poon, R., Syed, A. M., Milne, J. & Zhitomirsky, I. New developments in non-covalent surface modification, dispersion and electrophoretic deposition of carbon nanotubes. *Carbon* **130**, 584-598 (2018). <https://doi.org/10.1016/j.carbon.2018.01.066>
- 70 Qi, Z., Younis, A., Chu, D. & Li, S. A facile and template-free one-pot synthesis of Mn<sub>3</sub>O<sub>4</sub> nanostructures as electrochemical supercapacitors. *Nano-micro letters* **8**, 165-173 (2016).
- 71 An, G. *et al.* Low-temperature synthesis of Mn<sub>3</sub>O<sub>4</sub> nanoparticles loaded on multi-walled carbon nanotubes and their application in electrochemical capacitors. *Nanotechnology* **19**, 275709 (2008).
- 72 Yang, S., Song, X., Zhang, P. & Gao, L. Crumpled nitrogen-doped graphene–ultrafine Mn<sub>3</sub>O<sub>4</sub> nanohybrids and their application in supercapacitors. (2013).
- 73 Fan, Y., Zhang, X., Liu, Y., Cai, Q. & Zhang, J. One-pot hydrothermal synthesis of Mn<sub>3</sub>O<sub>4</sub>/graphene nanocomposite for supercapacitors. *Materials Letters* **95**, 153-156 (2013).
- 74 Rorabeck, K. & Zhitomirsky, I. Dispersant Molecules with Functional Catechol Groups for Supercapacitor Fabrication. *Molecules* **26**, 1709 (2021).
- 75 Heiba, Z. K., Deyab, M. A., El-naggar, A. M. & Mohamed, M. B. Electrochemical performance of quaternary (1-x)ZnMn<sub>2</sub>O<sub>4</sub>/(x)MgFe<sub>2</sub>O<sub>4</sub> solid solution as supercapacitor electrode. *Ceramics International* **47**, 7475-7486 (2021). <https://doi.org/10.1016/j.ceramint.2020.11.088>
- 76 Yamanaka, T., Shimazu, H. & Ota, K. Electric conductivity of Fe<sub>2</sub>SiO<sub>4</sub>–Fe<sub>3</sub>O<sub>4</sub> spinel solid solutions. *Physics and Chemistry of Minerals* **28**, 110-118 (2001).
- 77 Yamanaka, T. *et al.* Enhancement of electrical conductivity to metallization of Mn<sub>3-x</sub>Fe<sub>x</sub>O<sub>4</sub> spinel and postspinel with elevating pressure. *Journal of Physics and Chemistry of Solids* **167**, 110721 (2022).

- 
- <https://doi.org:https://doi.org/10.1016/j.jpccs.2022.110721>
- 78 Liang, W., Yang, W., Sakib, S. & Zhitomirsky, I. Magnetic CuFe<sub>2</sub>O<sub>4</sub> Nanoparticles with Pseudocapacitive Properties for Electrical Energy Storage. *Molecules* **27**, 5313 (2022).
- 79 Bharadwaj, P. S. J., Gannavarapu, K. P., Kollipara, V. S. & Dandamudi, R. B. Study of magneto-supercapacitance properties of nickel cobalt ferrite-activated carbon composite. *Journal of Energy Storage* **36**, 102444 (2021).  
<https://doi.org:https://doi.org/10.1016/j.est.2021.102444>
- 80 Wallar, C., Poon, R. & Zhitomirsky, I. High areal capacitance of v<sub>2</sub>o<sub>3</sub>-carbon nanotube electrodes. *Journal of The Electrochemical Society* **164**, A3620 (2017).
- 81 Chen, R., Puri, I. & Zhitomirsky, I. Polypyrrole-carbon nanotube-FeOOH composites for negative electrodes of asymmetric supercapacitors. *Journal of The Electrochemical Society* **166**, A935 (2019).
- 82 Hiremath, V., Cho, M. & Seo, J. G. Self-assembled Mn<sub>3</sub>O<sub>4</sub> nano-clusters over carbon nanotube threads with enhanced supercapacitor performance. *New Journal of Chemistry* **42**, 19608-19614 (2018).
- 83 Jiang, M. *et al.* Facile electrodeposition of Mn<sub>3</sub>O<sub>4</sub> nanoparticles on wood-derived porous carbon for high-performance asymmetric supercapacitor. *Diamond and Related Materials* **118**, 108506 (2021).
- 84 Yang, Z. *et al.* Facile synthesis of coaxial CNTs/MnO<sub>x</sub>-carbon hybrid nanofibers and their greatly enhanced lithium storage performance. *Scientific reports* **5**, 17473 (2015).

---

# **Chapter 10 Electrochemical and scanning transmission X-ray microscopy studies of MnO<sub>2</sub> and Mn<sub>3</sub>O<sub>4</sub> for supercapacitor cathodes: influence of fabrication method and electrochemical activation on charge storage**

Wenjuan Yang,<sup>1§</sup> Haytham Eraky,<sup>2§</sup> Chunyang Zhang,<sup>1,3</sup> Adam P. Hitchcock<sup>1</sup> and Igor

Zhitomirsky<sup>2\*</sup>

<sup>1</sup>Dept of Materials Science and Engineering, McMaster University, Hamilton, ON

Canada L8S4M1

<sup>2</sup>Dept. of Chemistry & Chemical Biology, McMaster University, Hamilton, ON

Canada L8S4M1

<sup>3</sup>Dept. of Chemical Engineering, McMaster University, Hamilton, ON Canada

L8S4M1

<sup>§</sup>These authors contributed equally

Electrode materials fabrication and electrochemical test of SC was performed by

Wenjuan Yang, and STXM synchrotron measurements were performed at the CLS,

which is operated and analyzed by Haytham Eraky

\* Corresponding author, email: [zhitom@mcmaster.ca](mailto:zhitom@mcmaster.ca)

Copyright 2024, reproduced with permission from Elsevier.

---

## 10.1 Abstract

This investigation is motivated by increasing interest in  $\text{Mn}_3\text{O}_4$  as a promising alternative to  $\text{MnO}_2$  for supercapacitors with high active mass and the need for better understanding of charging and electrode activation mechanisms. High energy ball milling (HEBM) of chemically precipitated  $\text{MnO}_2$  and  $\text{Mn}_3\text{O}_4$  in the presence of quercetin resulted in significant capacitance increase. The use of  $\text{Mn}^{2+}$  salts for  $\text{Mn}_3\text{O}_4$  synthesis facilitated the application of quercetin as a new chelating capping agent for synthesis of  $\text{Mn}_3\text{O}_4$ , which showed higher capacitance, compared to HEBM  $\text{Mn}_3\text{O}_4$ . The capacitance of  $\text{Mn}_3\text{O}_4$  prepared using quercetin was  $6.0 \text{ F cm}^{-2}$  ( $149.50 \text{ F g}^{-1}$ ) for cyclic voltammetry at  $2 \text{ mVs}^{-1}$  and  $8.03 \text{ F cm}^{-2}$  ( $200.93 \text{ F g}^{-1}$ ) for chronopotentiometry at  $3 \text{ mA cm}^{-2}$ , which is on-par with the capacitance of  $\text{MnO}_2$ . The time-consuming activation procedure, which limits  $\text{Mn}_3\text{O}_4$  applications, was significantly accelerated for HEBM  $\text{Mn}_3\text{O}_4$  and practically eliminated for  $\text{Mn}_3\text{O}_4$  prepared using quercetin as a capping agent. Soft X-ray scanning transmission X-ray microscopy (STXM), an advanced synchrotron based analytical microscopy, was used at the O 1s and Mn 2p edges to identify and quantitatively map the Mn oxidation states present in  $\text{Mn}_3\text{O}_4$  materials. Variable and fixed sweep rate electrochemical cycling procedures were used for the analysis of oxidation state of Mn and charging mechanism using STXM analysis coupled with electrochemical testing. The combination of STXM and electrochemistry provided valuable insights into the activation kinetics and charging mechanism. The STXM results showed that the tested materials contained mixtures of

Mn<sup>2+</sup>, Mn<sup>3+</sup> and Mn<sup>4+</sup> oxides. A small amount of MnO phase in the tested samples indicated partial reduction. The higher content of MnO<sub>2</sub> phase in the tested Mn<sub>3</sub>O<sub>4</sub> prepared using quercetin as a capping agent, compared to HEBM Mn<sub>3</sub>O<sub>4</sub>, correlated with higher capacitance and the ability to eliminate the activation procedure.

## 10.2 Introduction

Manganese oxides, such as MnO<sub>2</sub> and Mn<sub>3</sub>O<sub>4</sub>, are promising materials for the cathodes of energy storage supercapacitors (SC) <sup>1-3</sup>. MnO<sub>2</sub> has a high theoretical capacitance (1370 F g<sup>-1</sup>) <sup>4,5</sup> and a relatively large operational voltage window in neutral electrolytes, such as Na<sub>2</sub>SO<sub>4</sub> and K<sub>2</sub>SO<sub>4</sub>. The theoretical capacitance of MnO<sub>2</sub> was estimated based on the Mn<sup>4+</sup>/Mn<sup>3+</sup> redox reactions and electrolyte cation adsorption and intercalation<sup>6</sup>. It is widely accepted that the charge storage mechanism of MnO<sub>2</sub> in neutral electrolytes involves the following reaction <sup>4,6</sup>:



where C<sup>+</sup> = K<sup>+</sup>, Na<sup>+</sup>, Li<sup>+</sup>, H<sup>+</sup>. The variation of the valence of Mn ions during charge-discharge has been confirmed by X-ray photoelectron spectroscopy <sup>7</sup>. However, investigations also showed that the charge storage mechanism is more complicated. It was found that electrolyte anions can contribute to charge compensation of Mn ions <sup>7</sup>. A hole redistribution model was proposed to explain higher-than-theoretical capacitance observed in experimental studies of MnO<sub>2</sub>. It was hypothesized that not only change in the valence of the Mn ions, but also hole redistribution toward the

---

oxygen sites, contribute to the charge-discharge mechanism <sup>7</sup>. These studies highlighted the benefits of non-stoichiometric MnO<sub>x</sub> phases for energy storage and generated interest in investigating charge storage by both Mn and O sites <sup>7</sup>. The formation of oxygen vacancies in MnO<sub>2</sub> was found to be a promising avenue for enhancing conductivity and capacitance <sup>8,9</sup>.

Equation (10-1) predicts that MnO<sub>2</sub> particle size reduction can potentially improve electrolyte access to the electrode material surface and enhance capacitance. Many investigations demonstrated capacitance increase <sup>10,11</sup> in nanostructured MnO<sub>2</sub>.

However, experimental studies did not find correlation between BET surface area and pseudocapacitance <sup>12,13</sup>. The materials with lower surface area showed higher capacitance, compared to the electrodes with higher surface area <sup>12</sup>. It was demonstrated that the charging mechanism is influenced by various factors, such as the nature of electrolyte, and MnO<sub>2</sub> transformation to a stable Mn<sub>3</sub>O<sub>4</sub> spinel phase <sup>4</sup>.

Operando Raman spectroscopy studies<sup>14</sup> revealed the electrolyte cation size effect on charge storage of MnO<sub>2</sub> electrodes. Other investigations showed the effect of physisorbed water <sup>15</sup>, pH and other factors <sup>16</sup> on pseudocapacitance. *In-situ* quartz crystal microbalance studies <sup>17</sup> demonstrated the effect of ion desolvation kinetics at the electrode surface on capacitance. The variety of MnO<sub>2</sub> crystal structures provides multiple avenues for electrochemical performance optimization <sup>7</sup>. Despite the tremendous progress achieved in the synthesis of MnO<sub>2</sub>, further advances are necessary to reach the full potential of this material in high active mass electrodes

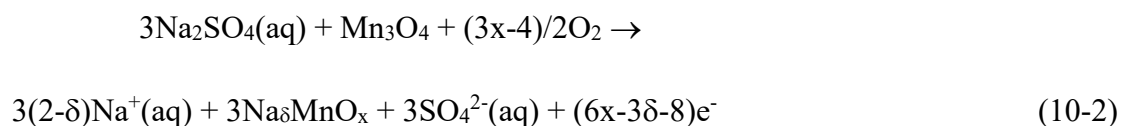
---

(HAME) <sup>10</sup>. There is a high demand to improve the materials performance in HAME due to specific capacitance reduction with increasing active mass (AM), especially at fast charging speeds <sup>10</sup>.

A major drawback of MnO<sub>2</sub> synthesis procedures is the need for permanganate precursors such as KMnO<sub>4</sub> or NaMnO<sub>4</sub>, which react with organic capping agents. Therefore, it is challenging to reduce particle size and eliminate agglomeration during synthesis. The synthesis of MnO<sub>2</sub> from KMnO<sub>4</sub> solutions usually results in the formation of K<sub>x</sub>MnO<sub>2+y</sub> phases, which showed deviation from ideal capacitive behavior as was indicated by the appearance of redox peaks in the cyclic voltammograms <sup>6</sup>. Such redox peaks were not observed for pure MnO<sub>2</sub>. However, the K-cation pre-inserted K<sub>x</sub>MnO<sub>2+y</sub> phases <sup>6</sup> showed higher capacitance, compared to MnO<sub>2</sub>.

Mn<sub>3</sub>O<sub>4</sub> represents a promising alternative to MnO<sub>2</sub> for charge storage in supercapacitor cathodes. The synthesis of Mn<sub>3</sub>O<sub>4</sub> nanoparticles of controlled size is facilitated by the beneficial use of Mn<sup>2+</sup> salts, which are chemically compatible with various organic capping agent molecules. Another attractive property of Mn<sub>3</sub>O<sub>4</sub> is its ability to form solid solutions with other spinel compounds. Therefore, the properties of Mn<sub>3</sub>O<sub>4</sub> can be modified by doping with different elements. The bottleneck limiting Mn<sub>3</sub>O<sub>4</sub> applications in HAME is the need for electrode activation <sup>18</sup>. Cycling of Mn<sub>3</sub>O<sub>4</sub> in Na<sub>2</sub>SO<sub>4</sub> electrolyte resulted in a gradual capacitance increase <sup>18</sup>. This activation procedure is time-consuming and the activation process is influenced by

sweep rate. It was hypothesized that activation leads to oxidation of Mn and adsorption of Na to form  $\text{Na}_\delta\text{MnO}_x$  species:



The charging mechanism for the activated  $\text{Mn}_3\text{O}_4$  was suggested to be similar to that of  $\text{MnO}_2$  and involved  $\text{Na}_\delta\text{MnO}_x$  species in reaction (10-1). However, as it was described above, the charging mechanism of  $\text{MnO}_2$  is not well understood. It is influenced by oxygen stoichiometry, hole redistribution, contribution of O sites, and other factors. Therefore, further investigations are necessary to better understand the charging mechanism and thereby develop advanced HAME.

Scanning transmission X-ray microscopy (STXM)<sup>19-21</sup> is a synchrotron-based technique that provides X-ray absorption based spectroscopic identification and spatially resolved quantitative mapping of chemical components with a spatial resolution of  $\sim 30$  nm<sup>19-22</sup>. Chemical speciation is provided by near-edge X-ray absorption fine structure (NEXAFS) spectroscopy<sup>23</sup>. Most electrochemical applications, in particular, those related to energy conversion and storage, involve chemical reactions that take place at an electrode - electrolyte interface<sup>22, 24</sup>. STXM analysis can provide insight into electrochemical charging and discharging processes in different systems, particularly, supercapacitors. Thus, STXM is a useful tool to investigate the activation of  $\text{Mn}_3\text{O}_4$  based-electrodes as well as the charging/discharging mechanism<sup>18</sup>.

In this investigation  $\text{MnO}_2$  and  $\text{Mn}_3\text{O}_4$  high active mass supercapacitor electrodes were fabricated using chemical precipitation followed by high energy ball milling (HEBM) or by synthesis of  $\text{Mn}_3\text{O}_4$  using quercetin as a capping agent. Two different activation procedures were applied. Electrochemical testing methods were then used to investigate capacitive behaviour while X-ray diffraction (XRD) and STXM were used to identify the oxidation state(s) of the Mn oxides in the electrodes at different conditions and with different electrode activation procedures.

## 10.3 Experimental procedures

### 10.3.1 Materials

$\text{KMnO}_4$ ,  $\text{Mn}(\text{NO}_3)_2 \cdot 4\text{H}_2\text{O}$ , ethanol, quercetin (QC),  $\text{Na}_2\text{SO}_4$ , poly(vinyl butyral) (PVB), NaOH, (MilliporeSigma), multiwalled carbon nanotubes (MWCNT, ID 4 nm, OD 13 nm, length 1–2  $\mu\text{m}$ , Bayer,) and commercial Ni foam (Vale) current collectors were used for material synthesis, electrode fabrication and electrochemical testing.

Commercial trimanganese tetraoxide ( $\text{Mn}_3\text{O}_4$ ), manganese dioxide ( $\text{MnO}_2$ ) (MilliporeSigma) and manganosite ( $\text{MnO}$ ) (Alfa Aesar) were used to obtain reference spectra for STXM analysis.

---

### 10.3.2 Fabrication of $\text{MnO}_2$ and $\text{Mn}_3\text{O}_4$ for electrodes

$\text{MnO}_2$  was prepared by dissolving 1.6 g of  $\text{KMnO}_4$  in 50 mL water, followed by a gradual addition of 25 mL ethanol and stirring continuously for 2 h. The reaction of  $\text{KMnO}_4$  and ethanol formed  $\text{MnO}_2$ . Synthesis of  $\text{MnO}_2$  was performed without a capping agent, because  $\text{KMnO}_4$  reacts with organic capping agent molecules. After washing, filtration, and drying steps,  **$\text{MnO}_2$ -a** powder was obtained.

$\text{Mn}_3\text{O}_4$  was synthesized according to the previously described procedure<sup>314</sup> by dissolving 1.8 g  $\text{Mn}(\text{NO}_3)_2 \cdot 4\text{H}_2\text{O}$  in 100 ml of water and slowly adding 0.01M NaOH solution to obtain pH=10. The resulting suspension was then subjected to centrifugation, washing, and drying, resulting in  **$\text{Mn}_3\text{O}_4$ -a** powder.

**$\text{MnO}_2$ -b** and  **$\text{Mn}_3\text{O}_4$ -b** powders were prepared by high energy ball milling (HEBM) of corresponding  **$\text{MnO}_2$ -a** and  **$\text{Mn}_3\text{O}_4$ -a** powders. HEBM in aqueous medium was performed with a Mixer Mill MM 500 Nano (Retsch GmbH, Haan, Germany) at a frequency of 15 Hz during 2 h. QC was used as a dispersant. The mass ratio of manganese oxide: QC was 10:1. After HEBM the obtained  **$\text{MnO}_2$ -b** and  **$\text{Mn}_3\text{O}_4$ -b** powders were washed with water and dried.

The procedure for preparation of  **$\text{Mn}_3\text{O}_4$ -c** was similar to that for preparation of  **$\text{Mn}_3\text{O}_4$ -a**. However, in this case QC was added as a capping agent for synthesis. The mass ratio of  $\text{Mn}(\text{NO}_3)_2 \cdot 4\text{H}_2\text{O}$ :QC was 13:1. The obtained suspension was then subjected to centrifugation, washing, and drying, resulting in the  **$\text{Mn}_3\text{O}_4$ -c** powder.

HEBM was not used for  $\text{Mn}_3\text{O}_4\text{-c}$ .

### **10.3.3 Fabrication of electrodes for supercapacitors**

Suspensions for impregnation of Ni foam contained manganese oxide, MWCNT and PVB in ethanol in a mass ratio of 80:20:3. PVB was dissolved in ethanol prior to suspension fabrication. The suspensions were ultrasonicated for 30 min. The total mass of the impregnated material after drying was  $0.04 \text{ g cm}^{-2}$ . The impregnated Ni foams were pressed to 25% of their original thickness (1.6 mm). The area of electrodes used for electrochemical testing was  $1 \text{ cm}^{-2}$ .

### **10.3.4 X-ray diffraction and electrochemical studies.**

A Bruker SMART CCD 600 Diffractometer with a  $\text{Cu K}\alpha$  radiation source was used for X-ray diffraction (XRD) characterization of the synthesized materials. The diffraction patterns were obtained at a scan speed of  $0.5 \text{ deg min}^{-1}$ . Cyclic voltammetry (CV), chronopotentiometry (CP) and electrochemical impedance spectroscopy (EIS) studies were performed in aqueous  $0.5 \text{ M Na}_2\text{SO}_4$  electrolyte using a SP300 Biologic potentiostat. The three-electrode cell contained a working electrode, saturated calomel electrode (SCE) reference and Pt mesh counter electrode. Cyclic Voltammetry (CV), Chronopotentiometry (CP) and Electrochemical Impedance Spectroscopy (EIS) studies were performed in the ranges of sweep rates 2-

---

100 mV s<sup>-1</sup>, current densities 3-10 mA cm<sup>-2</sup> and frequencies 10 mHz-100Hz, respectively. The capacitances  $C_m$  (F g<sup>-1</sup>) and  $C_s$  (F cm<sup>-2</sup>) were calculated as described in previous investigations<sup>10,25</sup>.

### 10.3.5 Scanning Transmission X-ray Microscopy

STXM imaging and spectromicroscopy measurements were performed using the STXM at the Softi-MAX beamline at Max IV (Lund, Sweden). Details of the SoftiMAX beamline<sup>26</sup> and the principles of STXM<sup>27</sup> have been presented elsewhere. Investigations were performed on both as-prepared and electrochemically tested samples. After electrochemical testing, particulate matter was scratched from the Ni foam substrate. The powders were drop-cast on a silicon nitride (SiN<sub>x</sub>) window (Norcada Inc.). After removing weakly adhering particles, the SiN<sub>x</sub> window was attached to a standard trapezoidal STXM sample plate using double sided tape<sup>28</sup>. Spectra, images, and image sequences (stacks<sup>29</sup>) were measured at the Mn 2p (L<sub>3</sub>) and O 1s (K) edges. After mounting the sample in the STXM, the chamber was evacuated to <10<sup>-2</sup> mbar and kept pumped during measurements. Spectromicroscopic data was obtained by recording multi-energy stacks at X-ray energies from ~10 eV below to ~40 eV above the Mn 2p and O 1s absorption onset. All STXM data was analyzed using aXis2000 software<sup>30</sup>. After alignment, the transmission signal was converted to optical density (*OD*) using as  $I_0$  the spectrum from areas of the SiN<sub>x</sub> window devoid of sample. After OD conversion and energy calibration, the stacks

were fit to quantitative (OD1) reference spectra of MnO, Mn<sub>3</sub>O<sub>4</sub> and MnO<sub>2</sub>. The method to set the absolute intensity scales is outlined in detail elsewhere<sup>23</sup>. The Mn 2p reference spectra were used in a stack fit analysis of Mn 2p<sub>3/2</sub> (L<sub>3</sub>) stacks recorded from each sample. The stack fit produces component maps for each Mn species, a map of a constant signal (no spectral variation), and the residual of the fit. Since quantitative reference spectra are used, the intensity scales of the resulting component maps are the component thickness in nm<sup>19</sup>.

## 10.4 Results and discussion

### 10.4.1 Electrochemical and microstructure characterization

Figure 10-1 shows XRD patterns of the **MnO<sub>2</sub>-a**, **Mn<sub>3</sub>O<sub>4</sub>-a** and **Mn<sub>3</sub>O<sub>4</sub>-c** materials. The XRD studies of **MnO<sub>2</sub>-a** revealed the formation of weakly crystallized material, which showed peaks corresponding to the birnessite phase (JCPDS file 00-018-0802). The general chemical formula of birnessite<sup>31,32</sup> is C<sub>x</sub>MnO<sub>2+y</sub>, where C is K<sup>+</sup> or Na<sup>+</sup>. It is known<sup>31</sup> that the oxidation state of Mn in this phase is typically 3.6-3.8, which is due to the dominant content of Mn<sup>4+</sup> and minor Mn<sup>3+</sup> and Mn<sup>2+</sup> content. The XRD patterns of **Mn<sub>3</sub>O<sub>4</sub>-a** and **Mn<sub>3</sub>O<sub>4</sub>-c** materials showed the peaks of the hausmannite Mn<sub>3</sub>O<sub>4</sub> phase (JCPDS file 04-007-1841).

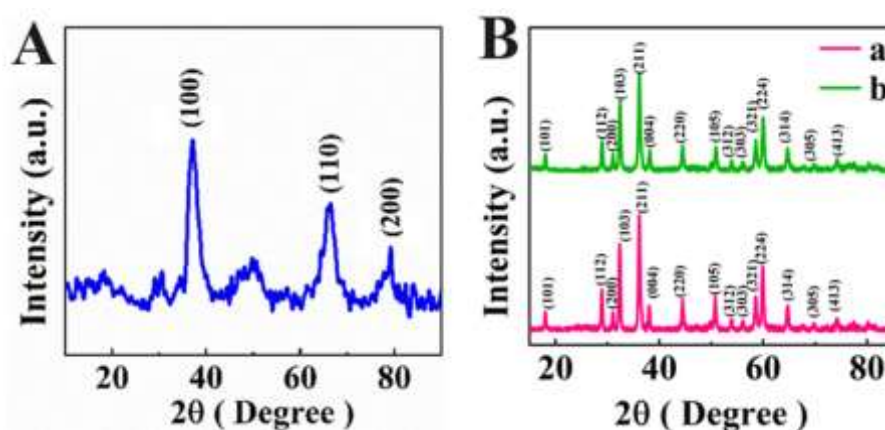


Figure 10- 1 XRD patterns of (A)  $\text{MnO}_2\text{-a}$  and (B) (a)  $\text{Mn}_3\text{O}_4\text{-a}$  and (b)  $\text{Mn}_3\text{O}_4\text{-c}$ .

The crushing and grinding of the  $\text{MnO}_2\text{-a}$ ,  $\text{Mn}_3\text{O}_4\text{-a}$  particles and their agglomerates during HEBM resulted in the formation of high energy surfaces, which can promote particle agglomeration. Therefore, HEBM was performed in the presence of the QC additive. It was hypothesized that QC adsorption on such surfaces during HEBM can prevent agglomeration. Moreover, QC was used as a capping agent to prevent particle growth and agglomeration in the synthesis of  $\text{Mn}_3\text{O}_4\text{-c}$ . The selection of QC for modification of manganese oxide particles was based on the unique chelating and adsorption properties of this molecule<sup>33</sup>. QC belongs to the group of natural flavonoid chelating agents produced in plants. The chelating properties of QC are important for various plant physiological processes<sup>34</sup>. Figure 10-2A shows the chemical structure of QC, which has aromatic rings and three chelating sites. Investigations showed the formation of QC complexes with Mn<sup>35</sup>. All three complexation sites (Figure 10-2B) can be involved in bonding Mn ions<sup>35</sup>. Of particular importance is the catechol ligand (Figure 10-2A). Previous investigations

showed<sup>36</sup> strong adsorption of different catecholates on metal oxide particles by complexation of surface atoms on the particle surface. The adsorption mechanism is similar to that of mussel protein adsorption to inorganic materials, which involves catecholate monomers.

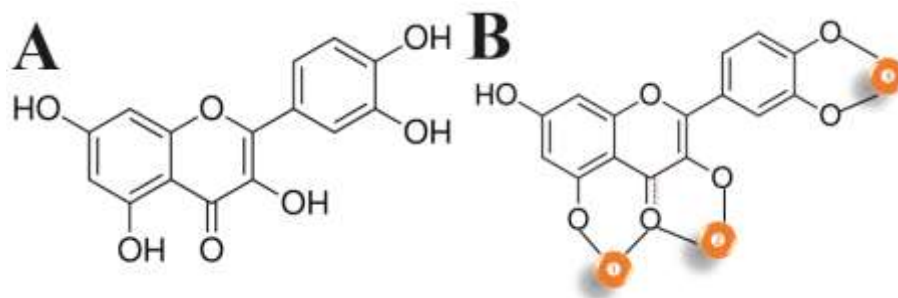


Figure 10- 2 (A) Chemical structure of QC. (B) Bonding sites of QC for metal ions.

CV data for the **MnO<sub>2</sub>-b** electrodes showed higher capacitance at low scan rates, compared to the capacitance of **MnO<sub>2</sub>-a** (Figure 10-3 A-C). Capacitances of 4.75 F cm<sup>-2</sup> (118.78 F g<sup>-1</sup>) and 6.42 F cm<sup>-2</sup> (160.53 F g<sup>-1</sup>) were obtained for **MnO<sub>2</sub>-a** and **MnO<sub>2</sub>-b**, respectively, at 2 mV s<sup>-1</sup>. However, HEBM resulted in enhanced capacitance only for sweep rates below 20 mV s<sup>-1</sup>. EIS studies (Figure 10-3 D) showed slightly higher resistance ( $R=Z'$ ) of **MnO<sub>2</sub>-b** compared to **MnO<sub>2</sub>-a**, which could be the result of QC adsorption. HEBM had only a slight effect on frequency dependencies of the complex capacitance components (Figure 10-3 E, F). CP studies (Figure 10-3G, H, I) showed an effect of HEBM on duration of charge-discharge at different current densities. The capacitances at 3 mA cm<sup>-2</sup> were 7.00 F cm<sup>-2</sup> (175.06 F g<sup>-1</sup>) and 8.51 F cm<sup>-2</sup> (212.68 F g<sup>-1</sup>) for **MnO<sub>2</sub>-a** and **MnO<sub>2</sub>-b**, respectively. However, the difference in capacitances of **MnO<sub>2</sub>-a** and **MnO<sub>2</sub>-b** decreased with increasing current density. In

---

contrast to MnO<sub>2</sub> electrodes, the HEBM had a strong effect on capacitive performance of Mn<sub>3</sub>O<sub>4</sub>. The capacitive performance of **Mn<sub>3</sub>O<sub>4</sub>-a** was reported in a previous investigation<sup>18</sup>. Testing of **Mn<sub>3</sub>O<sub>4</sub>-a** showed a need for an electrode activation procedure. The electrode activation was dependent on sweep rate. Therefore, the electrode activation was investigated using different strategies. Electrochemical testing showed the influence of HEBM performed in the presence of QC (**Mn<sub>3</sub>O<sub>4</sub>-b**) and Mn<sub>3</sub>O<sub>4</sub> synthesis using QC as a capping agent (**Mn<sub>3</sub>O<sub>4</sub>-c**) on the capacitive properties of the electrodes. Two different CV testing modes were used<sup>18</sup>, which are labelled variable sweep rate and fixed sweep rate procedures (VSRP and FSRP). VSRP involved CV testing at sweep rates of 2, 5, 10, 20, 50 and 100 mV s<sup>-1</sup>, whereas in FSRP the electrochemical cycling was performed at a fixed sweep rate of 50 mV s<sup>-1</sup> for 1000 cycles<sup>18</sup>.

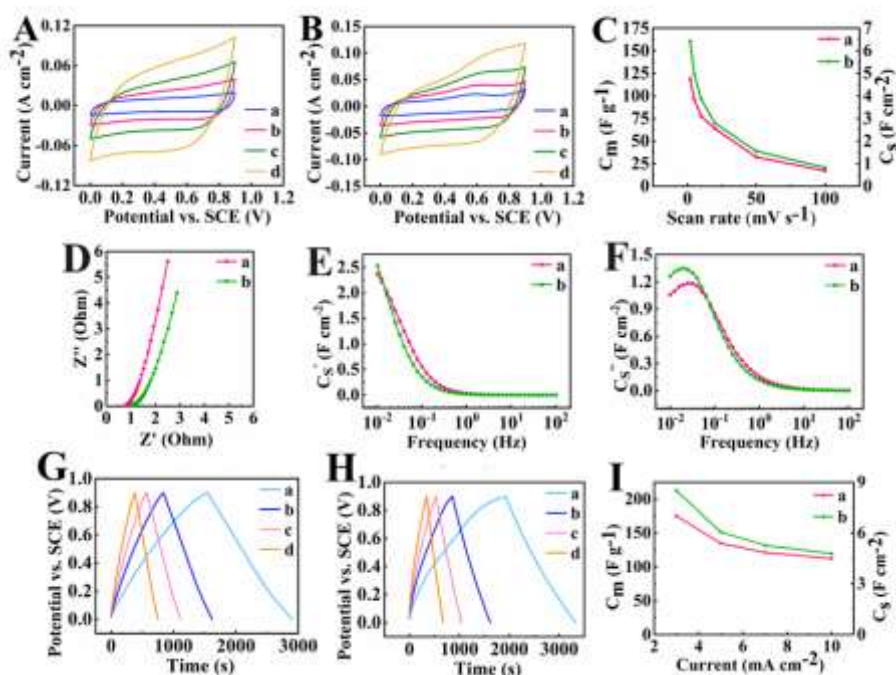


Figure 10- 3 (A,B) CV data for (A)  $\text{MnO}_2\text{-a}$  and (B)  $\text{MnO}_2\text{-b}$  at (a) 2, (b) 5, (c) 10 and (d)  $20 \text{ mV s}^{-1}$ , (C)  $C_s$  and  $C_m$  versus scan rate, calculated from the CVs for (a)  $\text{MnO}_2\text{-a}$  and (b)  $\text{MnO}_2\text{-b}$ , (D,E,F) EIS data for complex impedance and capacitance: (D) Nyquist plot, (E)  $C_s'$  versus frequency, (F)  $C_s''$  versus frequency for (a)  $\text{MnO}_2\text{-a}$  (b)  $\text{MnO}_2\text{-b}$ , (G,H) CP data at (a) 3, (b) 5, (c) 7 and (d)  $10 \text{ mA cm}^{-2}$  for (G)  $\text{MnO}_2\text{-a}$ , and (H)  $\text{MnO}_2\text{-b}$ , (I)  $C_s$  and  $C_m$  as functions of current density for (a)  $\text{MnO}_2\text{-a}$  and (b)  $\text{MnO}_2\text{-b}$ , calculated from CP data.

In this investigation, similar testing strategies were used for comparison. VSRP1 showed a capacitance of  $1.5 \text{ F cm}^{-2}$  for  $\text{Mn}_3\text{O}_4\text{-a}$ <sup>18</sup>. The capacitance gradually increased<sup>18</sup> with increasing VSRP numbers, and it was found to be to  $3.3 \text{ F cm}^{-2}$  for VSRP5 at  $2 \text{ mV s}^{-1}$ . Figure 10-4 (A-C) shows testing results for  $\text{Mn}_3\text{O}_4\text{-b}$  and  $\text{Mn}_3\text{O}_4\text{-c}$  for VSRP1. HEBM resulted in a capacitance of  $5.06 \text{ F cm}^{-2}$  ( $126.50 \text{ F g}^{-1}$ ) for VSRP1 for  $\text{Mn}_3\text{O}_4\text{-b}$  at  $2 \text{ mV s}^{-1}$ . The  $\text{Mn}_3\text{O}_4\text{-c}$  electrodes prepared using QC as a capping agent showed a capacitance of  $6.0 \text{ F cm}^{-2}$  ( $149.50 \text{ F g}^{-1}$ ) at  $2 \text{ mVs}^{-1}$ .

Therefore, HEBM had two major effects on the capacitance of  $\text{Mn}_3\text{O}_4$  electrodes: a significant increase in capacitance, and elimination of the need for electrode activation. The obtained capacitances for the  $\text{Mn}_3\text{O}_4\text{-b}$  and  $\text{Mn}_3\text{O}_4\text{-c}$  electrodes were comparable with those for the  $\text{MnO}_2\text{-a}$  and  $\text{MnO}_2\text{-b}$  electrodes.

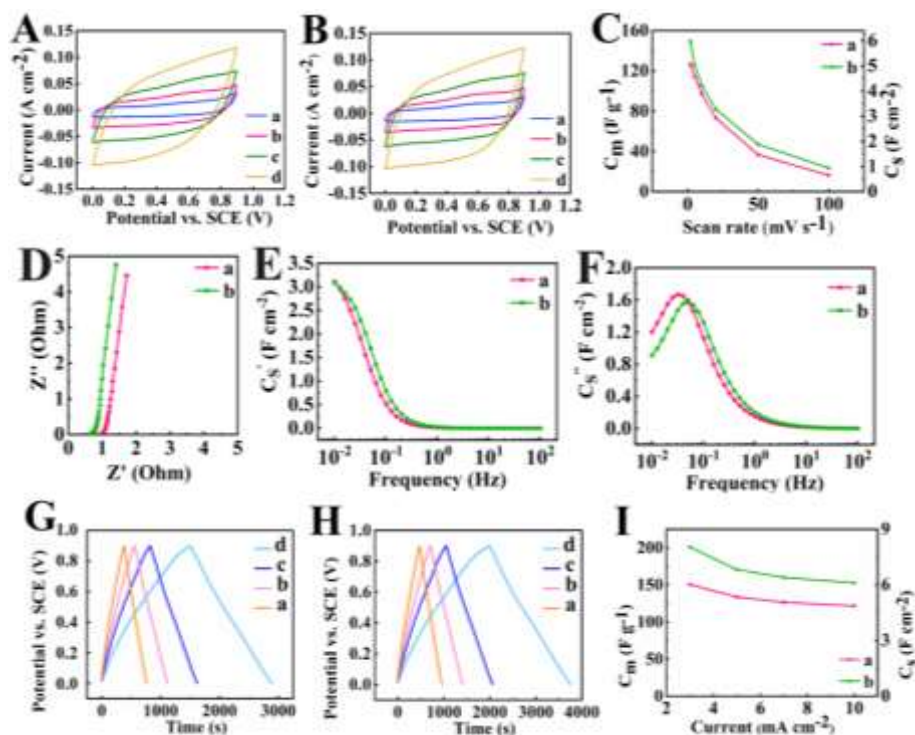


Figure 10- 4 (A,B) CV data for (A)  $\text{Mn}_3\text{O}_4\text{-b}$  and (B)  $\text{Mn}_3\text{O}_4\text{-c}$  at (a) 2, (b) 5, (c) 10 and (d) 20  $\text{mV s}^{-1}$ , (C)  $C_s$  and  $C_m$  versus scan rate, calculated from the CVs for (a)  $\text{Mn}_3\text{O}_4\text{-b}$  and (b)  $\text{Mn}_3\text{O}_4\text{-c}$ , (D,E,F) EIS data for complex impedance and capacitance: (D) Nyquist plot, (E)  $C_s'$  versus frequency, (F)  $C_s''$  versus frequency for (a)  $\text{Mn}_3\text{O}_4\text{-b}$  (b)  $\text{Mn}_3\text{O}_4\text{-c}$ , (G,H) CP data at (a) 3, (b) 5, (c) 7 and (d) 10  $\text{mA cm}^{-2}$  for (G)  $\text{Mn}_3\text{O}_4\text{-b}$ , and (H)  $\text{Mn}_3\text{O}_4\text{-c}$ , (I)  $C_s$  and  $C_m$  as functions of current density for (a)  $\text{Mn}_3\text{O}_4\text{-b}$  and (b)  $\text{Mn}_3\text{O}_4\text{-c}$ , calculated from CP data.

$\text{Mn}_3\text{O}_4\text{-b}$  and  $\text{Mn}_3\text{O}_4\text{-c}$  electrodes showed lower resistances compared to  $\text{MnO}_2\text{-a}$  and  $\text{MnO}_2\text{-b}$  electrodes, with the lowest resistances obtained for  $\text{Mn}_3\text{O}_4\text{-c}$ . Moreover,

the EIS data for **Mn<sub>3</sub>O<sub>4</sub>-c** showed higher relaxation frequency<sup>37</sup>, which corresponds to the maximum in the frequency dependence of  $C''$ , and reduction of  $C'$  in the corresponding frequency range. CP data obtained after VSRP1 (Figure 10-4 G-I) showed almost linear charging/discharging and capacitances of  $6.02 \text{ F cm}^{-2}$  ( $150.54 \text{ F g}^{-1}$ ) and  $8.03 \text{ F cm}^{-2}$  ( $200.93 \text{ F g}^{-1}$ ) for **Mn<sub>3</sub>O<sub>4</sub>-b** and **Mn<sub>3</sub>O<sub>4</sub>-c**, respectively at a current density of  $3 \text{ mA cm}^{-2}$ . The capacitances decreased with increasing current density and **Mn<sub>3</sub>O<sub>4</sub>-c** showed higher capacitances, compared to **Mn<sub>3</sub>O<sub>4</sub>-b**. Previous studies of **Mn<sub>3</sub>O<sub>4</sub>-a** electrode activation at  $50 \text{ mV s}^{-1}$  (FSRP) showed a continuous increase in capacitance during 1000 cycles and the capacitance for the first cycle was only 32.7% of the capacitance for cycle 1000. The FSRP testing of **Mn<sub>3</sub>O<sub>4</sub>-b** showed significant capacitance increase during the first 400 cycles and the capacitance remained nearly constant after 600 cycles. The capacitance for cycle 1 was 32.3% of the capacitance for cycle 1000. Therefore, FSRP at the high sweep rate showed significant acceleration of the electrode activation procedure. The FSRP for **Mn<sub>3</sub>O<sub>4</sub>-c** showed improved electrode performance. Notable capacitance increase was observed for the first 200 cycles, and relatively small variation was observed between cycle 200 and 400. The capacitance remained practically constant after 400 cycles. The capacitance for cycle 1 was 61.8% of the capacitance for cycle 1000. Therefore, the **Mn<sub>3</sub>O<sub>4</sub>-c** electrodes showed faster activation, compared to **Mn<sub>3</sub>O<sub>4</sub>-b** for FSRP at high sweep rate.

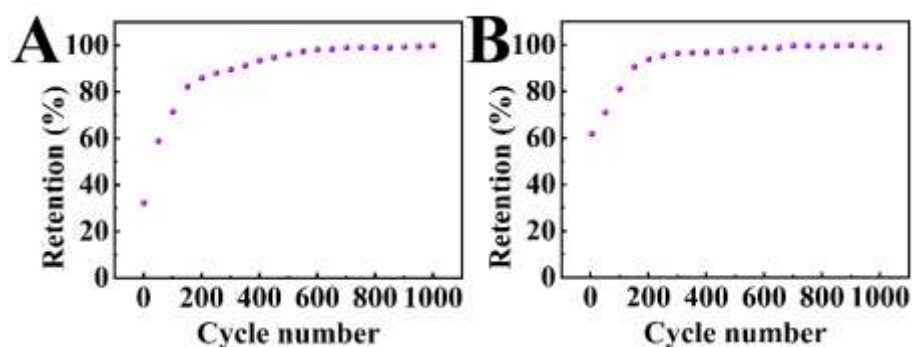


Figure 10- 5 Capacitance retention of (A)  $\text{Mn}_3\text{O}_4\text{-b}$  and (B)  $\text{Mn}_3\text{O}_4\text{-c}$  electrodes at a scan rate of  $50 \text{ mV s}^{-1}$ .

## 10.4.2 X-ray spectromicroscopy

### 10.4.2.1 MnO, $\text{Mn}_3\text{O}_4$ and $\text{MnO}_2$ reference spectroscopy

Figure 10-6 presents the O 1s and Mn 2p X-ray absorption spectra of MnO,  $\text{Mn}_3\text{O}_4$  and  $\text{MnO}_2$  on OD1 intensity scales, measured by STXM for this study. The characteristic features and positions of peaks in these spectra are in excellent agreement with those for absorption spectra of  $\text{Mn}_3\text{O}_4$  (hausmannite), MnO (manganosite) and  $\alpha\text{-MnO}_2$  reported in the literature<sup>38-40</sup>. These spectra were used as reference signals to identify, quantify and map the oxidation states of Mn in the supercapacitor electrode samples.

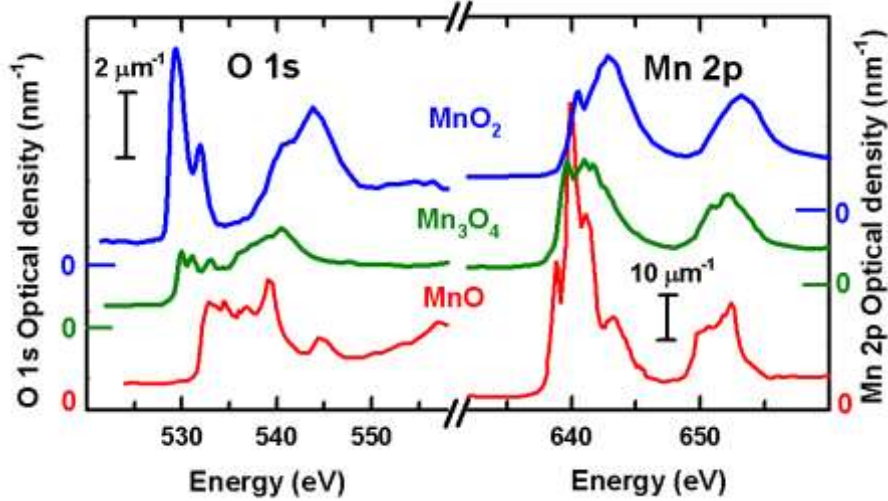


Figure 10- 6 O 1s and Mn 2p X-ray absorption spectra of MnO (red), Mn<sub>3</sub>O<sub>4</sub> (green) and MnO<sub>2</sub> (blue) plotted on an absolute intensity scale (OD1, optical density per nm thickness at standard densities).

#### 10.4.2.2 Mn 2p and O 1s spectroscopic results for the Mn<sub>3</sub>O<sub>4</sub> samples

Figure 10-7 A presents absorption spectra of **Mn<sub>3</sub>O<sub>4</sub>-b** and **Mn<sub>3</sub>O<sub>4</sub>-c** after VSRP and FSRP. Figure 10-7 B presents O 1s absorption spectra for **Mn<sub>3</sub>O<sub>4</sub>-c** after VSRP and FSRP. Based on the Mn 2p and O 1s spectral features, the **Mn<sub>3</sub>O<sub>4</sub>-c** sample contains 3 different MnO<sub>x</sub> species after VSRP while that after FSRP contains only 2 different species. Figure 10-7 C presents O 1s absorption spectra for **Mn<sub>3</sub>O<sub>4</sub>-b** after VSRP and FSRP. The O 1s spectra indicate that there are two different MnO<sub>x</sub> species present after both VSRP and FSRP tests. Figure 10-8 A is an expansion of the Mn 2p<sub>3/2</sub> spectra of **Mn<sub>3</sub>O<sub>4</sub>-c** after VSRP and after FSRP. This presentation shows more clearly the presence of both Mn<sub>3</sub>O<sub>4</sub> and MnO<sub>2</sub> in these samples. Figure 8 B is an expansion of the Mn 2p<sub>3/2</sub> spectra of **Mn<sub>3</sub>O<sub>4</sub>-b** after VSRP and after FSRP. Comparison with

the reference spectra of pure MnO, Mn<sub>3</sub>O<sub>4</sub> and MnO<sub>2</sub> indicates the presence of multiple oxidation states, with discernable features of all three species.

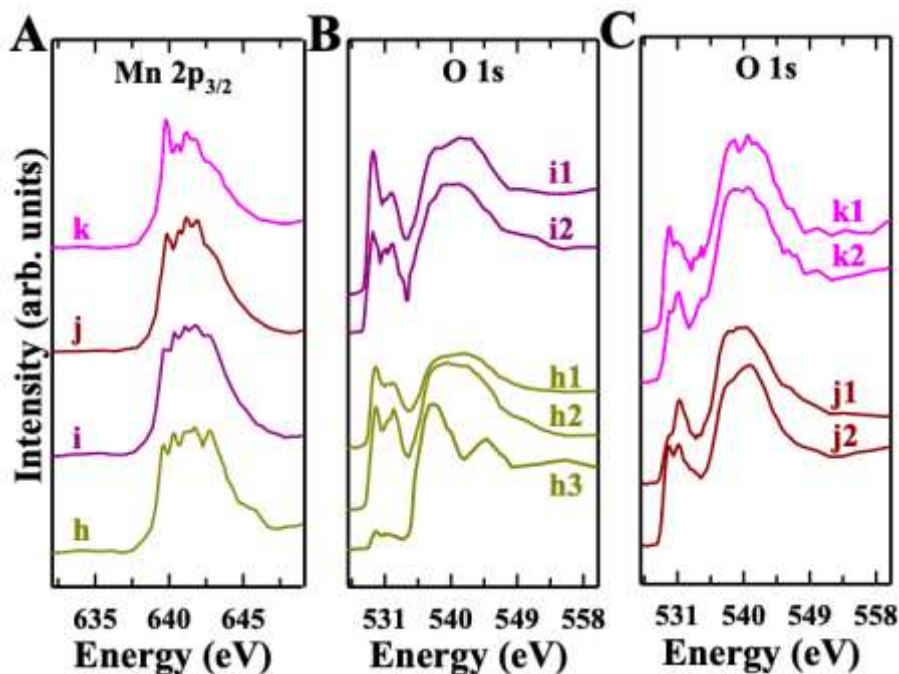


Figure 10- 7 (A) Mn 2p<sub>3/2</sub> absorption spectra of (h) Mn<sub>3</sub>O<sub>4</sub>-c after VSRP, (i) Mn<sub>3</sub>O<sub>4</sub>-c after FSRP, (j) Mn<sub>3</sub>O<sub>4</sub>-b after VSRP (k) Mn<sub>3</sub>O<sub>4</sub>-b after FSRP. B. O 1s spectra for Mn<sub>3</sub>O<sub>4</sub>-c after VSRP (h1-h3) and after FSRP (i1-i2) C. O 1s spectra for Mn<sub>3</sub>O<sub>4</sub>-b after VSRP (j1-j2) and after FSRP (k1-k2) . The sub-coding (1,2 and 3) indicate different regions of the same sample.

The Mn 2p<sub>3/2</sub> spectra of Mn<sub>3</sub>O<sub>4</sub>-c after VSRP and FSRP show that they are a mixture of Mn<sub>3</sub>O<sub>4</sub> and MnO<sub>2</sub> species (Figure 10-8 A). The sharp peak at 639.6 eV and the two small peaks at 641.1 eV and 641.7 eV are from Mn<sub>3</sub>O<sub>4</sub> while peaks at 640.4 eV and 642.8 eV are characteristic of MnO<sub>2</sub>. The MnO<sub>2</sub> signal is more intense in the VSRP than in the FSRP activated sample. On the other hand, the Mn 2p<sub>3/2</sub> spectra of Mn<sub>3</sub>O<sub>4</sub>-b after VSRP and FSRP showed much weaker MnO<sub>2</sub> signal than the correspondingly

activated  $\text{Mn}_3\text{O}_4\text{-c}$  sample (Figure 10-8 B). However,  $\text{Mn}_3\text{O}_4\text{-b}$  after FSRP shows significant increase in MnO signal.

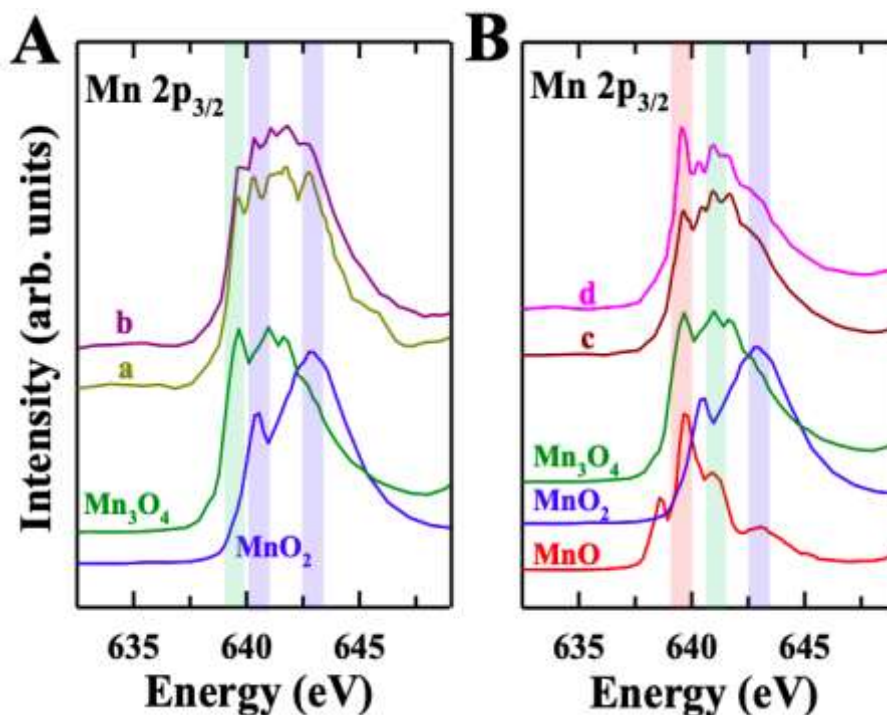


Figure 10- 8 Mn  $2p_{3/2}$  spectra of  $\text{Mn}_3\text{O}_4\text{-c}$  after (a) VSRP and (b) FSRP. **B.** Mn  $2p_{3/2}$  spectra of  $\text{Mn}_3\text{O}_4\text{-b}$  after (c) VSRP and (d) FSRP. In each panel a direct comparison is made to the reference spectra.

Figure 10-9 A is the average of STXM images measured at 64 energies in an O 1s stack measured on  $\text{Mn}_3\text{O}_4\text{-b}$  after VSRP. Figure 9 B presents a color-coded composite of the maps of MnO,  $\text{Mn}_3\text{O}_4$ , and  $\text{MnO}_2$  derived from a fit to the O 1s stack. Figure 10-9 (B1-B3) are the maps of each component. These results show clearly that Mn in various oxidation tend to be spatially localized. Figure 9 C plots the O 1s absorption spectra of the B-1, B-2 and B-3 regions, verifying the identity of these species.

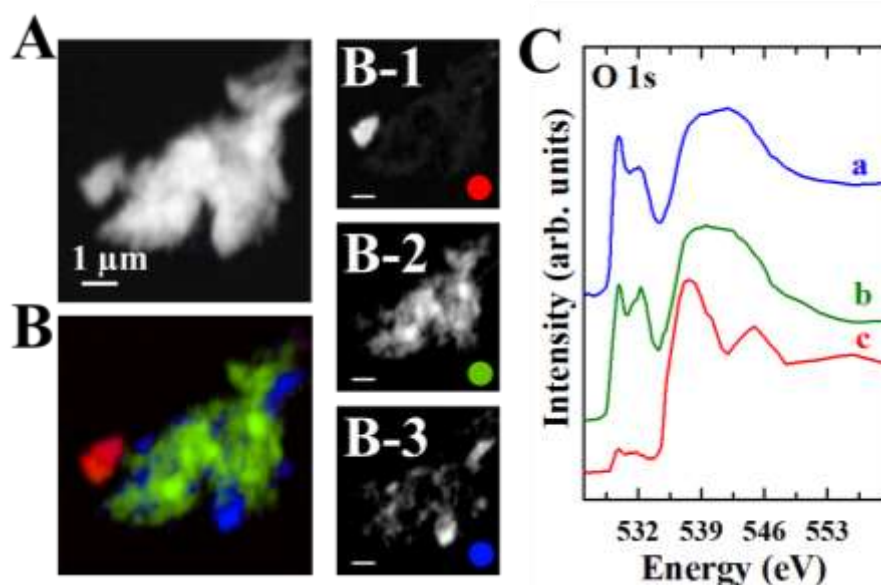


Figure 10- 9 **A.** average of 64 images of O 1s stack of the  $\text{Mn}_3\text{O}_4\text{-c}$  after VSRP. **B.** color coded composite of the MnO (red),  $\text{Mn}_3\text{O}_4$  (green) and  $\text{MnO}_2$  (blue) chemical maps derived from a stack fit to the O 1s stack. **B-1, B-2** and **B-3** are the component maps derived by fitting the O 1s stack to the O 1s spectra of MnO,  $\text{Mn}_3\text{O}_4$ , and  $\text{MnO}_2$ . **C.** O 1s spectra extracted from the **B-1, B-2** and **B-3** regions. The color of each spectrum corresponds to the color-coding of the spatial regions from which the spectra were extracted.

The O 1s spectra of  $\text{Mn}_3\text{O}_4\text{-c}$  after VSRP and FSRP are different (Figure 10-7 B). The O 1s spectra extracted from three different regions of  $\text{Mn}_3\text{O}_4\text{-c}$  after VSRP (Figure 10-9 C) show that it is a partially spatially segregated mixture of three different Mn oxidation states. The O 1s spectrum of the red area (Figure 10-9 B-1) showed low intensity peaks at 529.9 eV, 531.5 eV and 532.7 eV, which are a combination of the characteristic O 1s  $\rightarrow$  Mn 3d features of  $\text{Mn}_3\text{O}_4$  and  $\text{MnO}_2$ , and large broad peaks at 537.5 eV and 544.9 eV which correspond to MnO signals. The O 1s spectrum of the green area (Figure 10-9 B-2) exhibits O1s  $\rightarrow$  Mn 3d transitions at 529.8 eV, 532.3 eV

---

and a small shoulder peak at 531.5 eV, all of which correspond to Mn<sub>3</sub>O<sub>4</sub>. The O 1s spectrum of the blue area (Figure 10-9 B-3) has a high intensity O1s → Mn 3d peak at 529.8 eV and a weak peak at 532.1 eV corresponding to MnO<sub>2</sub>. Similarly, the different spectra extracted from different regions of **Mn<sub>3</sub>O<sub>4</sub>-c** after FSRP are presented in supplemental information, Figure S1 C. The O 1s spectrum of the red area (Figure 10-S1 B-1) showed high intensity peak at 529.4 eV and low intensity peak at 531.9 eV, which are close to the characteristic O 1s → Mn 3d features of MnO<sub>2</sub>. The O 1s spectrum of the green area (Figure 10-S1 B-2) showed sharp O1s → Mn 3d transition at 529.3 eV and weak peaks at 531.1 eV and 532.1 eV with a shoulder peak at 533.4 eV. These peaks represent a combination of the characteristic O 1s → 3d features of Mn<sub>3</sub>O<sub>4</sub> and MnO<sub>2</sub>.

Likewise, the O 1s spectra of **Mn<sub>3</sub>O<sub>4</sub>-b** after VSRP and FSRP show different O 1s → Mn3d features in different regions (see Figures 10-S2 and S3). The O1s → Mn 3d transition in spectra extracted from different regions of the **Mn<sub>3</sub>O<sub>4</sub>-b** after VSRP sample has two characteristic peaks at 529.9 and 531.1 eV with a small shoulder peak at 533 eV, corresponding to Mn<sub>3</sub>O<sub>4</sub>. However, the intensity of the first peak at 529.9 eV is significantly different in both spectra which suggests there are multiple Mn oxidation states. Similarly, the O 1s spectra extracted from two different regions of **Mn<sub>3</sub>O<sub>4</sub>-b** after FSRP showed different intensities of the first (529.9 eV) and second (531.1 eV) peaks. The speciation derived from the O 1s and Mn 2p spectra of the same spatial region are consistent for each of the four samples measured by STXM.

---

Together the Mn 2p and O 1s spectra indicate there is significant oxidation of the as-prepared Mn<sub>3</sub>O<sub>4</sub> to MnO<sub>2</sub>, even after only VSRP. The oxidation is more extensive in the **Mn<sub>3</sub>O<sub>4</sub>-c** than in the **Mn<sub>3</sub>O<sub>4</sub>-b** samples.

Figure 10-S4 C presents the Mn 2p<sub>3/2</sub> absorption spectra of the as-prepared **MnO<sub>2</sub>-a** sample in comparison with that of the as-prepared **MnO<sub>2</sub>-b**. The Mn 2p spectrum of **MnO<sub>2</sub>-a** sample indicates there is a mixture of oxidation states. The Mn 2p<sub>3/2</sub> characteristic features of MnO<sub>2</sub> at 640.5 eV and 642.8 eV are observed, while the low intensity peak at 639.8 eV arises from MnO and the weak signals at 641.2 eV and 642 eV are associated with Mn<sub>3</sub>O<sub>4</sub>. The component maps presented in Figure 10-S4 A indicate almost equal amounts of MnO and MnO<sub>2</sub> in the measured sample. Both samples showed considerable contribution of Mn<sub>3</sub>O<sub>4</sub> signals. In the contrast, the MnO signal (639.8 eV) in the Mn 2p<sub>3/2</sub> spectrum of **MnO<sub>2</sub>-b** is much lower than that in **MnO<sub>2</sub>-a**, indicating a dominant content of MnO<sub>2</sub>, as also indicated in the component maps presented in Figure 10-S4 B. The O 1s spectra of as-prepared **MnO<sub>2</sub>-a** and **MnO<sub>2</sub>-b** are similar (Figure 10-S5 B and D). They indicate there are mixed oxidation states in these samples, which are mapped in Figure 10-S5 A and C.

### 10.4.2.3 Chemical Mapping of Mn species in the tested samples

Figure 10-10 presents quantitative chemical maps of the MnO, Mn<sub>3</sub>O<sub>4</sub> and MnO<sub>2</sub> species for **Mn<sub>3</sub>O<sub>4</sub>-b** and **Mn<sub>3</sub>O<sub>4</sub>-c** after VSRP and FSRP, derived by fitting Mn 2p<sub>3/2</sub>

---

stacks (70 energies from 630 – 650 eV) to the quantitative OD1 reference spectra of MnO, Mn<sub>3</sub>O<sub>4</sub> and MnO<sub>2</sub> (Figure 6). Each image is a color coded composite of the component maps for MnO (red), Mn<sub>3</sub>O<sub>4</sub> (green) and MnO<sub>2</sub> (blue). The R-G-B color intensity scale bars indicate the thickness in nm of each species. The chemical mapping of the **Mn<sub>3</sub>O<sub>4</sub>-c** sample after VSRP (Figure 10 A) and after FSRP (Figure 10-10 B) clearly indicate extensive conversion of the as-synthesized Mn<sub>3</sub>O<sub>4</sub> to MnO<sub>2</sub>. In contrast, the chemical mapping of the **Mn<sub>3</sub>O<sub>4</sub>-b** sample after VSRP (Figure 10-10 C) and after FSRP (Figure 10-10 D) indicate a lower degree of conversion of the as-synthesized Mn<sub>3</sub>O<sub>4</sub> to MnO<sub>2</sub>. The curve fit analysis of the average Mn 2p spectrum of the **Mn<sub>3</sub>O<sub>4</sub>-c** sample after FRSP (Figure 10-11) indicates a similar amount of MnO<sub>2</sub> and Mn<sub>3</sub>O<sub>4</sub> with a very small amount of MnO, consistent with the color-coded composite in (Figure 10-10 B).

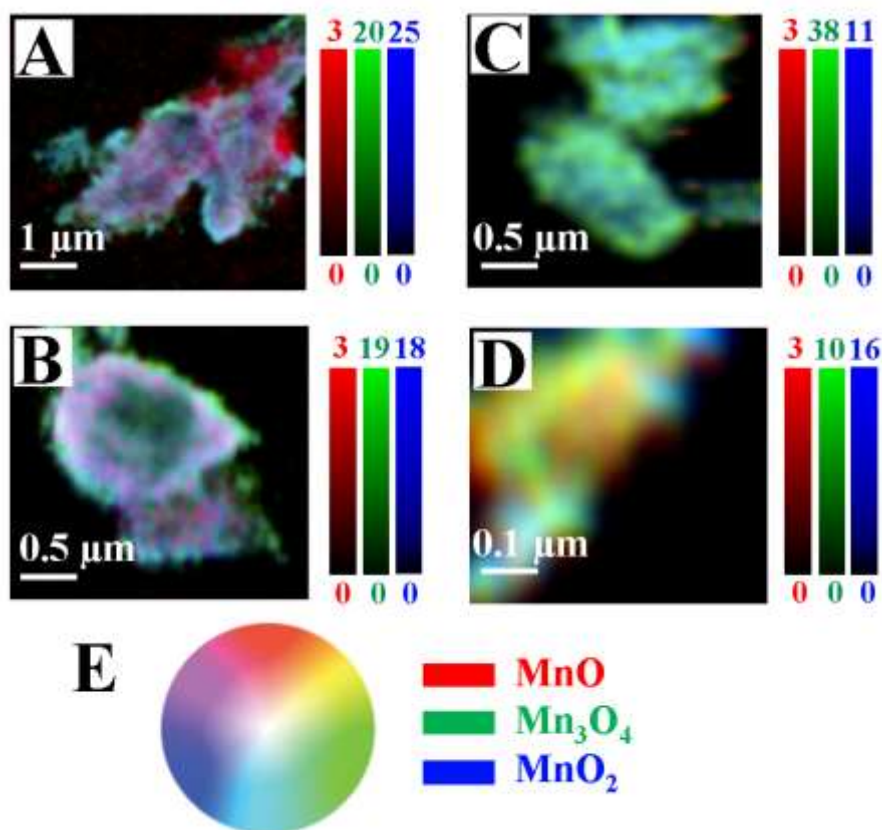


Figure 10- 10 Color coded composites of MnO (red), Mn<sub>3</sub>O<sub>4</sub> (green) and MnO<sub>2</sub> (blue) chemical maps derived by fitting Mn L<sub>3</sub> stacks. **A.** Mn<sub>3</sub>O<sub>4</sub>-c after VSRP. **B.** Mn<sub>3</sub>O<sub>4</sub>-c after FSRP **C.** Mn<sub>3</sub>O<sub>4</sub>-b after VSRP. **D.** Mn<sub>3</sub>O<sub>4</sub>-b after FSRP. The intensity scale of each species is indicated. **E.** Is a color wheel indicating how the color at any pixel indicates a specific combination of the three species.

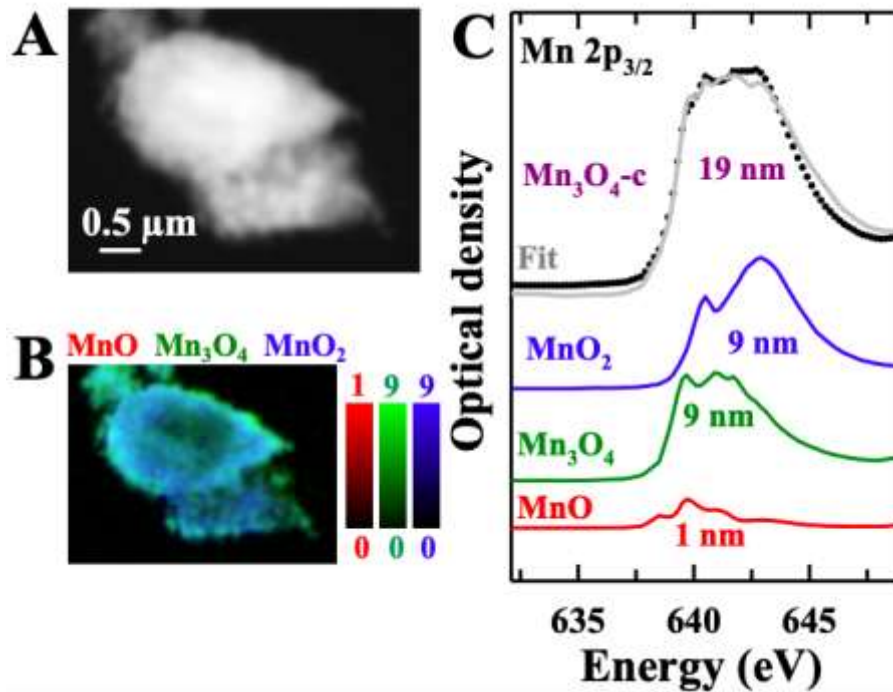


Figure 10- 11 Volume fraction determination of the composition of  $\text{Mn}_3\text{O}_4\text{-c}$  after FSRP. (A) average STXM image of the measured sample. (B) color-coded map in absolute scale. (C) average spectrum (dots) compared to the calculated curve fit (grey) using the area of each component and the average thickness of each component.

Figure 10-12 A and 10-12 B plot the average volume fractions of MnO,  $\text{Mn}_3\text{O}_4$  and  $\text{MnO}_2$  in  $\text{Mn}_3\text{O}_4\text{-b}$  and  $\text{Mn}_3\text{O}_4\text{-c}$  after VSRP and FSRP. The relative volume fractions were obtained from the product of the area of each manganese oxide determined by threshold masking the component map (see Figure 10- 10 and 11) and the average thickness of each species in the masked region. The volume fractions of each Mn component were calculated by ratio-ing the relative fraction of each species to the sum of that for all three species, expressed as a percentage. In this case the analysis shows that in  $\text{Mn}_3\text{O}_4\text{-b}$  subjected to FSRP, there is almost equal amounts of

Mn<sub>3</sub>O<sub>4</sub> (green, 46 ± 4 vol %) and MnO<sub>2</sub> (blue, 49 ± 4 vol %) with a small but measurable contribution of MnO (red, 5 ± 1 vol %). The same analysis showed **Mn<sub>3</sub>O<sub>4</sub>-c** consisted of 57 ± 2 vol % MnO<sub>2</sub> after VSRP and 49 ± 4 vol % after FSRP. In contrast, **Mn<sub>3</sub>O<sub>4</sub>-b** consisted of only 16 ± 1 vol % MnO<sub>2</sub> after VSRP and 34 ± 2 vol % after FSRP. There was a small amount of MnO in the **Mn<sub>3</sub>O<sub>4</sub>-c** sample after VSRP (5 ± 1 vol %) and after FSRP (5 ± 1 vol %). In contrast, for **Mn<sub>3</sub>O<sub>4</sub>-b** the amount of MnO was 2 ± 1 vol % after VSRP and increased to 10 ± 1 vol % after FSRP.

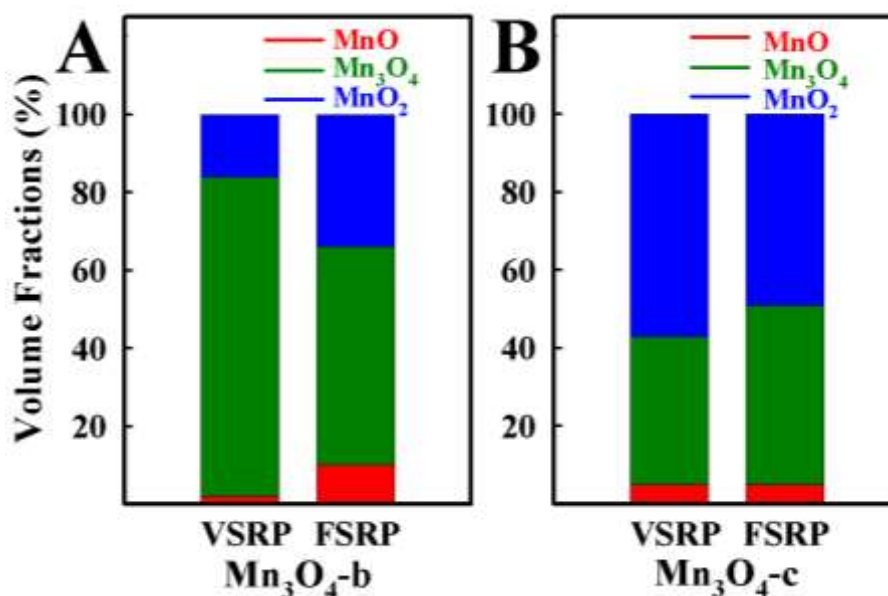


Figure 10- 12 Volume fractions of MnO (red), Mn<sub>3</sub>O<sub>4</sub> (green) and MnO<sub>2</sub> (blue) evaluated from the area and thickness of each component map (see the Supplemental Information for a description of the method). **A.** VSRP and FSRP for **Mn<sub>3</sub>O<sub>4</sub>-b**. **B.** VSRP and FSRP for **Mn<sub>3</sub>O<sub>4</sub>-c**.

Recently Suktha et al.<sup>41</sup> have estimated the average oxidation state of Mn from Mn K-edge (1s) X-ray absorption spectroscopy of Mn<sub>3</sub>O<sub>4</sub> supercapacitors. The morphology

---

of the nano-fibres they studied is quite different from the particulates studied in this work. Despite that, it is interesting to compare the average oxidation state values reported by Suktha et al.<sup>41</sup> to the results of this work. Suktha et al report the average oxidation state after first charge was 2.61 which decreased to 2.51 after the first discharge cycle. Moreover, after stability testing, the average Mn oxidation state decreased to 2.38. This decrease in average oxidation state is explained by reduction of  $\text{Mn}^{3+}$  to  $\text{Mn}^{2+}$  followed by extraction of  $\text{Mn}^{2+}$  from the crystal structure. These results are in reasonable agreement with the results of this study, where reduced (MnO) was found in all samples measured, especially in **Mn<sub>3</sub>O<sub>4</sub>-b** after FSRP. The as-prepared  $\text{Mn}_3\text{O}_4$  after VSRP and FSR was significantly oxidized in both the **Mn<sub>3</sub>O<sub>4</sub>-b** and **Mn<sub>3</sub>O<sub>4</sub>-c** samples. The average oxidation state for **Mn<sub>3</sub>O<sub>4</sub>-b** after VSRP was  $2.8 \pm 0.1$  and  $3.1 \pm 0.1$  after FSRP. The average oxidation state of **Mn<sub>3</sub>O<sub>4</sub>-c** was  $3.4 \pm 0.1$  after VSRP and  $3.3 \pm 0.1$  after FSRP, clearly indicating more oxidation of the  $\text{Mn}_3\text{O}_4$  in the **Mn<sub>3</sub>O<sub>4</sub>-c** samples.

The STXM analysis provided additional evidence of the beneficial effect of QC, which adsorbed on  $\text{MnO}_2$  and  $\text{Mn}_3\text{O}_4$  particles during HEBM and prevented their agglomeration. Moreover, QC adsorbed on  $\text{Mn}_3\text{O}_4$  particles during synthesis and acted as a capping agent, which prevented particle agglomeration and reduced particle growth. As a result, **MnO<sub>2</sub>-b** and **Mn<sub>3</sub>O<sub>4</sub>-b** showed higher capacitances, compared to **MnO<sub>2</sub>-a** and **Mn<sub>3</sub>O<sub>4</sub>-a**. Moreover **Mn<sub>3</sub>O<sub>4</sub>-c** electrodes showed significantly higher capacitance compared to that of the **Mn<sub>3</sub>O<sub>4</sub>-a** and **Mn<sub>3</sub>O<sub>4</sub>-b** electrodes. The

---

adsorption of QC on MnO<sub>2</sub> and Mn<sub>3</sub>O<sub>4</sub> was confirmed by FTIR studies (**Figure 10-S6**).

## 10.5 Summary

HEBM resulted in higher capacitances of **MnO<sub>2</sub>-b** and **Mn<sub>3</sub>O<sub>4</sub>-b**, compared to as-prepared **MnO<sub>2</sub>-a** and **Mn<sub>3</sub>O<sub>4</sub>-a**. QC is a promising chelating dispersant for HEBM and capping agent for Mn<sub>3</sub>O<sub>4</sub> synthesis. The **Mn<sub>3</sub>O<sub>4</sub>-c** electrodes showed significantly higher capacitance compared to that of the **Mn<sub>3</sub>O<sub>4</sub>-a** and **Mn<sub>3</sub>O<sub>4</sub>-b** samples. The capacitance of **Mn<sub>3</sub>O<sub>4</sub>-c** was 6.0 F cm<sup>-2</sup> (149.50 F g<sup>-1</sup>) for cyclic voltammetry at 2 mVs<sup>-1</sup> and 8.03 F cm<sup>-2</sup> (200.93 F g<sup>-1</sup>) for chronopotentiometry at 3 mA cm<sup>-2</sup>, which is on par with capacitance of MnO<sub>2</sub>. The time-consuming activation procedure, which limits Mn<sub>3</sub>O<sub>4</sub> applications, was significantly accelerated for **Mn<sub>3</sub>O<sub>4</sub>-b** and practically eliminated for **Mn<sub>3</sub>O<sub>4</sub>-c**. Therefore, **Mn<sub>3</sub>O<sub>4</sub>-c** is a promising alternative to MnO<sub>2</sub> for the fabrication of HAME with high capacitance and low impedance. Further progress in the development of Mn<sub>3</sub>O<sub>4</sub> HAME can potentially result in further improved performance compared to MnO<sub>2</sub>, due to the ability to use capping agents for synthesis and to form solid solutions with improved properties. A combination of STXM and electrochemical testing for VSRP and FSRP provided a platform for improved understanding of HEBM and capping agent effects on capacitance increase, charging and activation mechanisms. The STXM results showed that tested materials contained mixtures of Mn<sup>2+</sup>, Mn<sup>3+</sup> and Mn<sup>4+</sup> oxides. The small amount of MnO phase

---

in the tested samples indicated partial reduction. The higher content of  $\text{MnO}_2$  phase in the tested  $\text{Mn}_3\text{O}_4$  prepared using QC as a capping agent (**Mn<sub>3</sub>O<sub>4</sub>-c**), compared to HEBM  $\text{Mn}_3\text{O}_4$ , correlated with higher capacitance and ability to eliminate the activation procedure. The combination of STXM analysis and electrochemical testing opens an avenue for further progress in the development of  $\text{Mn}_3\text{O}_4$  and solid solution based HAME by the analysis of phase content of the tested electrodes and the ability to track variations in the oxidation states of ions during testing.

## 10.6 Acknowledgements

Research supported by the Natural Sciences and Engineering Research Council of Canada. STXM measurements were performed at the SoftiMAX beamline at Max IV (Lund, Sweden). We acknowledge MAX IV Laboratory for beamtime under Proposal 20221375. Research conducted at MAX IV, a Swedish national user facility, is supported by the Swedish Research council under contract 2018-07152, the Swedish Governmental Agency for Innovation Systems under contract 2018-04969, and Formas under contract 2019-02496. We thank Max IV for beamtime access and especially for the help of staff scientists, Dr. Igor Beinik, Dr. Claudiu Bulbucan and Dr. Karina Thånell in carrying out these experiments. Some STXM measurements were also carried out at the ambient STXM on beamline 10ID1 at the Canadian Light Source (CLS). CLS is funded by CFI, NSERC, NRC, CIHR, the Government of Saskatchewan, and the University of Saskatchewan. We thank SM staff scientists, Jian

---

Wang, Jay Dynes and Yingshen Lu for their support of the beamline, end-stations and assistance with measurements. Wenjuan Yang received support from the China Scholarship Council.

## 10.7 References

- 1 Tang, C. *et al.* Optimizing the electrons/ions diffusion kinetics in  $\delta$ -MnO<sub>2</sub> for realizing an ultra-high rate-capability supercapacitor. *Chemical Engineering Journal* **471**, 144784 (2023).
- 2 Zhu, H. *et al.* Coupling of graphene quantum dots with MnO<sub>2</sub> nanosheets for boosting capacitive storage in ionic liquid electrolyte. *Chemical Engineering Journal* **437**, 135301 (2022).  
<https://doi.org/https://doi.org/10.1016/j.cej.2022.135301>
- 3 Cheong, M. & Zhitomirsky, I. Electrophoretic deposition of manganese oxide films. *Surface Engineering* **25**, 346-352 (2009).  
<https://doi.org:10.1179/174329408X281786>
- 4 Jing, F. *et al.* Oxygen vacancy inducing phase transition during charge storage in MnO<sub>x</sub>@ rGO supercapacitor electrode. *Chemical Engineering Journal* **435**, 135103 (2022).
- 5 Zarshad, N. *et al.* Enhanced energy density and wide potential window for K incorporated MnO<sub>2</sub>@carbon cloth supercapacitor. *Chemical Engineering Journal* **415**, 128967 (2021).  
<https://doi.org/https://doi.org/10.1016/j.cej.2021.128967>
- 6 Jabeen, N. *et al.* Enhanced pseudocapacitive performance of  $\alpha$ -MnO<sub>2</sub> by cation preinsertion. *ACS applied materials & interfaces* **8**, 33732-33740 (2016).
- 7 Wang, J.-G., Kang, F. & Wei, B. Engineering of MnO<sub>2</sub>-based nanocomposites for high-performance supercapacitors. *Progress in Materials Science* **74**, 51-124 (2015).
- 8 Zhang, A. *et al.* Rich bulk oxygen Vacancies-Engineered MnO<sub>2</sub> with enhanced charge transfer kinetics for supercapacitor. *Chemical Engineering Journal* **417**, 129186 (2021).
- 9 Cui, P. *et al.* Plasma-assisted lattice oxygen vacancies engineering recipe for high-performing supercapacitors in a model of birnessite-MnO<sub>2</sub>. *Chemical Engineering Journal* **412**, 128676 (2021).  
<https://doi.org/https://doi.org/10.1016/j.cej.2021.128676>

- 
- 10 Chen, R., Yu, M., Sahu, R. P., Puri, I. K. & Zhitomirsky, I. The Development of Pseudocapacitor Electrodes and Devices with High Active Mass Loading. *Advanced Energy Materials* **10**, 1903848 (2020).  
<https://doi.org/https://doi.org/10.1002/aenm.201903848>
- 11 Li, J. & Zhitomirsky, I. Cathodic electrophoretic deposition of manganese dioxide films. *Colloids and Surfaces A: Physicochemical and Engineering Aspects* **348**, 248-253 (2009).  
<https://doi.org/https://doi.org/10.1016/j.colsurfa.2009.07.035>
- 12 Jeong, Y. & Manthiram, A. Nanocrystalline manganese oxides for electrochemical capacitors with neutral electrolytes. *Journal of the Electrochemical Society* **149**, A1419 (2002).
- 13 Reddy, R. N. & Reddy, R. G. Sol-gel MnO<sub>2</sub> as an electrode material for electrochemical capacitors. *Journal of Power Sources* **124**, 330-337 (2003).
- 14 Chen, D. *et al.* Probing the charge storage mechanism of a pseudocapacitive MnO<sub>2</sub> electrode using in operando Raman spectroscopy. *Chemistry of Materials* **27**, 6608-6619 (2015).
- 15 Ghaemi, M., Ataherian, F., Zolfaghari, A. & Jafari, S. M. Charge storage mechanism of sonochemically prepared MnO<sub>2</sub> as supercapacitor electrode: Effects of physisorbed water and proton conduction. *Electrochimica Acta* **53**, 4607-4614 (2008).  
<https://doi.org/https://doi.org/10.1016/j.electacta.2007.12.040>
- 16 Tanggarnjanavalukul, C., Phattharasupakun, N., Wutthiprom, J., Kidkhunthod, P. & Sawangphruk, M. Charge storage mechanisms of birnessite-type MnO<sub>2</sub> nanosheets in Na<sub>2</sub>SO<sub>4</sub> electrolytes with different pH values: In situ electrochemical X-ray absorption spectroscopy investigation. *Electrochimica Acta* **273**, 17-25 (2018).
- 17 Arias, C. R. *et al.* New insights into pseudocapacitive charge-storage mechanisms in Li-birnessite type MnO<sub>2</sub> monitored by fast quartz crystal microbalance methods. *The Journal of Physical Chemistry C* **118**, 26551-26559 (2014).
- 18 Yang, W., Eraky, H., Zhang, C., Hitchcock, A. P. & Zhitomirsky, I. Scanning transmission X-ray microscopy studies of electrochemical activation and capacitive behavior of Mn<sub>3</sub>O<sub>4</sub> supercapacitor electrodes. *Journal of Materials Chemistry A* **10**, 18267-18277 (2022). <https://doi.org/10.1039/D2TA04702K>
- 19 Hitchcock, A. P. *Soft X-ray imaging and spectromicroscopy, Chapter 22 in Volume II of the Handbook on Nanoscopy, eds. Gustaaf Van Tendeloo, Dirk Van Dyck and Stephen J. Pennycook (Wiley), p 745-791. (2012).*
- 20 Hitchcock, A. P. Soft X-ray spectromicroscopy and ptychography. *Journal of Electron Spectroscopy and Related Phenomena* **200**, 49-63 (2015).
- 21 Ade, H. & Hitchcock, A. P. NEXAFS microscopy and resonant scattering: Composition and orientation probed in real and reciprocal space. *Polymer* **49**, 643-675 (2008).

- 
- 22 Hitchcock, A. P. & Toney, M. F. Spectromicroscopy and coherent diffraction imaging: focus on energy materials applications. *Journal of Synchrotron Radiation* **21**, 1019-1030 (2014).
- 23 Stöhr, J. *NEXAFS spectroscopy*. (Springer Series in Surface Sciences Vol. 25, (Springer, Germany, 1992)).
- 24 Arul, K. T., Chang, H.-W., Shiu, H.-W., Dong, C.-L. & Pong, W.-F. A review of energy materials studied by in situ/operando synchrotron x-ray spectromicroscopy. *Journal of Physics D: Applied Physics* **54**, 343001 (2021).
- 25 Shi, K. & Zhitomirsky, I. Asymmetric Supercapacitors Based on Activated-Carbon-Coated Carbon Nanotubes. *ChemElectroChem* **2**, 396-403 (2015). [https://doi.org:https://doi.org/10.1002/celec.201402343](https://doi.org/https://doi.org/10.1002/celec.201402343)
- 26 Schwenke, J., Thanell, K., Beinik, I., Roslund, L. & Tyliczszak, T. Soft/MAX-A new Soft X-ray Microscopy and Coherent Imaging Beamline at the MAX IV Facility. *Microscopy and Microanalysis* **24**, 232-233 (2018).
- 27 Hitchcock, A. P. Soft X-ray imaging and spectromicroscopy. *Handbook of nanoscopy*, 745-791 (2012).
- 28 Kilcoyne, A. *et al.* Interferometer-controlled scanning transmission X-ray microscopes at the Advanced Light Source. *Journal of synchrotron radiation* **10**, 125-136 (2003).
- 29 Jacobsen, C., Wirick, S., Flynn, G. & Zimba, C. Soft X-ray spectroscopy from image sequences with sub-100 nm spatial resolution. *Journal of Microscopy* **197**, 173-184 (2000).
- 30 Hitchcock, A. P. Analysis of X-ray images and spectra (aXis2000): A toolkit for the analysis of X-ray spectromicroscopy data. *Journal of Electron Spectroscopy and Related Phenomena* **266**, 147360 (2023).
- 31 Ching, S., Petrovay, D. J., Jorgensen, M. L. & Suib, S. L. Sol-gel synthesis of layered birnessite-type manganese oxides. *Inorganic Chemistry* **36**, 883-890 (1997).
- 32 Wei, J. & Zhitomirsky, I. Electrosynthesis of manganese oxide films. *Surface Engineering* **24**, 40-46 (2008). [https://doi.org:10.1179/174329408X271363](https://doi.org/10.1179/174329408X271363)
- 33 Kasprzak, M. M., Erxleben, A. & Ochocki, J. Properties and applications of flavonoid metal complexes. *Rsc Advances* **5**, 45853-45877 (2015).
- 34 Singh, P., Arif, Y., Bajguz, A. & Hayat, S. The role of quercetin in plants. *Plant Physiology and Biochemistry* **166**, 10-19 (2021).
- 35 Malacaria, L. *et al.* Insights into the complexation and oxidation of quercetin and luteolin in aqueous solutions in presence of selected metal cations. *Journal of Molecular Liquids* **369**, 120840 (2023).
- 36 Ata, M., Liu, Y. & Zhitomirsky, I. A review of new methods of surface chemical modification, dispersion and electrophoretic deposition of metal oxide particles. *Rsc Advances* **4**, 22716-22732 (2014).

- 
- 37 Shi, K. & Zhitomirsky, I. Asymmetric Supercapacitors Based on Activated-Carbon-Coated Carbon Nanotubes. *ChemElectroChem* **2**, 396-403 (2015).
- 38 Gilbert, B. *et al.* Multiple scattering calculations of bonding and X-ray absorption spectroscopy of manganese oxides. *The Journal of Physical Chemistry A* **107**, 2839-2847 (2003).
- 39 Toner, B., Fakra, S., Villalobos, M., Warwick, T. & Sposito, G. Spatially resolved characterization of biogenic manganese oxide production within a bacterial biofilm. *Applied and environmental microbiology* **71**, 1300-1310 (2005).
- 40 Risch, M., Morales, D. M., Villalobos, J. & Antipin, D. What X-ray absorption spectroscopy can tell us about the active state of earth-abundant electrocatalysts for the oxygen evolution reaction. *Angewandte Chemie International Edition* **61**, e202211949 (2022).
- 41 Suktha, P., Phattharasupakun, N., Dittanet, P. & Sawangphruk, M. Charge storage mechanisms of electrospun Mn<sub>3</sub>O<sub>4</sub> nanofibres for high-performance supercapacitors. *RSC advances* **7**, 9958-9963 (2017).

## 10.8 Supporting Information

### Section S.1 O 1s chemical mapping of different regions in Mn<sub>3</sub>O<sub>4</sub>-c sample after FSRP

Figure 10-S1 A shows average of STXM images measured at 64 energies in an O 1s stack measured on **Mn<sub>3</sub>O<sub>4</sub>-c** after FSRP. Figure S1 B presents a color-coded composite of the maps of the two spectra extracted from different region of the sample. Figure 10-S1 (B1-B2) are the maps of each component. Figure 10-S1 C presents the O 1s absorption spectra of the regions of each component, verifying the identity of these species.

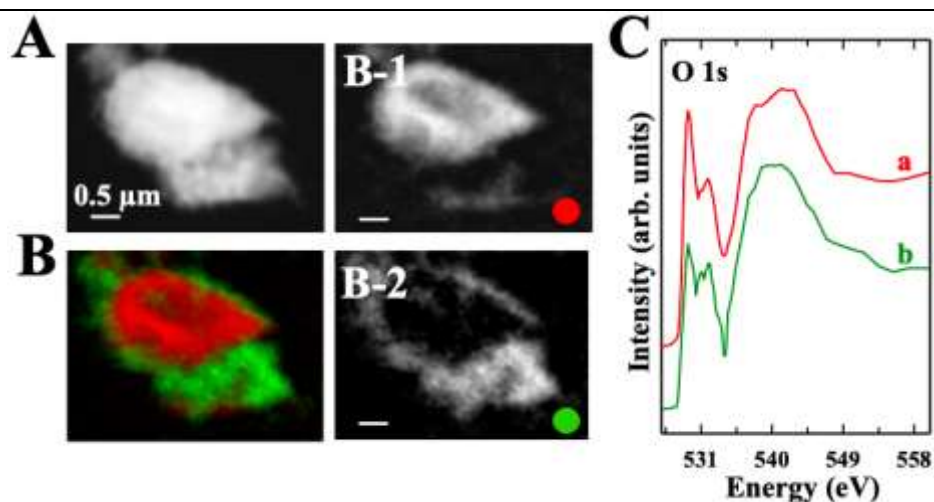


Figure 10-S 1 **O 1s chemical mapping**. **A.** average of 64 images of O 1s stack of the  $\text{Mn}_3\text{O}_4\text{-c}$  after FSRP. **B.** color coded composite of two different Mn oxides regions derived from a stack fit to the O 1s stack. **B-1** and **B-2** are the component maps of the two Mn oxides regions. **C.** O 1s spectra extracted from different region of the sample. The color of each spectrum corresponds to the color-coding in **B.**

## Section S.2 O 1s chemical mapping of different regions in $\text{Mn}_3\text{O}_4\text{-b}$ sample after VSRP

Figure 10-S2 A presents average of STXM images in an O 1s stack measured on  $\text{Mn}_3\text{O}_4\text{-b}$  after VSRP. Figure 10-S2 B presents a color-coded composite of the maps of the two spectra extracted from different region of the sample. Figure 10-S2 (B1-B2) are the maps of each component. Figure 10-S2 C presents the O 1s absorption spectra of the regions of each component, verifying the identity of these species.

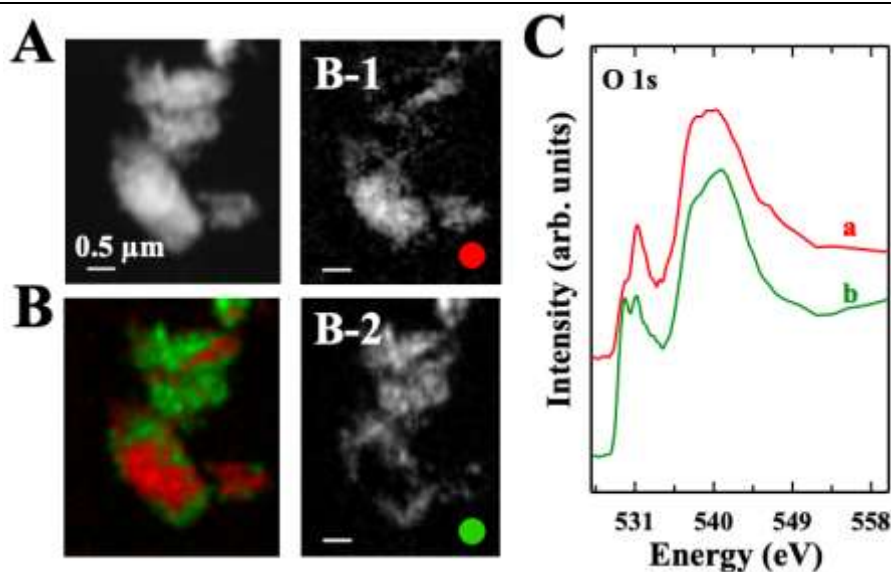


Figure 10-S 2 O 1s chemical mapping. **A.** average of 64 images of O 1s stack of the Mn<sub>3</sub>O<sub>4</sub>-b after VSRP. **B.** color coded composite of two different Mn oxides regions derived from a stack fit to the O 1s stack. **B-1** and **B-2** are the component maps of the two Mn oxides regions. **C.** O 1s spectra extracted from different region of the sample. The color of each spectrum corresponds to the color-coding in **B.**

## Section S.2 O 1s chemical mapping of different regions in Mn<sub>3</sub>O<sub>4</sub>-b sample after FSRP

Figure 10-S3 A presents average of STXM images in an O 1s stack measured on Mn<sub>3</sub>O<sub>4</sub>-b after FSRP. Figure 10-S3 B presents a color-coded composite of the maps of the two spectra extracted from different region of the sample. Figure 10-S3 (B1-B2) are the maps of each component. Figure 10-S3 C presents the O 1s absorption spectra of the regions of each component, verifying the identity of these species.

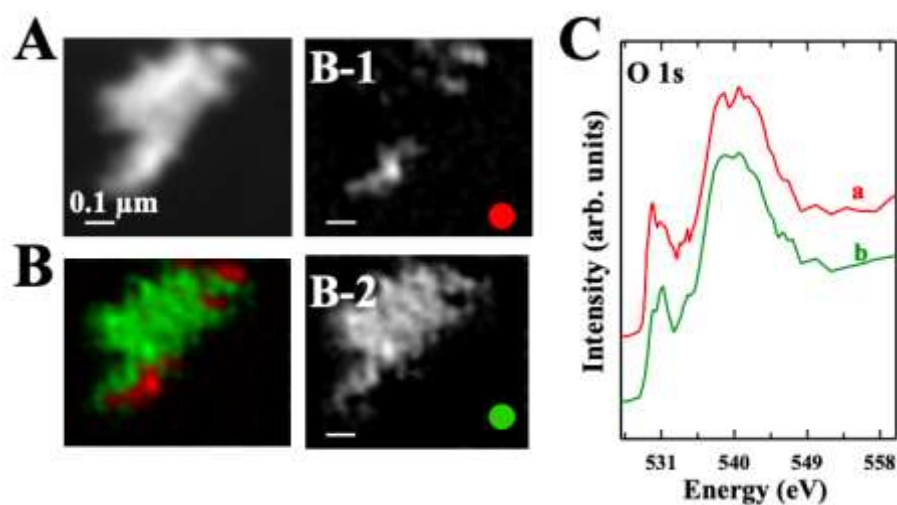


Figure 10-S 3 O 1s **chemical mapping**. **A.** average of 64 images of O 1s stack of the **Mn<sub>3</sub>O<sub>4</sub>-b** after FSRP. **B.** color coded composite of two different Mn oxides regions derived from a stack fit to the O 1s stack. **B-1** and **B-2** are the component maps of the two Mn oxides regions. **C.** O 1s spectra extracted from different region of the sample. The color of each spectrum corresponds to the color-coding in **B.**

#### Section S.4 Mn 2p chemical mapping of the as-prepared MnO<sub>2</sub>-a and MnO<sub>2</sub>-b samples

Figure 10-S4 A and B present quantitative chemical maps of the MnO, Mn<sub>3</sub>O<sub>4</sub> and MnO<sub>2</sub> species for **MnO<sub>2</sub>-a** and **MnO<sub>2</sub>-b**, derived by fitting Mn 2p<sub>3/2</sub> stacks (70 energies from 630 – 650 eV) to the quantitative OD1 reference spectra of MnO, Mn<sub>3</sub>O<sub>4</sub> and MnO<sub>2</sub> (Figure 10-6). Figure 10-S4 C presents Mn 2p<sub>3/2</sub> absorption spectra of the as-prepared **MnO<sub>2</sub>-a** in comparison to that of **MnO<sub>2</sub>-b**.

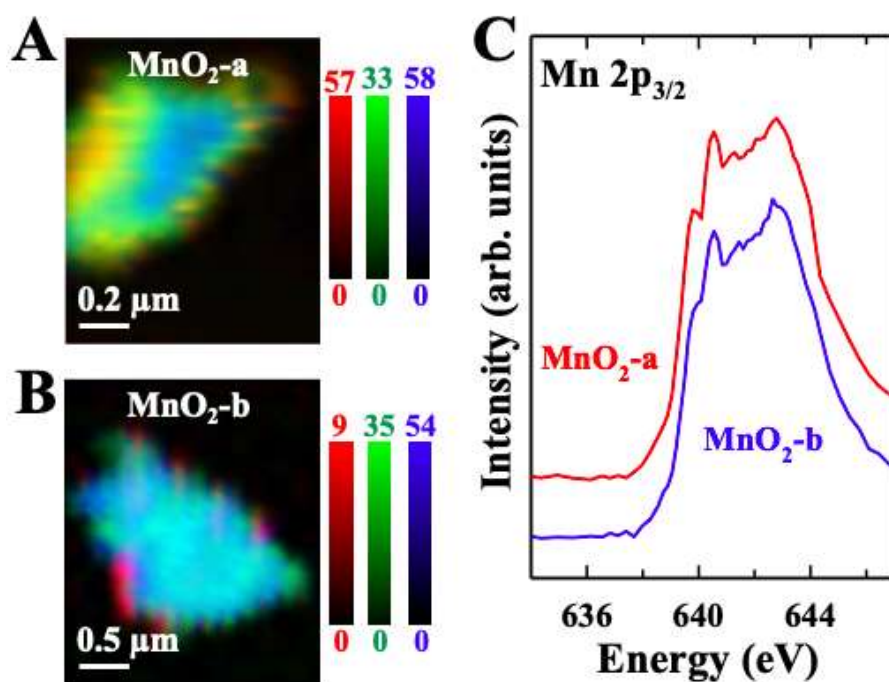


Figure 10-S 4 Color coded composites of MnO (red), Mn<sub>3</sub>O<sub>4</sub> (green) and MnO<sub>2</sub> (blue) chemical maps derived by fitting Mn L<sub>3</sub> stacks. **A. MnO<sub>2</sub>-a** **B. MnO<sub>2</sub>-b** **C.** Mn 2p<sub>3/2</sub> absorption spectra of the as-prepared **MnO<sub>2</sub>-a** in comparison to that of **MnO<sub>2</sub>-b**

### Section S.5 O 1s chemical mapping of different regions in MnO<sub>2</sub>-a and MnO<sub>2</sub>-b samples

Figure 10-S5 A presents a color-coded composite of the maps of the two spectra extracted from different region of **MnO<sub>2</sub>-a** sample (A1 and A2). Figure 10-S5 B presents the O 1s absorption spectra of the regions of each component, verifying the identity of these species. Figure 10-S5 C presents a color-coded composite of the maps of the two spectra extracted from different region of **MnO<sub>2</sub>-b** sample (C1 and C2). Figure 10-S5 D presents the O 1s absorption spectra of the regions of each

component, verifying the identity of these species.

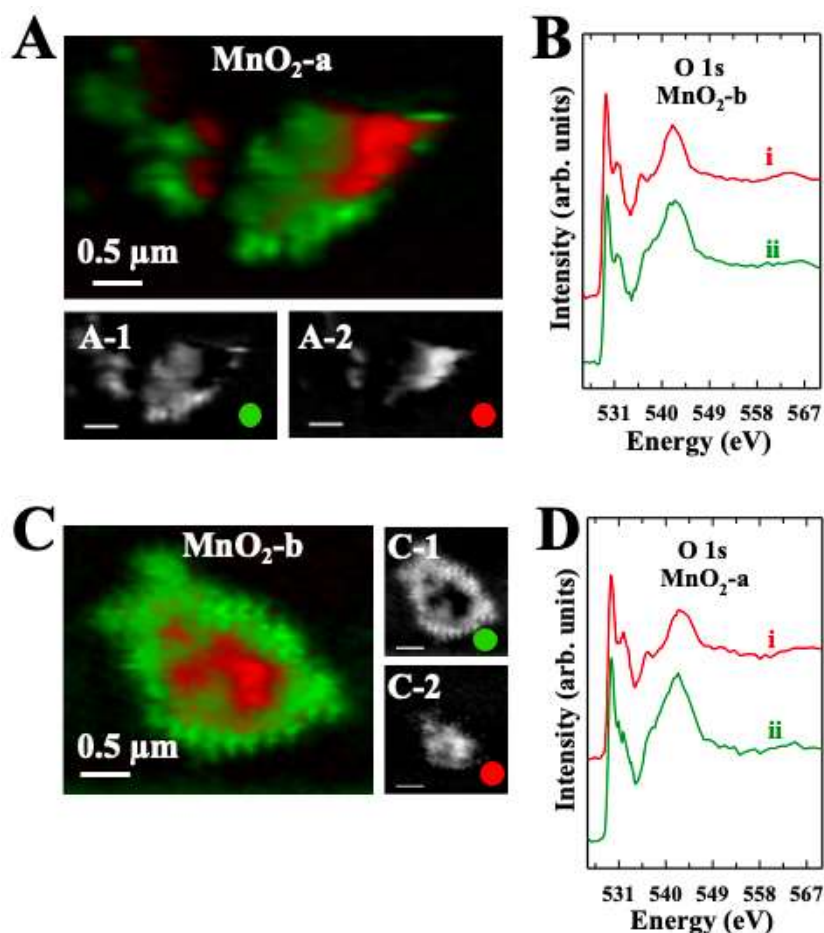


Figure 10-S 5 **O 1s chemical mapping of MnO<sub>2</sub>-a**. **A**. color coded composite of two different Mn oxides regions derived from a stack fit to the O 1s stack. **A-1** and **A-2** are the component maps of the two Mn oxides regions. **B**. O 1s spectra extracted from different region of the sample. The color of each spectrum corresponds to the color-coded in **A**. **O 1s chemical mapping of MnO<sub>2</sub>-b**. **C**. color coded composite of two different Mn oxides regions derived from a stack fit to the O 1s stack. **C-1** and **C-2** are the component maps of the two Mn oxides regions. **D**. O 1s spectra extracted from different region of the sample. The color of each spectrum corresponds to the color-coding in **C**.

## Section S.6 FTIR testing results for MnO<sub>2</sub>-a, MnO<sub>2</sub>-b, Mn<sub>3</sub>O<sub>4</sub>-a, Mn<sub>3</sub>O<sub>4</sub>-b,

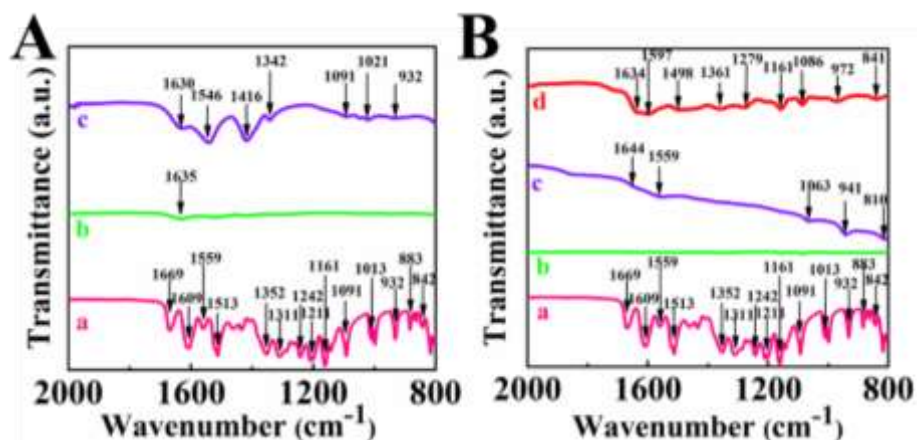
**Mn<sub>3</sub>O<sub>4</sub>-c** and QC.

Figure 10-S 6 FTIR spectra obtained using a Bruker Vertex 70 spectrometer for (A) (a) as-received QC, (b) MnO<sub>2</sub>-a, (c) MnO<sub>2</sub>-b, (B) (a) as-received QC, (b) Mn<sub>3</sub>O<sub>4</sub>-a, (c) Mn<sub>3</sub>O<sub>4</sub>-b, (d) Mn<sub>3</sub>O<sub>4</sub>-c.

The major peaks of QC<sup>1-3</sup> are related to C=O stretching at 1669 cm<sup>-1</sup>, C—C stretching of aromatic rings in the range of 1400-1600 cm<sup>-1</sup>, OH bending in the range of 1200-1400 cm<sup>-1</sup>, C-H vibrations in the range of 1000-1100 cm<sup>-1</sup>. Such absorptions were not observed in the spectra of MnO<sub>2</sub>-a and Mn<sub>3</sub>O<sub>4</sub>-a. However, similar peaks were observed in the spectra of MnO<sub>2</sub>-b, Mn<sub>3</sub>O<sub>4</sub>-b, and Mn<sub>3</sub>O<sub>4</sub>-c and confirmed QC absorption.

## Reference

- 1 Kumari, A., Yadav, S. K., Pakade, Y. B., Singh, B. & Yadav, S. C. Development of biodegradable nanoparticles for delivery of quercetin. *Colloids and Surfaces B: Biointerfaces* **80**, 184-192 (2010).
- 2 Abd El-Rahmanand, S. N. & Suhailah, S. Quercetin nanoparticles: Preparation and characterization. *Indian Journal of Drugs* **2**, 96-103 (2014).

- 
- 3 Wang, Y., Liu, Y. & Zhitomirsky, I. Surface modification of MnO<sub>2</sub> and carbon nanotubes using organic dyes for nanotechnology of electrochemical supercapacitors. *Journal of Materials Chemistry A* **1**, 12519-12526 (2013).

# **Chapter 11 Preparation of ferromagnetic perovskite $\text{La}_{0.65}\text{Sr}_{0.35}\text{MnO}_3$ electrodes for supercapacitor applications.**

Wenjuan Yang and Igor Zhitomirsky\*

Department of Materials Science and Engineering,  
McMaster University, Hamilton, ON L8S 4L7, Canada

\*Corresponding author: [zhitom@mcmaster.ca](mailto:zhitom@mcmaster.ca)

Phone 905-525-9140

Copyright 2024. Reproduced with permission from Springer

## 11.1 Abstract

Ferromagnetic perovskite  $\text{La}_{0.65}\text{Sr}_{0.35}\text{MnO}_3$  (LSM) is prepared as an active material for electrodes with high active mass loading of  $40 \text{ mg cm}^{-2}$  for applications in supercapacitors. The experimental approach of this investigation is based on the use of high energy ball milling and application of gallocyanine as an advanced catecholate-type chelating dispersant. We report a high capacitance of  $3.75 \text{ F cm}^{-2}$  from cyclic voltammetry data at  $2 \text{ mV s}^{-1}$  and  $4.59 \text{ F cm}^{-2}$  from chronopotentiometry data at  $3 \text{ mA cm}^{-2}$  for LSM. The electrodes show nearly ideal pseudocapacitive behavior and a low resistance. The capacitance of ferromagnetic perovskite LSM electrodes in a positive potential range is higher or on a par with capacitances of spinel ferrimagnetic electrodes for operation in a negative potential range in the same electrolyte. Cycling at fast charge-discharge rates shows capacitance increase, which is attributed to morphology changes and oxidation of Mn ions. The LSM electrodes were used for application in magnetic asymmetric devices, containing ferromagnetic LSM cathodes and ferrimagnetic  $\text{CoFe}_2\text{O}_4$  based anodes with high active mass for operation in a neutral  $\text{Na}_2\text{SO}_4$  electrolyte.

## 11.2 Introduction

The combination of advanced electric and magnetic properties in a single material is promising for fabrication of devices, based on magnetoelectric (ME) effects.

---

Magnetically ordered pseudocapacitor (MOPC) materials<sup>1</sup> exhibit a unique combination of outstanding electric and magnetic properties. In contrast to other ME materials, such as multiferroic compounds<sup>2-4</sup>, many MOPC materials exhibit high spontaneous magnetization and high capacitance at room temperature. Advanced spinel ferrimagnetics, such as  $\text{Fe}_3\text{O}_4$ <sup>5,6</sup>,  $\text{CuFe}_2\text{O}_4$ <sup>7,8</sup>,  $\text{MnFe}_2\text{O}_4$ <sup>9</sup>,  $\text{NiFe}_2\text{O}_4$ <sup>10,11</sup>,  $\gamma\text{-Fe}_2\text{O}_3$ <sup>12,13</sup> and solid solutions<sup>14,15</sup> exhibit high pseudocapacitance, which is by six to eight orders of magnitude higher than electrical capacitance of multiferroics. The change of valence state and magnetic moments of paramagnetic ions in redox reactions results in changing their superexchange interactions and magnetization. This provides a basis for novel ME phenomena. Of particular interest is the magnetohydrodynamic effect, which provides the ability to manipulate electrolyte ion diffusion by external magnetic fields or local magnetic fields of magnetic particles. The magnetohydrodynamic effect improves electrode capacitance by facilitating ion access to redox sites and charge storage reactions<sup>1,16,17</sup>. MOPC showed significant capacitance increase in a magnetic field, high capacitance at fast charging rates, improved cyclic stability, on/off magnetization switching by fast variation of electric potential, giant magnetoelectric coupling coefficient, ferromagnetic Curie temperature shift in an electric field and other ME effects<sup>1,18-22</sup>. The pseudocapacitive properties of spinels and other ferrites result from redox reactions and change of valence states of  $\text{Fe}^{3+} \rightarrow \text{Fe}^{2+}$ ,  $\text{Cu}^{2+} \rightarrow \text{Cu}^+$  and other paramagnetic ions<sup>7,14,23-26</sup>. Various spinel

---

ferrites are considered for applications in anodes of MOPC devices.

Many perovskite materials exhibit antiferromagnetic or weak ferrimagnetic properties because perovskite structure facilitates antiparallel orientation and ordering of magnetic moments of paramagnetic ions in their crystallographic octahedral positions<sup>3</sup>. The ordering of ions in BiFeO<sub>3</sub>, BiMnO<sub>3</sub> and other perovskites results from double exchange interactions<sup>3</sup>. In contrast to other perovskites, La<sub>1-x</sub>Sr<sub>x</sub>MnO<sub>3</sub> exhibits room temperature ferromagnetism, which results from double exchange interactions of Mn<sup>3+</sup> and Mn<sup>4+</sup> ions<sup>27-30</sup>. Moreover, La<sub>1-x</sub>Sr<sub>x</sub>MnO<sub>3</sub> exhibits giant magnetoresistance and electrochemical pseudocapacitance<sup>31</sup>. La<sub>1-x</sub>Sr<sub>x</sub>MnO<sub>3</sub> solid solutions are promising for application in MOPC cathodes. Redox reactions of paramagnetic Mn<sup>3+</sup> and Mn<sup>4+</sup> ions impart pseudocapacitive properties to this material. Moreover, the change of magnetic moments of the ions and energy of their double exchange interactions<sup>31</sup> in the redox reactions provides a basis for ME interactions.

The Curie temperature of La<sub>1-x</sub>Sr<sub>x</sub>MnO<sub>3</sub> can be changed by variation of Sr<sup>2+</sup> and Mn<sup>4+</sup> contents<sup>28,32</sup>. Mn<sup>3+</sup>—O—Mn<sup>4+</sup> ion hopping in La<sub>1-x</sub>Sr<sub>x</sub>MnO<sub>3</sub> results in metallic conductivity below Curie temperature<sup>28,33</sup>. La<sub>1-x</sub>Sr<sub>x</sub>MnO<sub>3</sub> shows colossal magnetoresistance, which results in significant resistivity decrease in a magnetic field<sup>27,32</sup>. A strong link was observed between colossal magnetoresistance, metallic conductivity and ferromagnetism in La<sub>1-x</sub>Sr<sub>x</sub>MnO<sub>3</sub><sup>28,34</sup>. The electrical conductivity of this material is by 6 orders of magnitude higher than that of MnO<sub>2</sub>, which is the most promising cathode material for asymmetric supercapacitors for operation in

---

neutral Na<sub>2</sub>SO<sub>4</sub> and K<sub>2</sub>SO<sub>4</sub> electrolytes<sup>35</sup>.

Table 11-S1 (Supplementary information) presents a summary of literature reports on capacitive properties of La<sub>1-x</sub>Sr<sub>x</sub>MnO<sub>3</sub>. Previous investigations focused on thin film electrodes with low active mass of about 1 mg cm<sup>-2</sup> for charge storage in KOH<sup>36,37</sup> and Na<sub>2</sub>SO<sub>4</sub><sup>38,39</sup> electrolytes. The areal capacitance of such electrodes was low. Therefore, the electrodes with higher active mass must be developed for matching the areal capacitances of advanced anodes. Other difficulties are related to non-ideal pseudocapacitive response of La<sub>1-x</sub>Sr<sub>x</sub>MnO<sub>3</sub>, as indicated by redox peaks in cyclic voltammograms and non-linear chronopotentiometry curves<sup>36,37,40</sup>, relatively high electrode resistance<sup>36-38,40</sup>, and high charge transfer resistance<sup>38</sup>. The goal of this investigation was the fabrication and testing of La<sub>0.65</sub>Sr<sub>0.35</sub>MnO<sub>3</sub> (LSM) electrodes for operation in a positive potential range.

In contrast to previous works in the field, we fabricated high active mass electrodes with a mass of 40 mg cm<sup>-2</sup> and achieved nearly ideal pseudocapacitive behavior in a neutral Na<sub>2</sub>SO<sub>4</sub> electrolyte. We report a high capacitance of 3.75 F cm<sup>-2</sup> from cyclic voltammetry data at 2 mV s<sup>-1</sup> and 4.59 F cm<sup>-2</sup> from chronopotentiometry data at 3 mA cm<sup>-2</sup> for this material. The high capacitance was achieved at a low electrode resistance. The obtained capacitance is significantly higher than literature data for LSM due to the use of new electrode fabrication methods and a novel chelating dispersant. We found that LSM combines advanced pseudocapacitive properties and high magnetization. We successfully addressed the problem of low capacitance of

magnetic materials for cathodes of magnetic supercapacitor devices, which is lower than the capacitance of magnetic anode materials. The obtained capacitance for LSM electrodes in a positive potential range is higher or on a par with capacitances of ferrite-type electrodes for operation in a negative potential range. We fabricated and tested an asymmetric device, containing ferromagnetic LSM based cathode and a ferrimagnetic  $\text{CoFe}_2\text{O}_4$  based anode.

## 11.3 Experimental procedures

### 11.3.1. Materials and fabrication methods

Gallocyanine (GLC),  $\text{La}_{0.35}\text{Sr}_{0.65}\text{MnO}_3$  (LSM),  $\text{Na}_2\text{SO}_4$ , ethanol, and poly(vinyl butyral) (PVB) were supplied from MilliporeSigma, Canada. Multiwalled carbon nanotubes (MWCNT) with an inner diameter of 4 nm, outer diameter of 13 nm, and length of 1–2  $\mu\text{m}$  were obtained from Bayer, Germany and used as conductive additives.

Suspensions of LSM particles, MWCNT, and dissolved GLC with mass ratio LSM:MWCNT:GLC = 8:2:1 were prepared by ultrasonication for 8 minutes. After washing, filtration, and drying, the obtained mixtures were used for fabrication of slurries in ethanol, containing dissolved PVB for the impregnation of commercial Ni foam (Vale, Canada) current collectors. The PVB content in the composite electrodes was 3%. The mass loading of the electrodes after drying was  $40 \text{ mg cm}^{-2}$ . Two

---

composites were prepared using the as-received LSM powder and high energy ball-milled LSM. High energy ball milling (HEBM) was performed using a Mixer Mill MM 500 Nano (Retsch GmbH, Germany) at a frequency of 15 Hz for a total milling time of 2 hours.

### **11.3.2 Characterization techniques**

The LSM powders were characterized using transmission electron microscopy (TEM, Talos 200X, Thermo Fisher Scientific, USA) and X-ray diffraction analysis (Bruker Smart 6000 X-ray diffractometer, CuK $\alpha$  radiation, Bruker, USA.). The microstructures of the electrodes were observed using scanning electron microscopy (SEM, JEOL, JSM-7000F microscope, Japan) at different magnifications. Magnetic measurements were performed using a Quantum Design Magnetic Properties Measurement System (MPMS, USA). A Bruker FTIR spectrometer (Vertex 70, USA) was applied for spectroscopy analysis. X-ray photoelectron spectroscopy (XPS) investigations were performed with a PHI Quantera II Scanning XPS Microprobe. Electrochemical studies were conducted in aqueous 0.5 M Na<sub>2</sub>SO<sub>4</sub> electrolyte using a PARSTAT 2273 (Ametek, USA) potentiostat for cyclic voltammetry (CV) and electrochemical impedance spectroscopy (EIS), while a BioLogic VMP 300 (Biologic, France) potentiostat was used for chronopotentiometry (CP) investigations. The testing was performed using a three-electrode electrochemical cell containing a working electrode (impregnated Ni foam), counter-electrode (Pt mesh), and a

reference electrode (SCE, saturated calomel electrode). The capacitances calculated from CV and CP data represented integral capacitances measured in a voltage window of 0–0.9 V versus SCE, while the capacitances calculated from EIS data represented differential capacitances measured at an open-circuit potential at a voltage amplitude of 5 mV. Capacitance was calculated from CV, CP and EIS data as it was discussed in Refs. <sup>41,42</sup>. The ferromagnetic LSM based cathodes and ferrimagnetic CoFe<sub>2</sub>O<sub>4</sub> based anodes were used for the fabrication of asymmetric device for operation in a voltage window of 1.5 V in 0.5 M Na<sub>2</sub>SO<sub>4</sub> electrolyte. The procedure for the fabrication of CoFe<sub>2</sub>O<sub>4</sub>-polypyrrole (PPy) anodes, containing CoFe<sub>2</sub>O<sub>4</sub> and PPy in a mass ratio of 1:1 was described in a previous investigation <sup>43</sup>. The mass of the individual electrodes was 40 mg cm<sup>-2</sup>. The electrodes were separated by a polypropylene (Vale) membrane with a thickness of 0.15 mm.

## 11.4 Results and Discussion

### 11.4.1 XRD studies and magnetic measurements

XRD studies confirmed the perovskite structure of LSM (Figure 1). Magnetic measurements indicated ferromagnetic behavior of LSM (Figure 2) with magnetization of about 50 emu g<sup>-1</sup>. It is known that the spontaneous magnetization of bulk LSM is typically in the range of 40-50 emu g<sup>-1</sup> <sup>44</sup>. The analysis of magnetization curve showed a low remnant magnetization. Such behavior is often observed in soft

ferromagnetics at temperatures below their Curie points.

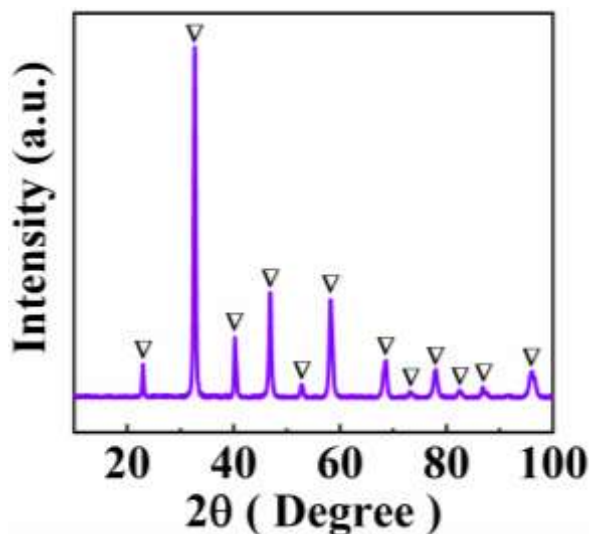


Figure 11- 1 X-ray diffraction pattern of LSM ( $\nabla$  - peaks corresponding to JCPDS file 89-0648).

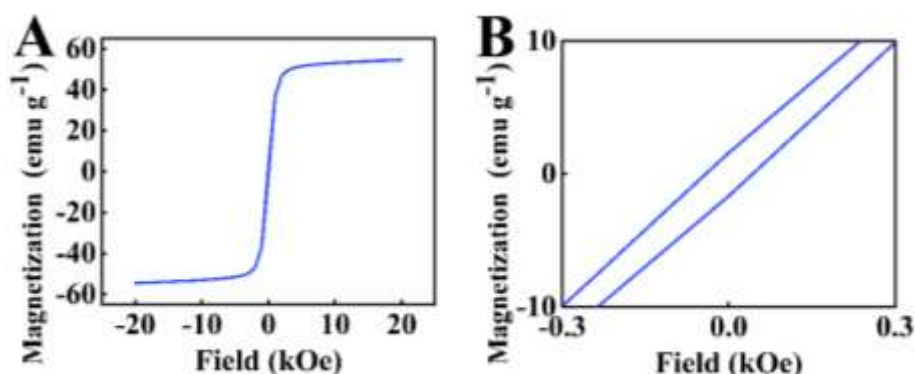


Figure 11- 2 (A,B) Magnetization versus magnetic field for LSM, (B) shows the magnetization curve in a low field range.

## 11.4.2 TEM and FTIR studies

TEM studies of as-received LSM (Figure 11-3A,B) showed many relatively large particles with size about 0.5-2  $\mu\text{m}$ . However, the as-received material also contained smaller particles. HEBM resulted in size reduction and the size of ball milled powders was below 0.5  $\mu\text{m}$  (Figure 11-3C, D).

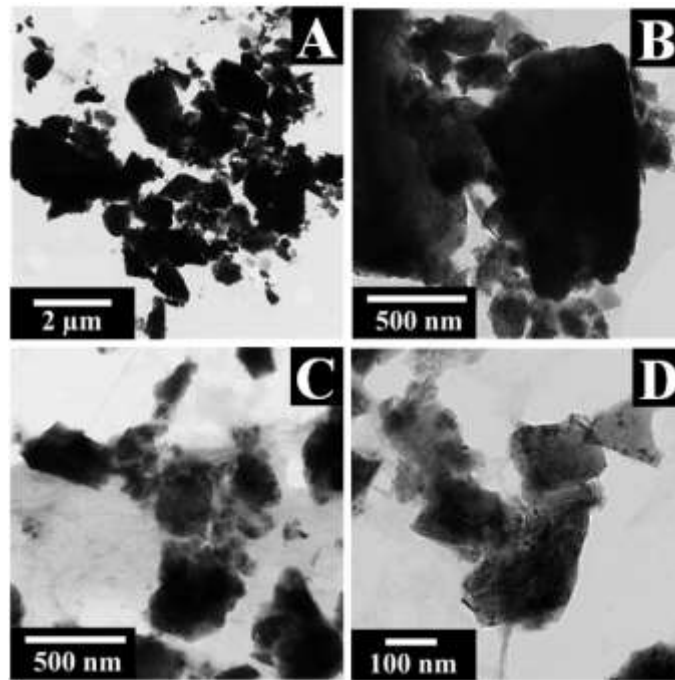


Figure 11- 3 TEM images at different magnifications for LSM: (A,B) as-received and (C,D) after HEBM.

In this investigation GLC was used as a co-dispersant for LSM and MWCNT.

Figure 11-4 shows a catechol type<sup>45</sup> adsorption of GLC on LSM, which involves deprotonation of phenolic OH groups and complexation of metal atoms on the LSM surface.

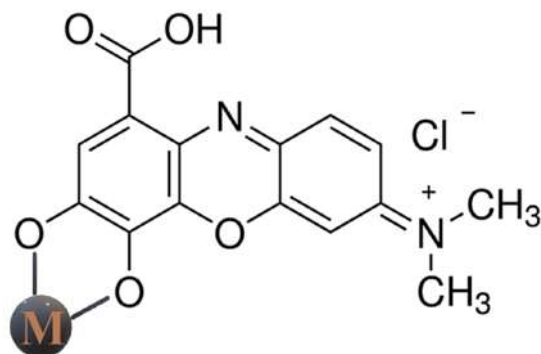


Figure 11- 4 Adsorption mechanisms of GLC on  $\text{La}_{0.35}\text{Sr}_{0.65}\text{MnO}_3$  by chelation (M = La, Sr or Mn).

The aromatic structure of GLC facilitated its adsorption on MWCNT through  $\pi$ - $\pi$  interactions. Figure 11-5 compares FTIR spectra of GLC, as-prepared LSM and LSM with adsorbed GLC. The spectrum of GLC shows multiple absorption peaks in the range of 1100-1900  $\text{cm}^{-1}$ . In contrast, LSM did not show absorptions in the same range. The absorption at 1722  $\text{cm}^{-1}$  in the spectrum of GLC is due to C=O stretching<sup>40</sup>. The multiple absorptions at 1586, 1555, 1526, 1483 and 1423  $\text{cm}^{-1}$  can be attributed to C=C and C-C vibrations of the aromatic rings<sup>47,48</sup>. It is suggested that similar absorption of GLC adsorbed on LSM resulted in a broad peak centered at 1504  $\text{cm}^{-1}$ . GLC showed absorptions at 1305, 1284 and 1260, which can result from C-N-C and C-O stretching<sup>12,49</sup>. Similar absorptions of GLC adsorbed on LSM resulted in a broad peak centered at 1292  $\text{cm}^{-1}$ . The characteristic peaks of LSM were observed at lower wavenumbers (Supplementary information, Figure 11-S1).

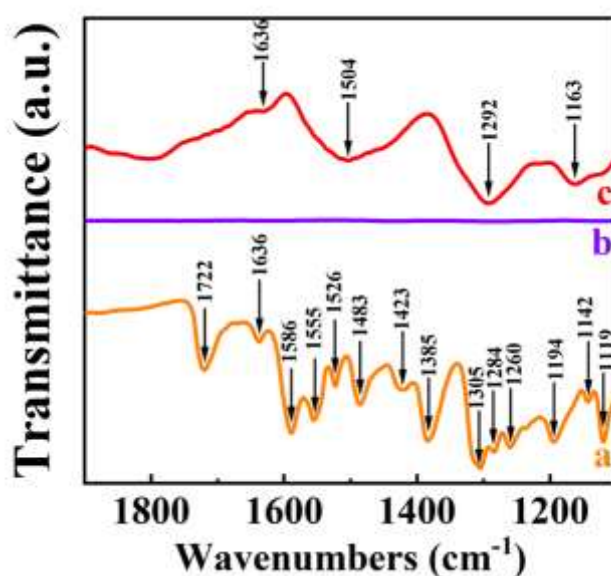


Figure 11- 5 FTIR spectra of (a) GLC, (b) LSM and (c) LSM with adsorbed GLC.

### 11.4.3 SEM and electrochemical studies of the electrodes

As received and ball milled LSM were used for the fabrication of electrodes for application in cathodes of supercapacitors. Figure 11-6 shows SEM images of composite electrodes. The analysis of SEM images at different magnifications showed that HEBM resulted in reduced LSM particle size and improved mixing of LSM and MWCNT, which facilitated the fabrication of electrodes with enhanced performance.

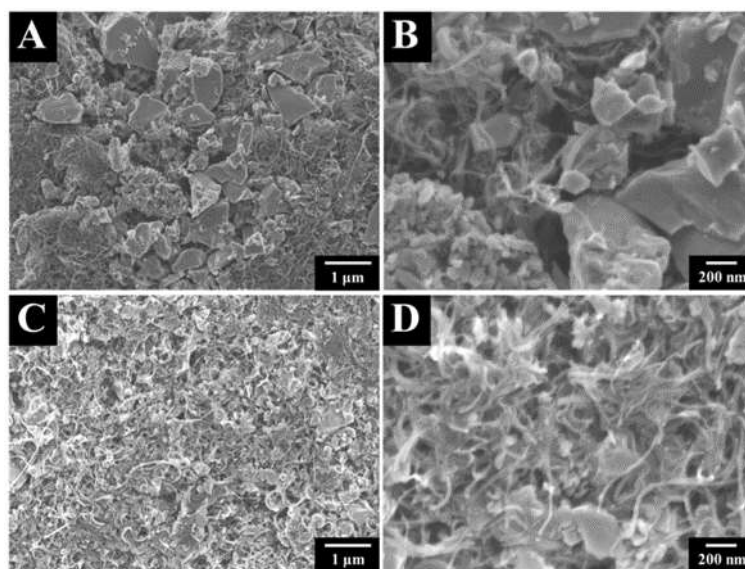


Figure 11- 6 SEM images at different magnifications for LSM-MWCNT electrodes prepared using (A,B) as-received LSM and (C,D) LSM after HEBM.

Figure 11-7 (A,B) shows CVs for electrodes prepared using as-received and HEBM LSM. The CV curves show nearly rectangular shape without obvious redox peaks. This contrasts with other investigations, which showed redox peaks<sup>36,40,50</sup>. The CVs for HEBM LSM exhibited significantly higher currents, compared to as-received LSM. As a result, HEBM LSM showed significantly higher capacitance. Figure 11-7C

shows capacitances of electrodes prepared using as-received and HEBM LSM. The electrodes showed capacitances of  $0.67 \text{ F cm}^{-2}$  ( $16.7 \text{ F g}^{-1}$ ) and  $3.75 \text{ F cm}^{-2}$  ( $93.8 \text{ F g}^{-1}$ ) for as-received and HEBM LSM, respectively, at  $2 \text{ mV s}^{-1}$ . CP data showed nearly triangular charge-discharge curves (Figures 11-7D and E) with longer charge-discharge times for HEBM LSM, which indicated higher capacitance. The capacitances (Figure 11-7F) were found to be  $1.15 \text{ F cm}^{-2}$  ( $28.7 \text{ F g}^{-1}$ ) and  $4.59 \text{ F cm}^{-2}$  ( $114.8 \text{ F g}^{-1}$ ) for as-received and HEBM LSM, respectively, at  $3 \text{ mA cm}^{-2}$ . The almost rectangular CV curves without redox peaks and triangular CP curves indicated nearly ideal pseudocapacitive behavior.

The charge storage properties of HEBMBFO-E and HEBMBFO-GCA-E were analyzed using equation<sup>51</sup>:

$$i = av^b \quad (11-1)$$

where  $i$  - current,  $v$  – CV sweep rate,  $a$  and  $b$  - parameters. Parameter  $b=1$  for pure double layer capacitive response and  $b=0.5$  for pure battery behavior. Literature data analysis for different materials<sup>52-56</sup> shows that electrodes with  $0.5 < b < 1$  exhibit a mixed battery and capacitive response. The capacitive behavior is dominant for  $0.8 < b < 1$ . The parameter  $b$  was 0.8 for as-received and HEBM LSM and indicated pseudocapacitive behavior.

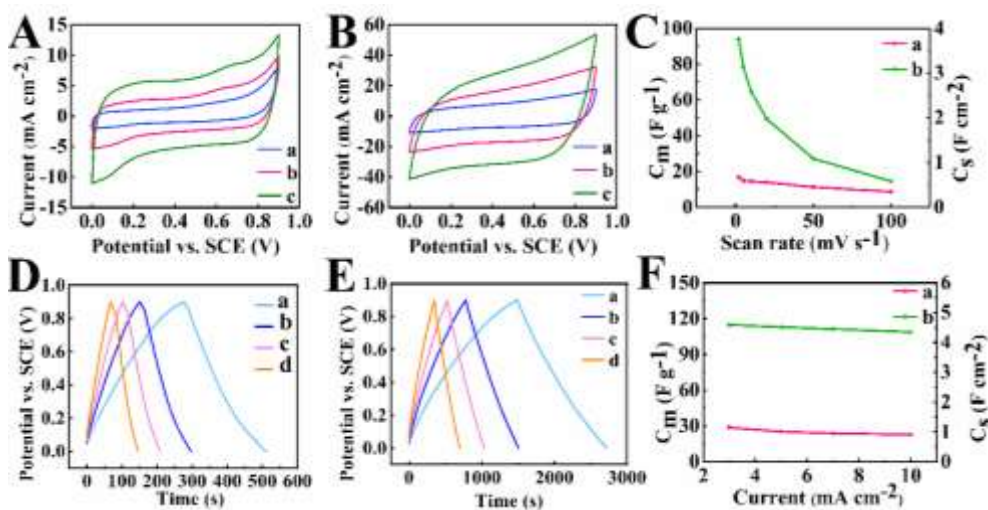


Figure 11- 7 (A,B) CVs at (a) 2, (b) 5 and (c) 10  $\text{mV s}^{-1}$ , (C) capacitance versus scan rate, (D,E) CP data at (a)3, (b)5, (c)7 and (d)10  $\text{mA cm}^{-2}$ , (F) capacitance versus current density for electrodes prepared using (A), (C(a)), (D), (F(a)) as received and (B), (C(b)), (E), (F(b)) HEBM LSM.

Testing results showed a strong effect of HEBM on capacitance of LSM. It is suggested that particle size reduction results in enhanced electrolyte access to the LSM surface and facilitates improved mixing with MWCNT, which was performed using GLC as a cationic co-dispersant. However, it should be noted that previous investigations of different materials didn't show a correlation between BET particle surface area and pseudocapacitance<sup>57-59</sup>. It was shown that very small pores accessible to gas molecules in BET experiments are not accessible to solvated ions during charge-discharge. As a result, some materials with higher BET surface area showed lower capacitance, compared to the electrodes with lower surface area<sup>57-59</sup>. EIS data (Figure 11-8A) showed reduction of electrode resistance  $R=Z'$  for the HEBM material. The resistances of electrodes at 10 mHz were found to be 8.20 and 3.01

Ohms for as-received and HEBM LSM, respectively. Despite the high active mass loading of the electrodes used in this study, the resistance of HEBM electrodes was significantly lower, compared to resistances of electrodes with low active mass loadings tested in other investigations<sup>40,60</sup>. Moreover, the analysis of the EIS data using an equivalent circuit developed in previous investigations<sup>61</sup> for electrodes with high active mass loadings (Figure 11-S2) showed very low charge transfer resistance of HEBM LSM electrodes, which was found to be 0.12 Ohm. The charge transfer resistance was lower than that reported in literature<sup>38</sup>. EIS data showed enhanced capacitance of the HEBM LSM electrodes, compared to the capacitance of as-received LSM electrodes (Figure 12-8 B,C). It should be noted that capacitances measured by different methods are dependent on different parameters, such as frequency and amplitude of AC signal in the EIS experiments, or voltage window, current density and scan rate in the CV and CP experiments.

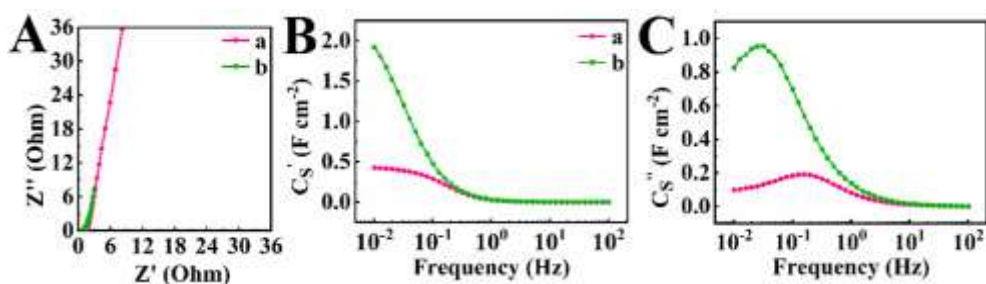


Figure 11- 8 (A) Nyquist graph and (B, C) components of complex capacitance versus frequency for electrodes prepared using (a) as-received and (b) HEBM LSM.

Areal capacitance of HEBM LSM electrodes is significantly higher than reported data for LSM (Table 11-S1). It is important to note that high areal capacitance is achieved

in a neutral electrolyte, which makes this material very promising for applications in cathodes of asymmetric magnetic supercapacitors. Ferrite spinel anodes of the same active mass of 40 mg cm<sup>-2</sup> showed capacitances of 1.53 F cm<sup>-2</sup> ( $\gamma$ -Fe<sub>2</sub>O<sub>3</sub><sup>12</sup>), 2.76 F cm<sup>-2</sup> (CuFe<sub>2</sub>O<sub>4</sub><sup>7</sup>) and 4.59 F cm<sup>-2</sup> (Fe<sub>3</sub>O<sub>4</sub><sup>62</sup>). The capacitance of HEBM LSM electrodes in a positive potential range is higher or on a par with capacitances of ferrite-type electrodes for operation in a negative potential range in Na<sub>2</sub>SO<sub>4</sub> electrolyte. The fabrication of asymmetric magnetic supercapacitor devices with practically important high active mass loadings<sup>41</sup> requires matching the areal capacitances of individual electrodes. Therefore, the LSM electrodes are promising for application in magnetic asymmetric devices, containing ferromagnetic LSM perovskite cathodes and ferrimagnetic spinel anodes with high active mass for operation in a neutral Na<sub>2</sub>SO<sub>4</sub> electrolyte.

The charge storage mechanism of LSM is not well understood and requires further investigation for the development of electrodes with higher capacitance. It is hypothesized that charging mechanism of LSM and other capacitive manganates can be related to redox reactions involving Mn<sup>3+</sup> and Mn<sup>4+</sup> ions<sup>38,63</sup>. XPS studies (Supplementary Information, Figure S3) showed that LSM contains Mn<sup>3+</sup> and Mn<sup>4+</sup> ions. It is suggested that the charging mechanism of LSM is like that of manganese oxides<sup>64</sup>, such as MnO<sub>2</sub> and Mn<sub>3</sub>O<sub>4</sub>. It involves adsorption of Na<sup>2+</sup> ions on the particle surface and subsequent charge-discharge reaction:



Investigations at relatively high scan rates, such as  $50 \text{ mV s}^{-1}$  revealed variation of capacitance during cycling. Figure 12-9 shows cycling behavior of as-prepared electrodes.

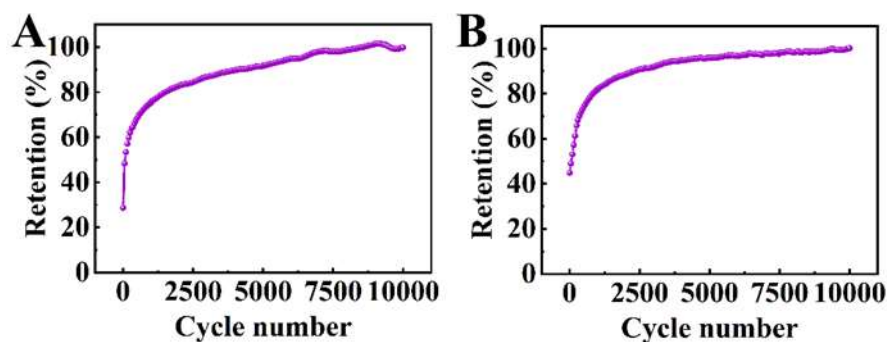


Figure 11- 9 Capacitance retention for electrodes, prepared using (A) as-received and (B) HEBM LSM at  $50 \text{ mV s}^{-1}$ . The capacitances were calculated for different CV cycles and normalized by capacitance value for the cycle 10,000.

Testing results showed significant increase in capacitance of as-prepared electrodes during cycling at  $50 \text{ mV s}^{-1}$ . It should be noted that such increase was not observed at  $2 \text{ mV s}^{-1}$  and at higher scan rates after obtaining first CV at  $2 \text{ mVs}^{-1}$ . Figure 9A shows capacitance versus cycle number for electrodes prepared using as-received LSM. The capacitance for the cycle 1 was 34.8% of the capacitance for cycle 10,000. Testing revealed significant capacitance increase during 7,000 cycles. This indicated the need in electrode activation procedures for applications at fast charge rates. The capacitance of electrodes prepared using HEBM was 39.5% of the capacitance for cycle 10,000 (Figure 12-9A). The electrodes showed faster activation. Significant variation of capacitance was observed for the first 3,000 cycles. SEM studies showed that capacitance increase can result form electrode morphology

changes during cycling. The comparison of electrode morphologies before (Figure 12-6) and after cycling (Supplementary information, Figure 12-S4) showed that cycling resulted in increased electrode porosity which facilitated electrolyte access to the bulk of the electrode material. XPS data showed that cycling resulted in increasing  $\text{Mn}^{4+}$  content and reducing  $\text{Mn}^{3+}$  content in LSM (Figure 12-S3). It is in this regard that previous investigations of  $\text{MnO}_x$  electrodes revealed capacitance increase during cycling due to oxidation of Mn species<sup>64,65</sup>. Therefore, the capacitance increase of LSM can also result from oxidation of  $\text{Mn}^{3+}$  ions.

The HEBM LSM electrodes were used as cathodes for the fabrication of an asymmetric device, containing ferrimagnetic  $\text{CoFe}_2\text{O}_4$ -PPy composite anodes. CV and CP data (Supplementary information, Figure 12-S5) showed pseudocapacitive behavior in a voltage window of 1.5 V. The device showed capacitances of 0.74 and 1.24  $\text{F cm}^{-2}$  for CV data at 2  $\text{mV s}^{-1}$  and CP data at 3  $\text{mA cm}^{-2}$ , respectively.

## 11.5 Conclusions

The use of HEBM and catecholate-type GLC facilitated the fabrication of advanced ferromagnetic LSM electrodes, which showed a high magnetization and high capacitance. The electrodes showed nearly ideal pseudocapacitive behavior without redox peaks. The obtained capacitances of 3.75  $\text{F cm}^{-2}$  from CV at 2  $\text{mV s}^{-1}$  and 4.59  $\text{F cm}^{-2}$  from CP at 3  $\text{mA cm}^{-2}$  are significantly higher compared to the literature data. The high capacitances of high active mass electrodes were achieved at a low electrode

---

resistance. The high capacitance obtained for ferromagnetic LSM in the positive potential range in the neutral Na<sub>2</sub>SO<sub>4</sub> electrolyte is higher or on a par with capacitances of ferrimagnetic spinel ferrite-type electrodes for operation in a negative potential range in the same electrolyte. Therefore, the LSM electrodes are promising for application in cathodes of magnetic asymmetric devices, containing ferromagnetic perovskite LSM cathodes and ferrimagnetic spinel anodes with high active mass for operation in a neutral Na<sub>2</sub>SO<sub>4</sub> electrolyte. Cycling at fast charge-discharge rates showed capacitance increase, which was attributed to morphology changes. The ferromagnetic LSM based cathodes and ferrimagnetic CoFe<sub>2</sub>O<sub>4</sub> based anodes were used for the fabrication of an asymmetric device for operation in a voltage window of 1.5 V in 0.5 M Na<sub>2</sub>SO<sub>4</sub> electrolyte.

## 11.6 Acknowledgments

SEM studies were performed at the Canadian Centre for Electron Microscopy.

Wenjuan Yang received support from the China Scholarship Council.

## 11.7 References

- 1 Sikkema, R. & Zhitomirsky, I. Magnetic supercapacitors: Charge storage mechanisms, magnetocapacitance, and magnetoelectric phenomena. *Applied Physics Reviews* **10**, 021307 (2023).
- 2 Schmid, H. Multi-ferroic magnetoelectrics. *Ferroelectrics* **162**, 317-338 (1994). <https://doi.org/10.1080/00150199408245120>

- 
- 3 Venevtsev, Y. N., Gagulin, V. V. & Zhitomirsky, I. D. Material science aspects of seignette-magnetism problem. *Ferroelectrics* **73**, 221-248 (1987). <https://doi.org/10.1080/00150198708227919>
  - 4 Vopson, M. M. Fundamentals of multiferroic materials and their possible applications. *Critical Reviews in Solid State and Materials Sciences* **40**, 223-250 (2015).
  - 5 Wang, S. & Wu, N. Operating characteristics of aqueous magnetite electrochemical capacitors. *Journal of applied electrochemistry* **33**, 345-348 (2003).
  - 6 Jawad, A. a. A. *et al.* Functionalize and supercapacitor performance of magnetic oxide nanoparticles. *Inorganic Chemistry Communications* **154**, 110884 (2023). <https://doi.org/10.1016/j.inoche.2023.110884>
  - 7 Liang, W., Yang, W., Sakib, S. & Zhitomirsky, I. Magnetic CuFe<sub>2</sub>O<sub>4</sub> nanoparticles with pseudocapacitive properties for electrical energy storage. *Molecules* **27**, 5313 (2022).
  - 8 Rushmittha, J., Radhika, S. & Padma, C. Investigation on ZrO<sub>2</sub> supported CuFe<sub>2</sub>O<sub>4</sub> based nanocomposite as a potential electrode for supercapacitors and magnetic applications. *Inorganic Chemistry Communications* **152**, 110720 (2023).
  - 9 Geng, L., Yan, F., Dong, C. & An, C. Design and Regulation of Novel MnFe<sub>2</sub>O<sub>4</sub>@C Nanowires as High Performance Electrode for Supercapacitor. *Nanomaterials* **9**, 777 (2019).
  - 10 Gao, X. *et al.* Partial sulfur doping induced lattice expansion of NiFe<sub>2</sub>O<sub>4</sub> with enhanced electrochemical capacity for supercapacitor application. *Electrochimica Acta* **426**, 140739 (2022).
  - 11 Kumar, S. *et al.* Investigations of structural, magnetic, and electrochemical properties of NiFe<sub>2</sub>O<sub>4</sub> nanoparticles as electrode materials for supercapacitor applications. *Materials* **16**, 4328 (2023).
  - 12 Zhang, C. & Zhitomirsky, I. Influence of High Energy Ball Milling and Dispersant on Capacitive Properties of Fe<sub>2</sub>O<sub>3</sub>—Carbon Nanotube Composites. *Journal of Composites Science* **6**, 177 (2022).
  - 13 Mahmood, J. M., Mahmoud, Z. H., Al-Obaidi, N. S. & Rahima, A. M. Gama-Fe<sub>2</sub>O<sub>3</sub> silica-coated 2-(2-benzothiazolyl azo)-4-methoxyaniline for supercapacitive performance. *Journal of Electrochemical Science and Engineering* **13**, 521-536 (2023).
  - 14 Jeevanantham, B. *et al.* Theoretical and Experimental Insights of Magnesium-doped Cobalt Ferrites for Supercapacitor Applications. *Electrochimica Acta* **470**, 143309 (2023).
  - 15 Mayakkannan, M. *et al.* One step microwave combustion synthesized spinel nano NiZnFe<sub>2</sub>O<sub>4</sub> as an electrode material for supercapacitors with superior performance. *Journal of Materials Science: Materials in Electronics* **34**, 1397 (2023).

- 
- 16 Ragsdale, S. R., Lee, J., Gao, X. & White, H. S. Magnetic field effects in electrochemistry. Voltammetric reduction of acetophenone at microdisk electrodes. *The Journal of Physical Chemistry* **100**, 5913-5922 (1996).
- 17 Chowdhury, A. *et al.* Theoretical model for magnetic supercapacitors—From the electrode material to electrolyte ion dependence. *The Journal of Physical Chemistry C* **124**, 26613-26624 (2020).
- 18 Molinari, A., Hahn, H. & Kruk, R. Voltage-Controlled On/Off Switching of Ferromagnetism in Manganite Supercapacitors. *Adv Mater* **30**, 1703908 (2018). <https://doi.org/10.1002/adma.201703908>
- 19 Molinari, A. *et al.* Hybrid supercapacitors for reversible control of magnetism. *Nat Commun* **8**, 15339 (2017). <https://doi.org/10.1038/ncomms15339>
- 20 Bharadwaj, P., Gannavarapu, K. P., Kollipara, V. S. & Dandamudi, R. B. Study of magneto-supercapacitance properties of nickel cobalt ferrite-activated carbon composite. *Journal of Energy Storage* **36**, 102444 (2021).
- 21 Chowdhury, A. *et al.* High performance magnetic pseudocapacitors-Direct correlation between specific capacitance and diffusion coefficients. *Electrochimica Acta* **397**, 139252 (2021).
- 22 Singh, M., Sahoo, A., Yadav, K. & Sharma, Y. Role of magnetism present in the cobaltites (ACo<sub>2</sub>O<sub>4</sub> A= Co, Mn, and Fe) on the charge storage mechanism in aqueous supercapacitor. *Applied Surface Science* **568**, 150966 (2021).
- 23 Ghasemi, A. K., Ghorbani, M., Lashkenari, M. S. & Nasiri, N. Facile synthesise of PANI/GO/CuFe<sub>2</sub>O<sub>4</sub> nanocomposite material with synergistic effect for superb performance supercapacitor. *Electrochimica Acta* **439**, 141685 (2023).
- 24 Lashkenari, M. S., Ghasemi, A. K., Khalid, M. & Shahgaldi, S. Facile synthesis of N-doped graphene oxide decorated with copper ferrite as an electrode material for supercapacitor with enhanced capacitance. *Electrochimica Acta* **465**, 142959 (2023).
- 25 Reghunath, B. S. *et al.* Hierarchical BiFeO<sub>3</sub>/Cr<sub>2</sub>CT<sub>x</sub> MXene composite as a multifunctional catalyst for hydrogen evolution reaction and as an electrode material for energy storage devices. *Electrochimica Acta* **461**, 142685 (2023).
- 26 Isacfranklin, M. *et al.* Perovskite rare earth porous hollow microspheres of SmFeO<sub>3</sub>/MWCNT battery type asymmetric hybrid supercapacitors. *Electrochimica Acta* **461**, 142519 (2023).
- 27 Ahmad, T., Ramanujachary, K. V., Lofland, S. E. & Ganguli, A. K. Reverse micellar synthesis and properties of nanocrystalline GMR materials (LaMnO<sub>3</sub>, La<sub>0.67</sub> Sr<sub>0.33</sub> MnO<sub>3</sub> and La<sub>0.67</sub> Ca<sub>0.33</sub> MnO<sub>3</sub>): Ramifications of size considerations. *Journal of Chemical Sciences* **118**, 513-518 (2006).
- 28 Dörr, K. Ferromagnetic manganites: spin-polarized conduction versus competing interactions. *Journal of Physics D: Applied Physics* **39**, R125 (2006).
- 29 Turkey, A. O., Rashad, M. M., Hassan, A. M., Elnaggar, E. M. & Bechelany, M. Optical, electrical and magnetic properties of lanthanum strontium

- 
- manganite  $\text{La}_{1-x}\text{Sr}_x\text{MnO}_3$  synthesized through the citrate combustion method. *Physical Chemistry Chemical Physics* **19**, 6878-6886 (2017).
- 30 Hizi, W., Rahmouni, H., Gassoumi, M., Khirouni, K. & Dhahri, S. Transport properties of  $\text{La}_{0.9}\text{Sr}_{0.1}\text{MnO}_3$  manganite. *The European Physical Journal Plus* **135**, 1-13 (2020).
- 31 Coey, J., Viret, M., von & Von Molnar, S. Mixed-valence manganites. *Advances in physics* **48**, 167-293 (1999).
- 32 Tokura, Y. & Tomioka, Y. Colossal magnetoresistive manganites. *Journal of magnetism and magnetic materials* **200**, 1-23 (1999).
- 33 Singh, A. N. *et al.* Effect of strontium doping on the electrochemical pseudocapacitance of  $\text{Y}_{1-x}\text{Sr}_x\text{MnO}_{3-\delta}$  perovskites. *Physical Chemistry Chemical Physics* **25**, 326-340 (2023).
- 34 Wei, Z. *et al.* Multifunctionality of lanthanum–strontium manganite nanopowder. *Physical Chemistry Chemical Physics* **22**, 11817-11828 (2020).
- 35 Lv, J. *et al.* Strontium doped lanthanum manganite (LSM) effects on electrochemical performance of LSM/ $\text{MnO}_2$  composites for supercapacitor. *Journal of Materials Science: Materials in Electronics* **28**, 17020-17025 (2017).
- 36 Lang, X., Mo, H., Hu, X. & Tian, H. Supercapacitor performance of perovskite  $\text{La}_{1-x}\text{Sr}_x\text{MnO}_3$ . *Dalton transactions : an international journal of inorganic chemistry* **46**, 13720-13730 (2017).  
<https://doi.org:10.1039/c7dt03134c>
- 37 Ye, X. *et al.* Enhancement in the Electrochemical Performance of Strontium (Sr)-Doped  $\text{LaMnO}_3$  as Supercapacitor Materials. *Coatings (Basel)* **12**, 1739 (2022). <https://doi.org:10.3390/coatings12111739>
- 38 Ma, P. P. *et al.* Effect of A-site substitution by Ca or Sr on the structure and electrochemical performance of  $\text{LaMnO}_3$  perovskite. *Electrochimica acta* **332**, 135489 (2020). <https://doi.org:10.1016/j.electacta.2019.135489>
- 39 Lü, J. *et al.* A preliminary study of the pseudo-capacitance features of strontium doped lanthanum manganite. *RSC advances* **5**, 5858-5862 (2015).  
<https://doi.org:10.1039/C4RA13583K>
- 40 Wang, X. W. *et al.* Structural and electrochemical properties of  $\text{La}_{0.85}\text{Sr}_{0.15}\text{MnO}_3$  powder as an electrode material for supercapacitor. *Journal of alloys and compounds* **675**, 195-200 (2016).  
<https://doi.org:10.1016/j.jallcom.2016.03.048>
- 41 Chen, R., Yu, M., Sahu, R. P., Puri, I. K. & Zhitomirsky, I. The development of pseudocapacitor electrodes and devices with high active mass loading. *Advanced Energy Materials* **10**, 1903848 (2020).
- 42 Shi, K. & Zhitomirsky, I. Asymmetric Supercapacitors Based on Activated-Carbon-Coated Carbon Nanotubes. *ChemElectroChem* **2**, 396-403 (2015).  
<https://doi.org:https://doi.org/10.1002/celec.201402343>
- 43 Tang, D. & Zhitomirsky, I. Pseudocapacitive properties of polypyrrole–ferrimagnetic  $\text{CoFe}_2\text{O}_4$  composites. *Electrochimica Acta* **475**, 143671 (2024).

- 
- 44 Gupta, K., Jana, P., Meikap, A. & Nath, T. Synthesis of La<sub>0.67</sub>Sr<sub>0.33</sub>MnO<sub>3</sub> and polyaniline nanocomposite with its electrical and magneto-transport properties. *Journal of Applied Physics* **107** (2010).
- 45 Ata, M., Liu, Y. & Zhitomirsky, I. A review of new methods of surface chemical modification, dispersion and electrophoretic deposition of metal oxide particles. *Rsc Advances* **4**, 22716-22732 (2014).
- 46 Ulusoy, H. İ. & Şimşek, S. Removal of uranyl ions in aquatic mediums by using a new material: gallocyanine grafted hydrogel. *Journal of hazardous materials* **254**, 397-405 (2013).
- 47 Ata, M. S., Sun, Y., Li, X. & Zhitomirsky, I. Electrophoretic deposition of graphene, carbon nanotubes and composites using aluminum as charging and film forming agent. *Colloids and Surfaces A: Physicochemical and Engineering Aspects* **398**, 9-16 (2012).  
<https://doi.org/https://doi.org/10.1016/j.colsurfa.2012.02.001>
- 48 Su, Y. & Zhitomirsky, I. Electrophoretic deposition of graphene, carbon nanotubes and composite films using methyl violet dye as a dispersing agent. *Colloids and Surfaces A: Physicochemical and Engineering Aspects* **436**, 97-103 (2013).
- 49 Gulley-Stahl, H. *et al.* Surface complexation of catechol to metal oxides: an ATR-FTIR, adsorption, and dissolution study. *Environmental science & technology* **44**, 4116-4121 (2010).
- 50 Nan, H.-s., Hu, X.-y. & Tian, H.-w. Recent advances in perovskite oxides for anion-intercalation supercapacitor: a review. *Materials Science in Semiconductor Processing* **94**, 35-50 (2019).
- 51 Wang, J., Polleux, J., Lim, J. & Dunn, B. Pseudocapacitive contributions to electrochemical energy storage in TiO<sub>2</sub> (anatase) nanoparticles. *The Journal of Physical Chemistry C* **111**, 14925-14931 (2007).
- 52 Chodankar, N. R. *et al.* Potentiodynamic polarization assisted phosphorus-containing amorphous trimetal hydroxide nanofibers for highly efficient hybrid supercapacitors. *Journal of Materials Chemistry A* **8**, 5721-5733 (2020).
- 53 Chodankar, N. R. *et al.* Solution-free self-assembled growth of ordered tricopper phosphide for efficient and stable hybrid supercapacitor. *Energy Storage Materials* **39**, 194-202 (2021).
- 54 Patil, S. J. *et al.* Ultra-stable flexible Zn-ion capacitor with pseudocapacitive 2D layered niobium oxyphosphides. *Energy Storage Materials* **45**, 1040-1051 (2022).
- 55 Okhay, O. & Tkach, A. Graphene/reduced graphene oxide-carbon nanotubes composite electrodes: From capacitive to battery-type behaviour. *Nanomaterials* **11**, 1240 (2021).
- 56 Gogotsi, Y. & Penner, R. M. Vol. 12 2081-2083 (ACS Publications, 2018).

- 
- 57 Reddy, R. N. & Reddy, R. G. Sol-gel MnO<sub>2</sub> as an electrode material for  
electrochemical capacitors. *Journal of Power Sources* **124**, 330-337 (2003).
- 58 Jeong, Y. & Manthiram, A. Nanocrystalline manganese oxides for  
electrochemical capacitors with neutral electrolytes. *Journal of the  
Electrochemical Society* **149**, A1419 (2002).
- 59 Dong, W., Sakamoto, J. S. & Dunn, B. Electrochemical properties of  
vanadium oxide aerogels. *Science and Technology of Advanced Materials* **4**,  
3-11 (2003).
- 60 Rocha, J. E. R. *et al.* Preparation and characterization of binder-free electrodes  
based on PEDOT and perovskites type La(1-x)SrxMnO<sub>3</sub> for use in  
supercapacitors. *Journal of solid state electrochemistry* (2023).  
<https://doi.org:10.1007/s10008-023-05450-9>
- 61 Wang, Y., Liu, Y. & Zhitomirsky, I. Surface modification of MnO<sub>2</sub> and  
carbon nanotubes using organic dyes for nanotechnology of electrochemical  
supercapacitors. *Journal of Materials Chemistry A* **1**, 12519-12526 (2013).
- 62 Boucher, C., Rubel, O. & Zhitomirsky, I. Supercapacitor Performance of  
Magnetite Nanoparticles Enhanced by a Catecholate Dispersant: Experiment  
and Theory. *Molecules* **28**, 1562 (2023).
- 63 Melkiyur, I. *et al.* Unique hierarchical mesoporous SmMnO<sub>3</sub>/MWCNT for  
highly efficient energy storage applications. *Electrochimica Acta* **450**, 142186  
(2023).
- 64 Yang, W., Eraky, H., Zhang, C., Hitchcock, A. P. & Zhitomirsky, I. Scanning  
transmission X-ray microscopy studies of electrochemical activation and  
capacitive behavior of Mn<sub>3</sub>O<sub>4</sub> supercapacitor electrodes. *Journal of  
Materials Chemistry A* **10**, 18267-18277 (2022).
- 65 Yang, W., Eraky, H., Zhang, C., Hitchcock, A. P. & Zhitomirsky, I.  
Electrochemical and scanning transmission X-ray microscopy studies of  
MnO<sub>2</sub> and Mn<sub>3</sub>O<sub>4</sub> for supercapacitor cathodes: Influence of fabrication  
method and electrochemical activation on charge storage. *Chemical  
Engineering Journal*, 149391 (2024).

## 11.8 Supplementary Information

Table 11-S 1 A comparison of the LSM-based cathode materials performances for

supercapacitors.

Materials	RE	Electrolyte	Potential (V)	Current density (A g <sup>-1</sup> )	C <sub>m</sub> (Fg <sup>-1</sup> )	C <sub>s</sub> (F cm <sup>-2</sup> )	Mass loading (mg cm <sup>-2</sup> )	Ref.
La <sub>0.75</sub> Sr <sub>0.25</sub> MnO <sub>3</sub>	Ag/AgCl	1.0 M Na <sub>2</sub> SO <sub>4</sub>	-0.1 ~ 0.9	3	56	0.017	0.3	1
La <sub>0.85</sub> Sr <sub>0.15</sub> MnO <sub>3</sub> NPs	Hg/HgO	3 M KOH	-0.5 ~ 0.5	0.5	185.5	0.18	1	2
LMO@CC-PPy	SCE	6 M KOH	-0.8 ~ 0.4	1	720	0.28	0.4	3
					747	0.37	0.5	
					862	0.51	0.6	
La <sub>0.7</sub> Sr <sub>0.3</sub> MnO <sub>3</sub>	Ag/AgCl	3 M KOH	-0.8 ~ 0.4	1	145	0.29	2	4
La <sub>0.85</sub> Sr <sub>0.15</sub> MnO <sub>3</sub>	Hg/HgO	1M KOH	-0.96 ~ 0.65	0.5	198	0.59	3	5
La <sub>0.85</sub> Sr <sub>0.15</sub> MnO <sub>3</sub>	SCE	1M KOH	-0.8 ~ 0.5	1	102	0.1	1	6
La <sub>0.7</sub> Sr <sub>0.3</sub> MnO <sub>3</sub>					90	0.09		
La <sub>0.5</sub> Sr <sub>0.5</sub> MnO <sub>3</sub>					38	0.038		
La <sub>0.35</sub> Sr <sub>0.65</sub> MnO <sub>3</sub>	SCE	0.5 M Na <sub>2</sub> SO <sub>4</sub>	0 ~ 0.9	3	28.7	1.15	40	this work
La <sub>0.35</sub> Sr <sub>0.65</sub> MnO <sub>3</sub> (HEBM)				3	114.8	4.59		

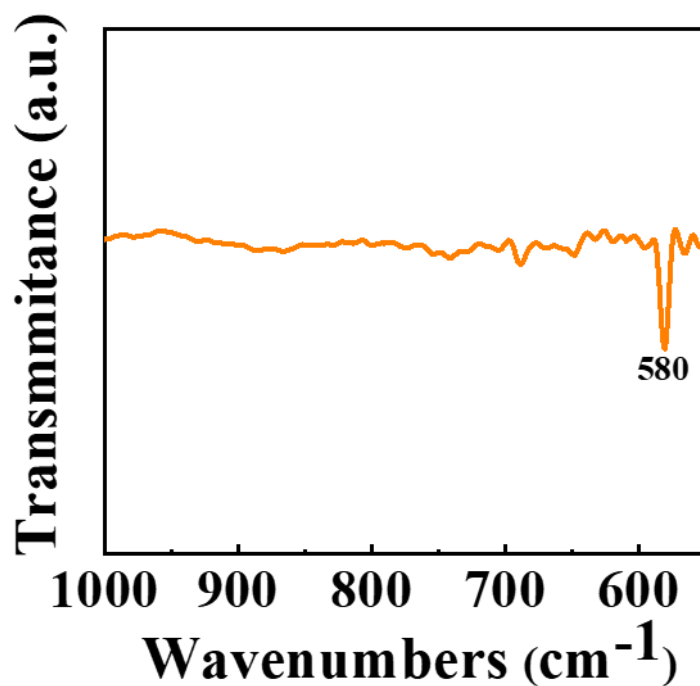


Figure 11-S 1. FTIR spectrum of as-received LSM in the low wavenumber range, which shows absorption peak of LSM related to Mn-O vibrations.

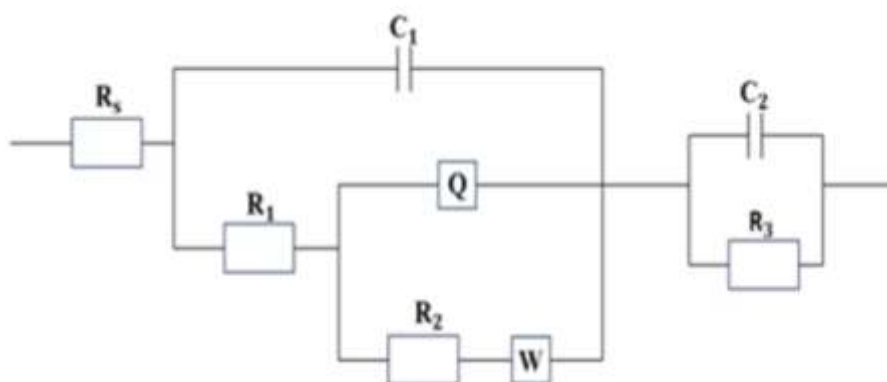


Figure 11-S 2. Equivalent circuit used for the analysis of EIS data using ZSimpWin software. It contains a solution resistance  $R_s$ , a transmission line  $R_1C_1(R_2Q)$  describing a porous electrode, Warburg impedance  $W$ , charge transfer resistance  $R_3$  and double layer capacitance  $C_2$ .

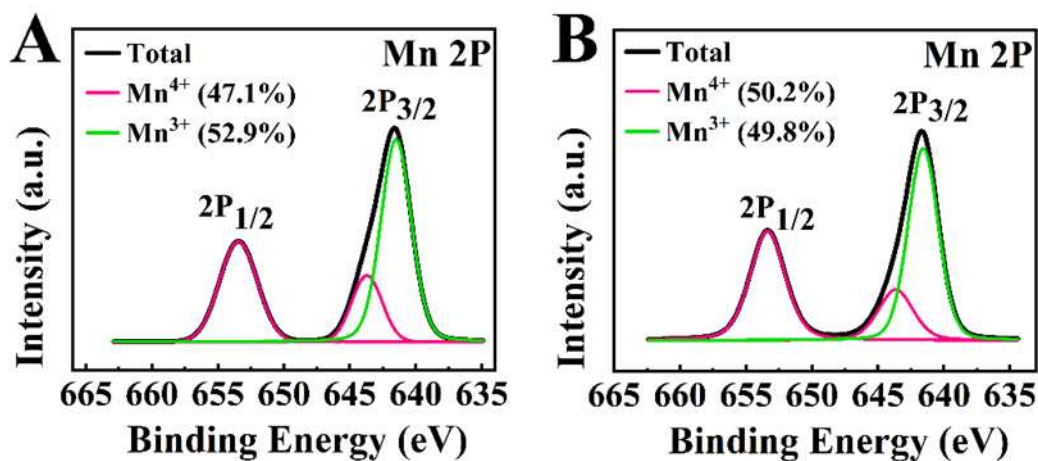


Figure 11-S 3. XPS data for LSM electrodes (A) before and (B) after 2000 CV cycles.

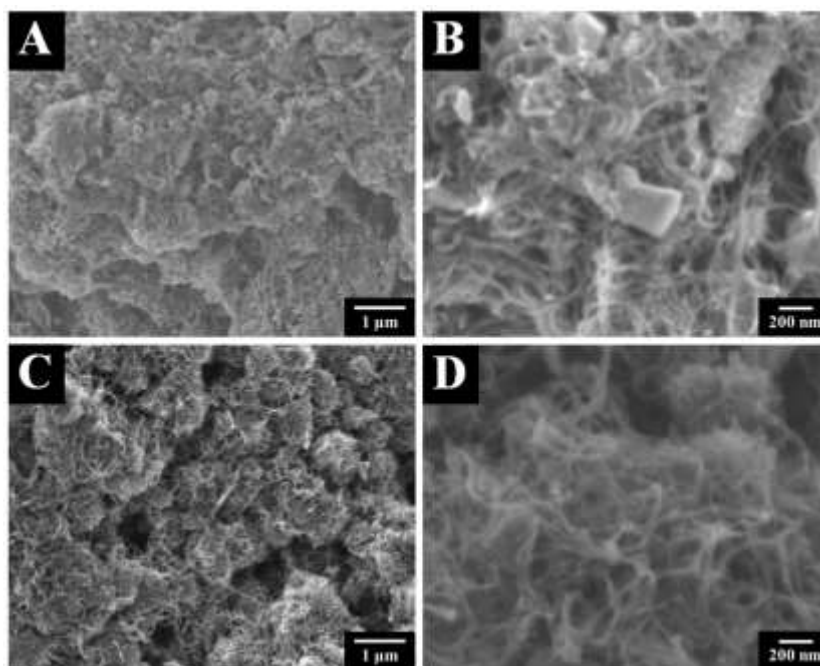


Figure 11-S 4. SEM images at different magnifications of LSM electrodes prepared without HEBM (A, B) and with HEBM (C, D) after 10,000 cycle retention test.

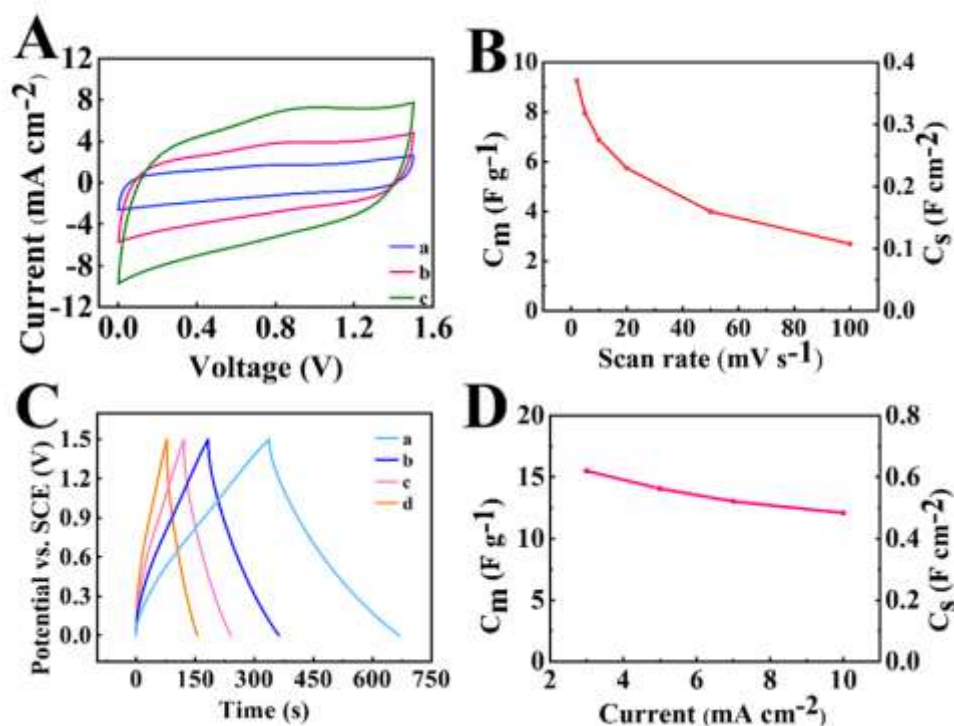


Figure 11-S 5. Testing results for a device, containing LSM cathodes and  $\text{CoFe}_2\text{O}_4$ -polypyrrole (PPy) anodes in  $0.5\text{M Na}_2\text{SO}_4$  electrolyte: (A) CVs at scan rates of (a) 2, (b) 5 and (c)  $10\text{ mV s}^{-1}$ , (B) capacitance calculated from CV data versus scan rate, (C) galvanostatic charge-discharge data at current densities of (a) 3, (b) 5, (c) 7 and (d)  $10\text{ mA cm}^{-2}$ , (D) capacitance calculated from the galvanostatic charge-discharge data versus current density. The gravimetric capacitance was normalized by the total mass of both electrodes ( $80\text{ mg cm}^{-2}$ ).

## SI Reference

- 1 Wu, W. *et al.* Evaluation of Ni80Cr20/(La0.75Sr0.25)0.95 MnO3 dual layer coating on SUS 430 stainless steel used as metallic interconnect for solid oxide fuel cells. *international journal of hydrogen energy* **39**, 996-1004 (2014).
- 2 Ye, X. *et al.* Enhancement in the Electrochemical Performance of Strontium (Sr)-Doped LaMnO3 as Supercapacitor Materials. *Coatings* **12**, 1739 (2022).
- 3 Sun, X. *et al.* Coaxial cable-like dual conductive channel strategy in polypyrrole coated perovskite lanthanum manganite for high-performance

- 
- asymmetric supercapacitors. *Journal of Colloid and Interface Science* **610**, 601-609 (2022).
- 4 Shafi, P. M. *et al.* Sr-and Fe-substituted LaMnO<sub>3</sub> Perovskite: Fundamental insight and possible use in asymmetric hybrid supercapacitor. *Energy Storage Materials* **45**, 119-129 (2022).
- 5 Wang, X. *et al.* Structural and electrochemical properties of La<sub>0.85</sub>Sr<sub>0.15</sub>MnO<sub>3</sub> powder as an electrode material for supercapacitor. *Journal of Alloys and Compounds* **675**, 195-200 (2016).
- 6 Lang, X., Mo, H., Hu, X. & Tian, H. Supercapacitor performance of perovskite La<sub>1-x</sub>Sr<sub>x</sub>MnO<sub>3</sub>. *Dalton transactions* **46**, 13720-13730 (2017).

# **Chapter 12 Ferrimagnetic pseudocapacitive $\text{MnFe}_2\text{O}_4$ electrodes and supercapacitor devices.**

Department of Materials Science and Engineering,

McMaster University, Hamilton, ON L8S 4L7, Canada

\*Corresponding author: [zhitom@mcmaster.ca](mailto:zhitom@mcmaster.ca)

Phone 905-525-9140

Copyright 2024, reproduced with permission from Elsevier.

---

## 12.1 Abstract

This investigation is motivated by the surge of interest in materials, combining high spontaneous magnetization and pseudocapacitance at room temperature.

Ferrimagnetic  $\text{MnFe}_2\text{O}_4$  offers benefits of high magnetization. However, the non-pseudocapacitive behavior, low capacitance and high resistance of  $\text{MnFe}_2\text{O}_4$  are limiting factors for its applications in magnetic pseudocapacitive devices. This investigation demonstrates that nearly ideal pseudocapacitive behavior can be achieved for  $\text{MnFe}_2\text{O}_4$  electrodes in  $\text{Na}_2\text{SO}_4$  electrolyte. High pseudocapacitance is observed in positive and negative potential ranges and two different charging mechanisms are proposed. High capacitance is achieved at a low impedance. The ability to achieve comparable and high areal capacitances in the positive and negative potential ranges facilitates the fabrication of a symmetric pseudocapacitive device, containing ferrimagnetic  $\text{MnFe}_2\text{O}_4$  as cathode and anode material for operation in enlarged voltage window of 1.6V. The symmetric device shows capacitance of 0.92 F  $\text{cm}^{-2}$  at a current density of 3 mA  $\text{cm}^{-2}$ . The individual electrodes and device show good cycling stability. The approach is based on the use of murexide and gallocyanine as redox-active dispersants and charge transfer mediators. The analysis of testing results provides an insight into the influence of chemical structure, charge and redox properties of the dispersants on the capacitive behavior. The ability to fabricate a pseudocapacitive device, containing two ferrimagnetic electrodes is promising for energy storage, water purification and novel applications based on magnetocapacitive

effects.

## 12.2 Introduction

Ceramic spinel materials exhibit valuable properties for many applications in magnetic and biomedical devices, sensors and catalysis<sup>1-4</sup>. The rich materials chemistry of spinel compounds provides a platform for the fabrication of advanced solid solutions with enhanced properties<sup>1,4-6</sup>. Especially interesting are properties of ceramic  $\text{MnFe}_2\text{O}_4$  for catalysis<sup>7</sup>, biomedical<sup>8,9</sup> and energy storage<sup>10-12</sup> applications.  $\text{MnFe}_2\text{O}_4$  is a spinel ferrimagnetic material, which exhibits high magnetization and high Neel temperature<sup>13-16</sup>. The advanced magnetic properties of this material result from high magnetic moments (5  $\mu\text{B}$ ) of  $\text{Mn}^{2+}$  and  $\text{Fe}^{3+}$  ions and their super exchange interactions<sup>13,17</sup>. The magnetization of  $\text{MnFe}_2\text{O}_4$  is influenced by distribution of  $\text{Mn}^{2+}$  and  $\text{Fe}^{3+}$  ions in tetrahedral and octahedral positions in the spinel structure<sup>15,17-19</sup>.  $\text{MnFe}_2\text{O}_4$  has many applications in various magnetic devices<sup>20,21</sup>.

There is currently a surge of interest in ceramic materials, combining advanced magnetic and electric properties<sup>22,23</sup>. Ferrimagnetic  $\text{MnFe}_2\text{O}_4$  has been utilized for the development of multiferroic two-phase composites with different ferroelectric phases, such as  $\text{K}_{0.5}\text{Na}_{0.5}\text{NbO}_3$ <sup>24</sup>,  $\text{BaTiO}_3$ <sup>25</sup>, and  $\text{PbZr}_{0.52}\text{Ti}_{0.48}\text{O}_3$ <sup>26</sup>. The magnetocapacitive effects in the composite materials usually involve mechanical strain generation by piezoelectric effect/magnetostriction in ferroelectric/magnetic phase and mechanical energy transfer to magnetic/electric energy in the magnetic/ferroelectric phase.

---

However, it is challenging to combine ferroelectricity and spontaneous magnetization in a single material at room temperature. Single phase multiferroic compounds rarely occur<sup>27,28</sup>. Single multiferroic compounds combine weak ferroelectricity with weak spontaneous magnetization and exhibit magnetocapacitive effects only at cryogenic temperatures<sup>27,28</sup>.

A relatively recent development is the discovery of electrical charge storage properties of spinel ferrites, which exhibit high magnetization at room temperature. Individual compounds, such as  $\gamma$ -Fe<sub>2</sub>O<sub>3</sub><sup>29</sup>, Fe<sub>3</sub>O<sub>4</sub><sup>30</sup>, NiFe<sub>2</sub>O<sub>4</sub><sup>31</sup>, and CuFe<sub>2</sub>O<sub>4</sub><sup>32</sup> showed nearly ideal pseudocapacitive behavior and exhibited a remarkably high capacitance, which was found to be 10<sup>6</sup>-10<sup>8</sup> times higher than that of ferroelectrics. Such magnetically ordered pseudocapacitor (MOPC) materials showed a remarkable combination of advanced magnetic and pseudocapacitive properties in a single phase at room temperature<sup>33</sup>. Moreover, new magnetocapacitive effects related to coupling of electrical and magnetic properties can be magnetically or electrochemically induced in single-phase MOPC<sup>33</sup>. Magnetocapacitive coupling in MOPC compounds resulted in Curie temperature shift in an electric field, capacitance increase in magnetic field, enhanced capacitance at fast charging rates in magnetic fields, improved cyclic stability, on/off magnetization switching by fast variation of electric potential and giant magnetoelectric coupling coefficient<sup>33</sup>. Electrochemical reactions of MOPC involve transfer of electrons, which have electric charge and magnetic spin moment. On the other hand, the energy of super exchange ordering interactions in spinel ferrimagnetics is

---

influenced by the total magnetic moments of the paramagnetic ions. This provides a basis for magnetocapacitive phenomena. Another mechanism involves magnetohydrodynamic effect, which facilitates electrolyte diffusion<sup>23,33</sup>.

MnFe<sub>2</sub>O<sub>4</sub> is currently under investigation as a promising MOPC material for energy storage<sup>34-37</sup> and capacitive deionization of water<sup>38</sup>. Table S1 (Supplementary Information) presents a summary of literature data on electrochemical testing of MnFe<sub>2</sub>O<sub>4</sub> and composite electrodes prepared by different methods. Electrochemical analysis was performed in different inorganic electrolytes (Table S1), such as Al<sub>2</sub>(SO<sub>4</sub>)<sub>3</sub>, KOH, H<sub>2</sub>SO<sub>4</sub>, and NaCl<sup>34-37</sup>. Various conductive additives (Table S1), such as carbon nanotubes, graphene, carbon, and conductive polymers<sup>34,39,40</sup>, were used to address a problem of low conductivity of MnFe<sub>2</sub>O<sub>4</sub> by fabricating composite electrodes. Previous investigations focused on electrodes with relatively small active mass of 0.2-4.0 mg cm<sup>-2</sup>, which was significantly smaller than that required for practical applications<sup>41</sup>. In many investigations<sup>34,35,39,42,43</sup>, cyclic voltammetry data showed redox peaks, indicating a battery-type behavior. Such peaks are usually not observed for materials with ideal pseudocapacitive response<sup>44-46</sup>. Previous investigations also reported a relatively high impedance of the MnFe<sub>2</sub>O<sub>4</sub> based electrodes<sup>34,35,43,47-49</sup>, which is detrimental for supercapacitor applications. MnFe<sub>2</sub>O<sub>4</sub> and composite electrodes were used for the fabrication of symmetric and asymmetric devices for operation in different electrolytes (Table S2). The capacitance of such devices was reported to be in the range of 0.08-0.44 F cm<sup>-2</sup>. MnFe<sub>2</sub>O<sub>4</sub> is especially promising for the fabrication of symmetric devices

---

containing two MOPC electrodes. However, the relatively low areal capacitance, high impedance and non-pseudocapacitive behavior of  $\text{MnFe}_2\text{O}_4$  are limiting factors for the development of such devices. Significant difficulties result from agglomeration of highly magnetic  $\text{MnFe}_2\text{O}_4$  nanoparticles, which is a bottleneck in the fabrication of nanocomposites.

The goal of this investigation was the fabrication of  $\text{MnFe}_2\text{O}_4$  cathodes and anodes with high active mass loading and symmetric supercapacitor device for operation in a neutral  $\text{Na}_2\text{SO}_4$  electrolyte. The approach was based on the use of anionic and cationic chelating dispersing agents with redox properties for dispersion of  $\text{MnFe}_2\text{O}_4$  nanoparticles and fabrication of  $\text{MnFe}_2\text{O}_4$ -multiwalled carbon nanotube (MWCNT) electrodes. Testing results provided an insight into the influence of the chemical structure, electric charge and redox properties of the dispersing agents on adsorption mechanism, charge transfer and electrode performance. The electrodes with high active mass loading of  $40 \text{ mg cm}^{-2}$  showed pseudocapacitive behavior without redox peaks and low impedance. The capacitances of the individual composite electrodes in positive and negative potential ranges and symmetric MOPC device for operation in a voltage window of 1.6 V were significantly higher, compared to the literature data. The charge storage properties of the electrodes in the negative and positive potential range were discussed. The function of the redox-active dispersants as charge transfer mediators was outlined.

---

## 12.3 Experimental

Murexide (MRX), galloxyanine (GLC),  $\text{MnFe}_2\text{O}_4$  (MFO, nanoparticles, size <100 nm), ethanol,  $\text{Na}_2\text{SO}_4$ , poly(vinyl butyral) binder (PVB, MilliporeSigma, Canada), MWCNT (13 nm diameter, 1–2  $\mu\text{m}$  length, Bayer, Germany) and industrial Ni foam current collectors (95% porosity, 1.6 mm thickness, Vale, Canada) were used.

MFO and MWCNT were co-dispersed in water using murexide and galloxyanine as dispersants. The mass ratio of MFO:MWCNT:dispersants was 8:2:1. The mixtures underwent washing, drying, and re-dispersion in ethanol containing dissolved PVB binder. The obtained slurries were then utilized for electrode fabrication by impregnating current collectors. The PVB binder constituted 3% of the total mass of MFO and MWCNT. The final mass of the impregnated material after drying was  $40 \text{ mg cm}^{-2}$ . The impregnated foams were pressed to 25% of their original thickness. The mass loading of all electrodes was  $40 \text{ mg cm}^{-2}$  and it included the total mass of  $\text{MnFe}_2\text{O}_4$ , MWCNT and PVB binder. The mass loading of  $40 \text{ mg cm}^{-2}$  was used for the calculation of mass specific capacitance.

Microstructure investigations involved the use of scanning electron microscopy (SEM, JEOL, JSM-7000F microscope, Japan). X-ray diffraction (XRD) analysis was conducted on a Bruker D8 diffractometer (Coventry, UK) using  $\text{Cu-K}\alpha$  radiation at a scan rate of 0.01 degrees per second. Magnetic measurements were performed using a Quantum Design SQUID magnetometer.

Electrochemical investigations were performed in aqueous 0.5 M  $\text{Na}_2\text{SO}_4$  electrolyte.

---

Cyclic voltammetry (CV) and electrochemical impedance spectroscopy (EIS) were performed using PARSTAT 2273 potentiostat (AMETEK, USA), while galvanostatic charge-discharge (GCD) experiments were carried out utilizing the BioLogic VMP 300 potentiostat (BioLogic, France). Testing was performed using a 3-electrode electrochemical cell with a working electrode (impregnated Ni foam), counter-electrode (Pt mesh), and a reference electrode (SCE, saturated calomel electrode). The capacitive properties of electrode material were characterized in gravimetric ( $C_m$ ,  $F g^{-1}$ ) and areal ( $C_s$ ,  $F cm^{-2}$ ) capacitance forms. Capacitances  $C_m$  and  $C_s$  were computed based on the data obtained from CV, EIS, and GCD tests, following the methodologies outlined in the previous investigation<sup>50</sup>. The capacitances calculated from the CV and GCD data represented integral capacitances measured in the working potential window of -0.8–0V or 0–0.9 V versus SCE. The complex capacitances extracted from the EIS data represented differential capacitances measured at an open circuit potential at a voltage amplitude of 5 mV. The symmetric device, containing two  $MnFe_2O_4$ -MWCNT electrodes was tested in a voltage window of 1.6 V.

## 12.4 Results and discussion

X-ray diffraction studies and magnetic measurements (Figure 12-1) confirmed that as-received MFO was a spinel-type soft ferrimagnetic material, which exhibited a spontaneous magnetization of about  $30 \text{ emu g}^{-1}$  in agreement with literature data<sup>15</sup>. The

high magnetization of MFO makes this material promising for MOPC applications.

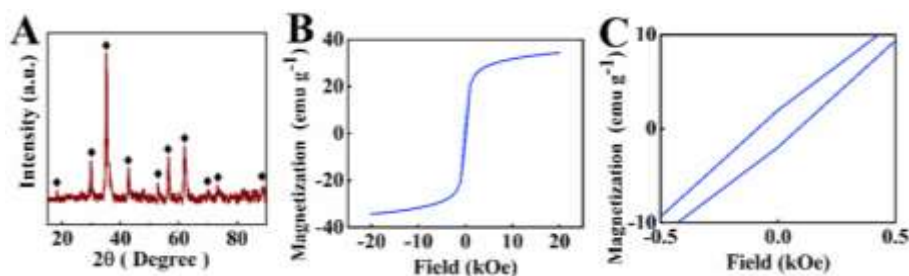


Figure 12- 1 (A)X-ray diffraction pattern (♦- peaks, corresponding to JCPDS 74-2403 file); (B) magnetization (M) versus magnetic field (H), (C) enlarged view of M–H curve at low magnetic field for MFO.

In this investigation, MRX and GLC were used as dispersing agents for the fabrication of MFO based electrodes. Figure 12-2 shows chemical structures of the dispersant molecules. The chemical structure of anionic MRX contains two barbiturate rings. GLC is a polyaromatic cationic molecule. MRX and GLC exhibit chelating properties and form complexes with different metal ions. MRX forms tridentate complexes<sup>51,52</sup>, whereas a catechol-type GLC forms bidentate complexes<sup>53</sup> (Figure 12-2). The interactions of the barbiturate rings of the MRX molecules with carbon rings of MWCNT promoted MRX adsorption on MWCNT. The polyaromatic structure of GLC facilitated adsorption of this molecule on MWCNT by a mechanism, which involves  $\pi$ - $\pi$  interactions. The electric charge of anionic MRX and cationic GLC resulted in electrostatic co-dispersion of MFO and MWCNT. MRX and GLC are redox active molecules<sup>54,55</sup>. MRX showed multiple redox peaks in the positive and negative potential range, whereas the electrochemical redox reactions of GLC were observed in negative potential range<sup>54,55</sup>. It should be noted that due to the high molecular mass of such

molecules and small amounts used, their contribution to the electrode capacitance is negligibly small. However, such molecules can act as charge transfer mediators<sup>55</sup>.

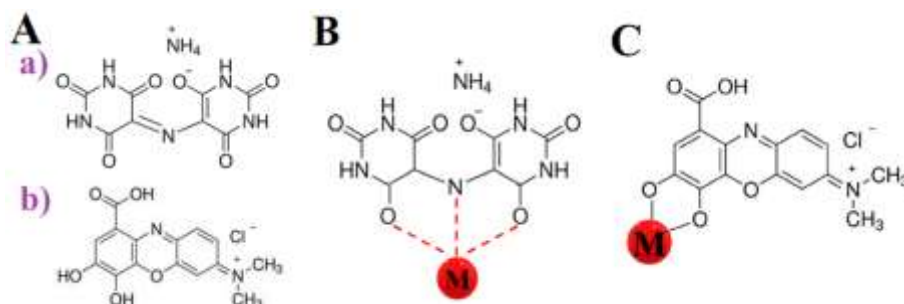


Figure 12- 2 (A) Chemical structures of (a) MRX and (b) GLC, (B) tridentate chelating bonding of MRX and (C) bidentate chelating bonding of GLC to metal ions ( $M=\text{Cu}^{2+}$ ,  $\text{Fe}^{3+}$ ) on the MFO particle surface.

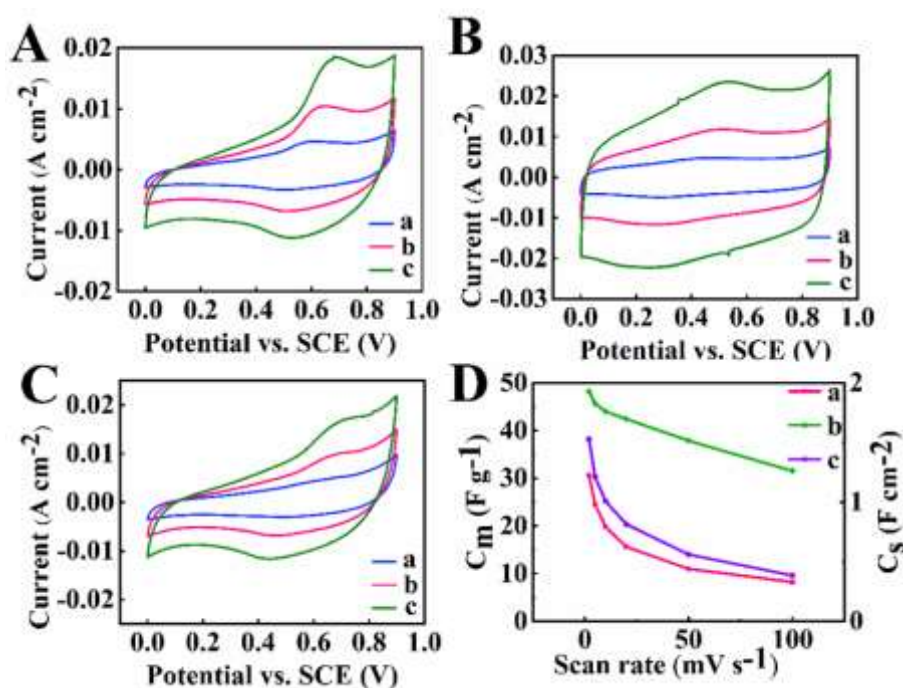


Figure 12- 3 (A-C) CVs at (a) 2, (b) 5 and (c) 10  $\text{mV s}^{-1}$  and (D) capacitances versus scan rate for (A) and (D(a)) MFO, (B) and (D(b)) MFO-MRX, (C) and (D (c)) MFO-GLC.

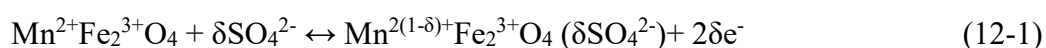
Figure 12-3 shows CV data for MFO electrodes. The MFO electrodes prepared without

additives and tested in in 0.5 M Na<sub>2</sub>SO<sub>4</sub> electrolyte showed redox peaks in the positive potential range. As pointed out above, redox peaks for MFO electrodes were also observed in other electrolytes<sup>34,35,39,42,43</sup>. However, MFO electrodes prepared using MRX (MFO-MRX) showed nearly rectangular CVs with larger area. The MFO electrodes prepared using GLC (MFO-GLC) showed redox peaks in CVs, which deviated significantly from the rectangular shape. The capacitance of MFO-MRX electrodes was significantly higher than capacitances of MFO-GLC and MFO electrodes (Figure 12-3). The capacitance at 2 mV s<sup>-1</sup> of MFO-MRX was found to be 1.93 F cm<sup>-2</sup>, whereas the capacitances of MFO and MFO-GLC were 1.23 and 1.53 F cm<sup>-2</sup>, respectively.

MFO-MRX showed capacitance retention of 65% in the range of 2-100 mV s<sup>-1</sup>, whereas the retention for MFO and MFO-GLC was 27 and 25 %, respectively. Therefore, MFO-MRX showed significant improvement in capacitance at high scan rates (Figure 12-3 D).

GCD studies (Figure 12-4) showed significantly longer charge/discharge times for MFO-MRX, compared to MFO and MFO-GLC at the same current densities. As a result, MFO-MRX exhibited higher capacitance. The capacitances of MO, MFO-GLC and MFO-MRX were found to be 1.76, 1.80 and 2.67 F cm<sup>-2</sup> at 3 mA cm<sup>-2</sup>.

Charging behavior of the electrodes in the positive potential range in the Na<sub>2</sub>SO<sub>4</sub> electrolyte can be attributed to the following redox reaction:



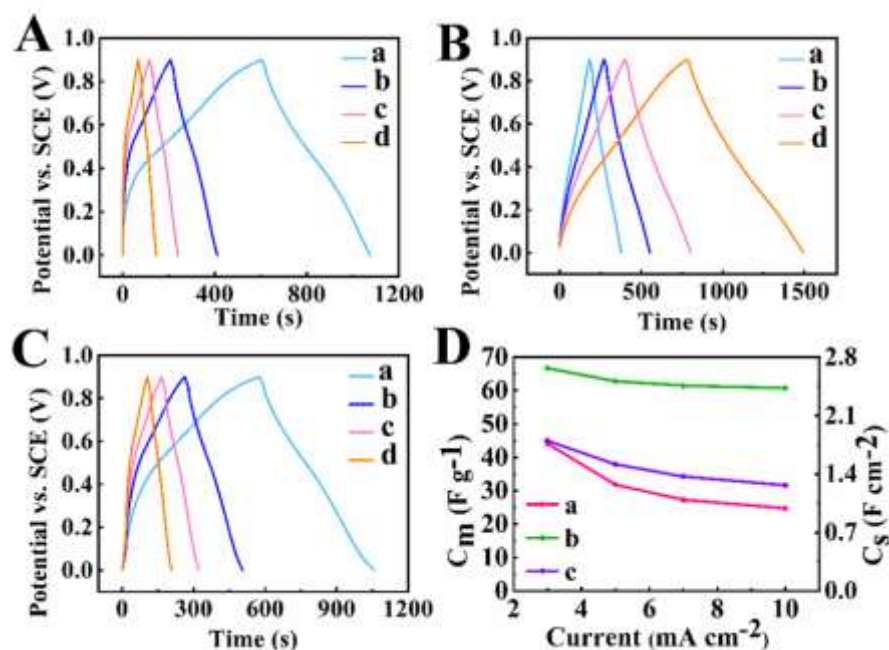


Figure 12- 4 (A-C) GCD data at (a) 3, (b) 5, (c) 7, and (d) 10 mA cm<sup>-2</sup> and (D) capacitance versus current density for (A) and (D(a)) MFO, (B) and (D(b)) MFO-MRX, (C) and (D (c)) MFO-GLC.

Electrochemical testing in the negative potential range (Figure 12-5) did not show redox peaks for MFO and MFO-MRX. However, CVs for MFO-GLC showed redox peaks, which can result from a redox reaction of adsorbed GLC<sup>55</sup> (Figure 12-6). As pointed out above, the direct contribution of GLC to the capacitance was small due to the large molecular mass of GLC and small amount of GLC used. However, GLC can act as a charge transfer mediator<sup>55</sup>.

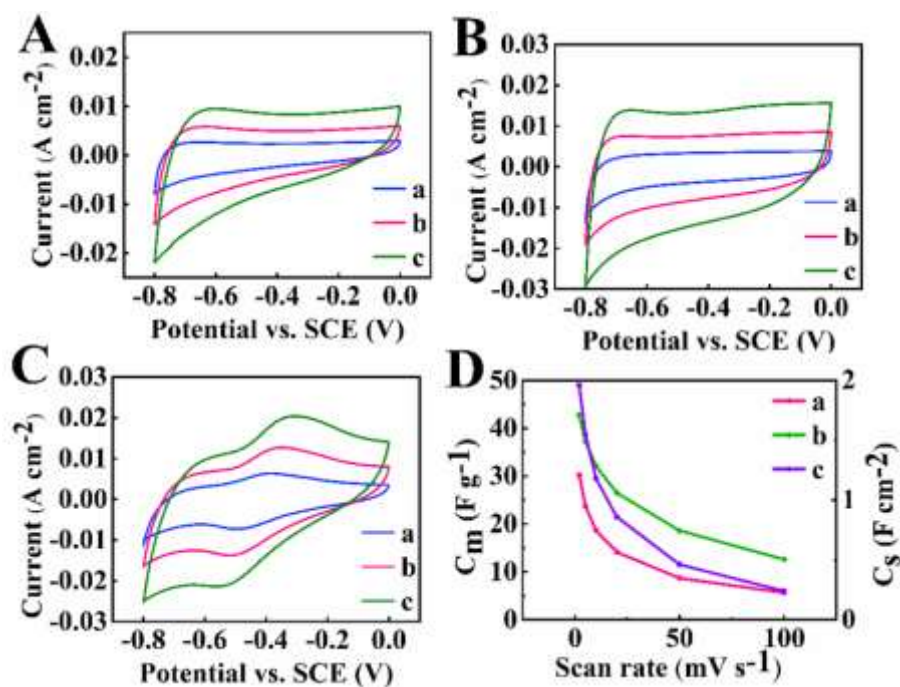


Figure 12- 5 (A-C) CVs at (a) 2, (b) 5 and (c) 10 mV s<sup>-1</sup> and (D) capacitances versus scan rate for (A) and (D(a)) MFO, (B) and (D(b)) MFO-MRX, (C) and (D (c)) MFO-GLC.

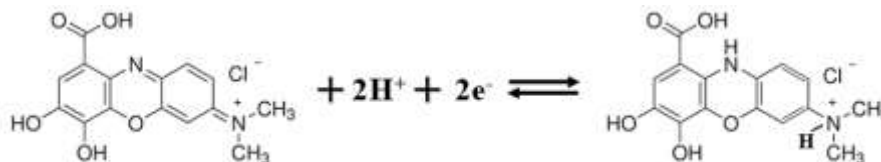


Figure 12- 6 Redox reaction of GLC.

MFO-MRX showed nearly rectangular CV shapes. The capacitances of MFO, MFO-MRX and MFO-GLC were found to be 1.21, 1.71 and 1.96 F cm<sup>-2</sup>, respectively at 2 mV s<sup>-1</sup>. However, MFO-MRX showed better capacitance retention with increasing scan rate. Moreover, MFO-MRX offers advantage of the highest capacitance at scan rates in the range of 10-100 mV s<sup>-1</sup>.

Figure 12-7. Shows GCD testing results at different current densities in the negative potential range.

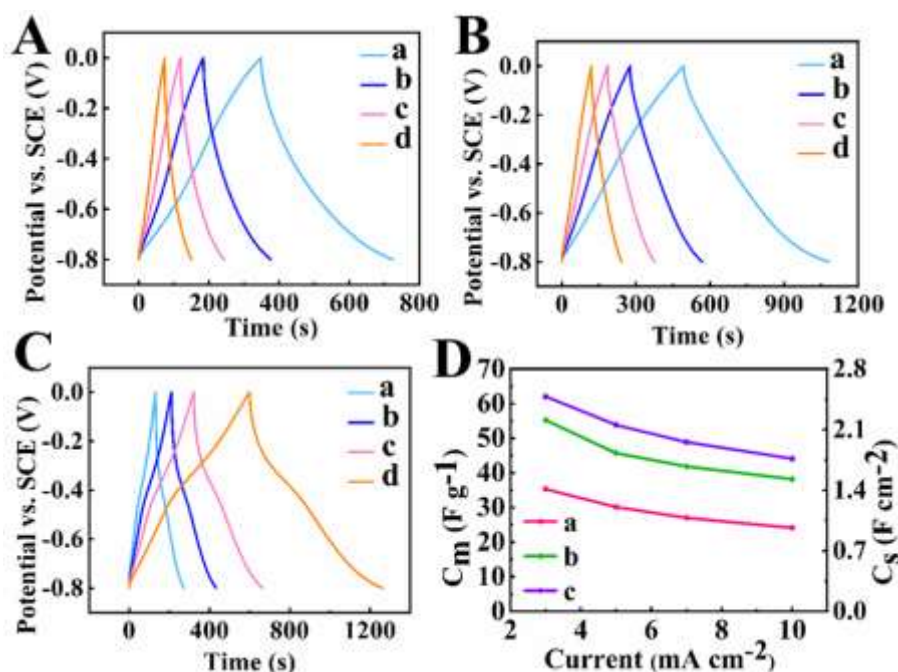


Figure 12- 7(A-C) GCD data at (a) 3, (b) 5, (c) 7, and (d) 10 mA cm<sup>-2</sup> and (D) capacitance versus current density for (A) and (D(a)) MFO, (B) and (D(b)) MFO-MRX, (C) and (D (c)) MFO-GLC.

The MFO-GLC electrodes showed longest charge-discharge times. The capacitances of MFO, MFO-MRX and MFO-GLC electrodes were found to be 1.41, 2.21 and 2.48 F cm<sup>-2</sup>, respectively at 3 mA cm<sup>-2</sup>.

The charge storage mechanism of MFO in the negative potential range can result from the following redox reaction:



EIS studies showed that MFO-MRX exhibited significantly lower real and imaginary components of complex impedance  $Z=Z'-iZ''$ , compared to MFO and MFO-GLC

(Figure 12-8A). The low  $Z'$  is beneficial for supercapacitors, because it indicates low resistance.

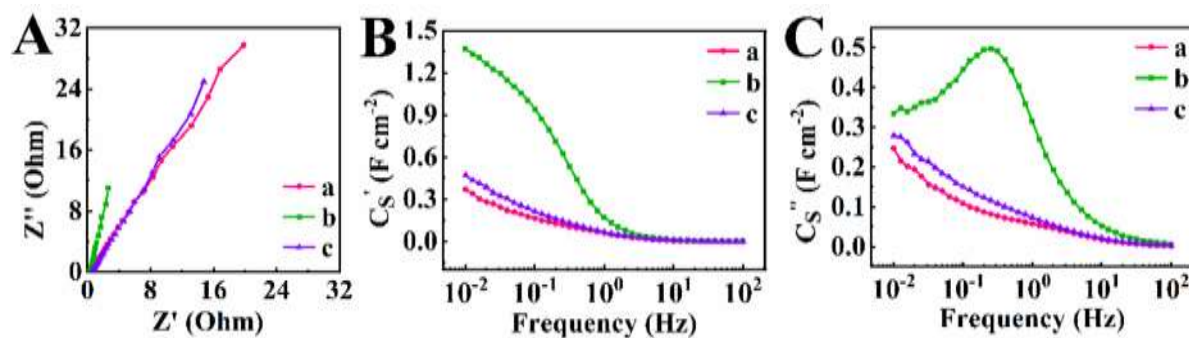


Figure 12- 8 EIS data: (A) Nyquist plot and (B,C) complex capacitance components versus frequency for (a) MFO, (b) MFO-MRX and (c) MFO-GLC.

The resistance of MFO-MRX electrodes was significantly lower than the resistances reported in other investigations<sup>34,35,43,47-49</sup>. The lower  $Z''$  of MFO-MRX, compared to MFO and MFO-GLC (Figure 12-8A) indicated higher capacitance. Indeed MFO-MRX showed significantly higher capacitance in a wide frequency range (Figure 12-8B). The location of the maximum of imaginary component of complex capacitance at a relatively high relaxation frequency of about 0.5 Hz (Figure 12-8C) indicated good performance of MFO-MRX at high charge-discharge rates in agreement with enhanced capacitance retention observed in the CV testing data. The higher slope of the Nyquist plot for MFO-MRX also indicated improved capacitive behavior.

Electrochemical testing results indicated good capacitive behavior of MFO-MRX electrodes in both positive and negative potential ranges in  $Na_2SO_4$  electrolyte. The capacitance of MFO-MRX was higher than literature data for MFO electrodes in other

electrolytes, reported in literature (Table 12-S1). The use of neutral  $\text{Na}_2\text{SO}_4$  electrolyte offers environmental benefits, compared to alkaline or acidic electrolytes. Good pseudocapacitive behavior, high capacitance and low impedance were achieved at high active mass. It is suggested that the use of MRX as a co-dispersant for MFO and MWCNT facilitated their enhanced mixing, which allowed for better utilization of capacitive properties of MFO-MRX and low resistance. Figure 12-9 shows SEM image of MFO-MRX electrode. The SEM image indicates good mixing of MFO and MWCNT and low agglomeration.

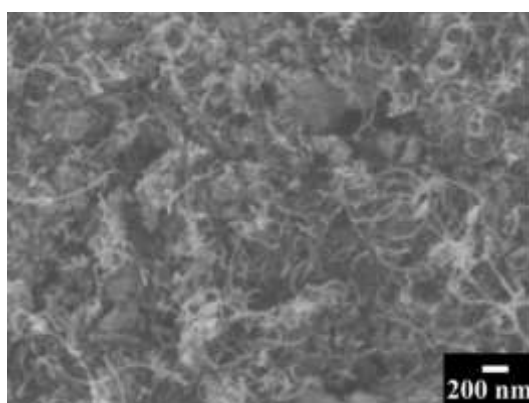


Figure 12- 9 SEM image of MFO-MRX electrode.

Good capacitive behavior and low resistance of the MFO-MRX electrode can also result from redox-active properties of MRX, which acted as a charge transfer mediator. It is in this regard that CV data for MRX showed redox reactions in positive and negative potential ranges<sup>54</sup>. MFO-MRX electrodes also showed good cyclic stability in the negative and positive potential ranges (Figure 12-10). In both potential windows the capacitance showed slight increase during the first 100 cycles. This minor enhancement in capacitance during cycling can be attributed to microstructural changes

in the electrode material or improved wetting of the electrodes by the electrolyte<sup>44,56</sup>.

After 5000 cycles the electrodes showed capacitance retention of 112.9 and 103.5% in the positive and negative potential ranges, respectively (Figure 12-10).

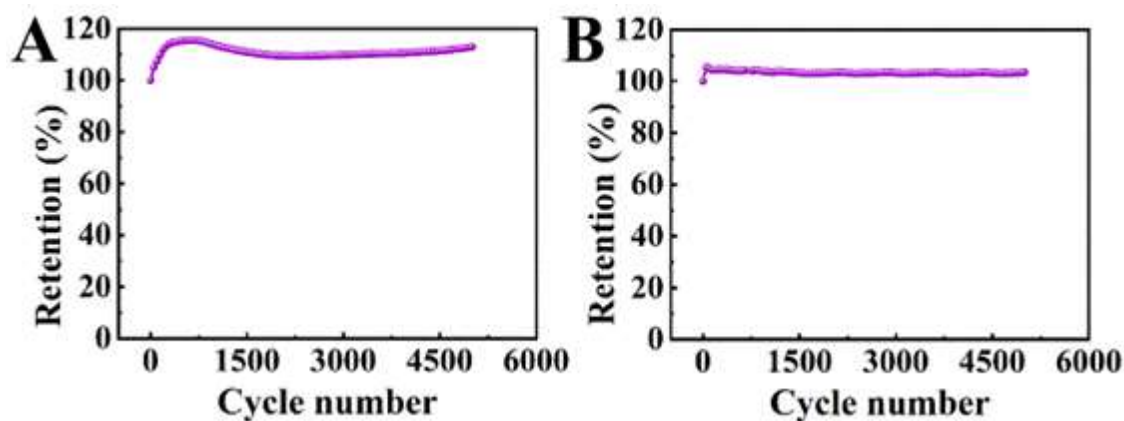


Figure 12- 10 Capacitance versus cycle number for MFO-MRX electrode in (A) positive (0 – +0.9 V) and (B) negative (-0.8 – 0 V) potential ranges at 50 mV s<sup>-1</sup>.

The MFO-MRX electrodes demonstrated promising capacitive behavior within the potential windows of 0 to +0.9V and -0.8 to 0V, suggesting their potential for use as both cathodes and anodes in symmetric supercapacitors. It is known that  $C_m$  of electrodes decreases drastically with increasing active mass<sup>50</sup> due to limited electrolyte access to the bulk of the active material and increased resistance. It is challenging to achieve high  $C_m$  for electrodes with high active mass. However, the high active mass of the electrodes is important for the increasing ratio of active material mass to the mass of a current collector and electrolyte. In this investigation, enhanced  $C_m$  was achieved using advanced dispersants, which also acted as charge transfer mediators. The rectangular-shaped CV profiles of each electrode are crucial for achieving a rectangular

---

CV profile in a symmetric device operating at voltages of 0-1.6 V. Consequently, MFO-MRX electrodes have been chosen for constructing symmetric supercapacitors. Figure 12-11A illustrates the CV profiles at various scan rates within a 0–1.6 V voltage range. The capacitance at  $2 \text{ mV s}^{-1}$ , calculated from CV data, was  $0.89 \text{ F cm}^{-2}$  and it decreased with increasing scan rate (Figure 12-11B). The total resistance of the device included the contributions from both electrodes and the electrolyte within the membrane pores (Figure 12-11C).

Figures 12-11D, E show the frequency dependencies of the real  $C_s'$  and imaginary  $C_s''$  components of AC capacitance, derived from impedance data. The capacitance decreased with frequency increase. The analysis of cycling behavior showed slight increase in capacitance during the first 50 cycles, reaching 104%, before decreasing slightly and stabilizing at approximately 101% (Figure 12-11F). Figure 12-11G presents the GCD profiles for the symmetric device at various current densities, with nearly symmetrical triangular shapes indicating robust capacitive behavior. When the current was increased from 3 to  $10 \text{ mA cm}^{-2}$ , the  $C_s$ , calculated from GCD profiles, declined from  $0.92$  to  $0.71 \text{ F cm}^{-2}$ , as shown in Figure 12-11H. This trend is consistent with the results obtained from CV curves. The capacitance of the symmetric device was found to be significantly higher than the capacitances reported in the literature (Table 12-S2). The ability to fabricate a pseudocapacitive device, containing two ferrimagnetic electrodes is promising for magnetic field enhanced energy storage and capacitive water deionization devices, as well as novel applications based on magnetocapacitive effects.

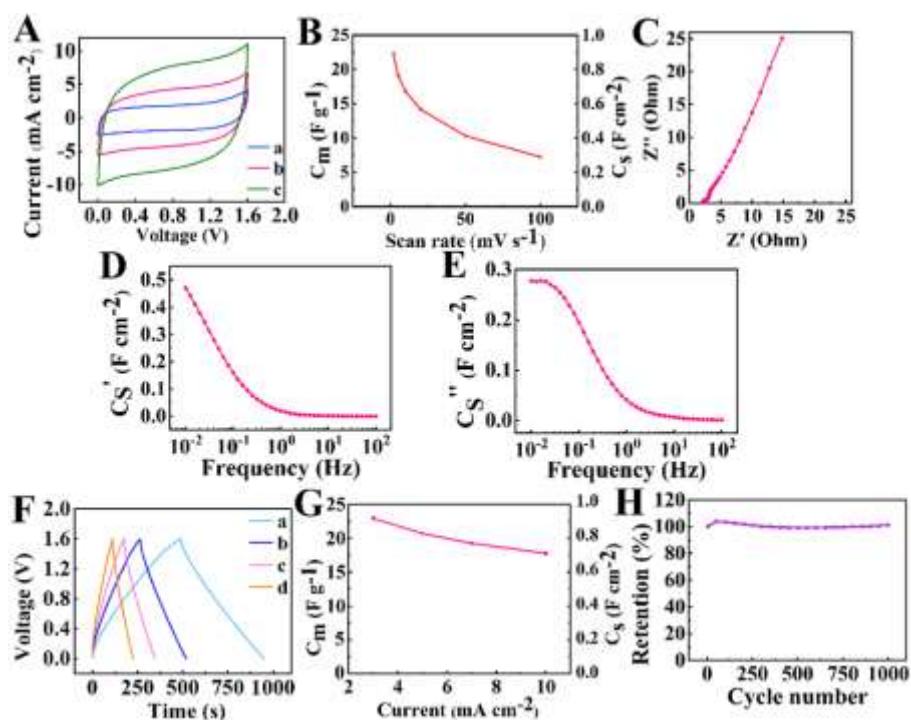


Figure 12- 11 (A) CVs at (a) 2, (b) 5 and (c) 10  $\text{mV s}^{-1}$ , (B) capacitances versus scan rate, (C) Nyquist plot, (D,E) frequency dependences of components of complex capacitance (D)  $C_s'$  and (E)  $C_s''$ , (F) GCD curves at (a) 10, (b) 7, (c) 5, and (d) 3  $\text{mA cm}^{-2}$ , (G) capacitances versus current density, (H) capacitance retention for symmetric MFO-MRX device.

## 12.5 Conclusions

Pseudocapacitive behavior of MFO based electrodes was achieved in negative and positive potential ranges and related charging mechanisms were proposed. Nearly ideal pseudocapacitive response was achieved at high active mass loading and low electrode resistance using MRX as a redox-active dispersant. MRX and GLC acted as dispersants and charge transfer mediators. MFO-MRX showed improved performance, compared to the MFO and MFO-GLC. The capacitance of MFO-MRX in the positive and negative potential ranges was significantly higher, compared to the literature data. The

---

ability to achieve comparable areal capacitances of MFO-MRX in the positive and negative potential ranges facilitated the fabrication of a symmetric device, which showed a capacitance of  $0.92 \text{ F cm}^{-2}$  at  $3 \text{ mA cm}^{-2}$ . The device showed higher capacitance, compared to literature data, and offers benefits of large voltage window of  $1.6 \text{ V}$  and more environmentally friendly neutral electrolyte. The individual electrodes and devices showed good cyclic stability. The ability to fabricate a pseudocapacitive device, containing two ferrimagnetic electrodes is promising for magnetic field enhanced energy storage and capacitive water deionization devices as well as novel applications based on magnetocapacitive effects.

---

## 12.6 Acknowledgments

Research supported by the Natural Sciences and Engineering Research Council of Canada, grant RGPIN-2018-04014 and CRC program. Electron microscopy studies were performed at the Canadian Centre for Electron Microscopy. Wenjuan Yang received support from the China Scholarship Council.

## 12.7 References

- 1 Akhlaghi, N. & Najafpour-Darzi, G. Manganese ferrite (MnFe<sub>2</sub>O<sub>4</sub>) Nanoparticles: From synthesis to application-A review. *Journal of Industrial and Engineering Chemistry* **103**, 292-304 (2021).
- 2 Arteaga-Cardona, F. *et al.* Tuning magnetic and structural properties of MnFe<sub>2</sub>O<sub>4</sub> nanostructures by systematic introduction of transition metal ions M<sub>2</sub><sup>+</sup> (M= Zn, Fe, Ni, Co). *Journal of Magnetism and Magnetic Materials* **490**, 165496 (2019).
- 3 Aslibeiki, B., Kameli, P. & Ehsani, M. MnFe<sub>2</sub>O<sub>4</sub> bulk, nanoparticles and film: A comparative study of structural and magnetic properties. *Ceramics International* **42**, 12789-12795 (2016).
- 4 Raland, R., Saikia, D., Borgohain, C. & Borah, J. Heating efficiency and correlation between the structural and magnetic properties of oleic acid coated MnFe<sub>2</sub>O<sub>4</sub> nanoparticles for magnetic hyperthermia application. *Journal of Physics D: Applied Physics* **50**, 325004 (2017).
- 5 Sharma, H. R. *et al.* Structural, electrical, and magnetic studies of Cu<sup>2+</sup> substituted MnFe<sub>2</sub>O<sub>4</sub> nanoferrites synthesized via solution combustion technique. *Journal of Materials Science: Materials in Electronics* **33**, 7528-7542 (2022).
- 6 Akhtar, M. & Younas, M. Structural and transport properties of nanocrystalline MnFe<sub>2</sub>O<sub>4</sub> synthesized by co-precipitation method. *Solid State Sciences* **14**, 1536-1542 (2012).
- 7 Salih, S. J. & Mahmood, W. M. Review on magnetic spinel ferrite (MFe<sub>2</sub>O<sub>4</sub>) nanoparticles: From synthesis to application. *Heliyon* (2023).
- 8 Thakur, K., Kumar, S., Kumar, S. & Thakur, N. Investigation of structural, dielectric, and magnetoelectric properties of K<sub>0.5</sub>Na<sub>0.5</sub>NbO<sub>3</sub>-MnFe<sub>2</sub>O<sub>4</sub> lead free composite system. *Journal of Alloys and Compounds* **857**, 158251 (2021).
- 9 Khan, M. A. *et al.* Optimization of magnetoelectric coupling in BiFeO<sub>3</sub>-

- 
- BaTiO<sub>3</sub>-MnFe<sub>2</sub>O<sub>4</sub> tri-phase composites for ultra-sensitive devices. *Journal of Alloys and Compounds* **947**, 169571 (2023).
- 10 Zhong, S. *et al.* Enhanced magneto-electric coupling properties of MnFe<sub>2</sub>O<sub>4</sub>-PbZr<sub>0.52</sub>Ti<sub>0.48</sub>O<sub>3</sub> multiferroic liquids tuning by volume fraction. *Journal of Materials Science: Materials in Electronics* **34**, 1733 (2023).
- 11 Venevtsev, Y. N., Gagulin, V. V. & Zhitomirsky, I. D. Material science aspects of seignette-magnetism problem. *Ferroelectrics* **73**, 221-248 (1987). <https://doi.org:10.1080/00150198708227919>
- 12 Schmid, H. Multi-ferroic magnetoelectrics. *Ferroelectrics* **162**, 317-338 (1994). <https://doi.org:10.1080/00150199408245120>
- 13 Zhang, C. & Zhitomirsky, I. Influence of High Energy Ball Milling and Dispersant on Capacitive Properties of Fe<sub>2</sub>O<sub>3</sub>-Carbon Nanotube Composites. *Journal of Composites Science* **6**, 177 (2022).
- 14 Wang, S. & Wu, N. Operating characteristics of aqueous magnetite electrochemical capacitors. *Journal of applied electrochemistry* **33**, 345-348 (2003).
- 15 Gao, X. *et al.* Partial sulfur doping induced lattice expansion of NiFe<sub>2</sub>O<sub>4</sub> with enhanced electrochemical capacity for supercapacitor application. *Electrochimica Acta* **426**, 140739 (2022).
- 16 Liang, W., Yang, W., Sakib, S. & Zhitomirsky, I. Magnetic CuFe<sub>2</sub>O<sub>4</sub> nanoparticles with pseudocapacitive properties for electrical energy storage. *Molecules* **27**, 5313 (2022).
- 17 Sikkema, R. & Zhitomirsky, I. Magnetic supercapacitors: Charge storage mechanisms, magnetocapacitance, and magnetoelectric phenomena. *Applied Physics Reviews* **10** (2023).
- 18 Zolfaghari, Y., Ghorbani, M. & Lashkenari, M. S. Electrochemical study on zeolitic imidazolate framework-67 modified MnFe<sub>2</sub>O<sub>4</sub>/CNT nanocomposite for supercapacitor electrode. *Electrochimica Acta* **380**, 138234 (2021).
- 19 Gupta, M., Tyagi, S. & Kumari, N. Electrochemical evaluation of highly stable Mn ferrite/PEDOT/rGO ternary nanocomposite for supercapacitor electrodes. *Journal of Materials Science: Materials in Electronics* **33**, 7838-7852 (2022).
- 20 Wang, H., Sun, Y., Li, Z., Li, H. & Guo, P. Electrocapacitive behavior of colloidal nanocrystal assemblies of manganese ferrite in multivalent ion electrolytes. *Colloids and Surfaces A: Physicochemical and Engineering Aspects* **572**, 326-332 (2019).
- 21 Sankar, K. V. & Selvan, R. K. The preparation of MnFe<sub>2</sub>O<sub>4</sub> decorated flexible graphene wrapped with PANI and its electrochemical performances for hybrid supercapacitors. *Rsc Advances* **4**, 17555-17566 (2014).
- 22 Su, L. *et al.* Sprinkling MnFe<sub>2</sub>O<sub>4</sub> quantum dots on nitrogen-doped graphene sheets: the formation mechanism and application for high-performance supercapacitor electrodes. *Journal of Materials Chemistry A* **6**, 9997-10007 (2018).
- 23 Geng, L., Yan, F., Dong, C. & An, C. Design and Regulation of Novel

- 
- MnFe<sub>2</sub>O<sub>4</sub>@C Nanowires as High Performance Electrode for Supercapacitor. *Nanomaterials* **9**, 777 (2019).
- 24 Gogotsi, Y. & Simon, P. True Performance Metrics in Electrochemical Energy Storage. *Science* **334**, 917-918 (2011).  
<https://doi.org/doi:10.1126/science.1213003>
- 25 Abdullah, M. *et al.* Partial sulfur doping induced variation in morphology of MnFe<sub>2</sub>O<sub>4</sub> with enhanced electrochemical performance for energy storage devices. *Korean Journal of Chemical Engineering*, 1-11 (2023).
- 26 Makkar, P. & Ghosh, N. N. Facile synthesis of MnFe<sub>2</sub>O<sub>4</sub> hollow sphere-reduced graphene oxide nanocomposites as electrode materials for all-solid-state flexible high-performance asymmetric supercapacitors. *ACS Applied Energy Materials* **3**, 2653-2664 (2020).
- 27 Liang, W. & Zhitomirsky, I. MXene-carbon nanotube composite electrodes for high active mass asymmetric supercapacitors. *Journal of Materials Chemistry A* **9**, 10335-10344 (2021). <https://doi.org:10.1039/D0TA12485K>
- 28 Cheong, M. & Zhitomirsky, I. Electrophoretic deposition of manganese oxide films. *Surface engineering* **25**, 346-352 (2009).
- 29 Shi, K. & Zhitomirsky, I. Asymmetric Supercapacitors Based on Activated-Carbon-Coated Carbon Nanotubes. *ChemElectroChem* **2**, 396-403 (2015).  
<https://doi.org:https://doi.org/10.1002/celec.201402343>
- 30 Cai, W., Lai, T., Dai, W. & Ye, J. A facile approach to fabricate flexible all-solid-state supercapacitors based on MnFe<sub>2</sub>O<sub>4</sub>/graphene hybrids. *Journal of Power Sources* **255**, 170-178 (2014).
- 31 Ghadimi, L. S., Arsalani, N., Tabrizi, A. G., Mohammadi, A. & Ahadzadeh, I. Novel nanocomposite of MnFe<sub>2</sub>O<sub>4</sub> and nitrogen-doped carbon from polyaniline carbonization as electrode material for symmetric ultra-stable supercapacitor. *Electrochimica Acta* **282**, 116-127 (2018).
- 32 Vignesh, V., Subramani, K., Sathish, M. & Navamathavan, R. Electrochemical investigation of manganese ferrites prepared via a facile synthesis route for supercapacitor applications. *Colloids and Surfaces A: Physicochemical and Engineering Aspects* **538**, 668-677 (2018).
- 33 Chen, R., Yu, M., Sahu, R. P., Puri, I. K. & Zhitomirsky, I. The development of pseudocapacitor electrodes and devices with high active mass loading. *Advanced Energy Materials* **10**, 1903848 (2020).
- 34 Martin, R. L., White, A. H. & Willis, A. C. Structural studies in metal-purpurate complexes. Part 1. Crystal structures of potassium purpurate trihydrate and ammonium purpurate monohydrate (murexide). *Journal of the Chemical Society, Dalton Transactions*, 1336-1342 (1977).
- 35 Masoud, M., Kassem, T., Shaker, M. A. & Ali, A. Studies on transition metal murexide complexes. *Journal of thermal analysis and calorimetry* **84**, 549-555 (2006).
- 36 Ata, M., Liu, Y. & Zhitomirsky, I. A review of new methods of surface chemical modification, dispersion and electrophoretic deposition of metal

- oxide particles. *Rsc Advances* **4**, 22716-22732 (2014).
- 37 Mohran, H. S. An electrochemical investigation of the redox properties of murexide in aqueous and non-aqueous media. *American Journal of Applied Sciences* **6**, 964 (2009).
- 38 Seung-Hoon, S. & Young-Je, Y. Characteristics of mediated enzymatic nitrate reduction by gallocyanine-bound nanoporous electrode. *Journal of microbiology and biotechnology* **16**, 505-510 (2006).
- 39 Li, X., Zhu, J., Liang, W. & Zhitomirsky, I. MXene (Ti<sub>3</sub>C<sub>2</sub>T<sub>x</sub>) anodes for asymmetric supercapacitors with high active mass loading. *Materials Chemistry and Physics* **268**, 124748 (2021).

## 12.8 Supplementary Information

Table 12-S 1 Capacitive properties of MnFe<sub>2</sub>O<sub>4</sub> and composite electrodes

Materials	Potential Range (V)	RE	Electrolyte	Mass loading (mg cm <sup>-2</sup> )	C <sub>g</sub> (F g <sup>-1</sup> )	C <sub>s</sub> (F cm <sup>-2</sup> )	Current density (A g <sup>-1</sup> )	Ref.
MnFe <sub>2</sub> O <sub>4</sub> QDs /NG	-1 to 0	SCE	2 M KOH	1	517	0.52	1	<sup>1</sup>
3DSC-MFQDs	-1.5 to 0.5	Ag/AgCl	EMIMBF <sub>4</sub> IL	1.2	188.3	0.23	1	<sup>2</sup>
MnFe <sub>2</sub> O <sub>4</sub> /CNT/ZIF	-0.55 to 0.3	Ag/AgCl	6 M KOH	0.5	389	0.2	1	<sup>3</sup>
MnFe <sub>2</sub> O <sub>4</sub> nanosphere	-0.55 to 0.45	SCE	3.5 M KOH	1	173.3	0.17	1	<sup>4</sup>
MnFe <sub>2</sub> O <sub>4</sub>	-0.45 to 0.3	Ag/AgCl	1 M NaCl	1	45	0.05	7	<sup>5</sup>
MnFe <sub>2</sub> O <sub>4</sub> NPs	-0.2 to 0.6	Ag/AgCl	1 M H <sub>2</sub> SO <sub>4</sub>	1	53.8	0.05	3	<sup>6</sup>
MnFe <sub>2</sub> O <sub>4</sub> /PEDOT					76.6	0.08		

MnFe <sub>2</sub> O <sub>4</sub> /PANI	-0.2 to 1	SCE	1 M H <sub>2</sub> SO <sub>4</sub>	0.5	387	0.19	1	7
MnFe <sub>2</sub> O <sub>4</sub> /CPANI					329	0.16	0.5	
MnFe <sub>2</sub> O <sub>4</sub>	-0.1 to 0.8	Ag/ AgCl	1 M KOH	2.5	784	1.96	3	8
MnFe <sub>2</sub> O <sub>4</sub> /rGO	0 to 0.8	Ag/ AgCl	1 M H <sub>2</sub> SO <sub>4</sub>	0.2	300	0.06	0.3	9
MnFe <sub>2</sub> O <sub>4</sub> @C	0 to 1	SCE	2 M KOH	1.5	824	1.24	0.1	10
MnFe <sub>2</sub> O <sub>4</sub>	0 to 0.45	Ag/ AgCl	2 M KOH	4	282.4	1.13	1	11
MnFe <sub>2</sub> O <sub>4</sub>	0 to 0.55	Hg/ HgO	3 M KOH	2	178	0.36	8	12
80 MnFe <sub>2</sub> O <sub>4</sub>			3 M KOH + 0.1 M		592	1.2	1	
-20rGO			K <sub>4</sub> [Fe(CN) <sub>6</sub> ]		768	1.53	0.1	
MnFe <sub>2</sub> O <sub>4</sub>	0 to 0.9	SCE	Al <sub>2</sub> (SO <sub>4</sub> ) <sub>3</sub>	3.5	43.2	0.15	0.1	13
MnFe <sub>2</sub> O <sub>4</sub> (murexide)	-0.8 to 0	SCE	0.5 M Na <sub>2</sub> SO <sub>4</sub>	40	55.2	2.21	3	this wok
MnFe <sub>2</sub> O <sub>4</sub> (galloxyanine)					62	2.48		
MnFe <sub>2</sub> O <sub>4</sub> (murexide)	0 to 0.9				66.7	2.67		
MnFe <sub>2</sub> O <sub>4</sub> (galloxyanine)					45	1.80		

Table 12-S 2 A comparison of the recent  $\text{MnFe}_2\text{O}_4$ -based supercapacitor devices capacitance.

Cathode Materials	Anode Materials	Voltage (V)	Electrolyte	Mass loading ( $\text{mg cm}^{-2}$ )	$C_m$ ( $\text{F g}^{-1}$ )	$C_s$ ( $\text{F cm}^{-2}$ )	current density ( $\text{A g}^{-1}$ )	Ref.
$\text{MnFe}_2\text{O}_4$	$\text{MnFe}_2\text{O}_4$	0-1	2 M KOH	5	55.8	0.28	0.01	14
					88.4	0.44		
					20.2	0.1		
$\text{MnO}_2/\text{CNT}$	$\text{MnFe}_2\text{O}_4/\text{graphene}$	0-1.8	1 M $\text{Na}_2\text{SO}_4$	3.5	60	0.21	10	15
$80\text{MnFe}_2\text{O}_4 - 20\text{rGO}$	rGO	0-1.5	3 M KOH + 0.1 M $\text{K}_4[\text{Fe}(\text{CN})_6]$	2	90	0.18	1	12
AC	MGP	0-1.6	1 M NaCl	1.6	51.87	0.08	7	5
$\text{MnFe}_2\text{O}_4$	$\text{MnFe}_2\text{O}_4$	0-1.2	3.5 M KOH	1	97	0.1	2	4
$\text{MnFe}_2\text{O}_4$ QDs@C-NG	$\text{MnFe}_2\text{O}_4$ QDs@C-NG	0-1.5	2 M KOH	1	110	0.11	1	1
$\text{MnFe}_2\text{O}_4$	$\text{MnFe}_2\text{O}_4$	0-1.6	0.5 M $\text{Na}_2\text{SO}_4$	40	22.94	0.92	3	this work
					22.23	0.89		

PANI = polyaniline

CPANI = carbon material decorated with polyaniline

rGO = reduced graphene oxide

ZIF = Zeolite imidazole frameworks

3DSC-MFQDs = 3D space-confined  $\text{MnFe}_2\text{O}_4$  electrode

rGO = reduced graphene oxide

QDs = quantum dots

NG = nitrogen-doped graphene

$\text{MnFe}_2\text{O}_4$  QDs@C-NG =  $\text{MnFe}_2\text{O}_4$  quantum dots attached on NG are coated with a

---

thin carbon layer

PEDOT = poly (3, 4-ethylenedioxythiophene)

MG = MnFe<sub>2</sub>O<sub>4</sub> nanocube decorated flexible graphene composite

MGP = MG wrapped polyaniline

## SI References

- 1 Su, L. *et al.* Sprinkling MnFe<sub>2</sub>O<sub>4</sub> quantum dots on nitrogen-doped graphene sheets: the formation mechanism and application for high-performance supercapacitor electrodes. *Journal of Materials Chemistry A* **6**, 9997-10007 (2018).
- 2 Yang, C. *et al.* Interfacial electrochemical investigation of 3D space-confined MnFe<sub>2</sub>O<sub>4</sub> for high-performance ionic liquid-based supercapacitors. *Electrochimica Acta* **331**, 135386 (2020).
- 3 Zolfaghari, Y., Ghorbani, M. & Lashkenari, M. S. Electrochemical study on zeolitic imidazolate framework-67 modified MnFe<sub>2</sub>O<sub>4</sub>/CNT nanocomposite for supercapacitor electrode. *Electrochimica Acta* **380**, 138234 (2021).
- 4 Vignesh, V., Subramani, K., Sathish, M. & Navamathavan, R. Electrochemical investigation of manganese ferrites prepared via a facile synthesis route for supercapacitor applications. *Colloids and Surfaces A: Physicochemical and Engineering Aspects* **538**, 668-677 (2018).
- 5 Sankar, K. V. & Selvan, R. K. The preparation of MnFe<sub>2</sub>O<sub>4</sub> decorated flexible graphene wrapped with PANI and its electrochemical performances for hybrid supercapacitors. *Rsc Advances* **4**, 17555-17566 (2014).
- 6 Gupta, M., Tyagi, S. & Kumari, N. Electrochemical evaluation of highly stable Mn ferrite/PEDOT/rGO ternary nanocomposite for supercapacitor electrodes. *Journal of Materials Science: Materials in Electronics* **33**, 7838-7852 (2022).
- 7 Ghadimi, L. S., Arsalani, N., Tabrizi, A. G., Mohammadi, A. & Ahadzadeh, I. Novel nanocomposite of MnFe<sub>2</sub>O<sub>4</sub> and nitrogen-doped carbon from polyaniline carbonization as electrode material for symmetric ultra-stable supercapacitor. *Electrochimica Acta* **282**, 116-127 (2018).
- 8 Abdullah, M. *et al.* Partial sulfur doping induced variation in morphology of MnFe<sub>2</sub>O<sub>4</sub> with enhanced electrochemical performance for energy storage devices. *Korean Journal of Chemical Engineering*, 1-11 (2023).
- 9 Cai, W., Lai, T., Dai, W. & Ye, J. A facile approach to fabricate flexible all-solid-state supercapacitors based on MnFe<sub>2</sub>O<sub>4</sub>/graphene hybrids. *Journal of Power Sources* **255**, 170-178 (2014).
- 10 Geng, L., Yan, F., Dong, C. & An, C. Design and regulation of novel

- 
- MnFe<sub>2</sub>O<sub>4</sub>@ C nanowires as high performance electrode for supercapacitor. *Nanomaterials* **9**, 777 (2019).
- 11 Kwon, J. *et al.* Facile hydrothermal synthesis of cubic spinel AB<sub>2</sub>O<sub>4</sub> type MnFe<sub>2</sub>O<sub>4</sub> nanocrystallites and their electrochemical performance. *Applied Surface Science* **413**, 83-91 (2017).
- 12 Makkar, P. & Ghosh, N. N. Facile synthesis of MnFe<sub>2</sub>O<sub>4</sub> hollow sphere-reduced graphene oxide nanocomposites as electrode materials for all-solid-state flexible high-performance asymmetric supercapacitors. *ACS Applied Energy Materials* **3**, 2653-2664 (2020).
- 13 Wang, H., Sun, Y., Li, Z., Li, H. & Guo, P. Electrocapacitive behavior of colloidal nanocrystal assemblies of manganese ferrite in multivalent ion electrolytes. *Colloids and Surfaces A: Physicochemical and Engineering Aspects* **572**, 326-332 (2019).
- 14 Guo, P. *et al.* Electrochemical properties of colloidal nanocrystal assemblies of manganese ferrite as the electrode materials for supercapacitors. *Journal of Materials Science* **52**, 5359-5365 (2017).
- 15 Li, B., Fu, Y., Xia, H. & Wang, X. High-performance asymmetric supercapacitors based on MnFe<sub>2</sub>O<sub>4</sub>/graphene nanocomposite as anode material. *Materials Letters* **122**, 193-196 (2014).

## Chapter 13 Conclusions and Future work

Using innovative colloidal processing technology, several high-performance nanocomposite electrodes with high active mass loading were produced. These electrodes effectively utilized the synergistic effects of EDLC and pseudocapacitive material properties, contributing significantly to the development of hybrid supercapacitor devices.

The dissertation can be summarized as follows:

- 1)  $\text{Mn}_3\text{O}_4$  activation was analyzed for the first-time using STXM. The use of QC as a dispersant enhances the fabrication of composite electrodes with high active mass and capacitance. The effectiveness of QC, a catecholate-type polyaromatic compound, arises from its role in co-dispersing and efficiently mixing pseudocapacitive  $\text{Mn}_3\text{O}_4$  with conductive MWCNT additives. Capacitance changes were monitored using CV, EIS, and GCD, coupled with both VSRP and FSR activation methods. STXM analysis confirmed that the increase in capacitance was linked to the progressive oxidation of  $\text{Mn}_3\text{O}_4$  both on the surface and within the bulk of the particles, involving redox  $\text{Mn}^{3+}/\text{Mn}^{4+}$  reactions. This study's methods are expected to be applicable to other pseudocapacitive materials like  $\text{V}_2\text{O}_3$ .
- 2) For the first time, RL was used as a capping agent for  $\text{Mn}_3\text{O}_4$  nanoparticle

---

synthesis and as a dispersant for  $\text{Mn}_3\text{O}_4$  and CNTs, improving their dispersion and morphology. This facilitated the production of advanced cathode materials for asymmetric supercapacitors. Using RL in method 2 resulted in higher electrode capacitance than method 1, achieving up to  $6.11 \text{ F cm}^{-2}$ . This approach reduces the time-consuming activation typically required for  $\text{Mn}_3\text{O}_4$  electrodes, making it a popular material for supercapacitor applications.

- 3) Murexide was used as a capping agent for synthesizing  $\text{Mn}_3\text{O}_4$  nanoparticles and as a co-dispersant with CNTs. Its unique adsorption mechanisms facilitated enhanced electrostatic dispersion and mixing of these materials, significantly improving electrode capacitance in Method 2 compared to Method 1. This new approach led to record-high capacitances, achieving  $6.67 \text{ F cm}^{-2}$  from CV and  $7.55 \text{ F cm}^{-2}$  from GCD, eliminating the need for time-consuming electrode activation. This development marks a significant advancement in cathode technology for asymmetric supercapacitors in neutral electrolytes.
- 4) The use of TQ, CT, and GC as CAs significantly enhanced the synthesis of 5 nm  $\text{Mn}_3\text{O}_4$  platelet nanoparticles and their integration with conductive MWCNT additives. The catechol ligands of these agents facilitated their adsorption on  $\text{Mn}_3\text{O}_4$  during synthesis, contributing to a reduction in particle size. This reduction enabled the production of advanced  $\text{Mn}_3\text{O}_4$ -MWCNT cathodes with high active mass loadings, leading to substantially increased capacitance in a 0.5 M  $\text{Na}_2\text{SO}_4$  electrolyte. Notably, the smallest  $\text{Mn}_3\text{O}_4$  nanoparticles substantially

---

improved the electrochemical performance, achieving capacitance scores as high as  $9.13 \text{ F cm}^{-2}$  at low impedance, surpassing similar  $\text{MnO}_2$ -based cathodes.

This process also effectively eliminated the lengthy activation typically required for  $\text{Mn}_3\text{O}_4$ -based electrodes, setting a precedent for using nanostructured  $\text{Mn}_3\text{O}_4$  in high-capacity supercapacitor cathodes. This approach shows great promise for developing other advanced electrode materials for supercapacitors without the need for extensive activation.

- 5) HEBM enhanced the capacitances of  $\text{MnO}_2$ -b and  $\text{Mn}_3\text{O}_4$ -b, surpassing those of the as-prepared  $\text{MnO}_2$ -a and  $\text{Mn}_3\text{O}_4$ -a. QC proved effective as both a chelating dispersant for HEBM and a capping agent for  $\text{Mn}_3\text{O}_4$  synthesis, leading to significantly higher capacitance in  $\text{Mn}_3\text{O}_4$ -c electrodes. Specifically,  $\text{Mn}_3\text{O}_4$ -c reached capacitances of  $8.03 \text{ F cm}^{-2}$  via CP, matching those of  $\text{MnO}_2$ . The laborious activation process traditionally required for  $\text{Mn}_3\text{O}_4$  was substantially reduced for  $\text{Mn}_3\text{O}_4$ -b and eliminated for  $\text{Mn}_3\text{O}_4$ -c, making  $\text{Mn}_3\text{O}_4$ -c a promising candidate for high-capacitance, low-impedance hybrid aqueous metal electrodes. Continued development of that could potentially enhance performance further, leveraging the benefits of advanced synthesis techniques and solid solutions. STXM combined with electrochemical testing provided insights into the effects of HEBM and CAs on capacitance, revealing a blend of  $\text{Mn}^{2+}$ ,  $\text{Mn}^{3+}$ , and  $\text{Mn}^{4+}$  oxides in the materials tested. The predominance of the  $\text{MnO}_2$  phase in QC-capped  $\text{Mn}_3\text{O}_4$  correlated with higher capacitance and the elimination of

---

activation needs, pointing to further opportunities in  $\text{Mn}_3\text{O}_4$  development for improved energy storage solutions.

- 6) HEBM and catecholate-type GLC enabled the production of advanced ferromagnetic LSM electrodes that exhibited both high magnetization and capacitance. These electrodes demonstrated nearly ideal pseudocapacitive behavior without displaying redox peaks. Capacitances measured at  $4.59 \text{ F cm}^{-2}$  via CP significantly exceeded those reported in existing literature, achieved with low electrode resistance. Notably, the capacitance of ferromagnetic LSM in a positive potential range in neutral  $\text{Na}_2\text{SO}_4$  electrolyte matched or exceeded those of ferrimagnetic spinel ferrite-type electrodes in a negative potential range. This makes LSM electrodes highly suitable for cathodes in magnetic asymmetric devices with both ferromagnetic perovskite LSM cathodes and ferrimagnetic spinel anodes, operating effectively in neutral  $\text{Na}_2\text{SO}_4$  electrolytes. Additionally, fast charge-discharge cycling led to increased capacitance, likely due to changes in morphology.
- 7) MFO-based electrodes demonstrated pseudocapacitive behavior across both negative and positive potential ranges, enhanced by MRX, a redox-active dispersant, and GLC. These agents acted as dispersants and charge transfer mediators, boosting MFO-MRX's performance beyond that of MFO and MFO-GLC. MFO-MRX showed significantly higher capacitance in both potential ranges than previously reported, which facilitated the development of a

---

symmetric device with a capacitance of  $0.92 \text{ F cm}^{-2}$  at  $3 \text{ mA cm}^{-2}$ , outperforming existing models with a broad voltage window of  $1.6 \text{ V}$  and using an environmentally friendly neutral electrolyte. The device and its components showed robust cyclic stability, suggesting potential for applications in magnetic field-enhanced energy storage, capacitive water deionization, and devices exploiting magnetocapacitive effects.

The findings of this dissertation have tackled numerous challenges associated with the production of composite-type SC electrode materials and the construction of SCs. By employing galloyanine as a capping agent during the synthesis of  $\text{Mn}_3\text{O}_4$ , the fabricated electrode achieved a high capacitance of approximately  $8 \text{ F/cm}^2$ , which surpasses the capacitance of the  $\text{MnO}_2$  electrode at an identical active material mass loading of  $40 \text{ mg/cm}^2$ . Additionally, the pseudocapacitance properties of materials such as  $\text{Mn}_3\text{O}_4$ ,  $\text{MnO}_2$ , and LSM were enhanced through high-energy ball milling for 2 hours. This treatment significantly improved the performance of the electrodes, particularly for the LSM electrode, which exhibited a nearly sixfold increase in capacitance to  $3.75 \text{ F/cm}^2$ . Additional focus is required on the impact of magnetic properties on SC electrodes and devices. Certain spinel group substances, like  $\text{CuFe}_2\text{O}_4$ ,  $\text{MnFe}_2\text{O}_4$ , and  $\text{Y}_3\text{Fe}_5\text{O}_{12}$ , may be viable options for SCs. Observing the influence of material structure on electrochemical behavior is also crucial. To further advance the field, innovations in dispersants, colloidal synthesis methods, and HEBM along with further advancements, should be directed towards scalable manufacturing

and real-world applications.